

Multiple Degree of Freedom Force-State Component Identification

by

Brett P. Masters

B.S. Massachusetts Institute of Technology (1991)

SUBMITTED TO THE DEPARTMENT OF
AERONAUTICS AND ASTRONAUTICS
IN PARTIAL FULFILLMENT OF THE REQUIREMENTS
FOR THE DEGREE OF
S.M.
at the
Massachusetts Institute of Technology
February, 1994

© Massachusetts Institute of Technology, 1994. All rights reserved.

Signature of Author _____
Department of Aeronautics and Astronautics
January 12, 1994

Certified by _____
Edward F. Crawley
Professor of Aeronautics and Astronautics
Thesis Supervisor

Accepted by _____
Professor Harold Y. Wachman
Chairman, Department Graduate Committee

MASSACHUSETTS INSTITUTE
OF TECHNOLOGY

FEB 17 1994

LIBRARIES

Aero

Multiple Degree of Freedom Force-State Component Identification

by

Brett P. Masters

SUBMITTED TO THE DEPARTMENT OF AERONAUTICS AND ASTRONAUTICS
ON JANUARY 12, 1994, IN PARTIAL FULFILLMENT OF THE
REQUIREMENTS FOR THE DEGREE OF
S.M.

Force-state mapping is extended to allow the quasistatic characterization of realistic multiple degree of freedom systems whose constitutive relations are nonlinear, dissipative, coupled and depend on memory of past states. A general constitutive force-state model is formulated, which includes dynamic hysteresis phenomena typical of that found in deployable and rotary joint structures that include frictional interfaces. The model is specialized for deployable, erectable and rotary joint structures. A linear extended least squares analysis is used to evaluate component test inputs. Two iterative parameter identification algorithms are derived that depend on the nature of the component test inputs. A six degree of freedom force-state testing device was constructed, and used to obtain quasistatic data on deployable, erectable and rotary joint bays of typical space truss structures. Data and multiple degree of freedom model fits are presented that show the fundamental nonlinearities of these components. Structural dynamics models are assembled from updated component models and are used to predict the fundamental mode discrete frequency response with different levels of excitation amplitude, changes in component preload, and change in gravity environment. Predictions correlate well with modal data and modal parameter fits. Strongly nonlinear behavior is also predicted in structures containing the rotary joint.

Thesis Supervisor: Professor Edward F. Crawley
MacVicar Faculty Fellow, Professor of Aeronautics and Astronautics
Director, Space Engineering Research Center

Acknowledgments

First and foremost this thesis is dedicated, *con amore*, to my parents, Yvonne and Peter Masters. Without their foresight and self sacrifice I would not have had an opportunity to expand my perspective on the nature of things.

To my best friend and sweetheart, Debby, thank you for your caring, patience and advice.

I am indebted to my mentor, Ed., who used the tiller when necessary and let nature do the rest.

Special thanks to Tienie vanSchoor for his ideas and help. Thanks to Mark Barlow and Mark Anderson for their help.

Cheers to my family, especially my grandmother who relentlessly writes, reminding me of my roots.

Cheers to *the boys* in Aotearoa, a coupla trays of Red should fix them.

Thanks to the undergraduates that helped me. Chunder, Deb, and T.J.

Contents

1	Introduction	15
2	Background	19
2.1	MODE structures	19
2.2	Single degree of freedom force-state mapping	23
3	Multiple degree of freedom component modeling	27
3.1	General component model framework	28
3.2	Choosing the d.o.f. and the parameters of the component model . . .	29
3.3	Modeling specifics	31
3.4	Summary	50
4	Component model identification	51
4.1	Applying loads	51
4.2	Linear least squares parameter identification	56
4.3	Nonlinear least squares parameter identification	60
4.4	Weakly coupled loads identification	61
4.5	Decoupled d.o.f. identification	63
4.6	Summary	65
5	Experiment Hardware and Procedure	67
5.1	Hardware	67
5.2	Procedure	83
6	Experimental Results	87
6.1	Calibration bay	88
6.2	Adjustable pretension deployable bay	90
6.3	Erectable Bay	108
6.4	Alpha joint bay	115
6.5	Summary	130

7	Assembled component modeling and modal prediction	131
7.1	Assembled component structures	131
7.2	Model refinement	134
7.3	Iterated Response	136
7.4	Predictions and MODE modal data	141
7.5	Summary	154
8	Conclusions and recommendations	155
	References	159
A	Off-diagonal block models	163
A.1	Erectable bay	163
A.2	Alpha joint bay	164
B	Component tester drawings	167

List of Figures

2.1	Three test configurations of the STA, (Baseline, Alpha and L).	20
2.2	Torsion and shearing acceleration transfer functions for MODE base- line with high preload in adjustable pretension bays.	21
2.3	Torsion and shearing acceleration transfer functions for MODE base- line with low preload in adjustable pretension bay.	22
2.4	Torsion acceleration transfer function for MODE alpha with high preload in alpha joint.	23
2.5	Torsion acceleration transfer function for MODE alpha with low preload in alpha joint.	23
2.6	Representative single degree of freedom force-state maps.	25
3.1	Cantilevered component modeled as a twelve d.o.f. beam element. Twelve reactions, twelve applied loads and eight measurements of dis- placement are resolved into six generalized reactions, applied loads and unconstrained d.o.f. respectively.	32
3.2	Single slip dynamic hysteresis model.	35
3.3	An example dynamic hysteresis model, F_M , for the MODE deployable bay where the initial stiffness, K_b , is 1, and the slip force, F_s , is 1. . .	37
3.4	Erectable loose joint model including one-way displacement and veloc- ity dependent dissipation.	39
3.5	Examples of first order analytic nonlinearities for the erectable with loose joints.	40
3.6	Alpha joint axial rotation model with macro slip displacement depen- dent friction represented as the vertical spring arrangement and micro slip distribution represented by the multiple horizontal spring arrange- ments. The single spring K_1 represents a backbone stiffness.	42
3.7	Example slip distribution (a) \mathcal{P} which bifurcates into slipped, (b), and non slipped, (c), distributions \mathcal{P}_1 and \mathcal{P}_2 at every change in sense of direction. δ_b is determined at the change in sense of direction.	44

3.8	Computation flow of axial moment transmitted force from the micro slip distribution model.	45
3.9	Dynamic hysteresis model, F_{66} , for the MODE alpha joint where the initial stiffness, K_F , is 1, and the all slip deflection, δ , is 3.	47
3.10	Dynamic hysteresis model, F_{66} , for the high amplitude macro friction operation of the MODE alpha joint.	48
3.11	Deployable slip distributions \mathcal{P} . Initially all slip at δ then return slip distributions depend on the modified coordinate ξ so that the integral accumulation of slip force yields F_s for the return all slipped condition.	50
4.1	Typical applied load time history (odd about the peak ramp amplitude).	52
4.2	Linear single d.o.f. phase plane response sampled at $35.5\omega_o$	53
4.3	Zoom of phase plane response (ω_o Hz input sampled at $35.5\omega_o$ Hz) where the dashed boxes represent force-state map holes.	54
4.4	Block diagram of an Alternating Frequency Time-domain direct algorithm.	63
5.1	Plan and elevation of the MODE component tester.	69
5.2	MODE component tester with alpha joint bay as the test component.	71
5.3	Electronics block diagram of MODE component tester.	74
5.4	Simple calibration bay schematic with indicated test directions.	75
5.5	MODE partially deployed four bay section.	76
5.6	Deployable corner fitting, truss side view, with tension cable end receptacles (underneath) and longeron pin mechanism.	76
5.7	Knee joint.	77
5.8	Deployable longeron.	77
5.9	Deployable batten frame.	78
5.10	Tension cleat.	79
5.11	Erectable strut.	79
5.12	Erectable bay side view.	80
5.13	Erectable strut, standoff and node in a typical corner fitting.	81
5.14	Alpha joint in its operational configuration with high preload on the friction pad.	82
5.15	Alpha joint in its separated configuration with outer ring removed from the central mechanism.	83
6.1	High pretension MODE deployable bay data (left column) and model fits (right column) for the decoupled u_y , θ_y and θ_z applied load directions.	92

6.2	High pretension MODE deployable bay data, 90% linear stiffness removed, force-state maps for u_y , θ_y and θ_z tests (left column) with corresponding error maps (right column).	93
6.3	Medium pretension MODE deployable bay data (left column) and model fits (right column) for the u_y , θ_y and θ_z applied load directions.	95
6.4	Medium pretension MODE deployable bay data force-state maps for u_y , θ_y and θ_z (left column), 90% linear stiffness removed, with corresponding model fit error maps (right column).	96
6.5	Low pretension MODE deployable bay data (left column) and model fits (right column) for the u_y , θ_y and θ_z applied load directions.	98
6.6	Low joint preload MODE bay data force-state maps for u_y , θ_y and θ_z (left column), 90% linear stiffness removed, with corresponding model fit error maps (right column).	99
6.7	Measured data for MODE bay with locked and free joints with bracing wires removed.	100
6.8	Tight joint erectable MODE bay data force-state maps for diagonal u_x , θ_x and θ_z (left column), 90% linear stiffness removed, with corresponding model fit error maps (right column).	109
6.9	Tight joint erectable MODE bay data force-state maps for coupling in u_y , u_z , θ_y and θ_z tests, 90% linear stiffness removed. Left and right columns contrast the symmetric data; <i>e.g.</i> top row data corresponds to models F_{41} (left) and F_{14} (right).	110
6.10	7.5 Hz erectable MODE bay data force-state maps for diagonal u_x , u_y , u_z , θ_x , θ_y and θ_z tests. Connecting joints loosened.	112
6.11	7.5 Hz erectable MODE bay model error force-state maps for diagonal u_x , u_y , u_z , θ_x , θ_y and θ_z tests. Connecting joints loosened.	114
6.12	5 Hz MODE alpha joint data force-state maps for diagonal F_x , F_y , F_z , M_x , and M_y tests. Alpha joint in high preload.	117
6.13	5 Hz MODE alpha joint data force-state bicubic model error maps for diagonal F_x , F_y , F_z , M_x , and M_y tests. Alpha joint in high preload.	118
6.14	MODE alpha joint high preload low amplitude M_z data and dynamic hysteresis model.	121
6.15	MODE alpha joint high preload low amplitude M_z force-state map data and model fit error map.	122
6.16	MODE alpha joint high preload high amplitude M_z load-stroke data and fit model.	122

6.17	5 Hz MODE alpha joint data force-state maps for diagonal F_x , F_y , F_z , M_x , and M_y tests. Alpha joint in low preload.	124
6.18	5 Hz MODE alpha joint data force-state bicubic model error maps for diagonal F_x , F_y , F_z , M_x , and M_y tests. Alpha joint in low preload. . .	125
6.19	MODE alpha joint low preload low amplitude M_z data and dynamic hysteresis model.	127
6.20	MODE alpha joint low preload low amplitude M_z force-state map data and model fit error map.	128
6.21	MODE alpha joint low preload high amplitude M_z load-stroke data and fit model.	129
7.1	Ten d.o.f. model of MODE torsion axis. Adjustable pretension bay models are F_{D6i} . The center spring is the erectable F_{E6} or alpha F_{A6} respectively for the baseline and alpha analysis.	133
7.2	Flow for Direct Linearization Analysis.	139
7.3	Third generation updated and non updated ground baseline predictions.	141
7.4	Ground <i>vs</i> space comparison of modal data and 10 d.o.f. predicted response for MODE baseline with high pretension in the adjustable pretension bay.	144
7.5	Ground <i>vs</i> space comparison of modal data and 10 d.o.f. predicted response for MODE baseline with medium pretension in the adjustable pretension bay.	145
7.6	Ground <i>vs</i> space comparison of modal data and 10 d.o.f. predicted response for MODE baseline with low pretension in the adjustable pretension bay.	146
7.7	Ground <i>vs</i> space comparison of modal data and 10 d.o.f. predicted response for MODE alpha with high preload in the alpha joint bay. .	149
7.8	Comparison of ground modal data and 10 d.o.f. predicted response for MODE alpha with low preload in the alpha joint bay.	150
7.9	Comparison of space modal data and 10 d.o.f. predicted response for MODE alpha with low preload in the alpha joint bay.	151

List of Tables

3.1	Erectable example model parameters.	40
6.1	Six d.o.f. applied load to unconstrained d.o.f. compliance model of the calibration bay. Compliances are normalized by 10^{-5} and are given in units of m/N while σ_c is given in percent.	89
6.3	Six d.o.f. reaction force to unconstrained d.o.f. identification of the MODE bay in SI units (omitted for clarity).	104
6.4	Six d.o.f. off-diagonal block parameter discrepancies of the MODE deployable bay, using estimated reaction forces <i>vs.</i> using measured reaction forces (given in percent of the measured reaction force model parameters), at 7.6 Hz test frequency. For each parameter column the percentage difference in identified parameter is followed by the parameters participation percentage in the test force range, as predicted by the identification.	105
6.5	Six d.o.f. stiffness comparison of the MODE adjustable bay for original and replaced wires at 7.6 Hz test frequency(given in percent of original model parameters). For each parameter column the percentage difference in identified parameter is followed by that parameters participation percentage in the test force range.	107
6.6	Six d.o.f. applied load to unconstrained d.o.f. model of the MODE erectable bay in SI units (<i>e.g.</i> N/m , N/m^2 , N/m^3 and $N/m/s$ respectively for the first three diagonal elements) for 7.5 Hz test frequency. Each identified parameter is followed by its participation in the test applied load range.	111
6.7	Six d.o.f. bicubic model of the loosened joint MODE erectable bay, in SI units, for 7.5 Hz test frequency. Each identified parameter is followed by its participation in the test applied load range.	113
6.9	Low amplitude micro slip model parameters fit to the MODE alpha joint high preload M_z data.	120

6.10	High amplitude macro slip model parameters fit to the MODE alpha joint high preload M_z data.	123
6.12	Low amplitude micro slip model parameters fit to the MODE alpha joint low preload M_z data.	128
6.13	High amplitude macro slip model parameters fit to the MODE alpha joint low preload M_z data.	129
7.1	Input Torques for the MODE models.	142
7.2	Comparison of ground modal test and predicted natural frequencies and damping ratios for the MODE baseline configuration.	147
7.3	Comparison of space modal test and predicted natural frequencies and damping ratios for the MODE baseline configuration.	147
7.4	Comparison of ground modal test and predicted natural frequencies and damping ratios for the MODE alpha configuration.	152
7.5	Comparison of space modal test and predicted natural frequencies and damping ratios for the MODE alpha configuration.	153
A.1	Six d.o.f. reaction force to unconstrained d.o.f. model of the MODE erectable bay in SI units (<i>e.g.</i> N/m , N/m^2 , N/m^3 and $N/m/s$ respectively for the first three diagonal elements) for 7.5 Hz test frequency. Each identified parameter is followed by its participation in the test applied load range.	163
A.2	Six d.o.f. reaction force to unconstrained d.o.f. bicubic model of the high preload MODE alpha joint, in SI units, for 5 Hz test frequency. Each identified parameter is followed by its participation in the test applied load range.	164
A.3	Six d.o.f. (reaction force to unconstrained d.o.f.) bicubic model of the high preload MODE alpha joint continued.	165
A.4	Six d.o.f. reaction force to unconstrained d.o.f. bicubic model of the low preload MODE alpha joint, in SI units, for 5 Hz test frequency. Each identified parameter is followed by its participation in the test applied load range.	165
A.5	Six d.o.f. (reaction force to unconstrained d.o.f.) bicubic model of the low preload MODE alpha joint continued.	166

Chapter 1

Introduction

High performance prediction of open and closed loop structural response requires an accurate model of the structure, including potentially nonlinear joints and mechanisms. Typically a structural model evolves through three stages, beginning with a first generation model derived from design drawings and handbook material data. This model is available early in the design cycle, but its accuracy is limited by poor modeling (due to inexact elements, arbitrary simplifications, etc.), mismodeling (due to human error), and nonmodeling (of effects such as nonlinearities and dissipation).

A second generation of the model is formed by updating the original model with measurements made on structural components. Such measurements are commonly used to update the mass and stiffness terms [3]. However, within the state of the art, it is difficult to predict nonlinear and dissipative behavior based on component measurements. Third generation models incorporate information derived from dynamic modal testing data [3]. Full vehicle dynamic ground testing is not always possible, and when conducted yields data corrupted by gravity and suspension effects [46, 47, 32, 35]. In flight testing provides the most reliable model, but usually very late in the development program.

Nonlinearities within typical space structures complicate dynamics testing and modeling [4, 5, 8, 38]. Deployable structures typically include hinges, latches and tensioning cables for deployment. These mechanisms introduce nonlinearities into the structure. Deadband destiffening and accumulated microfriction from hinge and latch mechanisms contribute softening and increased dampening to a structure with increased excitation levels. Tensioning cables, that preload the structural members to significant fractions of their buckling loads, may slacken with dynamic excitation of the system providing a mechanism for higher harmonic generation within the structure. Dynamics testing of structures that include nonlinear components is an arduous task. Both forward and backward sine sweep tests at multiple forcing levels are typ-

ically performed. These tests take significantly more time than the typical random input linear system identification.

There is clearly a need to improve the process of component testing for the purposes of model updating. Three approaches are under development: substructural modal testing, multiple boundary condition testing, and force-state mapping. Substructural modal testing is most valuable when the modes of a substructure are in the same frequency range as the modes of the full structure [9]. Multiple boundary condition modal testing also obtains dynamic information, but at elevated frequencies and with artificial boundary conditions [46, 47]. Both techniques rely on the linearity of the structure when extrapolating the results. Force-state mapping, in which the weakly nonlinear behavior of a component is measured quasi statically, can be used with nonlinear and dissipative structures, but to date has been limited to single degree of freedom systems [11].

The objective of this work is to extend force-state mapping to the characterization of realistic multiple degree of freedom systems whose constitutive relations are nonlinear, dissipative, coupled and depend on memory of past states. The procedure produces the identified component information necessary for use in updating second generation structural dynamic models. A further objective of this work is to use the identified component models to provide simple assembled (nonlinear) component model predictions in terms of natural frequency and damping ratio shifts with different levels of excitation and change in gravity environment. System parameter bounds such as these are useful for structural control [21].

Research in this report is motivated by the results for the Structural Test Article (STA) of the Middeck 0-gravity Dynamics Experiment (MODE). A brief background of MODE is presented in chapter 2. Ground and space dynamics testing and Finite Element modeling of the MODE STA is discussed by Barlow [2, 15, 14]. chapter 2 also presents essential background on single degree of freedom (d.o.f.) force-state mapping [11, 12].

This report focuses on applying multiple d.o.f. force-state component identification to MODE structural components. Multiple d.o.f. component modeling is the topic of chapter 3. chapter 3 provides a general framework in which to model nonlinear component constitutive relations before turning attention to the specific MODE component models. Specifically, fundamental laws postulated by Prandtl [33] are unified with polynomial approximation theory [30] to provide both analytic and non analytic models of components.

Identification of the nonlinear component models of chapter 3 from component test data is the topic of chapter 4. Acquiring component test data by specifying a set

of test inputs is first discussed. *Ad hoc* identification algorithms are next developed which use data fitting routines that minimize the sum squared error between the model and the data. chapter 5 presents the unique component testing hardware designed and built to acquire the desired component test data. The tested component hardware is also described. The second major topic of chapter 5 is the experimental procedure used when testing a component. The procedure includes test calibration techniques as well as a description of estimation software used to prepare the data for the identification algorithms of chapter 4.

Component data and model fits are presented in chapter 6. A nominally linear calibration component is presented to justify the methodology of this report. Nonlinear MODE component data shows that components consisting of multiple frictional interfaces result in systems that include nonlinear memory. This result is fundamental to this report. A crucial link to this result is the introduction of memory models, which depend on bifurcating statistics and represent multiple frictional interfaces within a component (chapter 3). The multiple d.o.f. force-state identification method is shown to be a powerful tool for understanding inherent structural nonlinearity at a component level.

Simple models of the entire MODE structure are found by assembling the component models. Discrete frequency domain predictions based on these models are made using an algorithm developed for this report. The algorithm presented successively linearizes a nonlinear model at each excitation frequency and amplitude, converging on a linearized time domain response. The predicted frequency response, natural frequencies and damping ratios are compared to the MODE dynamics data presented by Barlow [2].

Chapter 2

Background

This chapter will present the background for this report, which includes the motivating experiment and existing theory for force-state identification. The motivating experiment is an open loop dynamics test of a typical jointed truss structure. Existing theory for component identification has been developed for single degree of freedom memoryless component testing and must be extended to include nonlinear memory mechanisms.

2.1 MODE structures

Research on component testing for model updating is motivated by the results for the Structural Test Article (STA) of the Middeck zero-gravity Dynamics Experiment (MODE). Open loop dynamics testing of the STA was performed both on orbit (on STS-48) and in the laboratory. The rationale for the experiment was to provide a benchmark study of the dynamics of multi-element, internally statically indeterminate space structures in both zero- and one-gravity.

The objectives of the MODE program are threefold. First, to determine the influence of the ground test technique on the measured properties of the STA. Second, to determine the influence of 0-gravity on the measured modal properties of the STA, and compare these with ground measurements. Third, to measure the linear and nonlinear component properties, and predict/correlate these with measured ground and on-orbit dynamics data. Results corresponding to the first two objectives are presented by Barlow and Crawley [2]. Results corresponding to the third objective are presented in this report herein.

The STA is an engineering scale model which consists of sections of wire braced deployable bays, linked in several configurations by erectable bays and/or a one bay rotary joint (see Figure 2.1). The deployable sections are four bays in length and

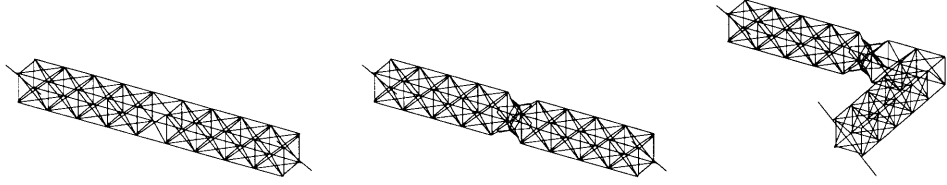


Figure 2.1: Three test configurations of the STA, (Baseline, Alpha and L).

joined by an erectable bay to give the nine bay baseline structure. The erectable bay is replaced by an articulating rotary (alpha) joint to give the alpha configuration. A combination of the deployable, alpha joint and erectable bays are used to construct the L configuration.

In one of the deployable sections an adjustable pretension bay was incorporated with three possible pretension settings in the bracing wires. The highest pretension setting is the same as the nominal pretension for the remainder of the fixed pretension bays of the deployable section. Two preload settings are available in the articulating joint; high, which essentially locks the rotation of the unit below a high differential torque and low, which allows mechanism rotation of the unit at low differential torque.

Input to the structure was applied at an end node by a proof mass actuator. Motion was sensed by eleven distributed accelerometers and was archived along with the measured input in a self contained experiment control computer. The measured structural response was to a steady state sinusoidal input at a preset series of several amplitudes.

The measured differences in the zero- and one-gravity linear and nonlinear behavior are quite striking. On average the data show softening in resonance frequency of 1% and increased damping of 0.5% in zero-gravity relative to one-gravity tests [15]. The data in both one- and zero-gravity show weak to moderate nonlinear response characteristics as a function of input force amplitude, with the nonlinearity causing softening and dampening with increased force, decreased pretension, and reduction in gravity level.

Figure 2.2 is an example of the space and ground acceleration/input force transfer function for the baseline (straight) configuration with high pretension in the adjustable bay. For the ground data reproduced in this chapter a 1 Hz plunge suspension system was used. Further details are reported in Barlow [2]. The nature of the nonlinear response suggests that both a softening spring and dynamic hysteresis phenomenon are present in the MODE deployable bay along with some other source of increased dissipation in space. The same transfer functions are shown in Figure 2.3 for low pretension in the adjustable pretension bay. Again the nonlinear nature of the structure is shown by the softening dynamic hysteresis, however the space data

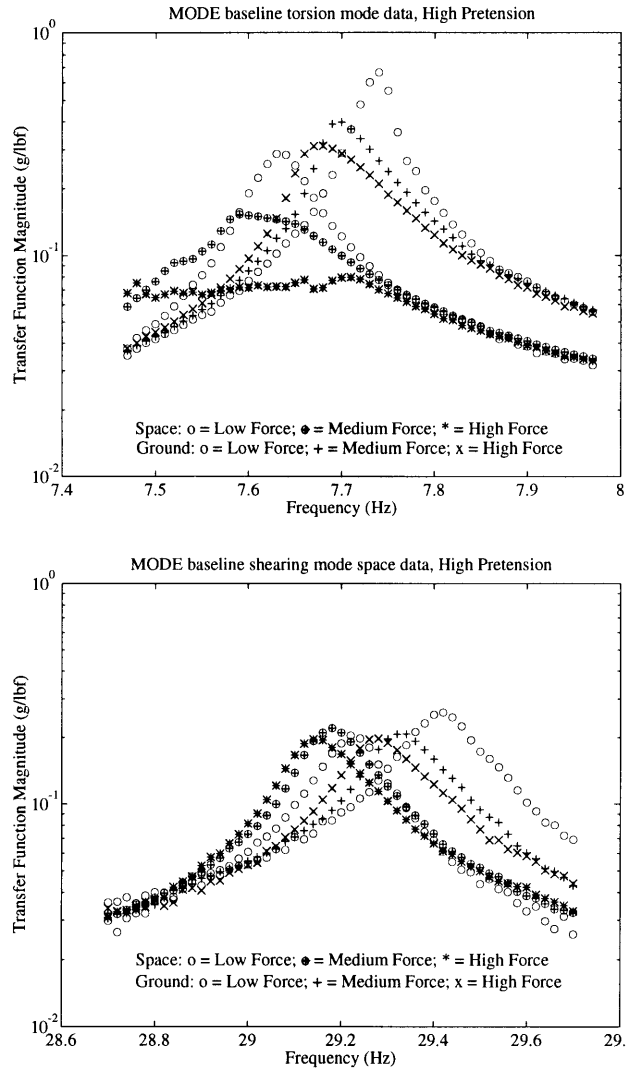


Figure 2.2: Torsion and shearing acceleration transfer functions for MODE baseline with high preload in adjustable pretension bays.

appears to be more adversely affected by the drop in bay pretension. Figures 2.4 and 2.5 are examples of the space and ground acceleration transfer functions for the alpha configuration torsion mode. The alpha joint high preload data again shows softening dynamic hysteresis with increased amplitude of input. The space data also shows a severely dampened and flattened response at high amplitudes. Low preload data shows jump phenomena in space that does not occur in the ground tests. Clearly, a modeling process by which the engineer can gain insight into the zero-gravity response from one-gravity experiments is required.

The models of the MODE STA which existed prior to flight were typical of first generation, undamped linear finite element models. Of course they failed to predict damping, changes in damping, changes in frequency and nonlinear behavior witnessed

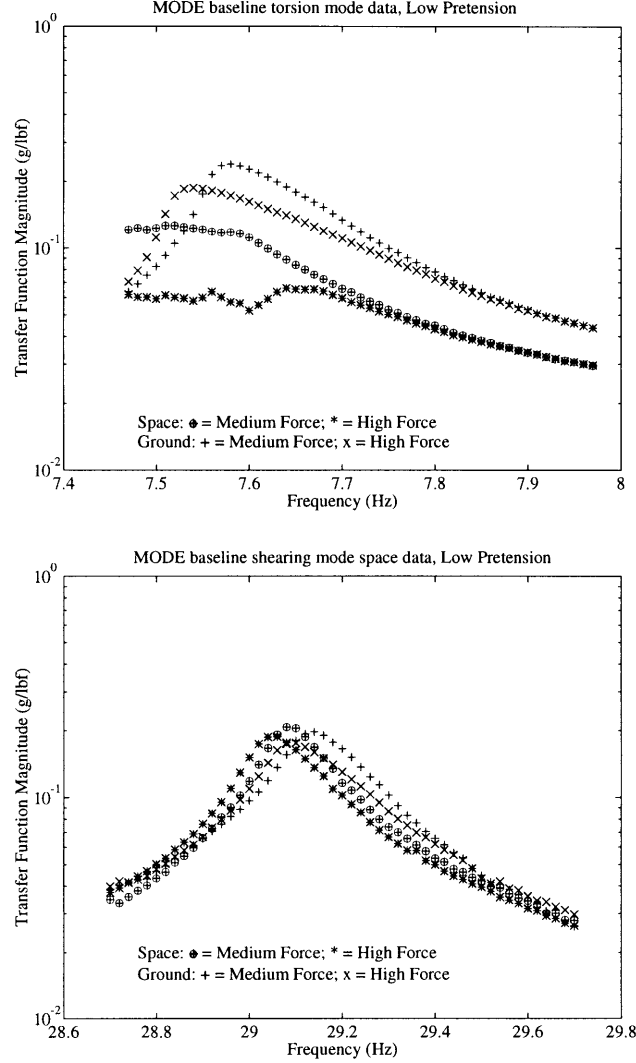


Figure 2.3: Torsion and shearing acceleration transfer functions for MODE baseline with low preload in adjustable pretension bay.

in the modal data. A modeling process which captures the linear effects of gravity stiffening and suspension is now available [35]. A process to characterize the damping and nonlinear behavior, and to obtain data for second generation model updates is presented in this report.

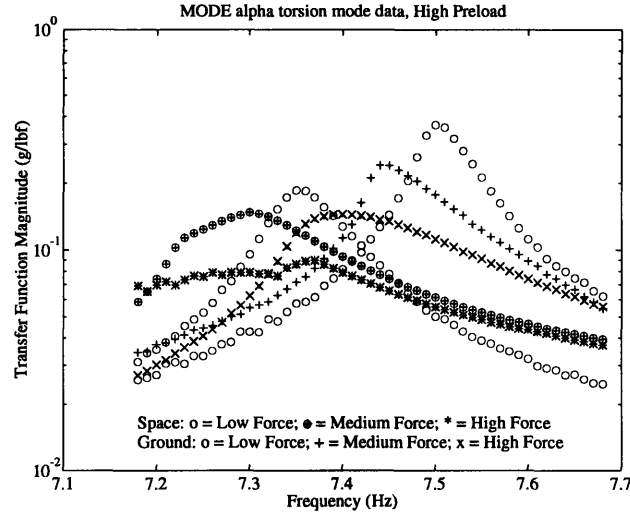


Figure 2.4: Torsion acceleration transfer function for MODE alpha with high preload in alpha joint.

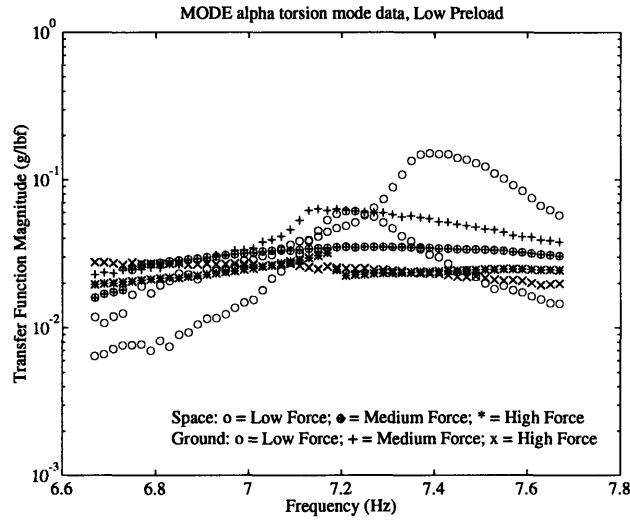


Figure 2.5: Torsion acceleration transfer function for MODE alpha with low preload in alpha joint.

2.2 Single degree of freedom force-state mapping

The basis for the characterization of damping and nonlinear behavior of a structural component can be found in single d.o.f. force-state mapping. Traditionally, the modeling of local nonlinearities (such as joints) has been approached using load-stroke test information. Transmitted force that depends explicitly on velocity or on true memory effects can only be (incompletely) inferred from static force-displacement measurements alone. This deficiency is addressed by quasi static force-state mapping.

Single degree of freedom force-state mapping of systems without memory has been developed for simple joints [11, 12] and applied to joints such as those incorporated in Langley Research Center's Mini Mast [8].

In single degree of freedom force-state mapping the force transmitted through the joint is represented as a function of the displacement and velocity across the joint. Equations 2.1 and 2.1 represent such a function.

$$\begin{aligned}
 f_{T_i} = & K_1 x_i + K_3 x_i^3 + K_n x_i^n + K_{DB} + F_f \text{sign}(\dot{x}_i) \\
 & + C + B_1 \dot{x}_i + B_n \dot{x}_i^n + G |x_i| \text{sign}(\dot{x}_i) \\
 & + H(x_i, \dot{x}_i) + B_{DB}
 \end{aligned}$$

$$K_{DB} = \begin{cases} k_{DB}(x_i - x_{DB}) & \\ 0 & \\ k_{DB}(x_i + x_{DB}) & \end{cases} \quad B_{DB} = \begin{cases} b_{DB}(\dot{x}_i) & x_{DB} \leq x \\ 0 & -x_{DB} \leq x \leq x_{DB} \\ b_{DB}(\dot{x}_i) & x \leq -x_{DB} \end{cases} \quad (2.1)$$

Analytic polynomials in stiffness and dissipation are present in Equation 2.1, *e.g.* $K_1 x_i + K_3 x_i^3$ and $B_1 \dot{x}_i + B_n \dot{x}_i^n$. Non analytic dependencies, *e.g.* $F_f \text{sign}(\dot{x}_i)$ and K_{DB} , are also represented. An additional memory term is added in Equation 2.1, $H(x_i, \dot{x}_i)$, as a general conditional dependence on the history of past states.

Experimentally, the force-state mapping approach requires the measurement or estimation of force, acceleration, displacement and velocity. The measured force, f_{T_i} , is corrected for the inertia *force*, $m\ddot{x}$, and conceptually plotted versus the displacement and velocity *states* of the system to produce the force-state map. Figure 2.6 shows representative maps of a linear plus cubic spring, and a deadband spring with coulomb friction (note the change in force as the velocity changes sign). If the joint dynamics are sufficiently high in frequency, then quasi static testing can be performed without the explicit inertia correction. In practice the quasi static testing should be performed a decade below the first fundamental frequency of the joint, in which case less than one percent systematic error is present when neglecting the joint inertia.

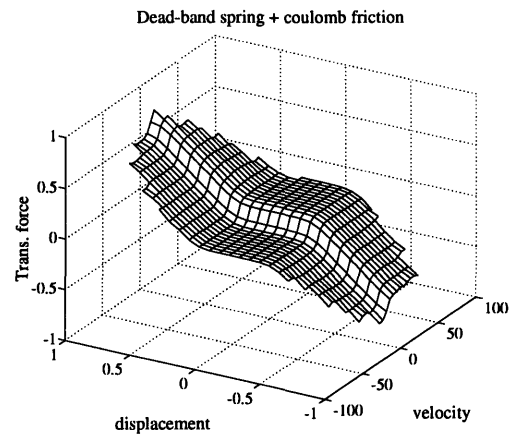
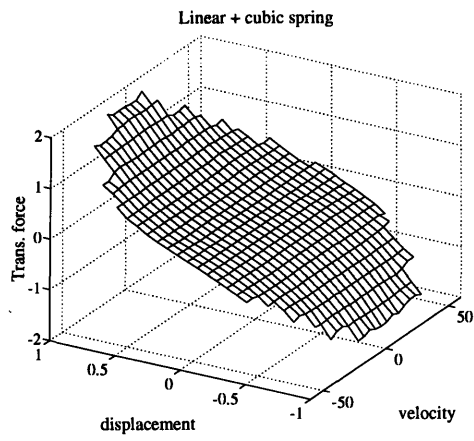


Figure 2.6: Representative single degree of freedom force-state maps.

Chapter 3

Multiple degree of freedom component modeling

In order to extract multiple degree of freedom (d.o.f.) structural component constitutive parameters, an extension of single degree of freedom force-state mapping is required. The extension expands the single d.o.f. analysis to include the coupling effects of a multi degree of freedom system. The multiple d.o.f. system description is similar to that presented in the single d.o.f. analysis in that it includes both analytic and non analytic terms that relate the motion of a component to the structural force transmitted by the component. In addition, memory terms have been added (see section 2.2) to the single d.o.f. analysis to incorporate the conditional nature of frictional structural response.

Multiple d.o.f. force-state mapping requires implicit choices of d.o.f. of the component model. Given the chosen d.o.f. and measurement data a set of parameters is chosen that relate the d.o.f. to the measured transmitted structural force.

This chapter illustrates the series of choices made when modeling the MODE component hardware. First, a general component model framework is developed. Within the component model, analytic, non analytic and memory terms are separated and summed to yield the overall transmission forces. Choices of d.o.f. of the component model and parameterization of these d.o.f. are then addressed. The unification of the d.o.f. of a component model together with a choice of parameters (a particular parameterization of the d.o.f.) defines a specialized component model. Before individual component model descriptions an argument is made for identification of a component constitutive model from applied load, reaction force and unconstrained d.o.f. measurements only. Next models are developed for specific components of the MODE hardware, the adjustable pretension bay, the erectable bay and the alpha joint. Knowledge of the individual MODE component data is required to make specific pa-

parameter choices for the component model. Brief forward references to the measured component data are given at the beginning of each of the component sections.

3.1 General component model framework

Extending single d.o.f. force-state mapping to multiple d.o.f. requires a general component model framework. As with the single d.o.f. analysis, small deflections are assumed, so as to capture the localized nonlinearities of a component about a desired operation point, and to eliminate any nonlinearity in the inertia tensor.

Equation 3.1 describes the modeled structural force transmitted by the component.

$$\begin{aligned}
F_{Ti} = & F_{1D}(x_i, \dot{x}_i) & + & F_{1ND}(x_j, \dot{x}_j)_{j \neq i} \\
& + F_{2D}(x_i^2, x_i \dot{x}_i, \dot{x}_i^2) & + & F_{2ND}(x_i x_j, x_i \dot{x}_j, \dot{x}_i \dot{x}_j)_{j \neq i} \\
& + F_{3D}(x_i^3, x_i^2 \dot{x}_i, x_i \dot{x}_i^2, \dot{x}_i^3) & + & F_{3ND}(x_i x_j x_k, x_i x_j \dot{x}_k, x_i \dot{x}_j \dot{x}_k, \dot{x}_i \dot{x}_j \dot{x}_k)_{j,k \neq i} \quad (3.1) \\
& + F_{DNA}(x_i, \dot{x}_i) & + & [NDNA] \\
& + F_{DM}(x_i, \dot{x}_i) & + & [NDM] + [HOT]
\end{aligned}$$

F_{Ti} is the i th generalized transmitted force through the component. F_{1D} , F_{2D} and F_{3D} represent first, second and third order *Diagonal* dependencies of the generalized force on the generalized displacements. F_{DNA} similarly represents *Diagonal Non Analytic* dependencies such as dead bands, material damping and Coulomb friction. These terms were present in the previously developed single d.o.f. force-state characterization [11]. Appended is the term F_{DM} describing *Diagonal Memory*. F_{DM} describes the conditional dependence of the i th transmitted force on the history of the i th d.o.f. and its rate. The added terms F_{1ND} , F_{2ND} and F_{3ND} describe the *Non Diagonal* coupling of the i th generalized force to the j th degree of freedom, in analytic form to third order. *Non Diagonal Non Analytic*, *Non Diagonal Memory*, and higher order analytic terms could be added to completely generalize the formulation.

F_{Ti} is the transmitted force excluding inertia terms. If the dynamic displacements are small, then the component inertia can be computed and subtracted from the total transmitted force to yield the net structural force of Equation 3.1. Alternatively, quasi static identification can be performed. If the dynamic displacements are large, then care must be taken to compute or possibly identify a nonlinear inertia matrix.

For the modeling in this report the dynamic displacements are assumed to be small and quasi static identification is performed.

3.2 Choosing the d.o.f. and the parameters of the component model

Given the general component model of the Equation 3.1 a choice of d.o.f. of the model must first be made. Parameters that relate these d.o.f. to the modeled transmitted force are then defined. This section details the choice of d.o.f. of the component model and the parameterization of these d.o.f. Analytic parameterizations are first presented as a simple and particular parameterization of the chosen d.o.f. Initial analytic parameterizations are also used as a tool for identifying and evolving a parameter set to include non analytic terms.

The choice of d.o.f. of the component model is influenced by the final structure analysis goal. If the identified component information is to be included in an assembled component model then the d.o.f. of the component model should be consistent with the d.o.f. of the assembled component model. Examples of assembled component models are linear finite element and Raleigh-Ritz structural dynamics formulations.

Another influence in the choice of d.o.f. of the component model is the component testing itself. Measurements are made in the laboratory in a physical coordinate system. The components were designed in a physical coordinate system. The nonlinearities of a component are therefore best presented in terms of physically independent d.o.f. rather than combinations of those physically independent d.o.f. An example of combined d.o.f. is the weighted summation of linear displacement and rotation d.o.f.

Given the choice of d.o.f. of the component model a parameter set that relates the d.o.f. to the transmitted force can be defined.

Modeling the transmitted force, F_{Ti} , as shown in Equation 3.1 is divided into analytic and non analytic terms. Analytic terms of order greater than one are strictly polynomial descriptions and are often used to describe measured nonlinear material properties that are smooth in the displacement variable. However, high order analytic terms are also used to provide a heuristic parameterization of potentially nonlinear force-state maps without regard to the physical mechanism or phenomena present. Modeling of nonlinear component mechanisms such as microfriction and dead-bands results in the addition of non analytic and memory terms, which are often conditional.

Pure analytic parameterizations of the component model can be made with no knowledge of the underlying physical mechanisms. Typical analytic parameterizations are cubic, bicubic, tricubic, biquartic, triquartic, quintaquartic, *etc.* For example Equation 3.2 represents a bicubic in the d.o.f. x_j with associated parameteriza-

tion, C_{mn} .

$$F_{T_i} = \sum_{m=0}^3 \sum_{n=0}^3 C_{mn} x_j^m \dot{x}_j^n \quad (3.2)$$

The prefix bi refers to the order of the states and the suffix cubic refers to the order of the analyticity. In Equation 3.2 the states representing the d.o.f. are a displacement and codirectional rate pair, x_j and \dot{x}_j .

Analytic models capture local curvature and slope only in the measured transmitted force range and are unreliable for extrapolation outside the data range. Analytic models also lose physical significance with increasing order. However, analytic parameterizations make good approximate models within a given range as they provide a model that couples the displacement and displacement rate states.

In order to model non analytic and memory terms in Equation 3.1 it is convenient to first fit high order analytic component models to the data. The high order analytic component models are used to approximate coupled d.o.f. effects in the measured transmitted force. Equations 3.3 through 3.5 show how third order analytic parameterizations are used to approximate the measured transmitted force due to two d.o.f., x_1 and x_2 .

$$f_{T_1} = F_{T_1} + e_1 \quad (3.3)$$

$$F_{T_1} = \sum_{m=0}^3 \sum_{n=0}^3 A_{mn} x_1^m \dot{x}_1^n + \sum_{k=0}^3 \sum_{l=0}^3 B_{kl} x_2^k \dot{x}_2^l \quad (3.4)$$

$$\tilde{f}_{T_1} = f_{T_1} - \sum_{k=0}^3 \sum_{l=0}^3 B_{kl} x_2^k \dot{x}_2^l \quad (3.5)$$

Equation 3.3 shows that the measured transmitted force f_{T_1} (data) can be written as a model, F_{T_1} , with an associated parameterization fit error, e_1 . The initial component model shown is two bicubic maps in the d.o.f. x_1 and x_2 . Non analytic and memory term modeling proceeds by using the fit parameters B_{kl} to approximate the measured transmitted force, minus the fit x_2 and \dot{x}_2 dependence (Equation 3.5). The approximate transmitted force, \tilde{f}_{T_1} , of Equation 3.5 is due to the d.o.f. x_1 only. Possible non analytic and memory dependence of f_{T_1} on x_1 is no longer obscured by the x_2 d.o.f. Now a model of the form Equation 3.5 can be postulated and fit to the data.

$$F_{T_1} = F_{DA}(x_1, \dot{x}_1) + F_{DNA}(x_1, \dot{x}_1) + F_{DM}(x_1, \dot{x}_1) + F_{NDA}(x_2, \dot{x}_2) \quad (3.6)$$

The model of Equation 3.6 includes a possibly reduced analytic term, F_{DA} , with inclusion of diagonal non analytic, F_{DNA} , and memory terms, F_{DM} . D.o.f. coupling is still recognized in this Equation as a non diagonal analytic term F_{NDA} .

Up to this point choice of d.o.f of the component model and the ensuing parameterization of these d.o.f. has been described. Specific modeling of the MODE components follows by defining the d.o.f. of the component model and first fitting the data with analytic parameterizations. Physical component models, which include non analytic and memory terms as well as reduced order analytic terms are derived from inspecting the preprocessed data and are presented.

3.3 Modeling specifics

In practice, the multiple d.o.f. force-state model represented by Equation 3.1 must be specialized to contain the terms of physical significance for a specific application. Multi d.o.f. component parameter identification for MODE is approached by individually modeling first a deployable truss bay, then an erectable truss bay and finally an alpha joint bay. Each component is modeled as a general twelve d.o.f. cantilevered beam element as shown in Figure 3.1. Nonlinearities associated with the diagonal bracing wires, knee joints, rotary and node mechanisms and joint slop are smeared, as are the linear components, within an equivalent continuum model of Equation 3.1.

An underlying assumption made when identifying MODE components as twelve d.o.f. beam elements is that, in principle, determinate measurements be made of: the six generalized applied loads (at the right or free end in Figure 3.1); the six generalized reactions (at the left or constrained end); and the motion of the six unconstrained d.o.f. (at the right end). In practice, indeterminant measurements of force and displacement are made with load and displacement transducers. Twelve reactions are measured as shown in the upper drawing of Figure 3.1. Prior to fitting any models twelve reactions are resolved into six generalized reactions about the elastic centroid of the constrained end. Also, twelve applied loads are measured and resolved into six generalized applied loads about the elastic centroid of the unconstrained end. Equivalently, eight measurements of displacement are resolved into six generalized d.o.f. at the unconstrained end.

In practice, the truss bay batten cross sections are constrained to be rigid in the experiment test rig. Fixing the batten cross section eliminates warping and shearing at the interfaces. In this way the components are reduced in d.o.f.. Extra d.o.f. that pertain to shearing and warping, with separate identification tests, can be added to complete a model of the component. Local truss node bending stiffnesses are not

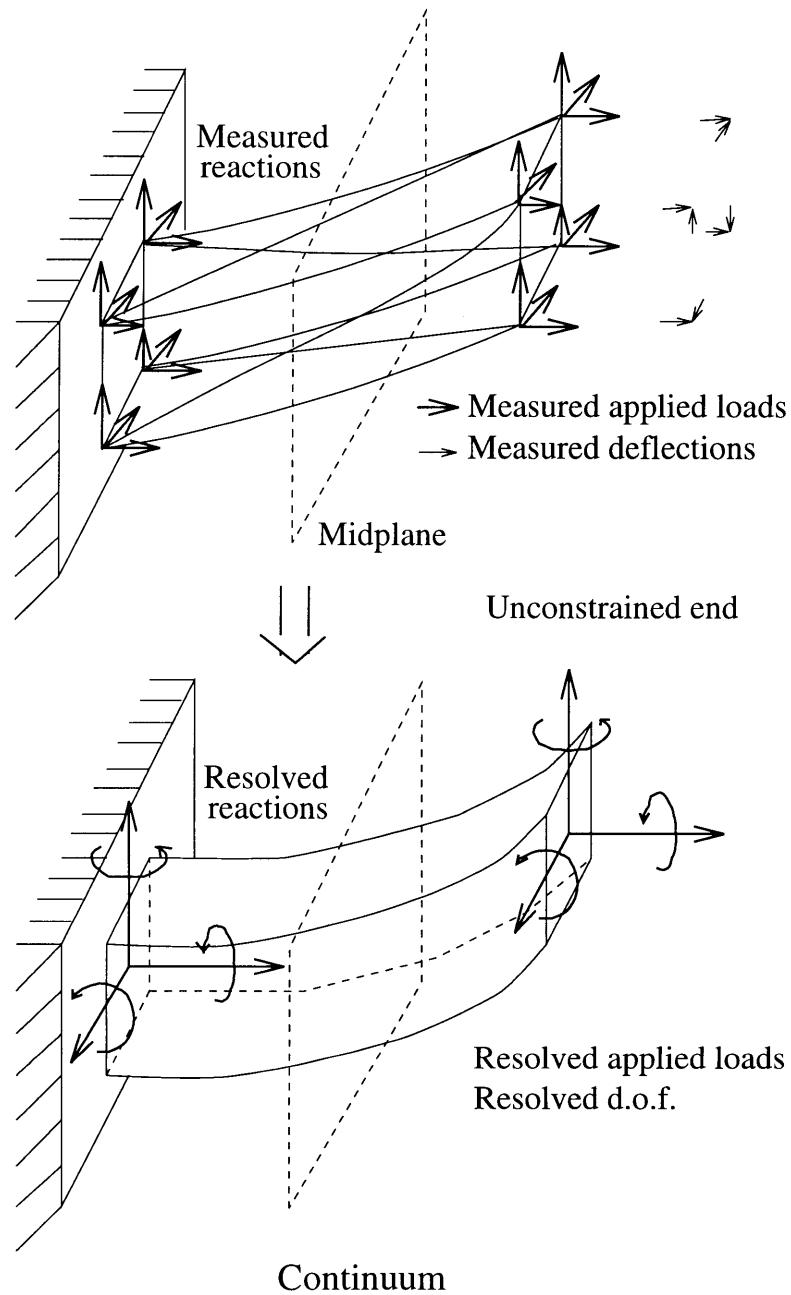


Figure 3.1: Cantilevered component modeled as a twelve d.o.f. beam element. Twelve reactions, twelve applied loads and eight measurements of displacement are resolved into six generalized reactions, applied loads and unconstrained d.o.f. respectively.

modeled when constraining the cross sections. This makes the assembled component model susceptible to error in predicting non beam-like modes, that is cross-section breathing or shearing modes, and localized modes.

Full identification of a twelve d.o.f. beam component model requires measurements of reactions, applied loads and unconstrained d.o.f. For example, if the component is linear and non dissipative then the constitutive relations are represented by Equation 3.7.

$$\begin{bmatrix} \underline{F}_u \\ \underline{F}_c \end{bmatrix} = \begin{bmatrix} K_{uu} & K_{uc} \\ K_{cu} & K_{cc} \end{bmatrix} \begin{bmatrix} \underline{x}_u \\ \underline{x}_c \end{bmatrix} \quad (3.7)$$

Where \underline{F}_u and \underline{x}_u represents the six generalized applied loads and d.o.f. at the unconstrained end respectively. The forces \underline{F}_c represent the six measured reactions at the constrained end. The d.o.f. \underline{x}_c are 0 by definition. The measurements of generalized load, reactions and unconstrained d.o.f. allows identification (*via* fitting the component model to data) of the 6×6 stiffness matrices K_{uu} and K_{cu} by simplifying Equation 3.7 into Equations 3.8.

$$\begin{aligned} \underline{F}_u &= K_{uu}\underline{x}_u \\ \underline{F}_c &= K_{cu}\underline{x}_u \end{aligned} \quad (3.8)$$

Physical interchanging the constrained and unconstrained ends of the component allows identification of K_{uc} and K_{cc} . If the component is symmetric about the midplane shown in Figure 3.1, then, within manufacturing tolerance and bolt-up repeatability, no physical interchanging of the component is required. This means that nominally K_{cc} and K_{uc} can be inferred from K_{uu} and K_{cu} respectively. The inference requires interchanging and negation of some matrix elements.

Now that the d.o.f. of the component model have been defined the remainder of this section focuses on the specific MODE component parameterizations.

Adjustable pretension bay

The adjustable bay is one bay of a four bay deployable truss sections, which will be described in more detail in chapter 5. This section presents the model for the MODE adjustable pretension bay motivated by the characteristics of the component data (for examples see Figures 6.5 and 6.6). Pertinent features of the component data are:

- Substantial linear stiffness component.

- Relatively high stiffness and low dissipation at low amplitudes.
- Increasing hysteretic softening with increasing amplitude after exceedance of a break amplitude.
- Stiffness asymptotes at high amplitudes.

Specialization of the model of Equation 3.1 for the MODE adjustable pretension bay is obtained by making two assumptions, both consistent with the data: the component is only weakly and smoothly nonlinear; and the majority of the strain energy is stored in the diagonal stiffness elements. A consequence of the first assumption is that quartic and higher order analytic terms in both displacement and velocity can be neglected. A consequence of the second assumption is that a less detailed parameterization of the non diagonal elements of F_{T_i} is necessary.

The MODE adjustable bay specific force-state model is thus written as

$$F_{T_i} = F_{D_i} + \sum_{j \neq i} F_{ND_{ij}} \quad (3.9)$$

$$\begin{aligned} F_{D_i} = & K_{1,i}x_i + D_{1,i}\dot{x}_i + K_{2,i}x_i^2 \\ & + K_{3,i}x_i^3 + F_{M_i}(x_i, \dot{x}_i) = F_{ii} \end{aligned} \quad (3.10)$$

$$\begin{aligned} F_{ND_{ij}} = & [K_{1,ij}x_j + D_{1,ij}\dot{x}_j + K_{2,ij}x_j^2 + K_{3,ij}x_j^3]_{j \neq i} \\ = & (F_{ij})_{j \neq i} \end{aligned} \quad (3.11)$$

$$f_{T_i} = F_{T_i} + e_i \quad (3.12)$$

Where F_{M_i} is a diagonal memory term defined below in Equation 3.13.

The modeled structural force component, F_{T_i} , is separated into diagonal and non-diagonal contributions. The diagonal functions, F_{D_i} , are represented by cubic stiffness polynomials, linear damping and a memory terms as shown in Equation 3.10. The nondiagonal contributions, $F_{ND_{ij}}$, are represented as cubic stiffness polynomials and linear damping terms but without memory terms, as shown in Equation 3.10. Contributions to the stiffness and dissipation from the neglected higher order analytic terms are projected onto decoupled d.o.f. space in such a way as to minimize the error, e_i , between the model, F_{T_i} , and the data, f_{T_i} (Equation 3.12).

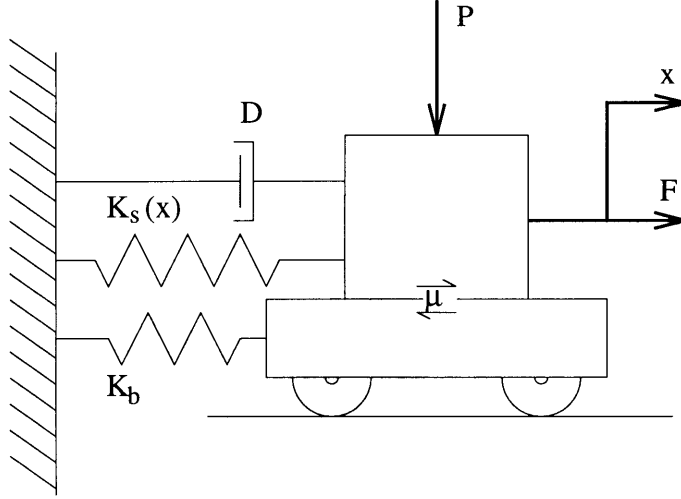


Figure 3.2: Single slip dynamic hysteresis model.

Inspection of the MODE adjustable bay data motivates the modeling of the non-linear memory, $F_{M_i}(x_i, \dot{x}_i)$. The data of Figures 2.2 and 2.3 suggest softening and dampening with increased amplitude, consistent with mechanical hysteresis postulated by Prandtl [33]. As translated by Dahl and Wilder [16] Prandtl's laws state that:

- (i) Immediately after reversal of the sense of deformation, the slope of the force-deflection curve has the same value as at the beginning of the first loading.
- (ii) The shape of any branch of the force-deflection curve is uniquely determined by the position of the point where the last reversal of the sense of deformation occurred.
- (iii) If the sense of direction is not reversed again, any such branch will pass through the point where the last but one reversal of the sense of deformation occurred; thereafter, the force-deflection curve continues as if the loop had never been formed.

The laws are applicable to the stress-strain properties of materials as well as to the load-stroke solid friction behavior of mechanical elements. Dahl proposed a dynamic hysteresis model (DHM) consistent with these laws that describes the stress-strain hysteresis in piezo-electric actuators. The memory function, $F_{M_i}(x_i, \dot{x}_i)$ for the MODE bay was developed to model similar dynamic hysteresis.

A simplified schematic of the hysteresis model is shown in Figure 3.2. The model represents dynamic hysteresis as a sliding massless block in frictional contact with

an elastically constrained massless cart. The two parameters, normal load P , and friction coefficient μ , are reduced to a slip force, F_s , which represents the force across the block/cart interface that initiates joint slip. This amalgamation of parameters is a consequence of assuming the joint preload P to be essentially constant. In the MODE experiment the time varying dynamic preload is a small percentage of the truss bay preload induced by the bracing wires.

Equations 3.13 through 3.19 are based on the physics of Figure 3.2, extended to model multiple slip dynamic hysteresis. This form of hysteresis typical of a bay which contains many slip interfaces which relax after a change in the sense of direction. In Figure 3.2 $K_s(x)$ represents the cubic stiffness polynomial of Equation 3.10 while D represents the linear damping term of Equation 3.10.

$$F_M(x, \dot{x}) = \begin{cases} K_b x & |K_b x| < |F_s| & \delta_n < \delta_c \\ C_3 \xi^3 + C_2 \xi^2 + C_1 \xi - F_s & x > -\delta_c & \dot{x} < 0 \\ -F_s & x < -\delta_c & \dot{x} < 0 \\ -C_3 \xi^3 - C_2 \xi^2 - C_1 \xi + F_s & x < \delta_c & \dot{x} > 0 \\ F_s & x > \delta_c & \dot{x} > 0 \end{cases} \quad (3.13)$$

$$\delta_c = \frac{F_s}{K_b} \quad (3.14)$$

$$\delta_n = |x| \text{ when } \dot{x} \text{ changes sign} \quad (3.15)$$

$$C_1 = K_b \exp\left(-\frac{|\delta_n - \delta_c|}{\delta_c}\right) \quad (3.16)$$

$$C_2 = \frac{6F_s - K_b(\delta_n + \delta_c)}{(\delta_n + \delta_c)^2} - \frac{2C_1}{(\delta_n + \delta_c)} \quad (3.17)$$

$$C_3 = \frac{-4F_s + K_b(\delta_n + \delta_c)}{(\delta_n + \delta_c)^3} + \frac{C_1}{(\delta_n + \delta_c)^2} \quad (3.18)$$

$$\xi = |x - \text{sign}(\dot{x})\delta_c| \quad (3.19)$$

The slip force, F_s , is the generalization of the total slip force required to slip all joints in the prescribed motion, while δ_c is the generalized slip deflection, and δ_n is the memory parameter. Just after all sliding joints within the component have been brought to rest and the sense of direction changes sign, the force-deflection curve of F_M has initial slope of K_b . This is in agreement with Prandtl's first postulated law. After the sense of direction changes sign, the individual friction surfaces progressively *break* into slip. As progressively more surfaces slip the transmitted force component due to F_M relaxes to $\text{sign}(\dot{x})F_s$. The process begins again at the next change in sense of direction. Smoothness of transition between conditions is determined by the

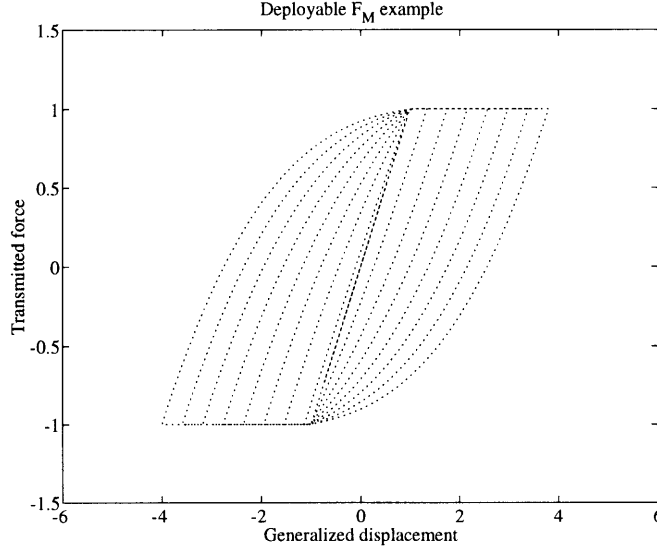


Figure 3.3: An example dynamic hysteresis model, F_M , for the MODE deployable bay where the initial stiffness, K_b , is 1, and the slip force, F_s , is 1.

cubic dependence and the exponential dependence of C_1 . The variable ξ is explicitly dependent on the memory parameter and therefore the cubic model is consistent with Prandtl's second postulated law. Prandtl's third postulated law is guaranteed by the conditional form of Equation 3.13. Note that replacing the cubic dependence on ξ by a locally linear dependence, $-\text{sign}(\dot{x}) K_b \xi$, and testing for magnitude and direction exceedance of the slip force, $\text{sign}(\dot{x}) F_s$, would recover the simpler single frictional interface model represented in Figure 3.2.

A simulated dynamic hysteresis model of Equations 3.13-3.19 is shown in Figure 3.3. An alternative way of motivating the deployable dynamic hysteresis model is as a distribution of slipping springs. At low amplitudes the model is undamped with stiffness K_b . When the generalized displacement amplitude F_s/K_b is exceeded the all joints slip instantaneously, yielding to a slip force, F_s , until a change in the sense of direction. After the sense of direction reverses the joints slip with an altered distribution described by the amplitude at the direction reversal and the displacement F_s/K_b . Further investigation of this model interpretation is presented in comparison with the alpha joint microfriction model in section 3.3.

Erectable bay

The erectable bay is the second MODE component to be tested and modeled. Erectable bay data motivated two types of models. The first model describes the essentially linear behavior of the bay with fastened joints. However, it was observed that vibration

induced loosening of the erectable joints led to tests of the component with sloppy joints. The second model describes sloppy joint behavior.

Examples of the dominantly tight joint data can be seen in Figure 6.8. Features of the tight joint data are

- Dominant linear stiffness component
- Low levels of dissipation present

These features lead to an essentially linear tight joint model that is fit to the data.

Equations 3.20 and 3.21 show the modeling of both diagonal and non diagonal terms of the tight joint erectable component model as cubic stiffness polynomials and linear damping terms. The higher order stiffness parameters were added to model possible (de)stiffening due manufacturing and material non idealities.

$$\begin{aligned} F_{D_i} &= K_{1i}x_i + D_{1i}\dot{x}_i + K_{2i}x_i^2 + K_{3i}x_i^3 \\ &= F_{ii} \end{aligned} \quad (3.20)$$

$$\begin{aligned} F_{ND_{ij}} &= [K_{1ij}x_j + D_{1ij}\dot{x}_j + K_{2ij}x_j^2 + K_{3ij}x_j^3]_{j \neq i} \\ &= (F_{ij})_{j \neq i} \end{aligned} \quad (3.21)$$

Multiple tests of the erectable bay loosened some of the connect joints at the nodes. Tests of the erectable bay with purposely loosened joints were performed in order to examine the loose joint behavior. The joint tightening sleeve was released until the joint behaved as designed (locked) at low applied force, approximately below 4 N shear and 0.5 N-m twist, but slipped at high applied force, approximately above 4 N shear and 0.5 N-m twist. The loose joint erectable bay data was initially fit with analytic bicubic parameterizations. The analytic bicubic models were used, as shown in Equations 3.3 through 3.5, to present the data as decoupled d.o.f. force-state maps.

Nonlinear loose joint data can be seen in force-state map form in Figure 6.10. Features of the loose joint data are

- Regions of increased dissipation dependent both velocity and displacement.
- Stiffness variation dependent on the sign of displacement.

From these loose joint nonlinear features more specific models than the bicubic parameterizations are postulated below. These erectable loose joint models are presented

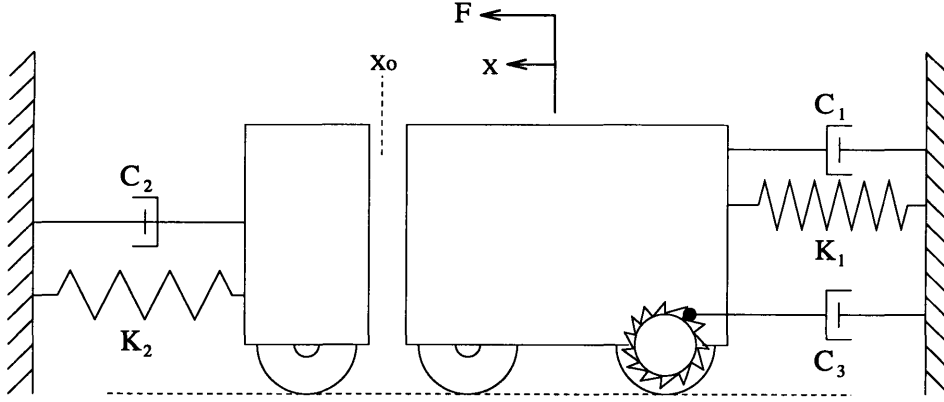


Figure 3.4: Erectable loose joint model including one-way displacement and velocity dependent dissipation.

here so that the loose joint force-state map data presented chapter 6 can be understood in terms of underlying mechanisms. The following loose joint models are not fit to the data but instead are presented for comparative purposes.

Viewing the decoupled data motivated the model shown in Figure 3.4. One-way displacement dependent dissipation is depicted as a separate nonlinear mechanism, $K_2(x)$ and $C_2(\dot{x})$, employed to the left of the initial state x_0 . One-way velocity dependent dissipation is shown as a frictionless ratchet mechanism operating with a state dependent (nonlinear) dashpot, C_3 . The dashpot, $C_3(\dot{x})$, is engaged for rightward motion while motion leftward disengages the dissipation.

Modeling one-way displacement and velocity dependent dissipation requires conditions on the sign of the states x and \dot{x} . Equation 3.22 represents the model shown in Figure 3.4. K_1 , K_2 , C_1 , C_2 and C_3 represent independent analytic stiffness and damping functions. The essence of the model is to capture the accumulated microfriction behavior of the loose joints with conditional analytic functions.

$$F_{T_i} = \begin{cases} (K_1(x) + K_2(x))x + (C_1(\dot{x}) + C_2(\dot{x}))\dot{x} & x > x_0 \quad \dot{x} > 0 \\ (K_1(x) + K_2(x))x + (C_1(\dot{x}) + C_2(\dot{x}) + C_3(\dot{x}))\dot{x} & x > x_0 \quad \dot{x} < 0 \\ K_1(x)x + (C_1(\dot{x}) + C_3(\dot{x}))\dot{x} & x < x_0 \quad \dot{x} < 0 \\ K_1(x)x + C_1(\dot{x})\dot{x} & x < x_0 \quad \dot{x} > 0 \end{cases} \quad (3.22)$$

Figure 3.5 shows example force-state maps for first order analytic functions in Equation 3.22. Table 3.1 lists the parameters used in the examples of Figure 3.5. Example 1 includes one-way displacement dependent stiffness and dissipation, K_2 and C_2 with one-way velocity dependent dissipation, C_3 , set equal to zero. Example 2 includes K_2 and C_3 while C_2 equals zero. More complicated map nonlinearities can

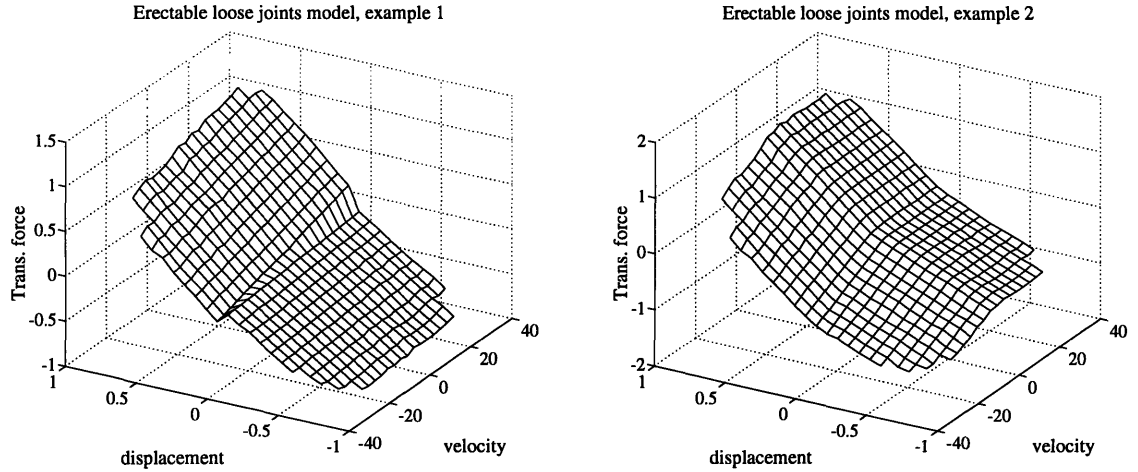


Figure 3.5: Examples of first order analytic nonlinearities for the erectable with loose joints.

Table 3.1: Erectable example model parameters.

Example No.	Parameters				
	K_1	K_2	K_3	C_1	C_2
1	1.0	0.4	.002	.006	.000
2	1.0	1.0	.000	.000	.020

be modeled by including higher order analytic parameters in the component model.

These simplified loose joint models are compared to the force-state map loose joints data in chapter 6.

Alpha joint bay

The alpha joint is the third MODE component to be tested and modeled. The alpha joint provided a means with which to articulate two substructures, consisting of deployable and erectable hardware, with an axial rotary mechanism. Two friction pad preloads, high and low, allowed frictional control of the break load for axial rotation of the joint. Axial rotation was permitted by a bearing race once the break load had been exceeded. Small axial angular deflections of the joint, due to its compliance before break load exceedance, employed the outer bearing race as well as micro slip of the friction pad. Large angular deflections of the joint caused the friction pad to macro slip allowing rotation under almost constant load.

Sample component data of the alpha joint is shown in Figures 6.12, 6.14 and 6.16.

Features of the data are:

- Transmitted force data other than that of the axial moment appears strongly nonlinear with nonlinear effects on the order of 10% of the dependent transmitted force.
- Axial moment data shows similar trends to the adjustable pretension bay at low amplitudes, increasing hysteresis while softening with increasing amplitude.
- High amplitude rotation axis shows strong friction behavior with displacement dependencies at the transmitted load extrema and low amplitude behavior after a change in sense of direction.

These features lead to an elaborate model of accumulated friction. This section will concentrate on the modeling of the axial moment transmitted force. Data corresponding to the five other generalized transmitted forces were fit to bicubic parameterizations only (an example for two d.o.f. is shown in Equation 3.2).

An analytic bicubic parameterization was first fit to all the data. Models of the five generalized transmitted forces other than axial moment were not perused further. Modeling of the non analytic axial rotation mechanism (axial moment) proceeded after viewing the decoupled d.o.f. force-state maps. The process of generating an approximate transmitted load, due to independent d.o.f only, was presented in Equations 3.3 through 3.5.

Two types of friction models are required to represent the rotation mechanism. Micro slip distributions were used to describe the conglomerate effect of slip interfaces at low amplitudes. Macro slip displacement dependent friction was used to describe the preloaded friction pad mechanism at high amplitudes. The micro slip model will first be described before introducing the macro slip model. Transition between the two models is described after the macro slip model.

Micro slip model

Figure 3.6 shows the axial rotation model as massless block frictionally loaded to a massless cart by a relative displacement dependent preload [24]. The cart is elastically restrained by a linear spring K_1 , as well as springs acting on numerous slip interfaces, which have total stiffness K_F . The slip interfaces are preloaded in a distributed fashion. At very low amplitude force, F , all the slip interfaces are locked and the block cart mechanism displaces as if restrained by one equivalent spring with stiffness $K_1 + K_F$. As the amplitude increases, yet remains small, progressively more interfaces break into slip (but not the displacement dependent interface) and the mechanism

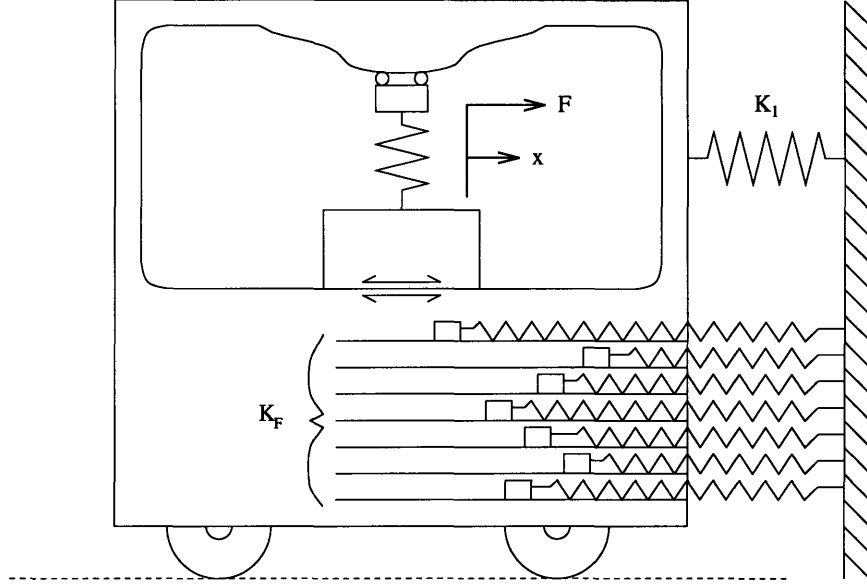


Figure 3.6: Alpha joint axial rotation model with macro slip displacement dependent friction represented as the vertical spring arrangement and micro slip distribution represented by the multiple horizontal spring arrangements. The single spring K_1 represents a backbone stiffness.

softens while the dissipation increases. The force created by this low amplitude micro friction behavior is modeled as follows,

$$\begin{aligned}
 F_{66} &= K_1 x + (1 - \mathcal{P}_1(\xi_s) - \mathcal{P}_2(\xi_{ns})) K_F (x - \delta_n) \\
 &\quad + f_{sf} + f_{nsf} + F_{66n} \\
 f_{sf} &= 2 \int d\mathcal{P}_1(\xi_s) K_F \xi_s \\
 f_{nsf} &= \int d\mathcal{P}_2(\xi_{ns}) K_F \xi_{ns}
 \end{aligned} \tag{3.23}$$

$$\begin{aligned}
 \delta_n &= |x| \text{ when } \dot{x} \text{ changes sign} \\
 F_{66n} &= F_{66} \text{ when } \dot{x} \text{ changes sign} \\
 \xi_{ns} &= |x| \\
 \xi_s &= \frac{|x - \delta_n|}{2}
 \end{aligned} \tag{3.24}$$

$$\text{at initial loading} \quad \delta_b = 0$$

$$\text{when } \dot{x} \text{ changes sign} \quad \begin{cases} \xi_s < \delta_b & \delta_b = \min(\delta, \xi_s) \\ \xi_s \geq \delta_b & \delta_b = \min(\delta, \xi_{ns}) \end{cases} \tag{3.25}$$

In Equation 3.23 K_1 represents the linear stiffness. K_F is the sum stiffness of the

restrained interfaces at low amplitudes and is premultiplied slip distribution function, $1 - \mathcal{P}$ which varies between 1 and 0. If all interfaces have slipped then \mathcal{P} is equal to 1. \mathcal{P} bifurcates into two distribution functions $\mathcal{P}_1(\xi_s)$ and $\mathcal{P}_2(\xi_{ns})$ at every change in sense of direction of the motion as shown in Figure 3.7. The split distributions account for the subset of interfaces that have slipped and those that have not slipped. The force created by non slipped interfaces is dependent on the absolute value of the state, ξ_{ns} , while the force created by slipped interfaces depends on a stretched coordinate ξ_s . The stretched coordinate defines the absolute displacement over which the slipped interfaces, accumulated during the last branch of constant direction, must traverse before slipping again. For example, a single spring displacing from its equilibrium extension requires twice the displacement to initial slip, in a direction opposite to the initial direction, to begin slipping again.

Figure 3.7 shows an example slip distribution \mathcal{P} and how the distribution bifurcates into \mathcal{P}_1 and \mathcal{P}_2 at every change in sense of direction. The vertical axis of the distributions represent normalized number of interfaces. For the model given in Equation 3.23 the actual number of interfaces is folded into the parameter K_F . The parameter δ represents the displacement past which all the the interfaces have slipped. The value of δ_b , the coordinate at which the parent distribution, \mathcal{P} , bifurcates, is conditionally determined at the change of sense of direction as shown in Equation 3.25. The parameter δ_b is chosen such that $\tilde{\mathcal{P}}$ represents the normalized number of interfaces that have slipped on the last branch of constant direction motion. Curve \mathcal{P}_1 takes the value of \mathcal{P} while $\xi_s < \delta_b$ and $\tilde{\mathcal{P}}$ otherwise. Curve \mathcal{P}_2 , describing the surfaces that have not slipped in the last branch, takes the value zero while $\xi_{ns} < \delta_b$ and $1 - \tilde{\mathcal{P}}$ for $\xi_{ns} > \delta_b$.

An important distinction between the distribution coordinates is that the non slipped coordinate $\xi_{ns} = |x|$, while the slipped coordinate, ξ_s , is reset to zero at every change in sense of direction. The distinction is that ξ_{ns} is an absolute coordinate while ξ_s is a relative coordinate. After a change in sense of direction ξ_{ns} initially decreases from near or equal to δ_b to zero before increasing after x changes sign. The consequence is a double transversal of the axis, $\mathcal{P}_2 = 0$, while $\xi_{ns} < \delta_b$. In contrast, ξ_s is always an increasing function.

In Equation 3.23 the premultiplier $(1 - \mathcal{P}_1(\xi_s) - \mathcal{P}_2(\xi_{ns}))$ accounts for the reduced stiffness, due to previous branch (constant direction) slipped and non slipped interfaces breaking into slip, while integral terms, f_{sf} and f_{nsf} , accumulate the slip forces for both the previously slipped and the non slipped interfaces. Both integral terms are reset to zero at a change in the sense in direction. The term f_{sf} accumulates the previous branch slipped interface slip forces. The integrand $d\mathcal{P}_1(\xi_s)K_F\xi_s$ is the force

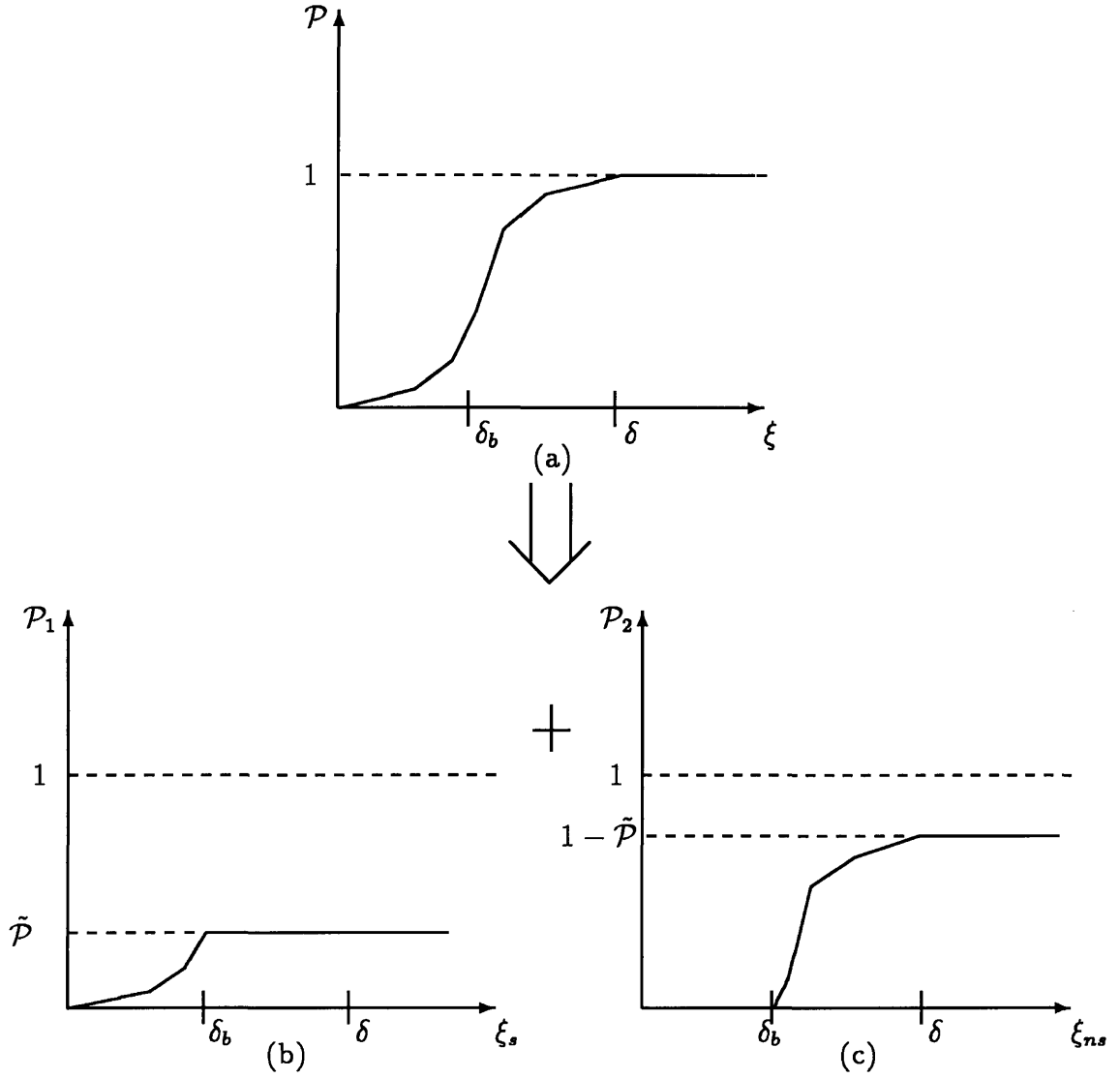


Figure 3.7: Example slip distribution (a) \mathcal{P} which bifurcates into slipped, (b), and non slipped, (c), distributions \mathcal{P}_1 and \mathcal{P}_2 at every change in sense of direction. δ_b is determined at the change in sense of direction.

at which $d\mathcal{P}_1$ interfaces break into slip. The factor 2 in front of the slipped force integral accounts for the vector addition between previous branch slip force and the current branch slip force. This factor does not occur in front of the non slipped force integral, f_{nsf} , as this integral accumulates the slip forces due to interfaces that have not slipped in the previous branch. The integrand of f_{nsf} , $d\mathcal{P}_2(\xi_{ns})K_F\xi_{ns}$, is the force at which $d\mathcal{P}_2$ interfaces break into slip. These slip force integrals are not well defined for every \mathcal{P} . In practice, these continuous integrals are approximated by a discrete summation.

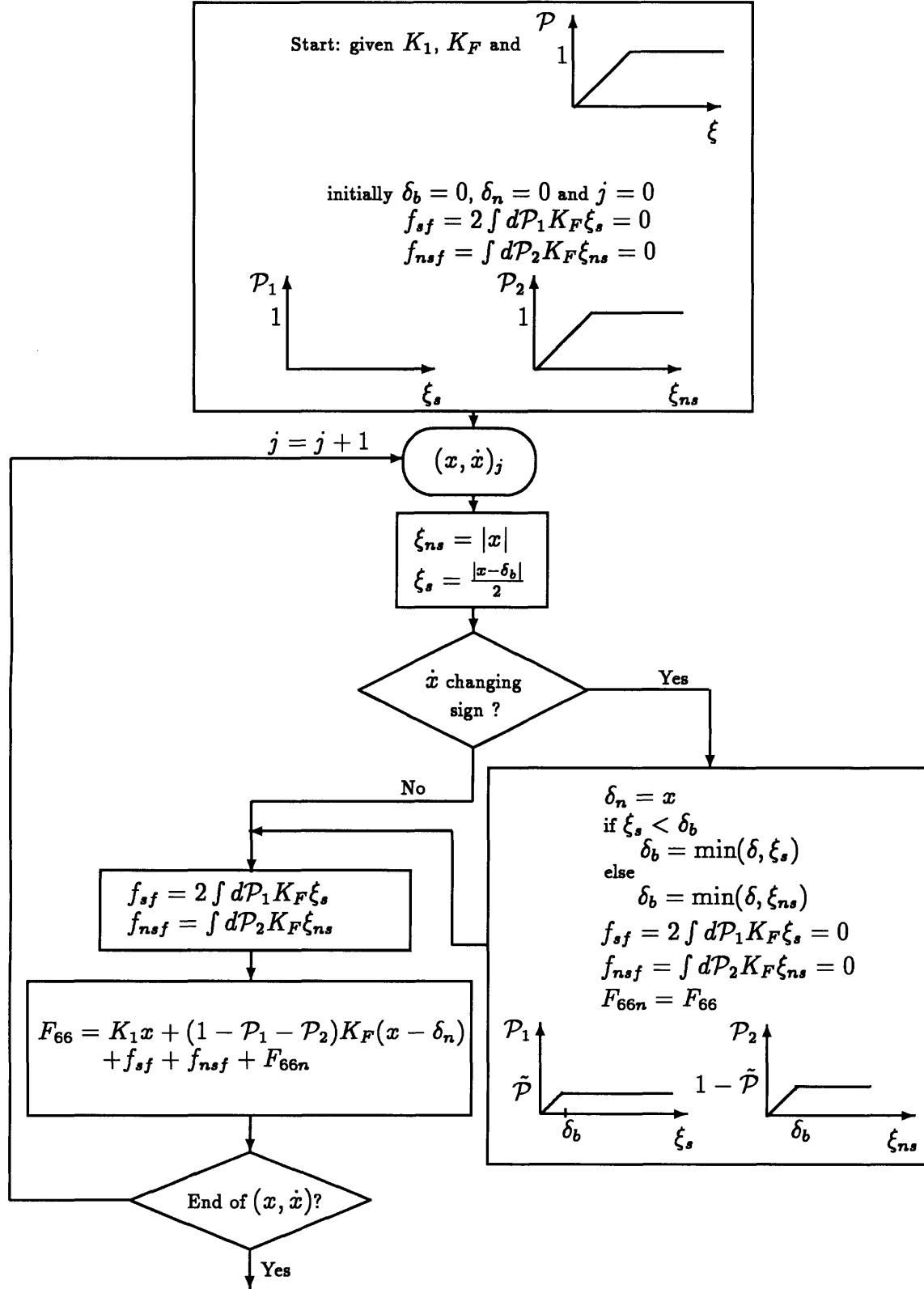


Figure 3.8: Computation flow of axial moment transmitted force from the micro slip distribution model.

The final term in Equation 3.23, F_{66n} , represents the structural force at the change of sense of direction and is necessary for maintaining the correct branch of the dynamic hysteresis model while accumulating the slip forces.

Computation of the model represented by Equations 3.23, 3.24 and 3.25 is conditional. The flow diagram shown in Figure 3.8 represents the logic used to compute the transmitted force F_{66} given the two stiffness parameters, K_1 and K_F , and a slip distribution function, \mathcal{P} . At a change in sense of direction of motion, δ_n , δ_b , f_{sf} , f_{nsf} , \mathcal{P}_1 , \mathcal{P}_2 and F_{66n} are redefined for the ensuing branch of constant motion direction. Coordinates, ξ_s and ξ_{ns} are continually computed as are the integrals giving the slip forces f_{sf} and f_{nsf} .

The presented micro slip model is an integral relation depending on the initial potential energy storage of the component and a parameterized (displacement dependent) slip distribution function. Prandtl's laws of section 3.3 are again preserved in this model. Law 1 is obeyed since initial stiffness is retrieved when the sense of deformation changes, by resetting ξ_s to zero, giving $\mathcal{P}_1 = 0$, and since ξ_{ns} initially decreases in x , giving $\mathcal{P}_2 = 0$. Law 2 is obeyed since the coordinate ξ_{ns} explicitly depends on the value of x at the last change in sense of direction. Law 3 is guaranteed by the distribution bifurcation which accounts for the slipped interfaces over the last branch of constant direction. This bifurcation guarantees that the load stroke curve will pass through the last-but-one point of direction reversal after a minor loop.

Inspection of the MODE alpha joint data (typified by Figures 6.12 and 6.14) led to the distribution function

$$\begin{aligned}\mathcal{P} &= 0 & \xi < \frac{\delta}{3} \\ &= 0.5 & \frac{\delta}{3} < \xi < \delta \\ &= 1.0 & \delta < \xi\end{aligned}\tag{3.26}$$

Where the interfaces slip at two discrete locations. Half of the interfaces slip at a displacement of $\frac{\delta}{3}$ and the remaining half slip at δ . Figure 3.9 shows the dynamic hysteresis model, with $K_1 = 0$.

Physically the discrete distribution of Equation 3.26 results from simultaneous relative micro slipping of the outer bearing race and the friction pad of the alpha joint.

Macro slip model

A model for the second functional mechanism range of the alpha joint, the macro friction regime, is now presented. The macro slip model describes the large angular deflection slipping and sticking of the friction pad and bearing race mechanism. Where

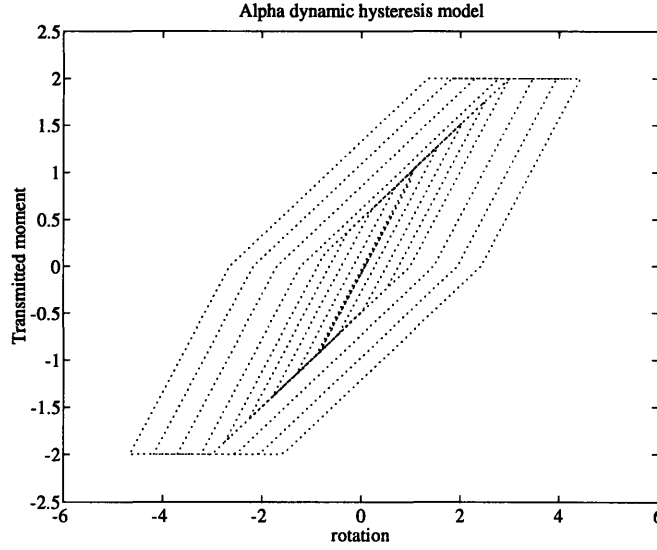


Figure 3.9: Dynamic hysteresis model, F_{66} , for the MODE alpha joint where the initial stiffness, K_F , is 1, and the all slip deflection, δ , is 3.

large angular deflection is that incurred upon full slipping motion of the friction pad. The macro slip model uses parameters from the micro slip model to describe the micro slip behavior of the friction pad immediately after a change in the sense of direction of the motion. The interfacing of the micro slip behavior to a large amplitude displacement dependent friction model results in the macro slip model for the alpha joint.

The Equations for the macro slip model are written as,

$$\begin{aligned}
 & \text{when } \dot{x} \text{ changes sign} \\
 F_{66} = & K_1(x)x + (1 - \mathcal{P}_1(\xi_s))K_F(x - \delta_n) \\
 & + 2 \int d\mathcal{P}_1(\xi_s)K_F\xi_s \\
 & + F_{66n} \\
 & \text{until } F_{66} \text{ exceeds } F_{macro} \text{ then} \\
 F_{66} = & \text{sign}(\dot{x})F_{ms}(\mu_1 + \mu_2 \exp(\frac{|x - \text{sign}(\dot{x})\delta_{ma}|}{\delta_r})) \\
 = & F_{macro}
 \end{aligned} \tag{3.27}$$

Equation 3.27 shows the model to have micro friction behavior after a change in sense of direction. At the change in sense of direction all the slipped interfaces have been brought to rest including the friction pad. Note that the non slipped distribution and the appropriate slip force accumulation integral have been removed from the structural force F_{66} as the bearing race and pad have been fully engaged in the motion. The alpha joint continues to soften as prescribed by the distribution

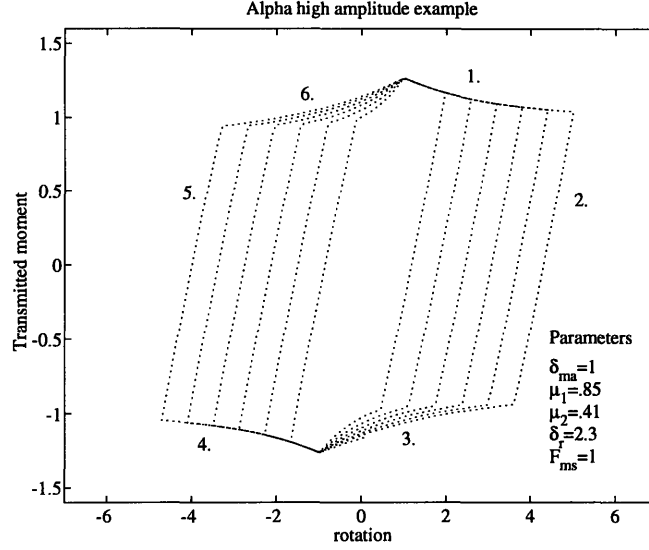


Figure 3.10: Dynamic hysteresis model, F_{66} , for the high amplitude macro friction operation of the MODE alpha joint.

\mathcal{P}_1 until the structural force exceeds F_{macro} . The displacement dependent frictional force, F_{macro} , is shown in Figure 3.6 as the vertical spring acting on the massless block. The displacement dependence of F_{macro} is represented by the relative displacement varying preload on the vertical spring in Figure 3.6.

In Equation 3.27 F_{macro} functionally depends on; the macro slip force, F_{ms} ; two relative weights, μ_1 and μ_2 ; the displacement of first F_{macro} exceedance; and an exponential relaxation constant, δ_r . The choice of an exponential form was heuristic and was made from inspection of the high amplitude data. Therefore this model is only valid in the tested range and should not be extrapolated to a larger or smaller range. Relative weights, μ_1 and μ_2 , and relaxation constant δ_r are a means to shape the model to accommodate slightly different branch behavior depending on the direction of the velocity and sign of the relative displacement across the joint.

Figure 3.10 shows an example of the macro slip model evaluated on typical alpha joint displacement and velocity data. The relative μ 's operate in the regions 3 and 6 indicated on the load stroke characteristic and are reset to 1, .27 respectively in the adjacent corners, 1 and 2. The softening slope after a change in sense of direction, *i.e.* regions 2 and 5, is attributed to the micro slip model parameters of Figure 3.9 evaluated as if all interfaces have previously slipped.

The exponential form of Equation 3.27 provides peak transmitted force at the break displacement, δ_{ma} . The break displacement approximates the displacement at which transition between micro and macro slip models occurs. It is at δ_{ma} that the sharp transition between micro and macro slip models is mathematically enforced.

The alpha joint data shows a complicated but smooth transition between micro and macro slip. This transition is not modeled in this report. The alpha joint micro and macro slip models are therefore fit in appropriate amplitude ranges and not in the transition range. The models are mathematically joined for assembled component modeling in chapter 7.

Now that the alpha joint micro and macro slip models have been defined a comparison can be drawn between the deployable dynamic hysteresis and the low amplitude alpha joint dynamic hysteresis.

Model comparison; adjustable bay *vs.* alpha joint bay

Comparing the two dynamic hysteresis models of the adjustable bay and the micro slipping alpha joint yields two findings. First, both hysteresis models are inherently conditional representing nonlinear memory. Second, both hysteresis models represent softening and dampening behavior and therefore share physical similarities. The adjustable pretension bay model of Equations 3.10 and 3.11 represents preloaded pin sliding joints. The micro slip alpha joint bay model of Equation 3.23 represents accumulated bearing and friction pad microfriction.

The adjustable pretension bay model can be seen as a class of the microfriction model developed to describe the alpha joint rotation at low amplitudes. The micro slip alpha joint model was physically motivated as a distribution of spring restrained slipping interfaces. The deployable model can be motivated as a distribution of spring restrained sliding pin joints. Similarities between Figure 3.3 and Figure 3.9 suggest that accumulated micro friction dominates the hysteretic behavior of both devices.

The adjustable pretension bay can also be modeled as a set of springs whose distribution of slip likelihood varies with mechanical state of the device. Initially all the interfaces slip together at $\delta = F_s/K_b$ yielding to the slip force F_s . After the all slip condition has been exceeded the return slip distribution changes based on the absolute value of the displacement at the last change in sense of direction, x_n , and the all slip parameter, δ . Essentially the ordinate axis of the slip distribution \mathcal{P} stretches in order to preserve the integrated slip force over the return to all slipped conditions.

Figure 3.11 shows the proposed distributions consistent with the dynamic hysteresis of Figure 3.3. The slope of the distribution is zero when the coordinate $\xi = 0$, *i.e.* at a change in sense of direction. The step in number distribution at $\xi = \delta$ is denoted $f(x_n, \delta)u(\xi - \delta)$. Where $u(\xi - \delta)$ is the unit step function in the coordinate ξ . The size of the step is given by the function $f(x_n, \delta)$. This function represents the number of micro springs required to model residual slope of the load stroke curve of

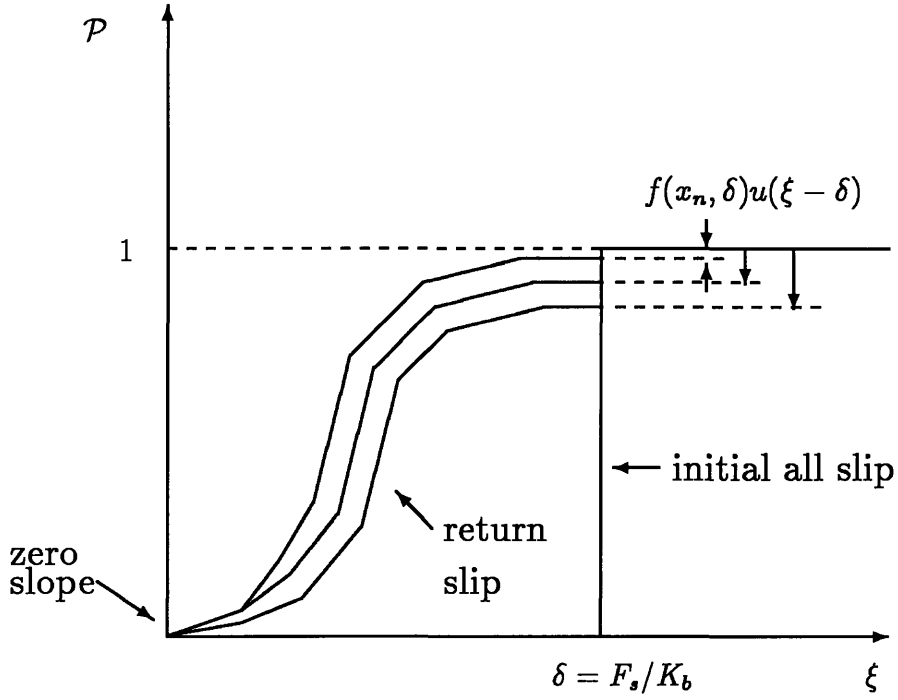


Figure 3.11: Deployable slip distributions \mathcal{P} . Initially all slip at δ then return slip distributions depend on the modified coordinate ξ so that the integral accumulation of slip force yields F_s for the return all slipped condition.

Figure 3.3 at $x = \pm\delta$. These varying slip distributions model the varying preload and surface contact conditions of the pin joints as a function of the slipped displacement.

3.4 Summary

In summary, a set of models that describe the MODE components has been presented. The models are based on a general twelve d.o.f. beam element description using physical coordinates. A general analytic parameterization was also presented both as a model and as a tool for modeling. Modeling multiple d.o.f. MODE components led to the discovery of fundamental dynamic hysteresis in both the adjustable pretension and alpha joint bays. Given this choice of parameterization, the problem is now to identify the parameters from component data and then evaluate the fidelity of the model fit.

Chapter 4

Component model identification

This chapter presents an approach to identifying the model parameters of a specific component. The problem of identifying these parameters involves a number of choices. First, there must be a choice of the appropriate time and directional history of applied loads. Second, the choice of applied load directions determines an identification algorithm which might include linear and nonlinear least squares fitting procedures.

The chapter first addresses the issues of applied load time history and direction. One time history and two choices of load directions are selected. An experimental procedure is outlined for determining an appropriate choice of applied loads. The use of linear least squares to fit the analytic component models is next described as is nonlinear least squares for fitting non analytic component models. Two identification algorithms, each of which incorporate either the linear least squares or the nonlinear least squares or both, are next described. The algorithms correspond to the two sets of applied load directions used for the MODE components. The first algorithm describes weakly coupled loads identification, where the intent was to apply generalized loads that were completely decoupled. The second algorithm describes decoupled d.o.f. identification, where the intent was to apply coupled loads that decoupled the response d.o.f.

4.1 Applying loads

In multiple d.o.f. component testing the loads with which to test the component must be specified. Choosing the applied loads amounts to choosing the time history and directions of the loads. In this section the applied load time history is discussed followed by the discussion of applied load directions. A experimental method for evaluating the directions chosen is presented. The method involves postulating sets

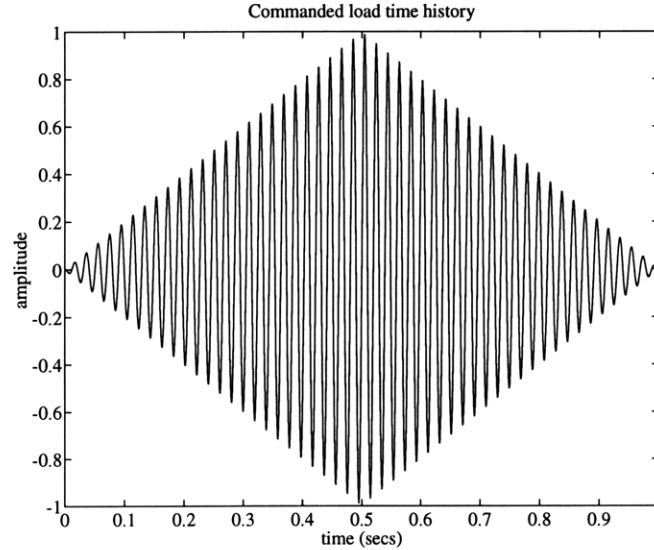


Figure 4.1: Typical applied load time history (odd about the peak ramp amplitude).

of test directions, testing those directions and evaluating the performance of the directions by comparing identified linear parameter standard deviations.

Applied load time history

The selection of applied load time history is driven by two requirements

- to have enough information in the d.o.f. hyperplane so that the component force-state maps could be generated, on a fine enough mesh, with no “holes” [11].
- to have enough information in the d.o.f. hyperplane so as to allow good fits of the specific component models presented in chapter 3.

The first requirement is for modeling purposes. As referred to in chapter 2, and by O'Donnell [11], a force-state map is a mesh of averaged transmitted force measurements. The averaging takes place over a rectangular grid of specified fineness in the state plane. A fine enough mesh is that which allows inspection of the data so that models can be postulated. “Holes” in the force-state map arise when the state plane information is insufficient to determine the mesh nodal values.

The second requirement means that not only should the number of data points greatly exceed the number of parameters of the component model but that those data points need to span a range in which the parameters are meaningful. The component model range is, in this case, ultimately determined by the need to understand the MODE dynamics test data. In this way the applied loads maximum amplitude need be commensurate with the desired component model range of dynamic loading.

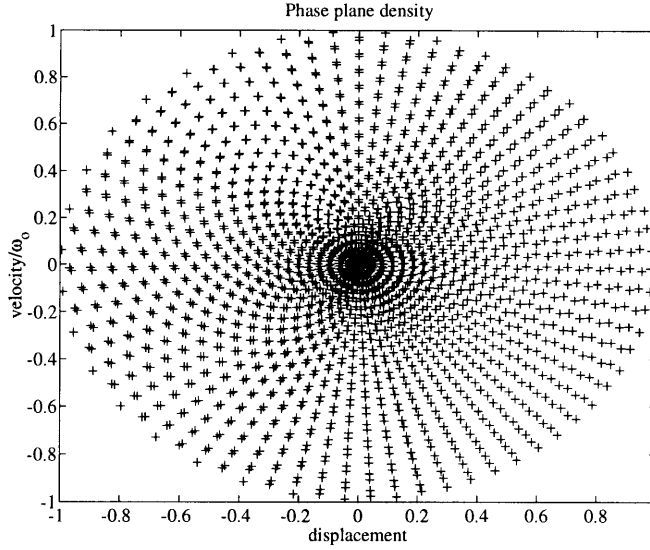


Figure 4.2: Linear single d.o.f. phase plane response sampled at $35.5\omega_o$.

A sinusoid which was ramped from zero amplitude to a peak amplitude and then back to zero amplitude again was used as the time history of applied load for the results presented in this report. The ramped sinusoid was made odd about the peak amplitude time so that the commanded loads had no net DC component. Figure 4.1 is an example of a 1 sec duration, ramped commanded input with sinusoidal frequency ω_o rad/sec. The sampled quasistatic response of a linear single d.o.f. component to the continuous applied load of Figure 4.1 is shown in a phase plane plot in Figure 4.2. In Figure 4.2 the sampling rate is $35.5\omega_o$. A force-state map of this system is made by casting a rectangular grid over the phase plane of Figure 4.2. Transmitted forces, measured at the '+'s shown, that fall within a rectangle of the grid are averaged to give a mesh nodal value (the mesh value at the center of the rectangle). The mesh is next smoothed by convolving it with a two-dimensional hat function which weights a nodal value with the four neighboring nodal values. The resulting nodal values are plotted as a function of the states corresponding to the centers of the grid elements. This is the force-state map.

Examination the phase plane, Figure 4.3, clearly shows "holes" in the state information (no data within some grid elements). If the desired mesh of the force-state map is of the order of the shown grid elements then more state information is required.

The density of the state data can be increased by increasing the ramp time or total time length of the signal keeping the same sampling frequency and peak amplitude. Increasing the test frequency, ω_o , and the sampling frequency while maintaining test time and peak amplitude also improves the data density. Both methods of increasing

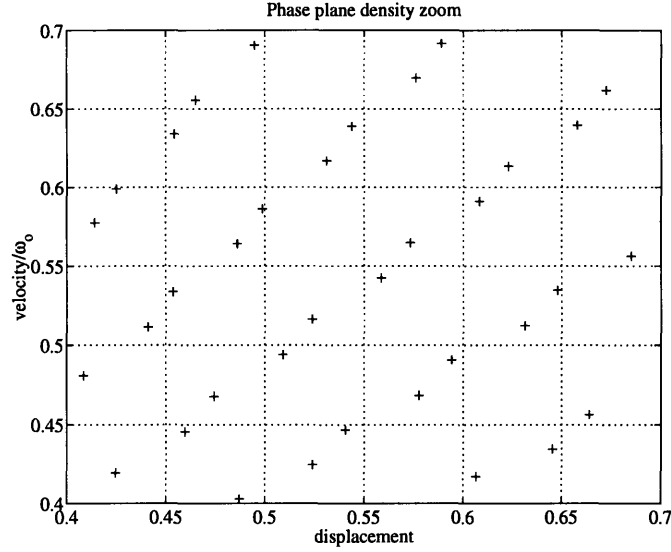


Figure 4.3: Zoom of phase plane response (ω_o Hz input sampled at $35.5\omega_o$ Hz) where the dashed boxes represent force-state map holes.

the state plane density are limited by data storage capability.

Applied load direction

Extension from single d.o.f. component testing to multiple d.o.f. allows the experiment designer to vary the applied load direction within the vectors of applied generalized forces (see Figure 3.1). By employing either a single test, during which the direction varies, or a series of tests, each with a fixed direction, data must be obtained which spans the applied load direction space. The appropriate set of test directions will depend on the arrangement of sensors, the sensor noise characteristics and the degree of stiffness coupling in the component being identified. The approach suggested, and used in this report, is to postulate several sets of directions; test the component with those sets of directions; and evaluate the directions by *a posteriori* data testing.

There are an infinity of choices of input directions. Two test directions suggested are those which decouple physical d.o.f. and those which decouple physical generalized input forces. These directions are good choices for two reasons; they are often close to the principle directions of a component; and they are often aligned with the sensitive directions of the sensors. However, in choosing directions the experimenter must be careful not to induce undesired nonlinear response.

A posteriori data testing involves the comparison of estimated standard deviations of the parameters of interest. The process of estimating parameter standard deviations

is described below.

Once data are taken over the selected sets of directions, an extended least squares analysis is used to identify the linear parameters of the model fit to the data and the standard deviations of the parameters. Equations 4.1 through 4.5 are written for the six d.o.f. identification of linear *compliance* parameters. The equations are inherently recursive. A full time sequence of test data is divided into L time histories ($l = 1, 2, \dots, L$) of sufficient number length, n = number of d.o.f. (6), to identify the 36 compliance parameters that describe the unconstrained motion resulting from generalized applied load. The recursive Equations are

$$\begin{bmatrix} \tilde{\underline{x}}_l \\ \tilde{\underline{C}}_l \end{bmatrix} = F_l \tilde{\underline{C}}_{l+1} + \begin{bmatrix} \underline{e}_x \\ \underline{e}_c \end{bmatrix} \quad (4.1)$$

$$\begin{aligned} \underline{e}_x &= \eta_x + \eta_f C_l + F_l \eta_{C_l} \\ \tilde{\underline{x}} &= \begin{bmatrix} \underline{x}_1^T & \underline{x}_2^T & \dots & \underline{x}_n^T & \tilde{\underline{C}}_l^T \end{bmatrix}^T \\ \tilde{\underline{C}} &= [C_{11} \ C_{22} \ \dots \ C_{16} \ C_{21} \ \dots \ C_{66}]^T \end{aligned}$$

$$F_l = \begin{bmatrix} \underline{f}_1^T & 0_{[1 \times 30]} \\ \vdots & \vdots \\ 0_{[1 \times 30]} & \underline{f}_6^T \\ & I_{[36 \times 36]} \end{bmatrix}$$

Where $\tilde{\underline{x}}_l$ is a vector of n time measurements of the displacement d.o.f., \underline{x} , augmented with the previous least squares solution of the compliance parameters, \underline{C}_l , also arranged as a vector. The matrix F_l consists of n measurements of applied load, arranged as shown, augmented with the identity representing pseudo measurement of the parameters. The error $[\underline{e}_x \ \underline{e}_c]^T$ is assumed Gaussian, zero mean, with covariance Ψ_0 . The vector \underline{e}_x includes error in the displacement measurement, η_x , error in force measurement, η_f , propagated through the last estimate of the compliance, \underline{C}_l , and error in the compliance parameters, η_{C_l} , multiplied by the next time increment of force, F_l . The vector \underline{e}_c represents the underlying assumption of the extended least squares that the parameters are inherently uncertain. The solution to 4.1 is found by multiplying both sides by $F_l^T \Psi_l^{-1}$ and solving for the next estimate of the parameters, $\tilde{\underline{C}}_{l+1}$. The recursive solution is shown in Equation 4.2 with the corresponding update

of the covariance matrix in Equation 4.3.

$$\tilde{\underline{C}}_{l+1} = \left(F_l^T \Psi_l^{-1} F_l \right)^{-1} F_l^T \Psi_l^{-1} \begin{bmatrix} \tilde{\underline{x}}_l \\ \tilde{\underline{C}}_l \end{bmatrix} \quad (4.2)$$

$$\Psi_{l+1} = \left[F_{l+1}^T \Psi_l^{-1} F_{l+1} \right]^{-1} \quad (4.3)$$

The matrix Ψ is initialized with variance estimates made from inspecting the time domain data, Ψ_0 . The results of the estimation process are the least squares solution to the compliance parameters and the covariance matrix, Ψ . The covariance can be partitioned into those elements associated with the states and parameters,

$$\Psi = \begin{bmatrix} \psi_x & \psi_{xC} \\ \psi_{Cx} & \psi_C \end{bmatrix} \quad (4.4)$$

$$\sigma_C = \sqrt{\frac{\text{diag}(\psi_C)}{m - 36}} \quad (4.5)$$

Where σ_C is the standard deviation of the estimated compliance parameters, m is the total number of measured data points used in the identification and 36 is the total number of identified parameters. The σ_C can then be normalized by the identified parameters to produce a vector of normalized standard deviations for eventual comparison of the various sets of test directions.

In order to use the presented analysis, the component is assumed, but not restricted, to be weakly nonlinear. Strong nonlinearities bias the linear parameter standard deviations and favoring those postulated test directions which yield the most linear response.

4.2 Linear least squares parameter identification

Having selected the applied load directions and time history, the general problem of identifying the physically nonlinear components can proceed. Identifying the physically nonlinear components comprises of fitting the models of the components to data. This section presents linear least squares parameter identification. Linear least squares parameter identification is used in the algorithms that fit the analytically nonlinear models to the data.

The objective of least squares is to minimize the summed squared error between

a component model and the data. To this end a simple example is presented in Equations 4.6 through 4.8. This example is used to motivate scaling of the data and the use of the singular value decomposition in the solution step. To avoid non physical optima in the solution step constrained optimization may be required. Quadratic programming with linear constraints is presented as a method to avoid non physical optima.

An example of an analytic model of the i th transmitted force, F_{Ti} through a component is

$$F_{Ti} = C_{10}x_i + C_{30}x_i^3 + C_{11}x_i\dot{x}_i + C_{31}x_i^3\dot{x}_i + C_{13}x_i\dot{x}_i^3 + C_{33}x_i^3\dot{x}_i^3 + C_{01}\dot{x}_i + C_{03}\dot{x}_i^3 \quad (4.6)$$

Here the analytic parameters, C_{mn} relate the motion of the single d.o.f., x_i , and its rate to the transmitted force. Given that test data is available, the error between the model and the data can be written as

$$\underline{e} = \underline{f}_{Ti} - \phi p \quad (4.7)$$

Where \underline{f}_{Ti} is the transmitted force data; p is the vector of parameters in Equation 4.6 arranged as shown in Equation 4.8; and ϕ is the d.o.f. data matrix, arranged column wise as shown in Equation 4.9. The objective is to minimize the sum of the squared error, \underline{e} .

$$p = [C_{10} \ C_{30} \ C_{11} \ C_{31} \ C_{13} \ C_{33} \ C_{01} \ C_{03}]^T \quad (4.8)$$

$$\phi = \begin{bmatrix} x_i & x_i^3 & x_i\dot{x}_i & x_i\dot{x}_i^3 & x_i^3\dot{x}_i & x_i^3\dot{x}_i^3 & \dot{x}_i & \dot{x}_i^3 \end{bmatrix} \quad (4.9)$$

The standard solution of the least squares problem p , is shown in Equation 4.10.

$$p = [\phi^T W \phi]^{-1} \phi^T W \underline{f}_{Ti} \quad (4.10)$$

In practice, the physical dimensions of the data \underline{x} and \dot{x} requires a weighting matrix W be used to scale the data. For x on the order of 10^{-6} , x^3 is of order 10^{-18} and $x^3\dot{x}^3$ is of order 10^{-30} . Weighting the data conditions ϕ for use in the solution step.

Equation 4.6 of the example is written for a single d.o.f. dependence. The right hand side (RHS) of Equation 4.6 can be easily extended to include multiple d.o.f. dependencies. The linear least squares solution equation , 4.10, remains unchanged for multiple d.o.f. dependencies. However, the vector of parameters, p , and data

matrix, ϕ , are extended to incorporate the multiple d.o.f. model.

Multiple d.o.f. linear least squares also requires special scaling of the data. The problem lies in forming the d.o.f. data matrix, ϕ in Equation 4.9. For an independent transmitted force model, F_{Ti} , a multiple d.o.f. response implies that the dimension of ϕ is $n(\text{data points}) \times (\text{d.o.f.} \times \text{no. of param.})$. Adding d.o.f. to a model results in more columns in ϕ . The higher dimension of ϕ introduces condition problems when computing the inverse of $\phi^T \phi$. Conditioning problems arise when the measured d.o.f. response are similar rendering the matrix $\phi^T \phi$ close to singular.

Two methods exist which contribute to the solution of this conditioning problem. These methods are presented next. Also, a method of constraining the linear least squares fit to return a physical model is described.

Scaling the d.o.f. data

The first method for conditioning the data is scaling the d.o.f. data via strain energy arguments. This determines the matrix W , to use in the solution step (in Equation 4.10 of the example).

Scaling via linear strain energy can be performed for a weakly nonlinear component. The finite element method is used so that the estimated stiffness matrix from *a priori* information scales the d.o.f. in ϕ . In particular, for each transmitted force direction, the corresponding row of the linear stiffness matrix is used. The elements of the row (using consistent coordinates) are each used to scale corresponding d.o.f. For example, a weighted data matrix for the i th transmitted force would be,

$$W\phi = \begin{bmatrix} K_{ii}x_i & K_{ii}x_i^3 & \cdots & K_{ij}x_j & K_{ij}x_j^3 & \cdots \end{bmatrix} \quad (4.11)$$

This scaling is physical and introduces modeling bias towards linear strain energy distribution.

Using the singular value decomposition

The second method of alleviating conditioning problems is using the singular value decomposition (SVD) to compute the inverse of $\phi^T W \phi$. The inverse is written as

$$\Psi^{-1} = \left[\phi^T W \phi \right]^{-1} \quad (4.12)$$

Where the SVD of Ψ is

$$\Psi = U \Sigma V \quad (4.13)$$

In this equation V and U are the right and left singular vectors respectively and Σ can be expressed as

$$\Sigma = \begin{bmatrix} \sigma_1^2 & 0 & \cdots & 0 \\ 0 & \sigma_2^2 & \cdots & 0 \\ \vdots & & \ddots & \\ 0 & 0 & \cdots & \sigma_n^2 \end{bmatrix} \quad (4.14)$$

The elements of Σ are ordered by their magnitudes so that the smallest singular value is the element in the bottom right corner. The inverse may then be computed by truncating rows and columns of V , U and Σ in accordance with a preset threshold.

$$\Psi^{-1} = V_{l \times l}^{-1} \begin{bmatrix} 1/\sigma_1^2 & 0 & \cdots & 0 \\ 0 & 1/\sigma_2^2 & \cdots & 0 \\ \vdots & & \ddots & \\ 0 & 0 & \cdots & 1/\sigma_l^2 \end{bmatrix}_{l \times n} U_{l \times l}^{-1} \quad (4.15)$$

This means that $\sigma_i > \sigma_{thres}$ for $i \leq l$.

Singular value truncation removes low level signal data and hence may bias quasi-static results in the compliant directions of the component. The compliant directions yield large signal in the d.o.f. measurements with respect to the stiff directions. Components with large directional stiffness disparities therefore require strain energy data scaling before the use of the SVD.

Constrained Optimization

In some cases the linear terms of the models returned by the above least squares process may be non physical, *e.g.* a non positive diagonal term in the linear stiffness or damping matrix. In this case the least squares problem is reformulated in terms of a quadratic program with linear constraints on the positivity of the stiffness matrix.

The linear least squares problem of Equation 4.8 can also be formulated as a quadratic program as shown in Equation 4.16. This allows incorporation of linear constraints on the allowable set of solutions [23]. Simple linear constraints are the positivity of the diagonal linear stiffness and damping terms. In this case A is a sparse matrix of -1 's multiplying the appropriate terms in the vector of parameters, p , and b is a zero vector. The quadratic program is written as

$$\underset{p}{\text{minimize}} \left\{ \frac{1}{2} p^T H p + c^T p \right\} \quad \text{subject to :} \quad A p \leq b \quad (4.16)$$

Again p represents the vector of parameters in the identification problem. The matrix H is equal to $\phi^T \phi$ where the data matrix, ϕ , is defined in Equation 4.8. The matrix c is equal to the data matrix transposed and multiplied by the measured forces, $\phi^T f_{Ti}$. As was the case in the linear least squares problem a weighting matrix can be introduced into Equation 4.16, in which case H is equal to $\phi^T W \phi$ and c is equal to $\phi^T W f_{Ti}$.

The positivity properties, enforced by the constraint, are important for some nonlinear integration routines. Such a routine was used for the weakly coupled loads identification of the MODE alpha joint bay component, presented in section 4.4.

4.3 Nonlinear least squares parameter identification

Nonlinear least squares may also be used in the algorithms that identify a component model from test data. Specifically, nonlinear least squares is used to fit a component model to the data when the component model contains non analytic and conditional terms. Nonlinear least square algorithms require an initial guess of the model parameters. An initial guess of the analytic parameters is derived from a purely analytic model that is initially fit to the data (using linear least squares). An initial guess of the non analytic and conditional parameters have to be inferred from the data.

In this work nonlinear least squares is performed by implementing the Levenberg-Marquart technique on the least squares cost function (minimizing the mean square error between the data and the model). Fletcher [19] provides a good reference for the technique while Spanos and Mingori [39] present useful insight into its application.

The Levenberg-Marquart technique is represented in Equation 4.17 as a modification to the classical Newton iteration.

$$p_{n+1} = p_n - [H_n + \mu_n I]^{-1} G_n \quad (4.17)$$

Where p_{n+1} is the next estimate of the parameters. H_n and G_n are the Hessian and gradient matrices respectively, computed at the n th step. The scalar μ_n is known as the Levenberg-Marquart parameter. When μ_n is zero Equation 4.17 reduces to the classic Newton iteration. Setting μ_n to be arbitrarily large results in an arbitrarily small step along the direction of steepest descent in parameter space. Convergence is dependent on the quality of the parameterization and initial guess.

4.4 Weakly coupled loads identification

Now that both the linear and nonlinear least squares methods have been defined the use of these methods in component model identification algorithms is discussed. For the following developments k distinct test directions which span the generalized applied load space were assumed. Two types of identification algorithms were required to identify the MODE components: a weakly coupled loads identification, described in this section; and a decoupled d.o.f. identification, described in section 4.5.

This section presents the weakly coupled loads identification by first defining when to use the algorithm. In order to use the algorithm the nonlinear component model has to be integrated to approximate the residual d.o.f. when the component is exercised by weak coupled (non dominant) applied loads. A description of the integration method follows the details of the algorithm.

Weakly coupled loads identification seeks to decouple the generalized applied loads. A single direction of generalized applied load can generate motion of multiple d.o.f. Even though completely decoupled loads data are the ideal the physical limitations of the testing device introduce weakly coupled loads other than the dominant applied load. The weakly coupled loads identification algorithm is designed to deal with this situation.

A possible solution to the identification problem, in the presence of testing device weak coupled loads, proceeds by augmenting the data vector f_{Ti} with the f_{Tj} , $j \neq i$, before performing a least squares fit to the component model. This results in large impractical least squares problems. Integration provides an avenue by which practical component model identification can proceed.

The procedure used in this report was to separate the weak coupled loads from a single load direction test (loads other than the dominant applied load) and drive the current component model with them. The component model was integrated using an alternating frequency time-domain (AFT) direct algorithm proposed by Lau, Cheung and Wu [26] to give the residual states resulting from the weak coupled loads. These states are then used to correct the measured states so that the strong applied load direction data can be fit to the model, F_{Ti} .

The basis of the weakly coupled loads algorithm is that; in order to fit the strong load direction model the measured states need to be corrected for the displacement and velocity contributions due to the measured weak coupled loads. In order to generate the state corrections a component model is needed. The weakly coupled loads iterative identification was formulated in the following algorithm where i is the index of the dominant applied load in the k th test,

Step 1: Initialization

$$\begin{aligned} \text{for } k &= 1, 6 \\ &\text{solve for } F_{Ti} \\ (f_{Ti})_k &= F_{Ti}(x) + e_i \end{aligned}$$

Step 2: Iteration on a loop of k .

$$\begin{aligned} \text{for } k &= 1, 6 \\ x_{AFT} &= AFT(F_{Tj}) \quad j \neq i \\ \tilde{x} &= x - x_{AFT} \\ &\text{solve for } F_{Ti} \\ (f_{Ti})_k &= F_{Ti}(\tilde{x}) + e_i \end{aligned}$$

Initially the algorithm proceeds as if no weakly coupled loads are present, *i.e.* as if $F_{Tj} = 0$ for $j \neq i$. Models of the strong load directions, $F_{Ti}(x)$ as explicit functions of the measured states, are identified first from the data, f_{Ti} , in step 1. $F_{Ti}(x)$ consists of both diagonal, F_{ii} , and non diagonal, F_{ij} $j \neq i$, models as expressed in the general form of Equation 3.1, and in the component specific models. Solving for the F_{Ti} of the component uses either linear or nonlinear least squares formulations, where appropriate.

The second step of the algorithm is to proceed using the previously determined parameters (the component model being iterated on) to correct for the coupled loads f_{Tj} , $j \neq i$. Previously identified parameters, of the models F_{Tj} , $j \neq i$, are used in the AFT integration to generate estimates of residual states. The estimated states, x_{AFT} , are then subtracted from the measured states, x , to give \tilde{x} . A least squares fit is next performed to the dominant load data f_{Ti} using the corrected states \tilde{x} . Iteration over all the k tests converges to the least squares result in which the error is treated as a vector with dimension equal to that of the applied loads vector (in this case 6).

Nonlinear integration such as the AFT allow the generation of states resulting from the weak coupling loads present in a dominant applied load test, given that the model is known. The AFT method is described below.

The direct integration AFT algorithm is illustrated in Figure 4.4. The weak coupled loads, sampled every T seconds, are Discrete Fourier Transformed using an FFT to give a matrix of driving forces in the discrete frequency domain, $f_T(\omega)$. Discrete frequency domain structural response, $X(\omega)$, is computed by multiplying the coupled loads by the inverse of the quasistatic linear structural operator, $\Delta = (K + j\omega C)$. After checking for convergence with the last estimate of the states, the discrete frequency domain response is converted back to the discrete time domain to give the

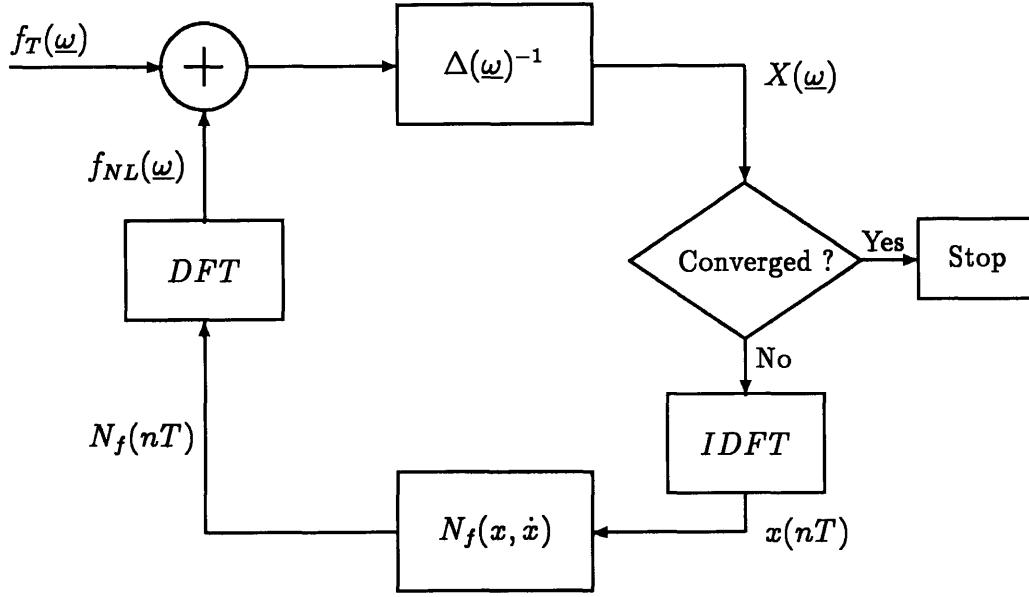


Figure 4.4: Block diagram of an Alternating Frequency Time-domain direct algorithm.

matrix of estimated states $x(nT)$. These estimates are used to generate the nonlinear contribution to the right hand side of the equation giving a residual nonlinear force matrix $N_f(nT)$. The nonlinear residual forces are then *DFT*'d and used to drive the linear integration kernel by summing them with the original weak coupled loads. Note that because the full discrete time history of the states are computed in all iterations conditional nonlinearities such as memory are easily incorporated into the integration.

Problems inherent to forward time domain integration such as frequency distortion and numerical damping [18] are traded in the AFT for *DFT* leakage and numerical aliasing [26]. Here, again, the time history choice of an odd ramped sinusoid, with frequency coinciding with a DFT frequency, benefits the data post processing. Aliasing is avoided by discrete time filtering $N_f(nT)$ before computing its DFT.

4.5 Decoupled d.o.f. identification

The second set of applied load directions used in this report to identify components were k directional tests which decoupled the resulting d.o.f. These sets of data did not require integration to estimate the residual states caused by coupled loads. Instead the all the loads present in each direction test were fit to the dominant d.o.f. response, of the respective test, in an iterative fashion. The basis of the decoupled d.o.f. algorithm is that in order to fit the dominant single d.o.f. models to the loads the measured

loads needed to be corrected for residual measured states (other than the dominant d.o.f.). In order to generate the corrections for the measured loads a model was required.

The decoupled d.o.f. algorithm iterates on the columns of models (fitting F_{ij} , $i = 1, 6$, $j = k$, for each k) rather than the rows of models (fitting F_{Ti} , i th load dominant, for each test k) as was the case in the weakly coupled loads analysis. The decoupled d.o.f. algorithm, which iterates on a matrix of error, e_{ik} , was implemented as follows;

Step 1: Initialization

```

for  $i, k = 1, 6$ 
  let  $F_{ij} = 0$   $j \neq i$ 
  solve for  $F_{ii}$ 
   $(f_{Ti})_k = F_{ii} + e_{ik}$ 

```

Step 2: Iteration on an outer loop of k and inner loop of i .

```

while  $r = 0 \rightarrow 1$ 
  for  $k = 1, 6$ 
    for  $i = 1, 6$ 
      if  $i = k$  solve for  $F_{ii}$ 
       $(f_{Ti})_k = F_{ii} + r \sum_{j \neq i} F_{ij} + e_{ik}$ 
      else solve for  $F_{ik}$ 
       $(f_{Ti})_k = r F_{ii} + (F_{ij})_{j=k} + r \sum_{j \neq i, j \neq k} F_{ij} + e_{ik}$ 

```

Where the measurements are the $(f_{Ti})_k$ (the i th component of total force transmitted taken in the k th test direction) and the d.o.f. (x_j, \dot{x}_j) are implicit in the F_{ii} and F_{ij} . The F_{ii} and F_{ij} are the component model specific equations in section 3.3.

Step 1 initializes the process by solving for the diagonal functions, F_{ii} , by iterating over the k distinct test directions while minimizing the error, e_{ii} , $i = 1, 6$. No information can be used from the F_{ij} in this step as they are yet to be determined.

Step 2 requires multiple iterations to fit the F_{ik} , $i = 1, 6$ for each k , minimizing the matrix of error e_{ik} , while varying the homotopy parameter, r . The homotopy parameter determines the weight on the previously identified non diagonal row models, F_{ij} $j \neq i, k$, and varies from zero to one. This allows numerical conditioning of the algorithm. In this step, two successive loops are performed, the inner loop over the i force components and the outer loop over the k dominant d.o.f. directions (test directions). The homotopy algorithm initializes with the assumption that the F_{ij}

are zero. The algorithm proceeds with identifying and eventually reidentifying the F_{ij} ($i, j = 1, 6$) using parameter models from the preceding iteration, and from the proceeding model fits during the current iteration. After the homotopy parameter is set equal to one, further iterations are performed until a norm of the error matrix is reduced to a preset threshold.

Both the coupled loads and decoupled d.o.f. algorithms involve subtraction and are therefore not robust to identifying parameters near the noise floor. Some combination of program control and user input is required to eliminate the possibility of errors made when fitting low level noise; *i.e.* identifying parameters that are nominally zero. The user also determines whether the model fit is either over or under specified by monitoring the fit convergence.

4.6 Summary

This chapter has provided the software algorithms with which to fit the models presented in section 3.3 to measured component data. The fitting routines of the algorithms were either linear or nonlinear least squares. The algorithms themselves were fashioned to identify component models using two types of desired applied loads to the components. The two types of desired applied loads were decoupled loads and decoupled d.o.f. tests.

Acquiring the data for the component model identification process requires a component tester designed for application and measurement of possibly coupled loads and measurement of multiple d.o.f. The component tester hardware with which to collect the data and the MODE component hardware are described next.

Chapter 5

Experiment Hardware and Procedure

This chapter describes the experiment hardware and the testing procedure used to acquire data for the component identification process. Section 5.1 describes the experiment hardware, which consists of unique six degree of freedom component tester, a calibration bay component, and the MODE structural components. section 5.2 presents the experiment procedure.

5.1 Hardware

In order to acquire the data required for the component model identification process a six degree of freedom component tester is required. This section first describes the requirements and specifications of the component testing hardware. The design and implementation of the component tester is next considered. Both mechanical and electrical aspects of the component tester system are presented. Finally, a calibration bay component and MODE component hardware are described.

Component tester requirements and specifications

The functional requirements for the component tester are that it

- accommodate test specimens of MODE component size
- be capable of six axes of independent and simultaneous actuation
- be instrumented such that measurement can be made of
 - six generalized applied loads about the elastic centroid of the unconstrained end of a component

- six reactions about the elastic centroid of the constrained end of a component
- six generalized deflections at the unconstrained end of the test components
- have fundamental frequency, with component mounted, greater than twice the quasistatic test frequency

The MODE component size is that of a typical bay unit in the truss structure, $8'' \times 8'' \times 8''$. Six axes of actuation requires at least six actuators in a geometrical arrangement. The load and stroke capability of the actuation must exceed the maximum dynamic range seen by the MODE STA components in full structure modal testing. Measurement of the reactions and deflections need be compatible in range and resolution with the MODE STA dynamics test loads and deflections [2].

Additional specifications on the mechanical aspects of the component tester are that it

- apply minimal mounting preload to the test component
- be capable of relieving preload induced by test rig weight
- be capable, within small deflections, of unconstrained six degree of freedom motion while taking maximum advantage of actuator stroke and load capabilities.

Specifications of the component testing electronics are that they

- provide at least six channels of independent amplified commanded input to the actuators
- condition, simultaneously anti-alias/filter, sample and store at least 18 channels of sensor measurement, so as to provide reaction force applied load and unconstrained d.o.f. data

Design and construction of the component tester

The MODE component tester consists of a mechanical testing device and support electronics. The mechanical testing device is first described in terms of the test frame, actuators and sensors. Electronics which drive the actuators and sampled the sensed data are next detailed.

A plan and elevation of the mechanical test rig is shown in Figure 5.1. The drawing is to scale with a scale length dimensioned of one foot shown. Further detailed drawings can be found in Appendix B. Figure 5.2 shows the component tester with the MODE alpha joint bay being tested.

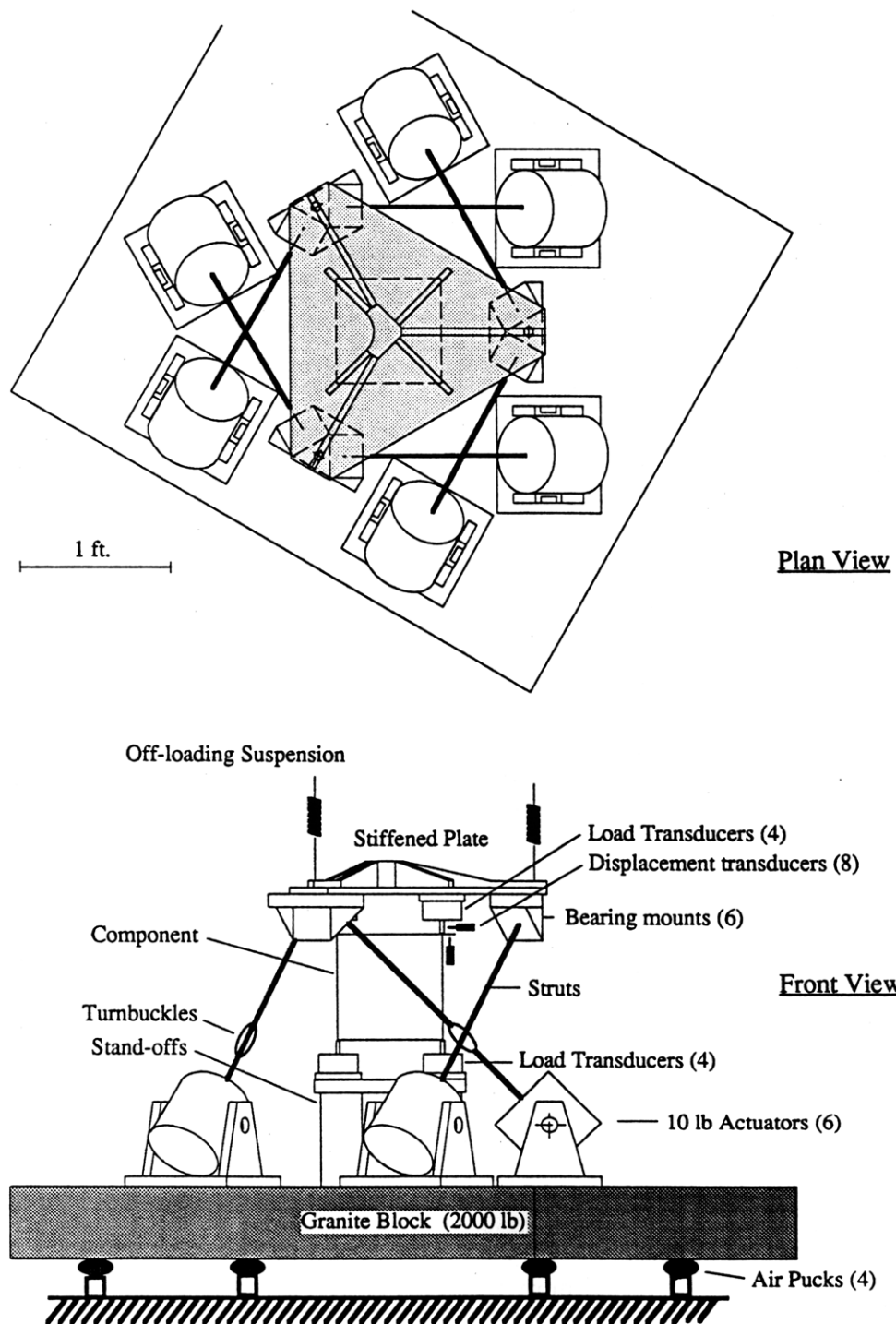


Figure 5.1: Plan and elevation of the MODE component tester.

Six voice coil actuators were mounted between a Rock Of Ages one ton granite surface plate and a stiffened aluminum plate in a Stuart platform arrangement (see Figure 5.1). The 4' x 4' granite base was air supported, on common air supply, so that building disturbances above 2.5 Hz were isolated from the tester. Struts connected the actuators to the stiffened plate. Bendix 6016-400 soft flexural bearings provided effective pins at both ends of the struts while maintaining stiffness in the extension load path. The pins allowed freedom in the bending and twist load paths. One strut in each of the three crossing pairs of struts incorporated a ring turnbuckle. The turnbuckle allowed the strut pair to cross while maintaining plan view axis symmetry of the test rig.

Load transducers were first appended to the test component before the component was mounted in the test rig. The instrumented component was mounted between the granite base and the stiffened plate using standoffs and interface plates, which provided for coarse height position adjustment. The strut turnbuckles were used for fine positioning and fit adjustment. Fine fitting adjustments were necessary to utilize the full stroke of the actuators.

Preload created by the weight of the stiffened plate, the transducers, and struts was off-loaded through an axial suspension system. Turnbuckles connected the suspension to the stiffened plate so that coarse off-loading adjustments could be made. Springs were chosen for the suspension system so that the plunge mode of the suspended stiffened plate (unconnected to the actuators) was approximately 3 Hz while the first internal mode of the springs was approximately 125 Hz.

Actuators

The Stuart platform geometry transforms linear force into six generalized forces about the centroid of the stiffened plate that are in turn applied about the elastic centroid of the mounted component. The load and stroke requirements, in conjunction with the geometrical arrangement, drove the actuator choice. The requirements for generalized load capacity called for maximum applied moments, by the stiffened plate to the test article, of 100 in-lb and maximum shear loads of 20 lb. Moments were taken with respect to the elastic centroid of the component. The elastic centroid of the component and the centroid of the stiffened plate coincide as shown in the plan view in Figure 5.1.

The stroke requirements dictated a maximum total linear actuator stroke of approximately 0.070 inches. Six Bruel & Kjaer 10 lb., ± 0.150 inches stroke, linear electromechanical actuators coupled through the geometry of the Stuart platform yielded the required stroke and loads. The resulting loads which that could be applied to the

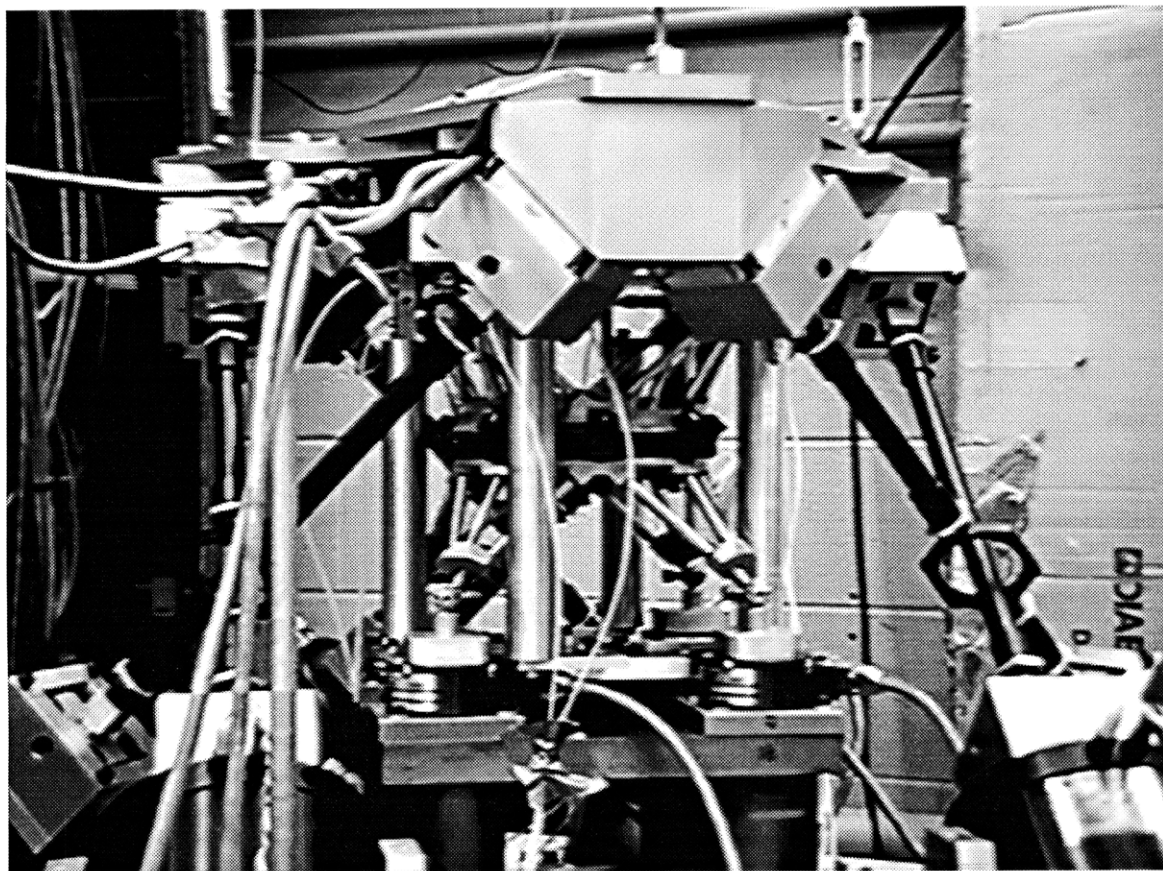


Figure 5.2: MODE component tester with alpha joint bay as the test component.

test article by the top plate were 40 lb force in the axial direction (with respect to the component), 34 lb in the shear direction and 140 in-lb of moment. The maximum stroke achieved with no test specimen mounted was approximately ± 0.080 inches and $\pm .01$ radians.

Sensors

The sensors used include both load and displacement transducers. The required displacement measurement range and resolution for the MODE components were ± 0.020 inches and 0.00005 inches respectively. Deflections of the unconstrained end of the MODE and calibration components were measured with inductive bridge Kaman 1U1-8200 series noncontacting sensors. Conductive targets were required for the non-contacting sensors. Each sensor was mounted onto a sensor cage using micrometers. The micrometers allowed sensor stroke adjustment so that the full sensor stroke could be utilized. The sensor cages were affixed to the stand-offs at the constrained end of the components and did not contact the component or load applying structure. For the calibration bay, adjustable pretension bay and erectable bay components the

sensor cages were internal to the bays. An external sensor cage was used for the alpha joint bay as its geometry did not allow an internal cage. The external sensor cage can be seen in Figure 5.2 as the vertical aluminum posts surrounding the alpha joint bay.

Eight displacement sensors were arranged so that six d.o.f. deflections/rotations of the unconstrained component end were measured about the elastic centroid. In principle, only six displacement sensors are required to make six d.o.f. measurements. However, in practice, eight displacement sensors were used in the arrangement as shown in Figure 3.1. This provided some averaging of information when resolving the generalized deflections and allowed enough freedom to measure rotations accurately. The information discarded in reducing the eight measurements to six are the in plane breathing and out of plane warping of the component, both highly constrained by the stiffened plate.

Calibration of the displacement sensors was performed on the laboratory bench in a micrometer stand. The targets used for calibration were similar to the actual testing targets. A calibration error of $\pm 3\%$ was accepted. Connectors for the load transducers at the unconstrained end were designed so that they provided flat conducting surfaces for displacement sensors targets.

The displacement sensors measured the back-electromotive-force due to the motion of a conducting surface in an essentially constant electric field. The electromotive force was sensed as an impedance variation in the sensor inductive coil. Oil, dirt and humidity had no effect on the displacement sensing system performance.

In order to resolve the generalized applied loads to the unconstrained end, and reaction forces at the constrained end of a tested component, eight load transducers were used. The load transducer measurement range for the MODE component tester were 50 lb and 150 in-lb with resolution of .1 lb and .3 in-lb respectively. Transmitted loads were measured with JR^3 TFS70-3012A75-U560 multiaxial load transducers. Each load transducer used had the capability of measuring three forces. The load transducers were attached to each node of the bay components as shown in Figure 3.1.

At both the constrained and unconstrained component interfaces twelve channels of calibrated load were measured, three channels at each of four interfacing nodes. Factory calibrations were used to decoupled independent load transducer measurements (each of the load transducers were factory calibrated and passed an acceptance test). In general only six channels at each interface would be needed, but twelve were used in the arrangement shown in Figure 5.3. Six generalized loads were computed at the elastic centroid of each interface by resolving the information from the twelve appropriate load measurements. The information discarded was in plane shearing

and out of plane warping loads.

Great care was taken to make exactly collocated and collinear force and displacement measurements. The arrangement of displacement and load transducers required that geometric lengths be used in the measurement of rotation and moments. A measurement error of $\pm .005$ inches was accepted for these lengths.

Aluminum connectors were designed to interface the various test components and the load transducers to the stiffened plate and base plate. The connectors were designed to have high stiffness while the load transducers were measured to have 80 N/ μ m axial stiffness. This ensured that deflection measurements were not corrupted by spurious compliance of the test rig. Bridging stiffness introduced by the load transducer cables (see Figure 5.2) was minimized by using laboratory stands and prebuckling the cables.

Electronics

Figure 5.3 shows a general block diagram of the component tester electronics . Six actuation time histories (voltages) were down loaded to the Lecroy Camac Crate by the experiment control personal computer. After initiating a test these time histories are passed through a zero order hold and provided on the output channels of the Lecroy function generator. The Lecroy function generator output is smoothed by Analog Devices programmable filters before being amplified by Crown 300A power amplifiers and passed to the experiment actuators. The corner frequency of the programmable filters was set at 38 Hz.

Twenty-four channels of force and eight channels of displacement were filtered and sampled as shown in Figure 5.3. In both the load and displacement transducers filtering in the factory provided signal conditioning was removed. External programmable filters were used to anti-alias filter the measurements. The nominally similar filters were Analog Devices BCD/Binary - programmable low pass active filters, 744/745 series. The corner frequency for the filters was set at 80 Hz which was 80% of the Nyquist frequency of the sampling A/D. In this way the same time (phase) delay was introduced into all load and displacement measurements.

Raw load and displacement sampled voltages were stored in binary format in the Camac Crate before being up loaded to the experiment control computer after each test run. Up load and down load capability was accomplished with a GPIB. Software written by Dr. M.C. vanSchoor was used for interfacing and converting the raw binary format voltages to *MATLABTM* format. *MATLABTM* software was then used to scale the data and resolve the data into six d.o.f. of generalized load and displacement information.

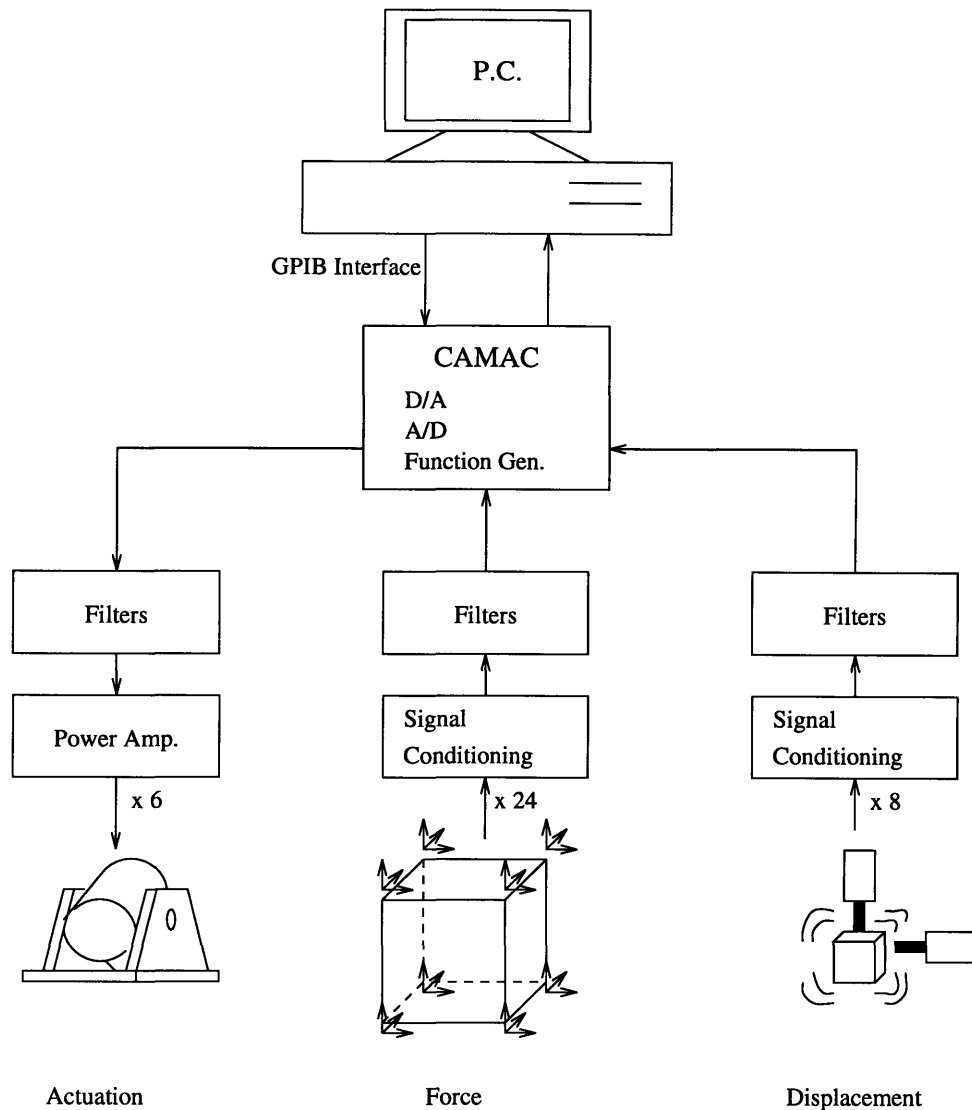


Figure 5.3: Electronics block diagram of MODE component tester.

The incorporation of the electronics and mechanical test rig provided the means with which to test the calibration and MODE components.

Calibration and MODE component hardware

Data on four test articles are presented in this report. This section describes the calibration bay, adjustable pretension deployable bay, erectable bay and alpha joint bay components respectively.

The component tester was first calibrated with a simple, nominally linear elastic, truss bay shown in Figure 5.4. The longerons, diagonals and battens are 3/8 in diameter Lexan rods, which are epoxied into 1.25" \times 1.25" aluminum nodes with Hysol EA 9394NA structural adhesive. Once erected the bay is 8" \times 8" \times 8" on

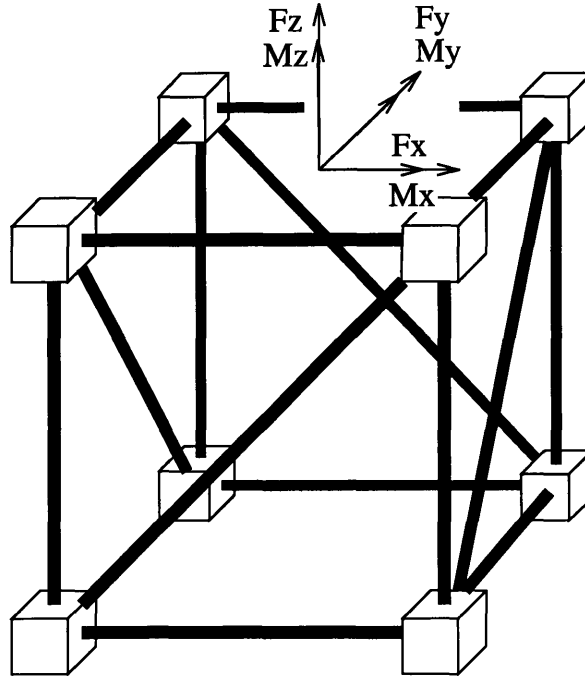


Figure 5.4: Simple calibration bay schematic with indicated test directions.

centers of the nodes. Calibration bay compliance was designed to approximately match the expected compliance of the the high preload MODE deployable bay. The bay diagonal geometry replicated that of the erectable MODE component.

Also shown in Figure 5.4 are the generalized load directions about the elastic centroid of the unconstrained component end. The same convention was used for all components.

The second test article is one deployable bay of the MODE STA, which incorporates a mechanism for varying the preload on the diagonal bracing wires [2]. This component is referred to as the adjustable pretension bay. Like all deployable structures, the STA deployable sections are potentially nonlinear. In addition to the pretensioned diagonal bracing wires, the bay contains four series 500 Lexan longerons with 6061 anodized aluminum locking knee joints, as shown in Figures 5.8 and 5.7. The Lexan is epoxied into the aluminum knee and corner fittings with Hysol EA 9394NA structural adhesive. During deployment, the two sections of the longeron fold at the knee joint, and pivot about a graphite pin at each of the two cross section frame attachments. A photographic image of a partially deployed four bay section is shown in Figure 5.5. A deployable cross section frame and corner fitting are shown in Figures 5.9 and 5.6 respectively.

Buckling loads of the bay longerons limits maximum pretension in the diagonal bracing wires at only 9% of their yield stress. Each wire is stranded type 304 stainless

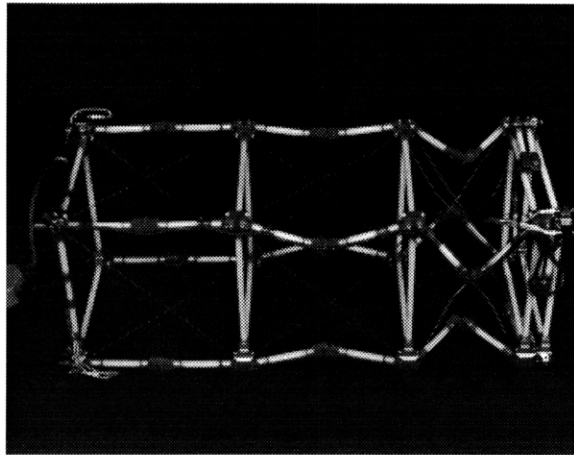


Figure 5.5: MODE partially deployed four bay section.

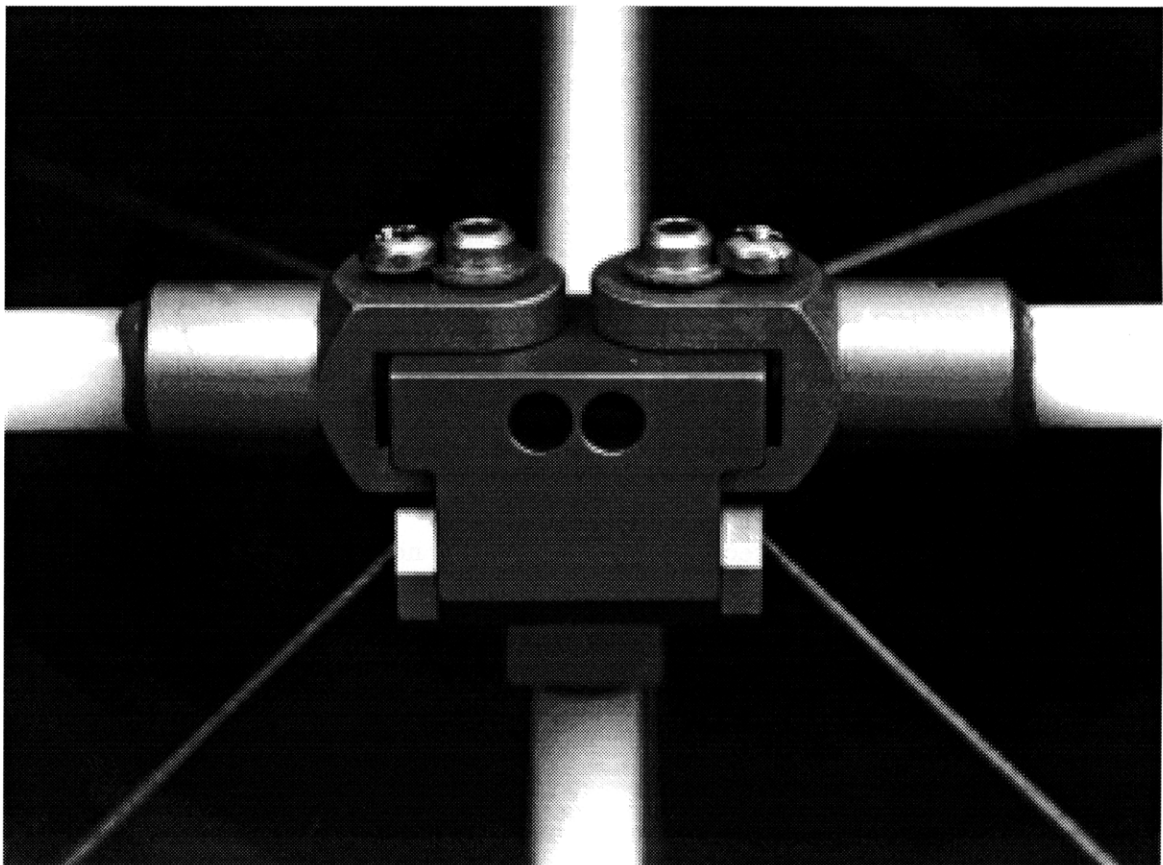


Figure 5.6: Deployable corner fitting, truss side view, with tension cable end receptacles (underneath) and longeron pin mechanism.

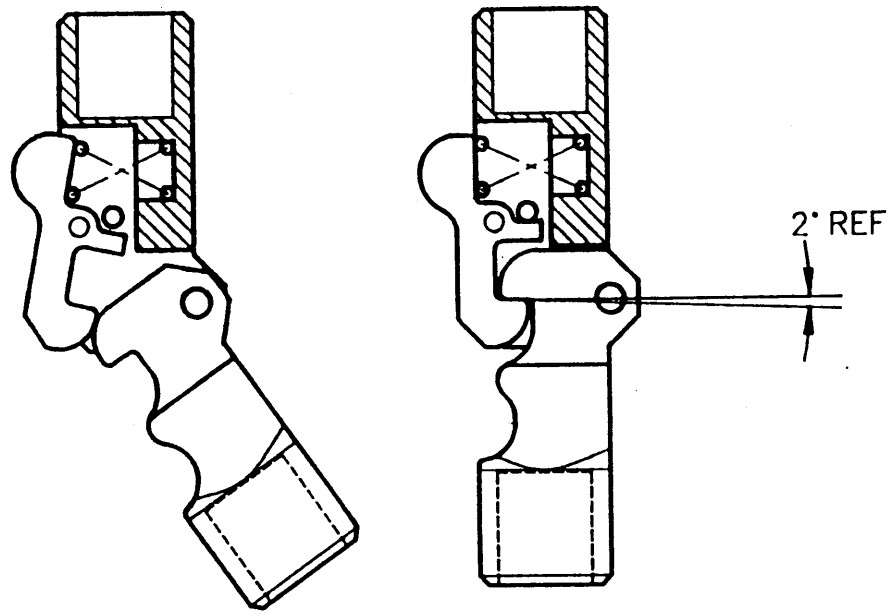


Figure 5.7: Knee joint.

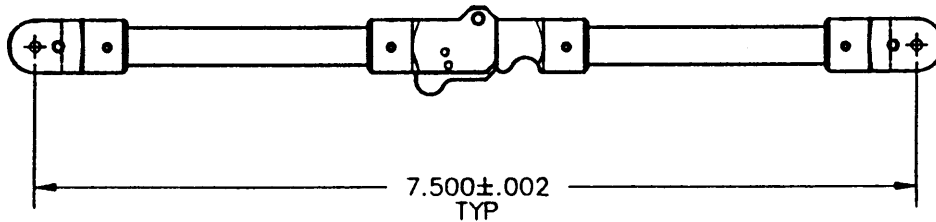


Figure 5.8: Deployable longeron.

steel with total outer diameter of 0.047 inches. The cables are terminated with a ball which seats in a spherical receptacle at the corner fittings of each batten frame. Wire pretension compresses the bay longerons to approximately 35 lb which is about 50% of their buckling load. In one of the deployable sections of the STA, the adjustable pretension bay was incorporated with three possible preload settings of approximately 7, 13 and 27 lb tension in the bracing wires. Tension adjustment was provided by cleats (see Figure 5.10) at each corner fitting of the adjustable bay. Identification of an identical component bay will be presented. The measured prestensions in the

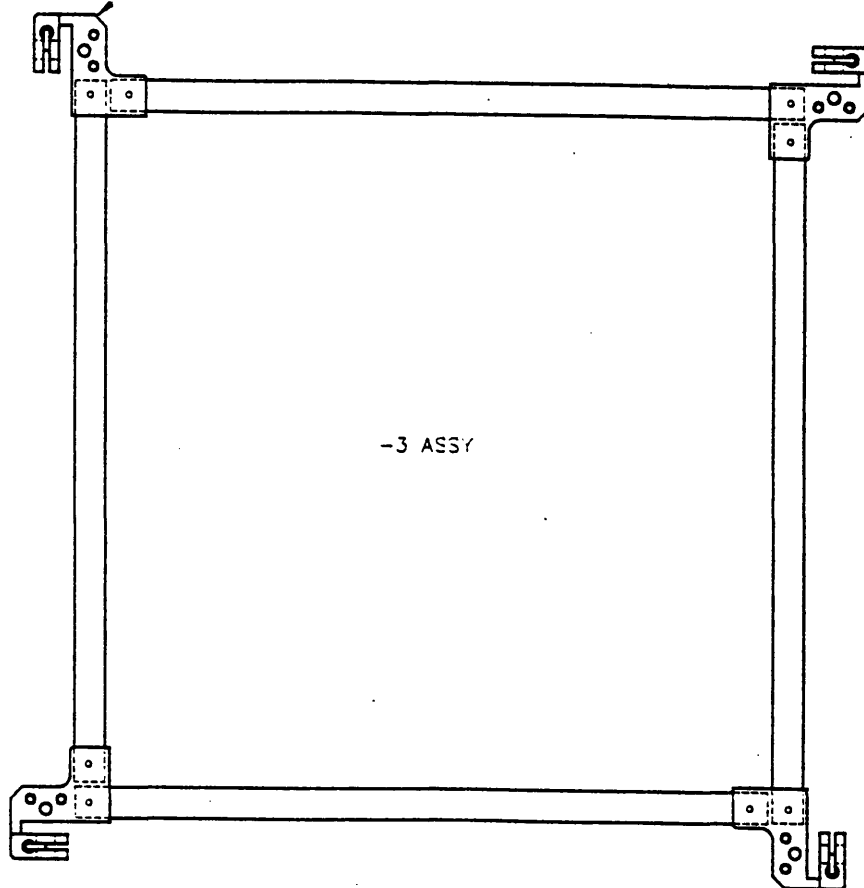


Figure 5.9: Deployable batten frame.

component adjustable bay are approximately 4, 15 and 32 lbs respectively.

Third to be tested was the erectable bay component. An erectable bay assembly was used in the MODE truss to mate the two deployable sections for the baseline configuration and to provide a corner unit for the L configuration. The erectable component hardware consists of struts, standoffs and nodes. The struts made up the diagonal, batten and longeron trusswork as shown in the side view of the erectable bay in Figure 5.12. Figure 5.11 shows the strut detail where the bulk of the strut is series 500 Lexan epoxied into an aluminum sleeved lug. Hysol EA 9394NA structural adhesive was used for all epoxied joints.

The lug fits into a cutout receptacle in the standoff unit. The standoffs are pre-

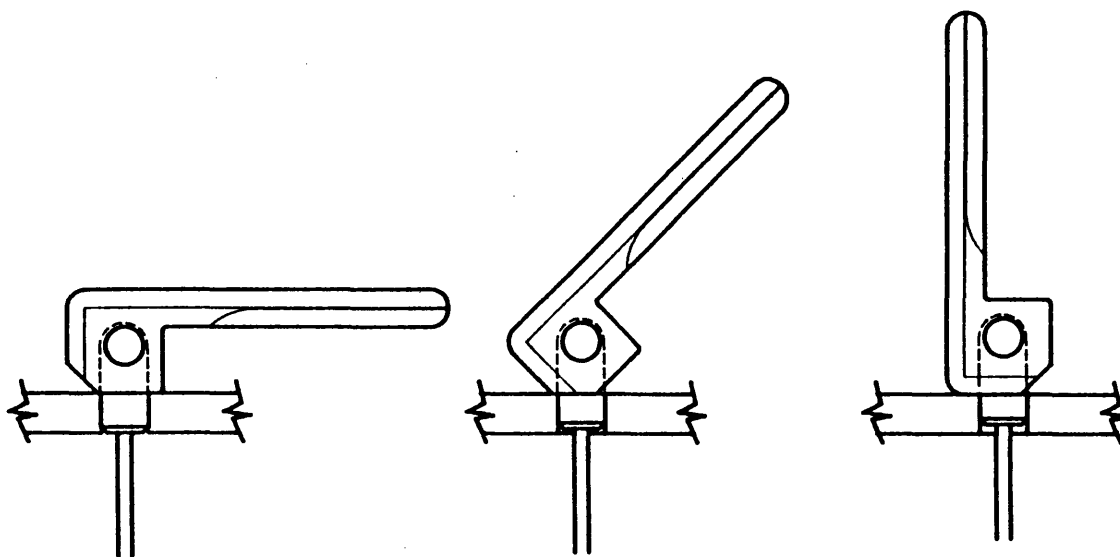


Figure 5.10: Tension cleat.

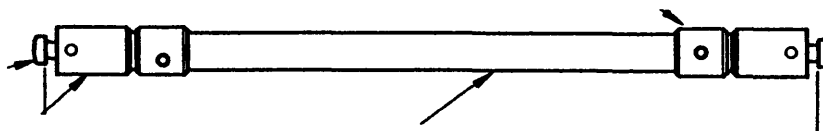


Figure 5.11: Erectable strut.

mounted to the aluminum nodes before receiving the struts. Once in place the internally threaded sleeve is screwed tight, pressing against the fixed standoff, thus fixing the strut to a node. Finger tightening provided a torque on the order of 1 in-lb which was acceptable for the MODE dynamics testing. The standoffs are tapered at the node end to allow # 6-32 screw mounting to the nodes, see Figure 5.13 for a typical corner fitting. The nodes were threaded holed so as to allow 26 axis symmetric positions in which to mount standoffs.

Figures 5.14 and 5.15 show the MODE alpha joint bay. This was the fourth component tested. Figure 5.14 shows the alpha joint in its operational configuration. Figure 5.15 shows the alpha joint in its separated configuration. Longitudinal axial rotation is permitted by the alpha joint about an axle centered at the two interfacing aluminum plates. A 5.5 millimeter stainless steel bearing race with an outer radius

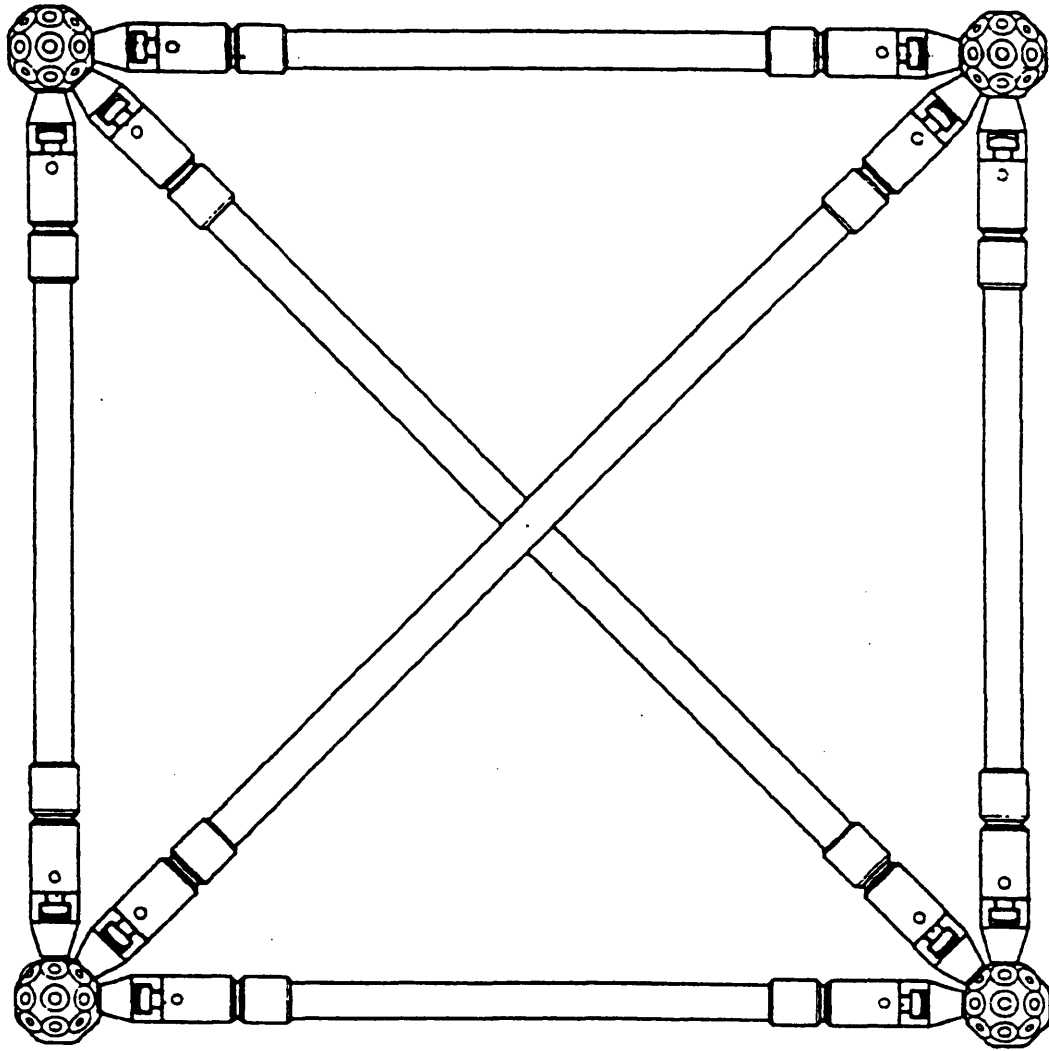


Figure 5.12: Erectable bay side view.

of 2.75 inches allows rotation about the axle when in its operational configuration. The bearing mechanism is approximately 6.25 in. diameter. At 45 degree intervals around the central mechanism, trios of Lexan rods are mounted radially, the ends of which converge to an aluminum plate. On the outer most surface of these aluminum plates a screw sleeve and lug assembly was fixed for attachment to a standoff which in turn was mounted to a bay node. In this fashion the axial rotation mechanism of the alpha joint was interfaced to the deployable truss units in both the MODE alpha and L configurations (see Figure 2.1).

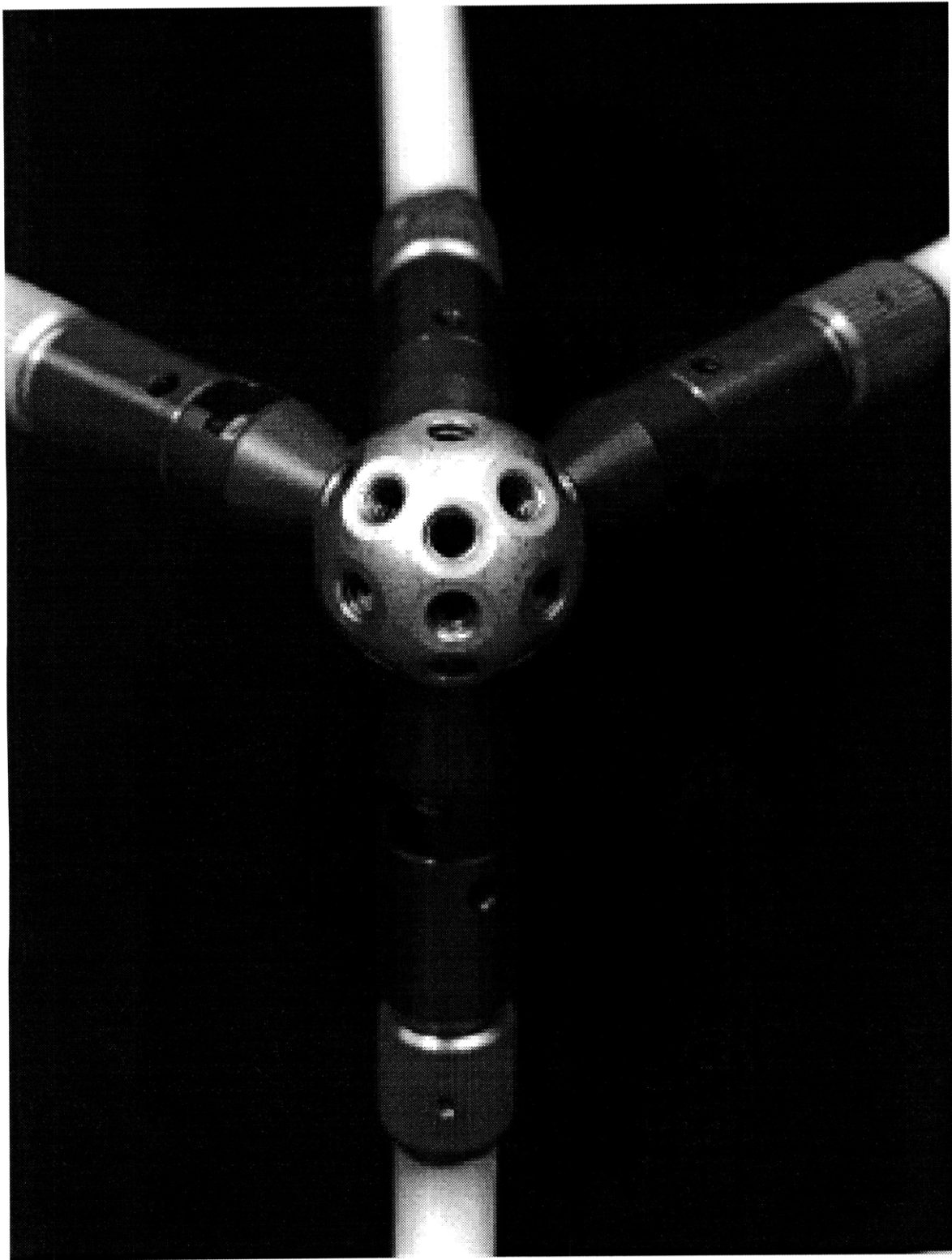


Figure 5.13: Erectable strut, standoff and node in a typical corner fitting.

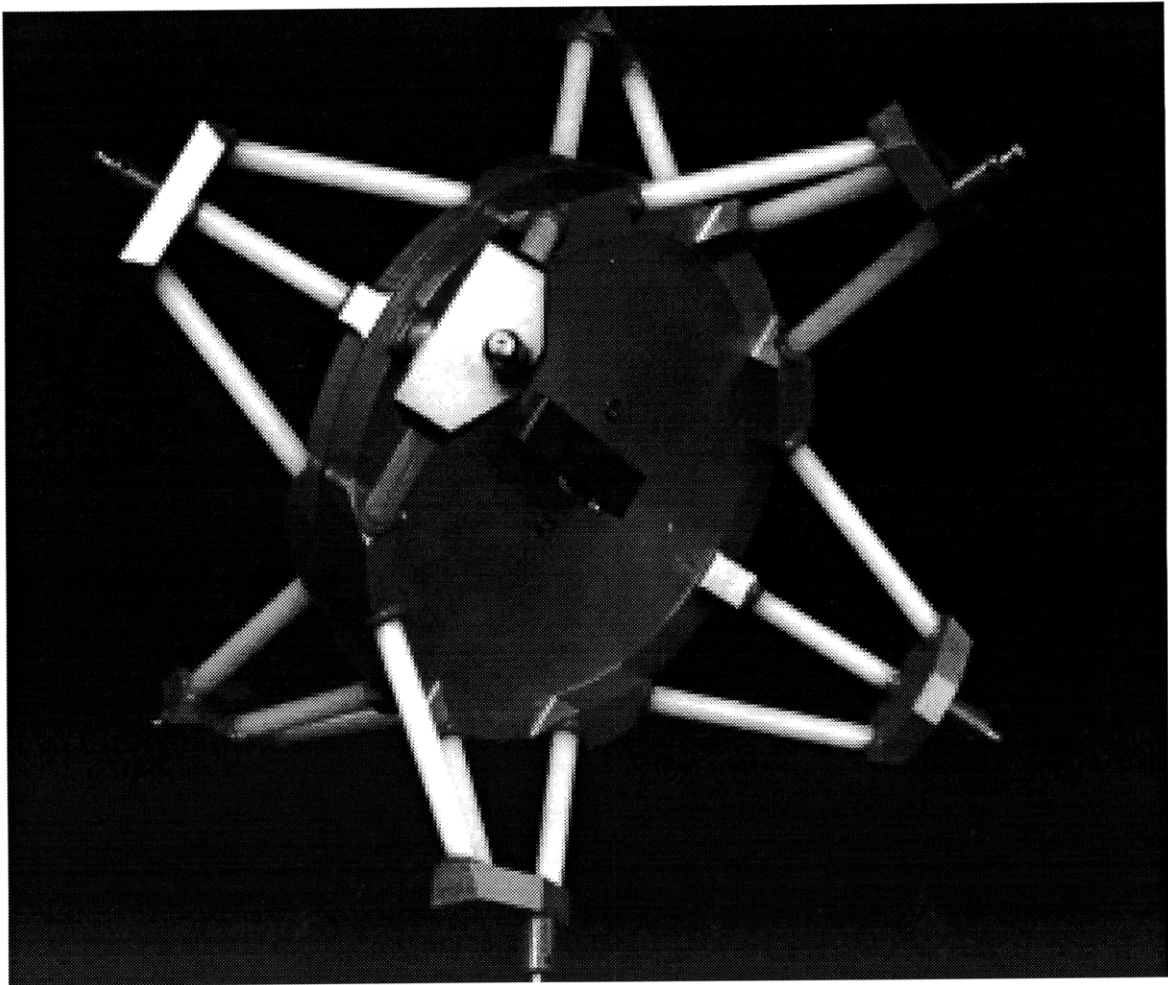


Figure 5.14: Alpha joint in its operational configuration with high preload on the friction pad.

A cleat, similar to that used in the adjustable pretension bay, was used at the center of the rotation mechanism to vary the axial rotation preload in the component. Two preloads were provided, denoted high and low, by adjusting the cleat. The cleat applies axial preload to a rotary friction pad. In Figure 5.14 the lever is in the high preload position resulting in an approximately 3.5 N.m axial torque break load. The low preload position, cleat perpendicular to bearing race, results in approximately 0.5 N.m break load.

The separated view shown in Figure 5.15 shows how the alpha joint can be separated. Eight captured thumb screws allow separation of an outer ring of aluminum and Lexan struts from the second interface plate. The rotation mechanism (two interfaced plates) remains in tact when separated.

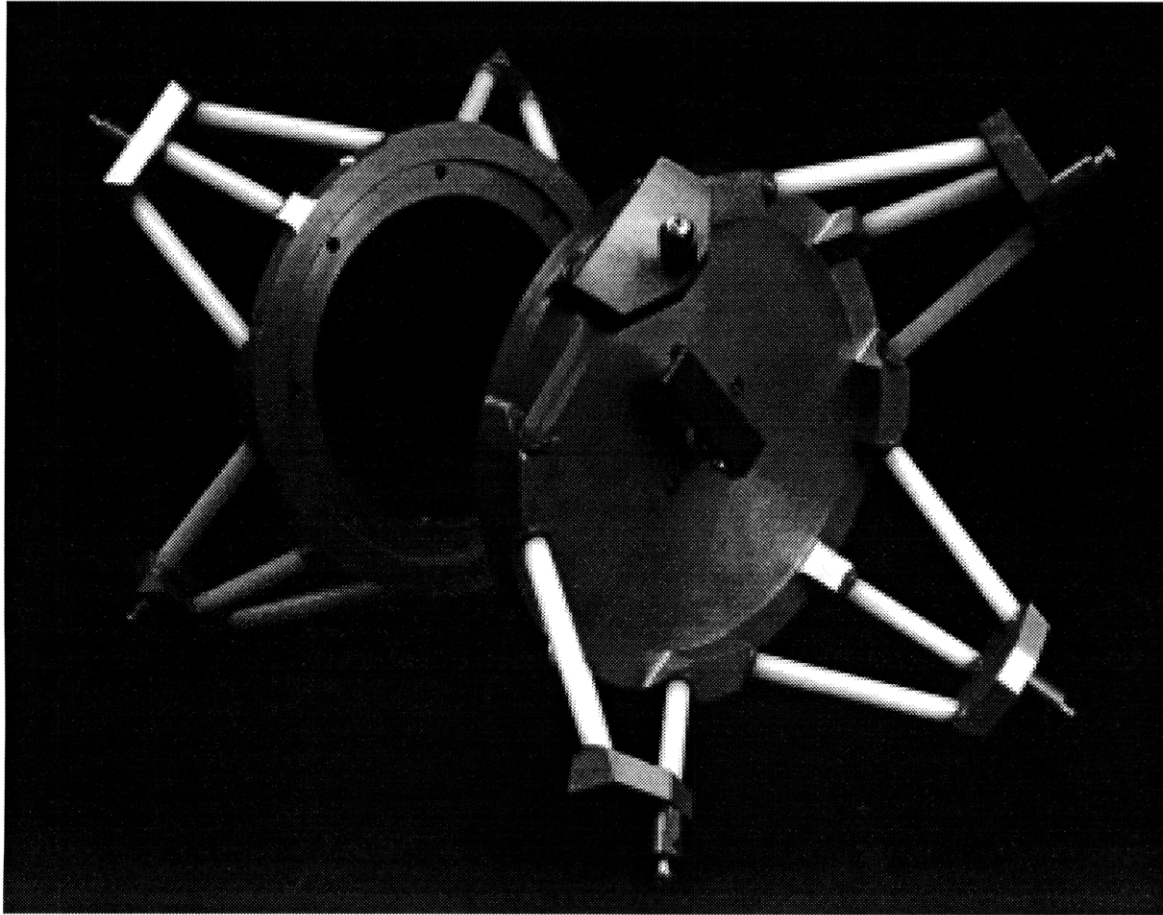


Figure 5.15: Alpha joint in its separated configuration with outer ring removed from the central mechanism.

5.2 Procedure

The experimental procedure followed when testing the components in the component tester includes component setup, excitation, calibration, data acquisition and data processing.

Care was taken to mount each test component with minimal deformation and preload induced by the test rig. Both force and displacement transducers were used in the setup process to indicate adverse loading on the test component.

The stand-off and base plate assembly were bolted to the granite surface plate. Stand-off heights were determined by the component, force transducer and interface plate dimensions and were accurate to ± 0.002 inches. The six Bruel & Kjaer actuators were then located and bolted down to the granite base.

Force transducers were next mounted to the constrained end of the test component with interfacing aluminum nodes and plates. After aligning the transducers the constrained end was lightly bolted to the base plate. Node connectors and force

transducers were aligned then fixed to the unconstrained end of the component. The sensor cage was simultaneously mounted to the base plate during the component bolt up. Displacement sensors were then positioned at the unconstrained end of the component and aligned with the respective sensor targets.

Interfacing plates were used to fix the suspended top plate to the unconstrained end of the component. Weights were used to lower the top plate from its suspended state. The component, once attached, was initially in axial tension. Flexural bearing gimbal attached to the load applying struts connected the actuators to the top plate. Each housing and strut configuration were constructed to have the same length $\pm .005$ inches.

After mounting the component the suspension turnbuckles were adjusted to minimize the axial tension and moment preload on the test component. Preload and predeformation was determined by acquiring data from the load and displacement sensors during the bolt up procedure. This data was continuously sampled and displayed on the experiment control computer as a twelve channel load and displacement meter. Shearing loads and axial moments were removed by successive relaxations of the bolt up configuration. Preloads as low as 1 N and .1 N-m were achieved. The displacement sensors were then centered in their stroke range by using set screwed micrometer head mounts.

Before testing a set of desired applied load directions were selected. Chosen test applied load directions were achieved by a process of calibrating the component/component tester system. An initial guess was made of the set of actuator inputs required to achieve the desired independent test directions. The initial guess was made using the geometry of the tester, a finite element model of the component and assuming perfect actuators. Test data were then taken and the next estimates of commands to the actuators computed using a preliminary linear least squares fit of the data. Iterating in this manner converged to the desired directions. However, because of the nonlinear geometry of the test rig, components with large disparity in directional compliance were more difficult to calibrate.

Tests were now performed in the directions resulting from the iterative process described. The tests are performed, as were the calibration tests, by using a component testing program from the experiment control computer. The program allows the user to determine the input signal shape, direction and amplitude, driving signal D/A rate, measurement sample rate, number of stored data points and testing time. Each test direction was treated as an independent test from which the data was stored with a test identifier before post processing.

After storing the data some preprocessing of the data was required before the

component identification software could be used. Twenty four channels of force measurement were resolved into six generalized loads about the elastic centroid of the component interfaces. Eight channels of displacement data were resolved into six d.o.f. motion of the elastic centroid of the unconstrained end of the component. Force state mapping requires generalized displacement rates as well as generalized displacements. Rates were estimated from the displacement data, in software, for a discrete data time window using the discrete fourier transform pair,

$$\dot{\underline{x}} \Leftrightarrow j\omega \underline{X}(\omega) \quad (5.1)$$

This method is extremely accurate (but time intensive) for a discrete data time window provided adequate sampling rate, sufficient data length and some symmetry in the data time history. Amplification of high frequency noise was avoided using narrow bandwidth frequency domain windowing. The frequency domain windows were 2 Hz boxcar windows centered at harmonics of the drive frequency (including DC). The estimated displacement rate S/N ratio was typically improved from approximately 15 to 40 by the windowing process.

With the generalized displacements, displacement rates, applied loads and reactions in hand the data was now ready for the component model identification. Component models were fit to the data using the appropriate identification procedures which were outlined in chapter 4. The data, model fits and measures of model fidelity are presented in chapter 6.

Chapter 6

Experimental Results

This chapter presents component test experiment data side by side with fit models and model fit error. The four components presented are; a calibration bay; the MODE adjustable pretension deployable bay; the MODE erectable bay; and the MODE alpha joint bay. Data shown in this chapter is a result of applying the developed calibration and testing procedure outlined in chapter 5. Models proposed in chapter 3 were fit using the identification procedures in chapter 4.

First, nominally linear calibration bay compliance fits are shown along with estimated parameter standard deviations. These serve to compare test parameters and identification methods against an *a priori* FEM model. The MODE component data and fit models follow, each with specified testing parameters and identification algorithm. Adjustable pretension bay data and models are given for three wire pretensions. For the adjustable pretension bay, applied load, and reaction force, to unconstrained d.o.f. identification is presented. Test data with bracing wires removed are also shown as proof of the underlying dissipative nonlinear mechanism. Repeatability of the adjustable pretension bay data is investigated by comparing model fits before and after the bracing wires are disassembled and reassembled. Erectable bay data and models are shown for tight and loosened connecting joints. Alpha joint bay data and models are shown for two preloads on the rotary friction restraint. For both the erectable bay and alpha joint bay only applied load to unconstrained d.o.f. identification is presented. Reaction force to unconstrained d.o.f. identification of the erectable and alpha joint bays is tabulated in appendix A.

For all components presented the parameter enumeration is with reference to the physical vectors shown in Figure 5.4. These will be referred to as

$$\underline{f}_T = [f_x \ f_y \ f_z \ M_x \ M_y \ M_z]^T \quad (6.1)$$

The vector \underline{f}_T represents the generalized applied loads (or reactions) about the elastic centroid of the attached component cross section. The corresponding generalized d.o.f. about are

$$\underline{x} = [u_x \ u_y \ u_z \ \theta_x \ \theta_y \ \theta_z]^T \quad (6.2)$$

These d.o.f. are unconstrained at the applied loads end of the component, and constrained at the reaction end of the component.

6.1 Calibration bay

Calibration bay identification results are presented as a proof of concept, experiment and as justification for assumptions made while subsequently testing the MODE components. In this section linear compliance fits of the unconstrained d.o.f to applied load data are presented for different test parameters. The test parameters investigated are applied load directions and test frequencies. All data taken on the calibration bay was sampled at 200 Hz over a test time of 10.235 seconds. Fits are performed using the extended least squares analysis presented in section 4.1 and the decoupled d.o.f. algorithm of section 4.5.

Table 6.1 lists the results of the identification of the 6x6 compliance matrix for the calibration bay (see Figure 5.4) for three sets of load directions and three frequencies. Only the dominant elements of the compliance matrix (*i.e.* the nominally non zero entries) are listed. The diagonal terms are listed first, followed by the coupling terms. The compliances have been normalized to the units m/N for comparison purposes (moments and angles have been normalized by $l = 0.2$ m). Comparison of a finite element model (FEM) with extended least squares (ELSQ) and the iterative least squares identification algorithm (see section 4.5) is made as an indication of the accuracy of the data. The precision of the identification process is indicated by the parameter standard deviations returned by ELSQ analysis. Consistency of the identification is checked by comparing those parameters which, by the FEM, should be nominally equal. Note that no attempt has been made to enforce symmetry on the compliance matrix during the identification process.

The finite element model, typical of non-updated first generation models, was constructed with handbook material data and geometrical measurement. Comparison of the FEM with the extended least squares and iterative least squares identification shows an average discrepancy 6% for the diagonal terms and 10% for the off diagonal terms. It is difficult to determine whether these discrepancies reflect on the

Table 6.1: Six d.o.f. applied load to unconstrained d.o.f. compliance model of the calibration bay. Compliances are normalized by 10^{-5} and are given in units of m/N while σ_c is given in percent.

Param.	FEM C	Linear Extended LSQ Fit										Iter. LSQ $\perp x$, 1 Hz C
		$\perp F$, 1 Hz		$\perp x$, 1 Hz		rand., 1 Hz		$\perp F$, 5 Hz		$\perp F$, 15 Hz		
		C	σ_C	C	σ_C	C	σ_C	C	σ_C	C	σ_C	
$C(1,1)$	0.269	0.266	4	0.277	4	0.270	13	0.266	5	0.276	3	0.264
$C(2,2)$	0.269	0.256	3	0.264	3	0.251	6	0.256	4	0.269	3	0.255
$C(3,3)$	0.033	0.034	13	0.036	20	0.035	18	0.034	17	0.035	19	0.035
$C(4,4)$	0.126	0.139	7	0.141	5	0.137	34	0.138	9	0.142	9	0.140
$C(5,5)$	0.126	0.138	5	0.142	8	0.142	56	0.138	7	0.142	7	0.139
$C(6,6)$	0.583	0.536	2	0.552	2	0.548	2	0.537	2	0.563	1	0.534
$C(1,4)$	0.061	0.071	14	0.072	11	0.068	75	0.071	18	0.076	18	0.074
$C(4,1)$	0.061	0.069	13	0.071	13	0.068	46	0.070	16	0.073	10	0.072
$C(1,5)$	0.064	0.072	11	0.076	16	0.069	123	0.072	14	0.078	14	0.072
$C(5,1)$	0.064	0.067	13	0.068	14	0.068	47	0.067	17	0.069	10	0.067
$C(2,4)$	-0.064	-0.068	14	-0.072	11	-0.068	73	-0.068	18	-0.072	18	-0.069
$C(4,2)$	-0.064	-0.074	11	-0.075	11	-0.062	233	-0.074	14	-0.078	9	-0.074
$C(2,5)$	0.061	0.065	12	0.069	17	0.073	115	0.066	15	0.069	15	0.066
$C(5,2)$	0.061	0.065	13	0.065	13	0.064	233	0.065	16	0.068	11	0.066
$C(3,6)$	-0.065	-0.070	6	-0.071	6	-0.071	6	-0.071	7	-0.074	4	-0.071
$C(6,3)$	-0.065	-0.069	14	-0.074	22	-0.073	21	-0.069	19	-0.072	22	-0.074

absolute accuracy of the FEM or the identified model. If this degree of inaccuracy were attributed to the finite element model, it would correspond to a 3 – 5% error in predicted frequency, which is well within the range of accuracy expected for a *first generation* FEM [14].

Precision of the measurements is indicated in Table 6.1 as the parameter standard deviation given as a percentage of the identified parameter. The torsion compliance, $C_{(6,6)}$, has the lowest standard deviation which is approximately 2%. It is not surprising that the torsion term is identified with lowest standard deviation since it is the most compliant direction identified and therefore the signal to noise ratio is high. For the same set of applied load directions the parameter standard deviations increase with decreased compliance. For example, the axial compliance has a standard deviation of 13% for the 1 Hz, orthogonal force case.

Consistency is indicated by examining the pairs of compliance parameters that should ideally be the same (as indicated by the finite element model). Good consistency is indicated in the diagonal shear terms, ($C(1,1)$ vs. $C(2,2)$) and the bending terms ($C(4,4)$ vs. $C(5,5)$), while more deviation is evident in the off-diagonal terms; e.g. ($C(1,4)$ vs. $C(4,1)$). The shear compliances differ by approximately 4% while the bending compliances differ by less than 1%. The off diagonals differ by 5% on average.

Three sets of applied load directions tested were: decoupled applied loads ($\perp F$); decoupled d.o.f. ($\perp x$), i.e. the set of forces which decoupled the generalized d.o.f.; and

a randomly selected set of forces (rand.). Each set of applied loads was normalized to have approximately the same input energy. The reported parameter $\underline{\sigma}_C$, developed in Equations 4.1 through 4.5, shows that for a diagonally dominant test article there is little difference between decoupled applied loads and decoupled d.o.f. tests, and that random applied loads generally produce poorer results. The randomly chosen set of directions in this experiment does not adequately span the applied load space. The choice of either decoupled applied loads or decoupled d.o.f. is strongly influenced by the sensor noise (see Equations 4.1 through 4.5). For the data presented in this report the noise floor was determined by the sampling process, independent of the physical sensors, and it is therefore not surprising that neither of these two options is clearly superior.

Identification at the three test frequencies with independent force sets showed no significant change in the standard deviation of the identified parameters. The compliance of the 1 and 5 Hz data is nearly identical while the 15 Hz compliance fits show approximately uniform softening of 4% when compared to the 1 Hz data. This trend indicates the increasing importance of the inertia terms, for which these data have not been corrected, as the frequency increases. For the calibration bay, the quasi static assumption produced an estimated 1% error due to inertia terms at 10 Hz. Both the data and this estimate therefore support the quasi static assumption in the 0-10 Hz test frequency range.

Comparison of extended least squares and decoupled d.o.f. iterative least squares methods show agreement within 2% in the diagonal terms and 3% in the off diagonal terms. This is due to the different treatment of the sum squared error in the respective methods. The ELSQ minimizes a scalar sum squared error while the decoupled d.o.f. identification algorithm minimizes each element in a sum squared error matrix.

In summary, the results of the calibration bay indicate acceptable accuracy, precision and consistency, a preference for decoupled d.o.f. or decoupled applied loads, and support the quasi static testing and iterative least squares parameter identification.

6.2 Adjustable pretension deployable bay

After investigating the nominally linear calibration component, multiple d.o.f. force-state component identification was applied to the more sophisticated MODE components. Full twelve d.o.f. (beam element) identification is now presented on the adjustable pretension bay. Data and models resulting from the applied load to unconstrained d.o.f. experiments are first shown. Models for the reaction force to unconstrained d.o.f. are next presented. Finally, repeatability of the component is

investigated by comparing applied load to unconstrained d.o.f. models before and after disassembling and assembling the bay bracing wires.

Data presented on the adjustable pretension bay were taken at 7.6 Hz for high, medium and low wire preloads, and with applied loads that decoupled the d.o.f. Data were sampled at 20 Hz over a test time of 10.235 seconds. For Figures 6.1, 6.2, 6.3, 6.4, 6.5, and 6.6 the transmitted force shown for each of the d.o.f. (x_i of Equation 6.2) is the relevant measured force, f_{T_i} (Equation 6.1), minus the contributions from other degrees of freedom ($(F_{ND_{ij}})_{j \neq i}$ in Equation 3.9),

$$\begin{aligned} f_y - (F_{ND_{2j}})_{j \neq 2} \\ M_y - (F_{ND_{6j}})_{j \neq 5} \\ M_z - (F_{ND_{6j}})_{j \neq 6} \end{aligned}$$

This implies that the figures present the transmitted force due to the abscissa d.o.f. only.

Applied load to unconstrained d.o.f. identification

Applied load to unconstrained d.o.f. identification of the MODE adjustable pretension bay is presented for three pretensions allowable in the bracing wires. The three pretensions are high, approximately 32 lb, medium, approximately 15 lb, and low, approximately 4 lb. The wire preloads are shown to affect the overall quasistatic nonlinear behavior of the component with increasing nonlinearity as the pretension decreases.

High preload data load stroke plots are shown in the left column of Figure 6.1 for typical diagonal d.o.f., u_y , θ_y and θ_z . The inference is that the u_x and θ_x d.o.f. data are similar to their counterparts, u_y and θ_y , and that the u_z data is predominantly linear. Model fits to the data, including tests not shown in Figure 6.1, are listed in Table 6.2. The load-stroke plots of Figure 6.1 show that the bay stiffness at high preloads is dominantly linear. However, within the load-stroke information shown, sufficient nonlinearities exist to cause the softening and dampening phenomena witnessed in the modal data of Figure 2.2. Some hysteresis is evident in the θ_z and u_y test data directions. The θ_y data have been corrupted by A/D quantization error due to small rotations (high bending stiffness). Model fits to the data were performed using the iterative decoupled d.o.f. algorithm with nonlinear least squares described in chapter 4.

In the high preload case, only the shear and torsion, F_{11} , F_{22} , and F_{66} were fit

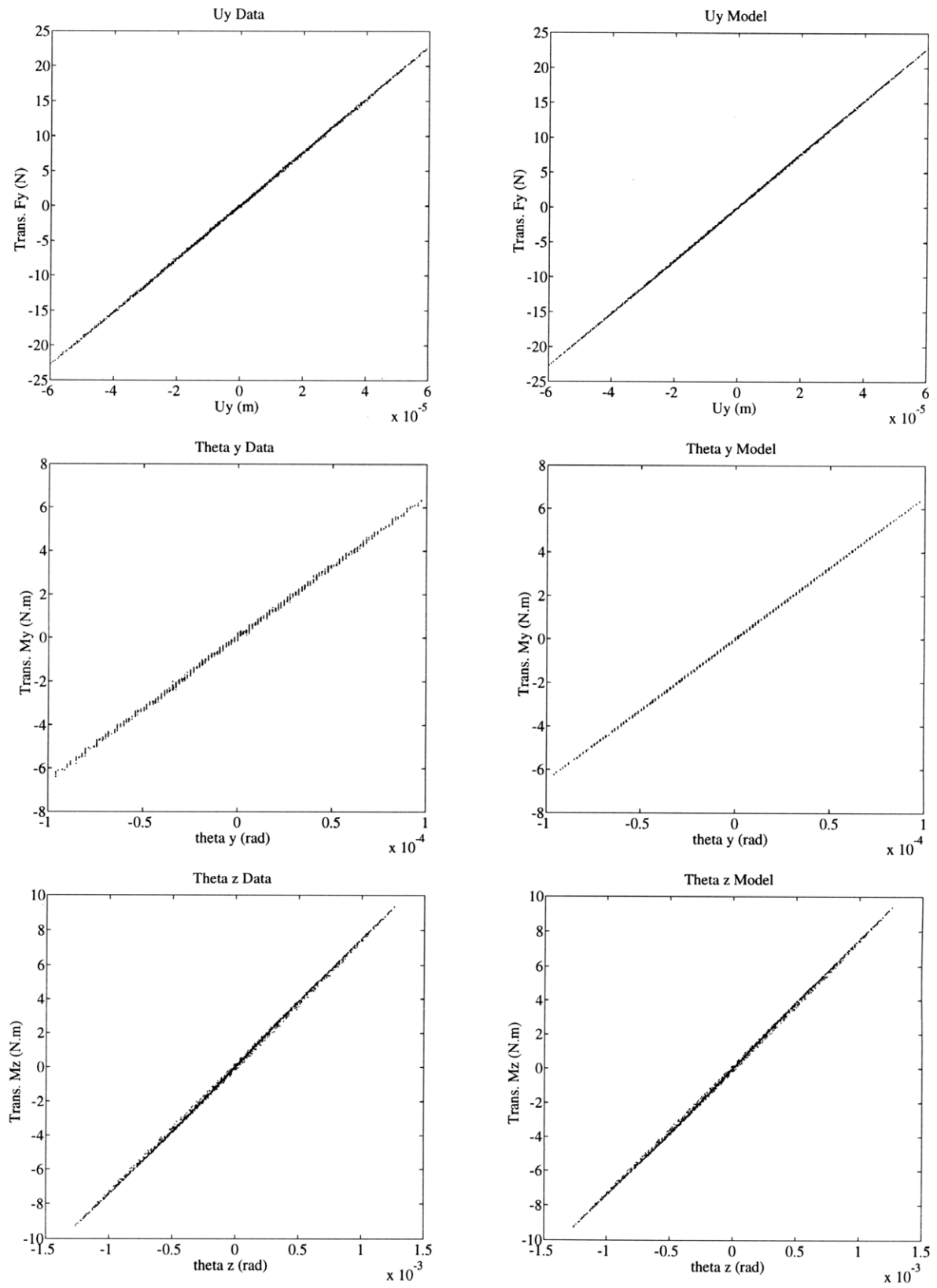


Figure 6.1: High pretension MODE deployable bay data (left column) and model fits (right column) for the decoupled u_y , θ_y and θ_z applied load directions.

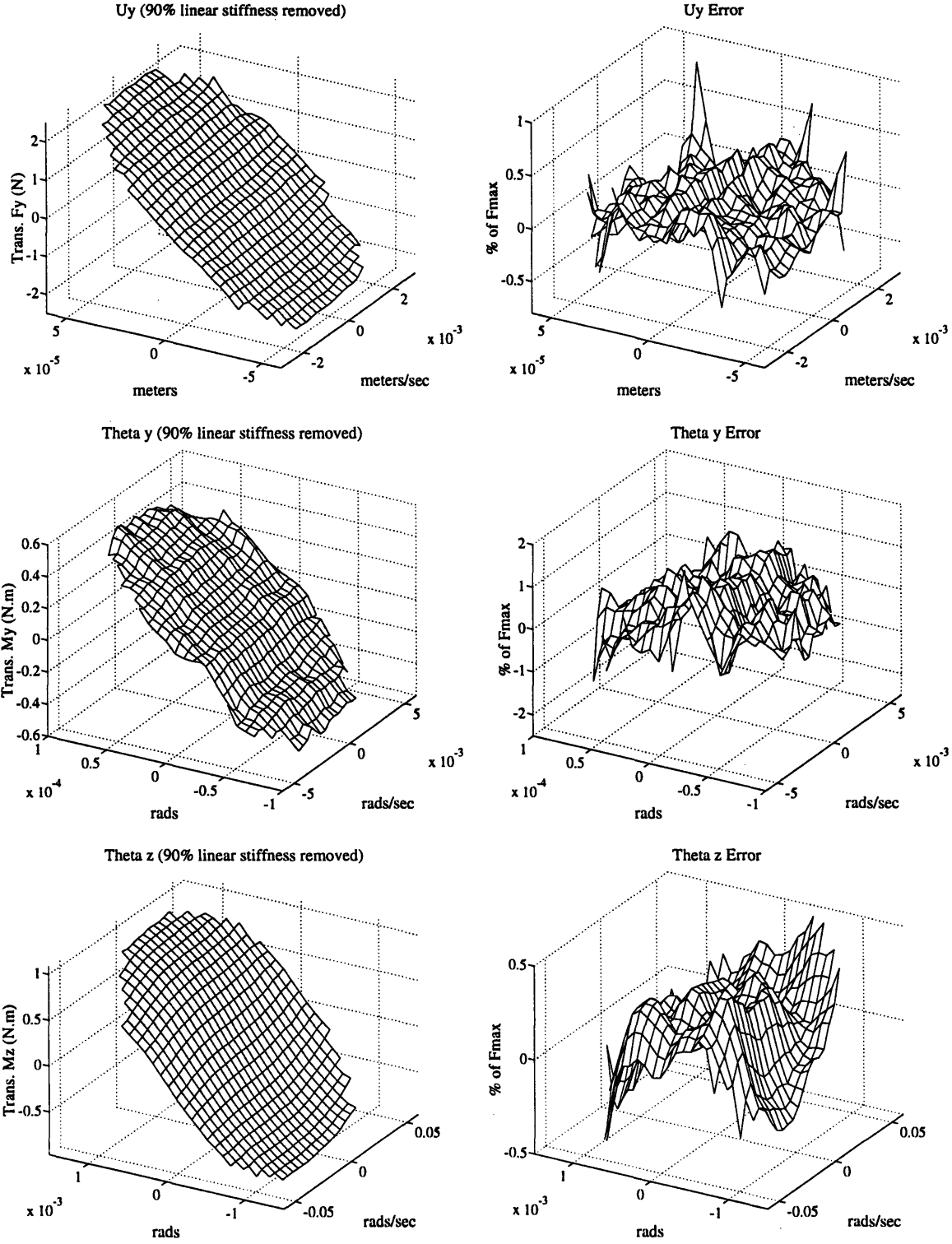


Figure 6.2: High pretension MODE deployable bay data, 90% linear stiffness removed, force-state maps for u_y , θ_y and θ_z tests (left column) with corresponding error maps (right column).

to the data using the full model of Equation 3.10, which includes a cubic stiffness polynomial, a linear damping term and a dynamic hysteresis model (DHM). The bending axes, F_{44} and F_{55} , were fit to the data using a cubic stiffness polynomial and linear damping term as were the non diagonal F_{ij} models and the axial model, F_{33} . Sample models are shown in the right hand column of Figure 6.1. The deployable DHM model does a good job of modeling the hysteresis in the transmitted M_z and transmitted f_y .

Figure 6.2 shows the hysteretic data, in force-state map form, minus 90% of the fit linear stiffness contribution (left column) along with the corresponding model fit error maps (right column) for the u_y , θ_y and θ_z test data. Each error surface is the data transmitted force minus the fit model transmitted force as a percentage of the maximum linear restoring force,

$$e_i = \frac{f_{T_i} - F_{T_i}}{F_{max}} \quad (6.3)$$

$$F_{max} = K_{1i}x_{i_{max}} \quad (6.4)$$

Where K_{1i} is the fit linear stiffness term corresponding i th d.o.f.

This will be the standard presentation of model fidelity for the remainder of the chapter. The error surfaces shown in Figure 6.2 show error within several percent for F_{22} , F_{55} and F_{66} . The error surfaces were used as an indicator of time domain error during the modeling and identification process. For example, evidence of analytic and non analytic terms in the error maps lead to the expansion of the model. The new model was then fit to the data to reduce the mismodeling.

Models of the bending axes typically under predicted what appears to be damping in the θ_y data. However, the load-stroke plot *line width* in the θ_y data is due to sufficiently random A/D noise and therefore the fit model returns low levels of dissipation.

Medium pretension load-stroke plots, model fits, force-state maps and error maps are shown in Figures 6.3 and 6.4 respectively for u_y , θ_y and θ_z tests. Again the left column of Figure 6.3 show the data in the left column and fit models in the right column.

The data of Figure 6.3 clearly show the dynamic hysteresis has increased with the decrease in pretension in all three tests. This is also shown by the increased force-state map curvature in Figure 6.4. In contrast to the high pretension data the dynamic hysteresis is now present in the bending test data, θ_y .

The models in Equation 3.10 were fit to the data to obtain F_{11} , F_{22} , F_{44} , F_{55} and F_{66} for medium pretension. Non diagonal data were fit with the model, F_{ij} , $i \neq j$,

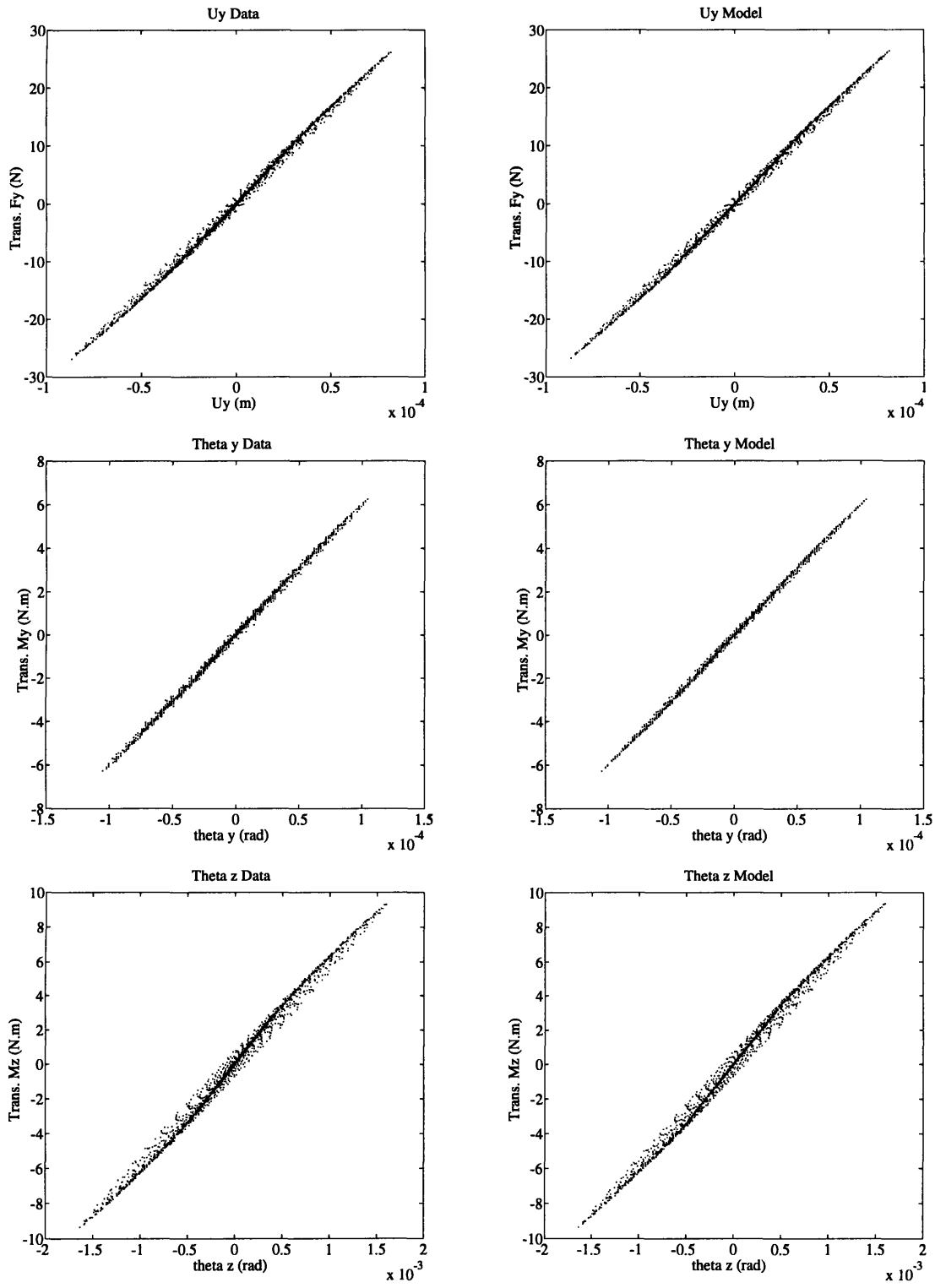


Figure 6.3: Medium pretension MODE deployable bay data (left column) and model fits (right column) for the u_y , θ_y and θ_z applied load directions.

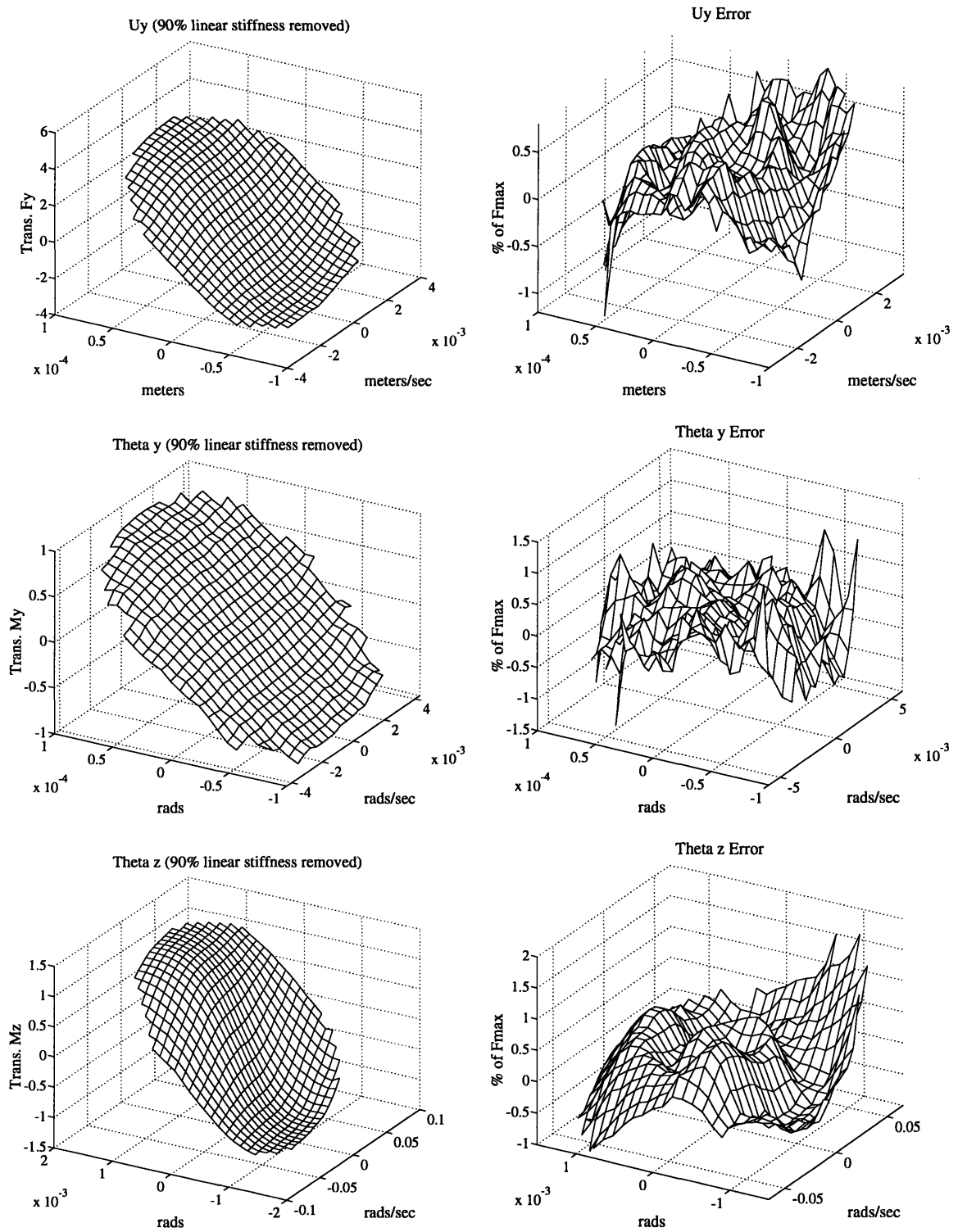


Figure 6.4: Medium pretension MODE deployable bay data force-state maps for u_y , θ_y and θ_z (left column), 90% linear stiffness removed, with corresponding model fit error maps (right column).

in Equation 3.11, which consists of a cubic stiffness polynomial and a linear damping term. Axial test data were fit with the F_{33} model, again a cubic stiffness polynomial and a linear damping term. Error mesh, shown in the right column of Figure 6.4, confirms that the model captures over 99% of the transmitted force for the range tested. This is considerable accuracy for an experimental procedure.

Overall nonlinear behavior in the data has increased with decreased pretension. Dynamic hysteresis is more evident as the preload on the deployable joints has decreased. This decreased preload enables increased joint participation in the test load range.

Low preload data are shown in Figures 6.5 and 6.6. Figure 6.5 (left column) shows, in the classic load stroke form, the diagonal transmitted forces, transmitted f_y , M_y and M_z , in the u_y , θ_y and θ_z applied load tests respectively. Force-state maps for the corresponding diagonal terms are shown in Figure 6.6 with 90% of the identified linear stiffness contribution removed. The u_y and θ_z data now show significant dynamic hysteresis with the decrease in pretension. The θ_y data shows yet more dynamic hysteresis at the low pretension, which now appears to have an antisymmetric component. This could be a result of coupled applied load influences not modeled in Equations 3.13 and 3.14. The axial data, not shown, is extremely linear as was the case for high and medium pretensions.

The model in Equations 3.10, 3.13 and 3.14 was fit, as in the medium pretension case, to obtain the F_{11} , F_{22} , F_{44} , F_{55} and F_{66} . The non diagonal F_{ij} in Equation 3.11 were again fit to the data as a cubic stiffness polynomial and linear damping term. Similarly the model F_{33} was fit to the axial data as a cubic stiffness polynomial and linear damping term.

Sample model fits are shown for the low preload case in Figure 6.5. The two parameter DHM along with cubic stiffness polynomial and linear damping term appears to fit the multi dimensional data well. Evidence of the fit fidelity is shown in Figure 6.6. Higher order unmodeled analytic dependencies can be seen in the error surfaces within several percent of the maximum transmitted force. These errors were deemed negligible and no further attempt was made to model them.

The implication from such a good fit of the deployable DHM to the hysteresis (shown in Figures 6.3 and 6.5) is that the joints begin to dominate the structural behavior at medium and low pretensions. The fits support the fact that the mechanism has been identified and that the hysteresis appears in the θ_y and θ_x data for medium and low joint preloads.

Further evidence of the deployable DHM resulting from joint friction is seen in Figure 6.7. In this experiment the diagonal bracing wires were completely removed

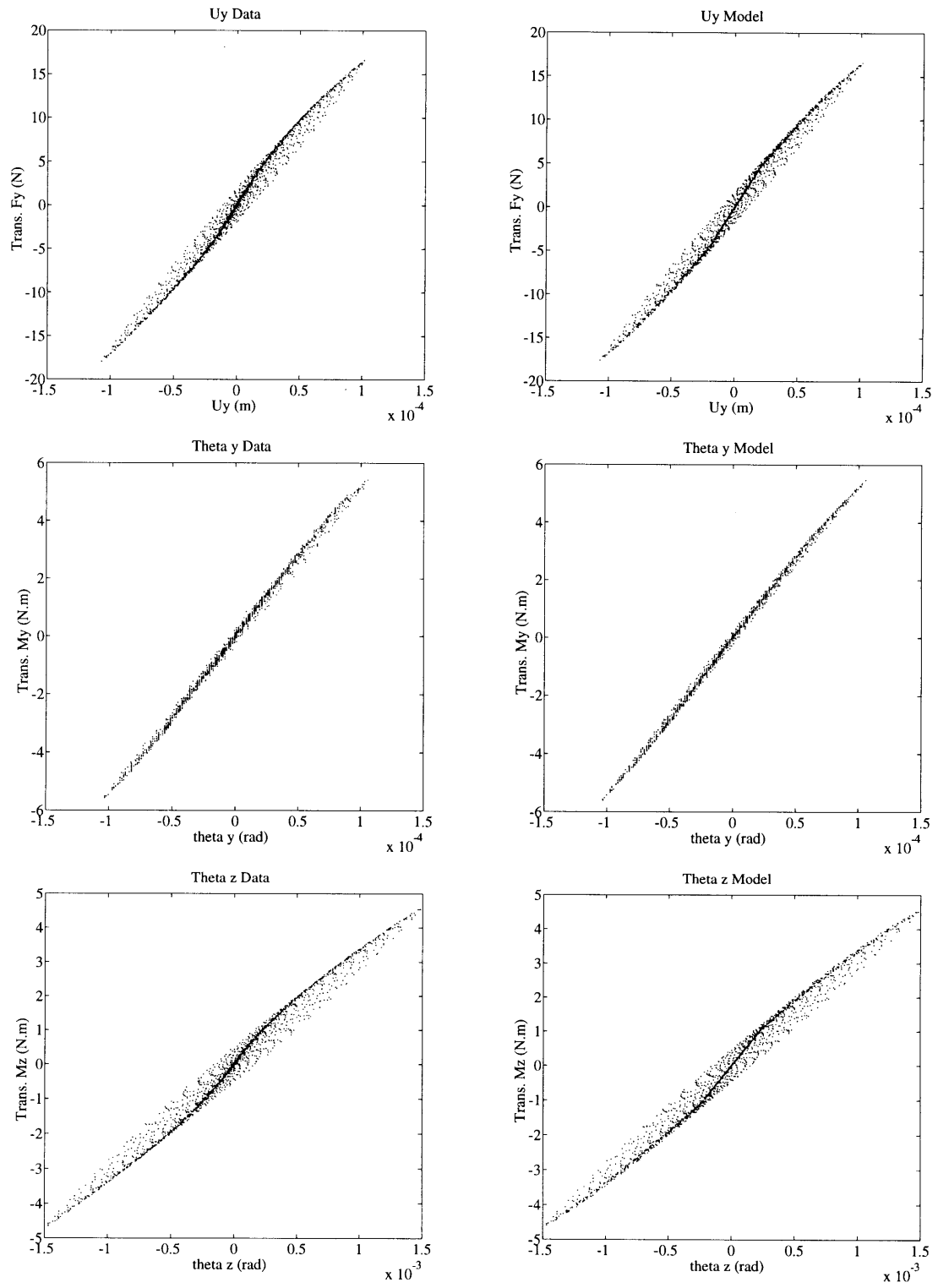


Figure 6.5: Low pretension MODE deployable bay data (left column) and model fits (right column) for the u_y , θ_y and θ_z applied load directions.

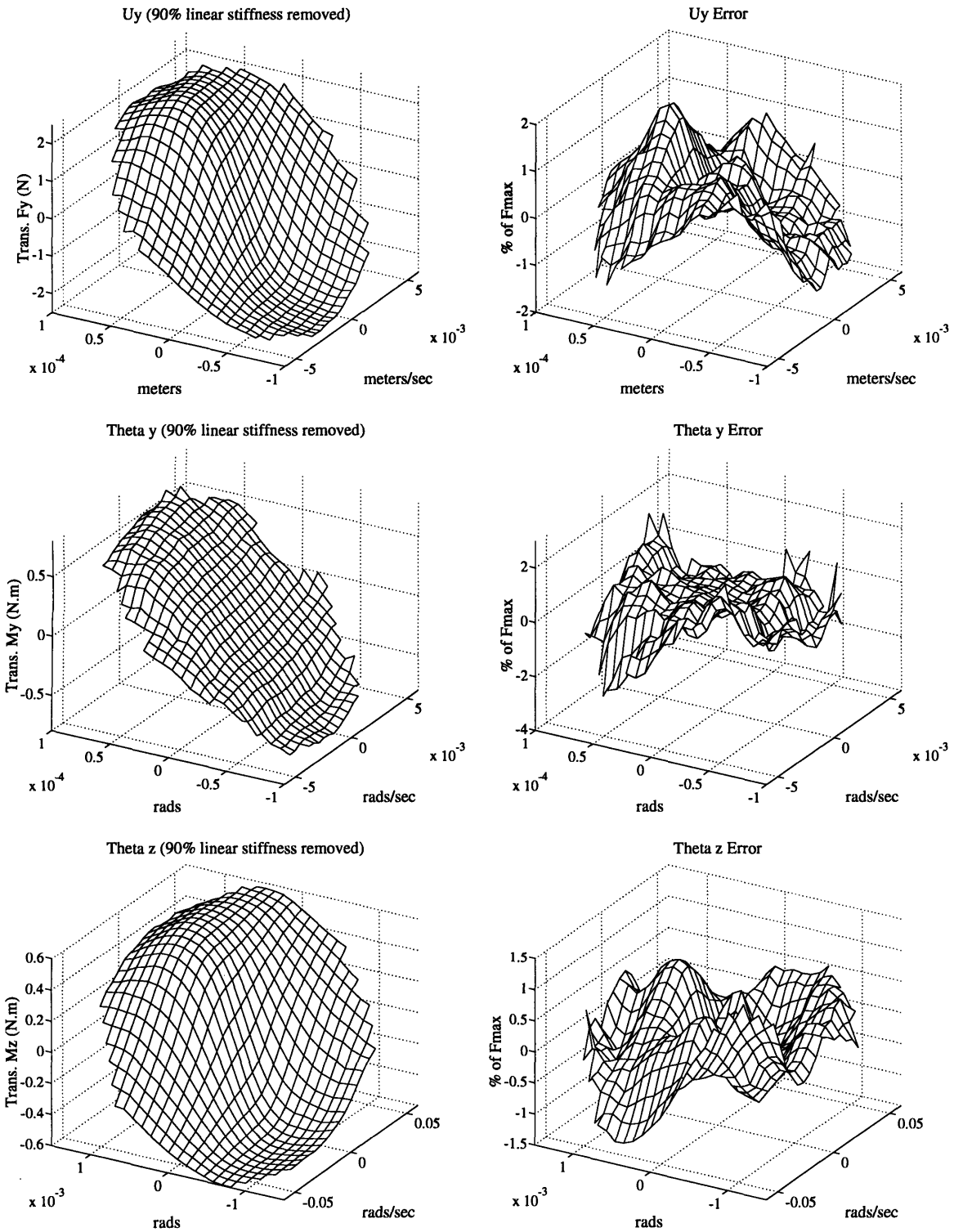


Figure 6.6: Low joint preload MODE bay data force-state maps for u_y , θ_y and θ_z (left column), 90% linear stiffness removed, with corresponding model fit error maps (right column).

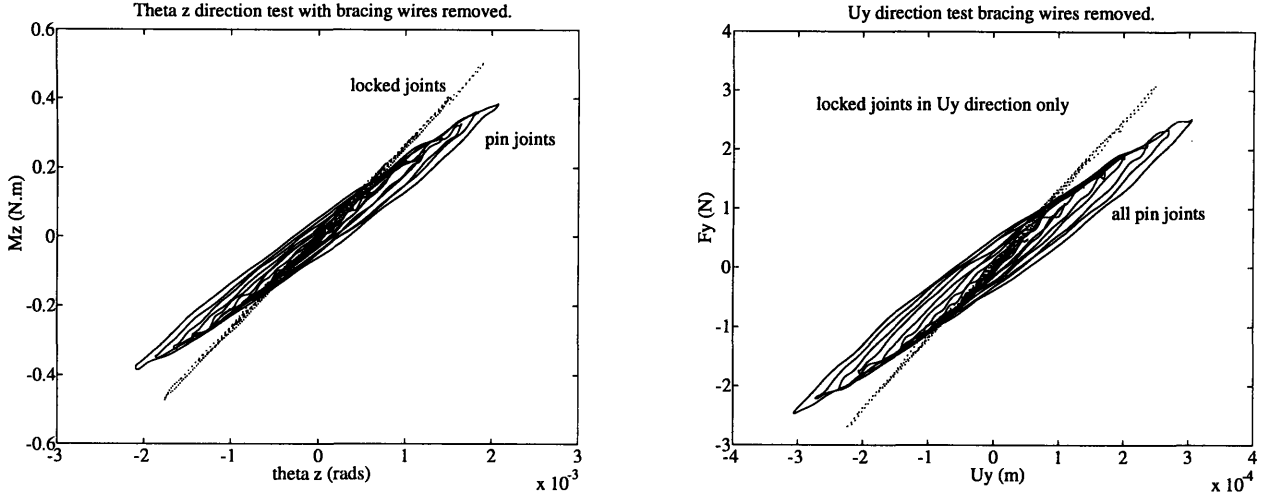


Figure 6.7: Measured data for MODE bay with locked and free joints with bracing wires removed.

from the bay so that the joint mechanism could be isolated and identified. Fortunately, the mechanism also included a set screw which could lock the longeron pin joints rigidly and thus eliminate any rotation at the pin joints.

Data shown in Figure 6.7 were for standard pinned joints *vs.* joints locked by set screw. In the torsion (θ_z) test all pins were locked. In the shear test (u_y) the four pins with rotation axis orthogonal to the forcing direction were locked and the four others were left free. The data of Figure 6.7 show that the stiffness measured with the joints locked was identical to the low amplitude stiffness when the joints were free. With the joints unlocked, strong hysteresis was present, while with the joints locked, virtually no hysteresis was present. Thus the low amplitude stiffness was consistent with the locked stiffness and the high amplitude hysteresis is consistent with the postulated DHM. Therefore, there is a strong indication that the softening and dampening of Figures 2.2 and 2.3, and Figures 6.3 through 6.6, was due to joint micro-slipping.

The fit parameter results for the assembled component are listed in Table 6.2. The units of the diagonal entries of Table 6.2 are in N/m and N-m/rad respectively, and N/rad and N-m/m respectively for the linear coupled stiffness terms, K_1 . Higher order analytic stiffnesses, K_2 and K_3 , and linear damping terms are in their respective SI units. The diagonal models F_{ii} are listed first. These are followed by the dominant coupling models F_{ij} . For clarity, as with the calibration bay, no attempt was made to constrain the elemental fit to be symmetric. For each parameter column in Table 6.2 the identified parameter is followed by the parameters participation in the test force range, F_m , in percent. The contribution weighting introduced here as $\%F_m$ will be used throughout the rest of this chapter as parameter participation factors.

Comparing the nominally identical linear stiffness terms for F_{11} and F_{22} (shear) with each other in each of the high, medium, and low pretension cases, and normalizing with respect to their average, yields 1%, 0.5% and 6% differences respectively. Comparing the linear stiffness terms of the bending models, F_{44} and F_{55} , in a similar fashion yields 0.1%, 3% and 2.5% respectively. For reference, the F_{15} and F_{51} linear terms compare with 8%, 11% and 26%. This trend shows that as the joint preload decreases the nominally similar axes become less consistent. In practice, the cables are not ideally preloaded to equal tension and their pretension strongly effects the overall component stiffness.

Fit parameters show softening in the linear stiffness terms of up to 60% when high and low pretension models are compared. Corrections were made for this effect by estimating the acceleration across the component and subtracting the inertial force contributions from the measured transmitted force data.

Nonlinear stiffness terms in Table 6.2, K_{2i} and K_{3i} , show the increased importance, $\%Fm$, of the higher order analytic stiffness at low pretensions. Low pretension diagonal models, F_{ii} , show that the cubic stiffness contributions to the transmitted force increase as a percentage of the linear stiffness contribution, as is shown in Figure 6.5. Cubic stiffness terms arise from eccentric prebuckling of the longerons. The quadratic stiffness force contribution, $K_{2i}x_i^2$, increases as the preload decreases for the F_{11} , F_{22} , and F_{66} fits. Quadratic dependencies result from cable slackening phenomenon, which is more likely at low pretension, and was visualized during the low and medium pretension experiments. Note however, that the quadratic and cubic dependencies are not the dominant nonlinearities of the component, as shown by their participation factors. Therefore, cable slackening and longeron prebuckling are a secondary effect in the load transmission of this component.

The linear damping terms, D_1 , in Table 6.2 are consistent in the diagonal models of the low and medium pretensions. In the high pretension models the D_1 parameter drops by approximately 50% which is consistent with the restraining of the dissipation mechanism within the component and the reduced participation of the term in the test force range.

Deployable DHM model parameters, F_s and K_b , are consistent, within reason, and show strong dependencies on the preload as expected. The difference between the low and high amplitude stiffnesses, K_b , decreases with increasing pretension as anticipated by inspecting the high, medium and low preload load stroke plots (Figures 6.1, 6.3 and 6.5). With increased pretension the low and high amplitude stiffnesses become comparable and therefore their difference, K_b , should decrease and participate less in the response. The slip force parameter, F_s , drops significantly in the high preload

Table 6.2: Six d.o.f. applied load to unconstrained d.o.f. identification of the MODE bay in SI units (omitted for clarity).

Models F_{ij}	Parameters											
	K_1	% F_m	K_2	% F_m	K_3	% F_m	D_1	% F_m	F_s	% F_m	K_b	% F_m
Low Pretension												
F_{11}	1.471×10^5	87.7	-8.894×10^7	6.3	-1.008×10^{12}	8.6	1.121×10^2	3.3	1.586×10^0	7.9	6.201×10^4	3.3
F_{22}	1.607×10^5	94.7	-1.729×10^7	.9	-1.157×10^{12}	8.4	1.193×10^2	4.0	1.292×10^0	6.8	6.219×10^4	2.6
F_{33}	5.405×10^5	105.1	-1.181×10^{10}	1.9	-2.046×10^{15}	2.8	2.066×10^3	2.3	no fit		no fit	
F_{44}	4.965×10^4	94.5	1.780×10^6	.3	-1.114×10^{11}	3.2	2.290×10^1	2.5	0.412×10^0	6.4	6.908×10^3	.9
F_{55}	4.840×10^4	89.0	-1.039×10^7	2.1	-8.823×10^{10}	1.9	2.209×10^1	2.4	0.525×10^0	9.5	7.775×10^3	1.6
F_{66}	3.023×10^3	95.2	-1.799×10^4	.8	-1.205×10^8	8.2	2.269×10^0	3.4	0.338×10^0	7.2	1.352×10^3	3.2
F_{15}	-2.450×10^4	95.8	-6.527×10^5	2.8	-8.539×10^{10}	3.7	-6.351×10^0	1.6	no fit		no fit	
F_{51}	-1.880×10^4	88.1	1.295×10^6	7.2	2.225×10^{10}	15.2	-3.939×10^1	9.4	no fit		no fit	
F_{24}	2.646×10^4	98.7	-1.433×10^5	.9	-4.456×10^{10}	2.6	1.438×10^1	3.6	no fit		no fit	
F_{42}	2.064×10^4	94.3	-4.733×10^5	2.3	-3.148×10^{11}	16.4	4.465×10^1	9.6	no fit		no fit	
Med. Pretension												
F_{11}	2.941×10^5	93.6	2.354×10^7	.7	-1.072×10^{10}	.0	1.200×10^2	1.8	1.964×10^0	6.7	4.861×10^4	1.1
F_{22}	2.957×10^5	95.2	7.322×10^7	2.0	-2.983×10^{12}	.7	1.191×10^2	1.8	1.466×10^0	5.5	3.729×10^4	.7
F_{33}	5.826×10^5	101.7	-1.936×10^9	.3	-2.152×10^{15}	2.6	2.050×10^3	1.9	no fit		no fit	
F_{44}	5.418×10^4	92.7	4.985×10^5	1.0	3.858×10^{10}	1.0	1.798×10^1	1.6	0.460×10^0	6.5	7.250×10^3	.9
F_{55}	5.588×10^4	93.9	-7.622×10^5	.1	-7.523×10^9	.1	1.958×10^1	1.7	0.365×10^0	5.9	5.569×10^3	.6
F_{66}	5.503×10^3	96.5	4.400×10^4	1.3	-7.954×10^7	3.7	3.035×10^0	2.5	0.665×10^0	7.1	1.237×10^3	1.6
F_{15}	-4.074×10^4	97.9	-6.565×10^5	1.7	2.260×10^9	.1	-9.494×10^0	1.2	no fit		no fit	
F_{51}	-3.638×10^4	95.2	-5.787×10^5	1.4	2.606×10^{11}	6.0	-3.736×10^1	4.5	no fit		no fit	
F_{24}	3.912×10^4	97.8	4.271×10^5	1.3	9.457×10^8	.0	9.673×10^0	1.2	no fit		no fit	
F_{42}	3.552×10^4	92.1	1.088×10^7	2.4	-2.362×10^{11}	4.6	2.918×10^1	3.6	no fit		no fit	
High Pretension												
F_{11}	3.683×10^5	99.4	5.314×10^5	.1	-4.891×10^{11}	.6	5.437×10^1	.7	0.332×10^0	1.4	9.359×10^3	.0
F_{22}	3.724×10^5	98.9	1.175×10^7	.3	-1.469×10^{11}	.1	3.250×10^1	.4	0.227×10^0	1.0	7.359×10^3	.0
F_{33}	6.140×10^5	105.4	-1.509×10^{10}	2.2	-1.687×10^{15}	2.0	9.861×10^2	.9	no fit		no fit	
F_{44}	6.538×10^4	101.9	1.390×10^7	2.4	-1.323×10^{11}	2.6	1.585×10^1	1.2	no fit		no fit	
F_{55}	6.529×10^4	101.2	8.922×10^5	.1	-7.812×10^{10}	1.2	1.502×10^1	1.2	no fit		no fit	
F_{66}	7.150×10^3	98.4	4.717×10^4	.8	-3.007×10^7	.7	1.106×10^0	.7	0.244×10^0	2.6	4.467×10^2	.2
F_{15}	-4.662×10^4	100.3	-4.852×10^5	1.0	2.348×10^{10}	.5	-4.429×10^0	.5	no fit		no fit	
F_{51}	-4.281×10^4	83.9	1.480×10^5	.2	2.236×10^{11}	1.9	-1.315×10^1	1.3	no fit		no fit	
F_{24}	4.571×10^4	98.6	1.132×10^7	2.7	-8.405×10^{10}	2.3	2.030×10^0	.2	no fit		no fit	
F_{42}	4.244×10^4	83.7	-9.976×10^4	.0	-3.431×10^{11}	2.4	8.000×10^0	.8	no fit		no fit	

case with respect to the low and medium pretensions. This physically indicates the decrease in joint participation as the pretension restrains the deployable joint mechanism which is a similar effect to the joint locking shown in Figure 6.7.

In summary the applied load to unconstrained d.o.f. models have been identified and dynamic hysteresis shown as the dominant nonlinear mechanism in the component.

Reaction force to unconstrained d.o.f. identification

Reaction force data was simultaneously stored for the high, medium and low pretension tests, while measuring the applied loads and unconstrained d.o.f. The reaction force and unconstrained d.o.f. measurements were fit with DHM's similar to that presented in section 3.3. This will be further referred to as identification of the *off* diagonal block of models as inferred in the linear undamped example presented in section 3.3 (K_{cu} of Equation 3.7). In this section only model fit parameters and relative model fit parameters are presented in tabulated form. The first table shows the results of fitting the DHM models to the reaction force data. The second table shows the error incurred when estimating the reaction force data from the measured applied loads.

Table 6.3 shows the off-diagonal block parameters identified using the reaction force measurement. Model subscripts for the off-diagonal block are written in hexadecimal. For example F_{A2} represents the 10th transmitted force, reaction M_x , to the second unconstrained d.o.f., u_y . The parameters are presented so that the models F_{71} through F_{C6} may be compared with Table 6.2 for all three pretensions. Note the negative sign on the models in the left most column. The models are in general similar to those that model the applied load to unconstrained d.o.f. within approximately 10%. Bending moment models should, of course, differ through the application of the shearing loads, to decouple the d.o.f., at a moment arm. However, models of the shearing, axial and torsion directions should nominally compare by Newtons third law, and they do to within 10% variation in the parameters. In the reaction force identification case models F_{75} through F_{A2} are not physically constrained to be similar to their symmetric counterparts, F_{B1} and F_{84} , within the off-diagonal block. Within the off-diagonal block of models there are no physical symmetry constraints.

Off-diagonal block models show similar increased dissipation and softening with decreased pretension and increased amplitude when compared to the diagonal block (applied load to unconstrained d.o.f.) models. Limited comparisons can be made between the coupling models of the off-diagonal block, F_{75} through F_{A2} , and the coupling models of the diagonal block, F_{15} through F_{42} (ignoring sign changes). The linear

Table 6.3: Six d.o.f. reaction force to unconstrained d.o.f. identification of the MODE bay in SI units (omitted for clarity).

Models F_{ij}	Parameters					
	K_1	K_2	K_3	D_1	F_s	K_b
Low Pretension						
$-F_{71}$	1.983×10^5	4.554×10^7	-6.856×10^{11}	1.220×10^2	1.752×10^0	7.359×10^4
$-F_{82}$	1.215×10^5	8.047×10^7	-3.059×10^{11}	2.309×10^1	1.760×10^0	7.439×10^4
$-F_{93}$	5.082×10^5	-1.796×10^9	-6.996×10^{15}	3.546×10^3	no fit	no fit
$-F_{A4}$	4.094×10^4	1.634×10^7	-1.643×10^{11}	1.016×10^1	0.345×10^0	7.607×10^3
$-F_{B5}$	4.022×10^4	2.090×10^7	-1.739×10^{11}	4.141×10^0	0.281×10^0	7.036×10^3
$-F_{C6}$	3.260×10^3	-1.942×10^5	-9.320×10^7	1.760×10^0	0.378×10^0	1.588×10^3
$-F_{75}$	-3.082×10^4	-1.340×10^7	-2.581×10^{10}	-1.761×10^1	no fit	no fit
$-F_{B1}$	2.451×10^4	-1.766×10^6	-4.382×10^{11}	4.259×10^1	no fit	no fit
$-F_{84}$	2.355×10^4	1.242×10^7	-7.501×10^8	6.144×10^0	no fit	no fit
$-F_{A2}$	-1.499×10^4	-9.272×10^5	9.267×10^{10}	-3.472×10^1	no fit	no fit
Med. Pretension						
$-F_{71}$	3.182×10^5	3.355×10^7	-2.397×10^{11}	1.095×10^2	1.858×10^0	5.242×10^4
$-F_{82}$	3.136×10^5	3.627×10^7	-4.027×10^{11}	9.889×10^1	1.020×10^0	3.291×10^4
$-F_{93}$	5.774×10^5	-2.818×10^{10}	-3.470×10^{14}	1.326×10^3	no fit	no fit
$-F_{A4}$	4.579×10^4	7.084×10^6	-6.043×10^{10}	1.672×10^1	0.616×10^0	6.837×10^3
$-F_{B5}$	4.895×10^4	-1.704×10^7	-5.727×10^{10}	1.100×10^1	0.223×10^0	3.188×10^3
$-F_{C6}$	5.688×10^3	-7.415×10^4	-8.899×10^7	2.808×10^0	0.835×10^0	1.609×10^3
$-F_{75}$	-4.393×10^4	1.074×10^7	1.167×10^{10}	-1.345×10^1	no fit	no fit
$-F_{B1}$	3.418×10^4	9.057×10^6	-4.352×10^{11}	2.701×10^1	no fit	no fit
$-F_{84}$	4.256×10^4	9.994×10^5	-2.107×10^9	1.216×10^1	no fit	no fit
$-F_{A2}$	-3.425×10^4	-3.088×10^6	3.634×10^{11}	-2.173×10^1	no fit	no fit
High Pretension						
$-F_{71}$	4.035×10^5	-3.595×10^7	9.043×10^{11}	2.724×10^1	0.337×10^0	9.042×10^3
$-F_{82}$	3.737×10^5	-1.103×10^7	1.537×10^{12}	4.202×10^1	0.323×10^0	9.543×10^3
$-F_{93}$	6.093×10^5	-1.256×10^{10}	5.698×10^{14}	5.022×10^2	no fit	no fit
$-F_{A4}$	5.617×10^4	4.006×10^6	-1.107×10^9	1.136×10^1	no fit	no fit
$-F_{B5}$	5.533×10^4	1.220×10^5	3.246×10^{10}	7.297×10^0	no fit	no fit
$-F_{C6}$	7.755×10^3	2.893×10^4	1.813×10^7	1.176×10^0	0.335×10^0	5.279×10^2
$-F_{75}$	-4.682×10^4	2.054×10^7	-9.187×10^{10}	-3.159×10^0	no fit	no fit
$-F_{B1}$	3.654×10^4	-6.239×10^5	3.774×10^{11}	0.922×10^0	no fit	no fit
$-F_{84}$	4.551×10^4	-7.686×10^6	-4.322×10^{10}	5.899×10^0	no fit	no fit
$-F_{A2}$	-3.553×10^4	6.148×10^5	-2.947×10^{11}	-2.114×10^0	no fit	no fit

stiffness and dissipation terms, K_1 and D_1 , of the off-diagonal block coupling models internally compare within 25%. Off-diagonal block coupling models contributed on the order of 10% to the overall reaction forces. The coupling models internal variations are therefore within a few percent of overall transmitted forces.

Table 6.4 shows the percent difference comparison of the off-diagonal block parameters, identified using an estimate of the reaction forces using resolved applied load measurements, and the off-diagonal block parameters, identified using the reaction force measurement. A comparison is made to show the measured similarity between parameters that should be nominally the same by Newtons third law. That is, the quasistatic reaction forces must balance the applied loads.

All data in Table 6.4 are shown as percentages. For each parameter column the percentage discrepancy in identified parameter is again followed by the parameters

Table 6.4: Six d.o.f. off-diagonal block parameter discrepancies of the MODE deployable bay, using estimated reaction forces *vs.* using measured reaction forces (given in percent of the measured reaction force model parameters), at 7.6 Hz test frequency. For each parameter column the percentage difference in identified parameter is followed by the parameters participation percentage in the test force range, as predicted by the identification.

Models F_{ij}	Parameters											
	$\%K_1$	$\%F_m$	$\%K_2$	$\%F_m$	$\%K_3$	$\%F_m$	$\%D_1$	$\%F_m$	$\%F_s$	$\%F_m$	$\%K_b$	$\%F_m$
Low Pretension												
F_{71}	.8	91.7	229.0	1.9	33.1	2.7	54.8	2.9	8.2	8.9	10.7	3.3
F_{82}	.7	94.7	5.1	11.0	1.5	7.5	85.1	.8	2.9	7.5	2.1	4.5
F_{93}	.4	115.7	297.0	.4	.8	16.7	16.7	4.1	no	fit	no	fit
F_{A4}	3.0	103.1	86.3	6.3	3.5	9.6	15.6	1.3	19.2	5.7	13.6	1.1
F_{B5}	1.3	110.7	4.7	8.4	2.1	10.1	12.4	.6	6.7	5.3	10.9	.9
F_{C6}	1.6	97.9	4.2	9.2	13.0	7.0	12.4	2.4	1.3	7.2	1.54	3.5
F_{75}	.1	101.9	74.6	6.4	195.3	1.8	57.9	3.0	no	fit	no	fit
F_{B1}	8.6	123.8	673.4	.8	.9	18.5	19.4	11.2	no	fit	no	fit
F_{84}	7.4	100.5	91.3	8.1	3323.0	.1	4.2	1.3	no	fit	no	fit
F_{A2}	9.4	118.9	1.9	13.2	4.6	23.6	21.8	13.0	no	fit	no	fit
Med. Pretension												
F_{71}	3.5	94.6	399.7	.8	286.4	.5	16.1	1.5	9.7	6.8	10.0	1.1
F_{82}	1.9	96.1	73.9	.8	60.7	.6	27.8	1.5	62.8	4.4	34.2	.5
F_{93}	1.2	105.0	80.7	4.5	258.3	.5	45.3	1.2	no	fit	no	fit
F_{A4}	4.1	95.4	96.8	1.9	62.4	2.1	9.1	1.8	21.5	10.0	28.8	1.4
F_{B5}	.5	102.5	5.9	4.1	58.8	1.6	11.5	1.2	17.6	4.1	16.7	.3
F_{C6}	.4	97.3	87.6	2.2	14.2	4.7	16.9	2.3	1.8	8.14	.1	2.3
F_{75}	.8	101.7	70.1	2.8	149.2	.4	11.9	1.6	no	fit	no	fit
F_{B1}	7.7	110.3	66.5	2.4	10.5	9.1	25.6	4.1	no	fit	no	fit
F_{84}	6.5	99.5	555.3	.3	2215.8	.1	22.6	1.5	no	fit	no	fit
F_{A2}	7.8	110.2	38.6	.7	10.5	6.0	19.7	3.4	no	fit	no	fit
High Pretension												
F_{71}	4.8	98.0	8.2	.5	215.8	.8	20.2	.3	126.9	1.3	115.5	0.0
F_{82}	2.0	97.1	203.8	.2	206.4	1.3	14.1	.6	34.4	1.5	34.4	0.0
F_{93}	.2	99.6	213.0	1.7	16.6	.6	54.3	.4	no	fit	no	fit
F_{A4}	.9	100.6	299.0	.8	1033.0	0.0	3.2	1.1	no	fit	no	fit
F_{B5}	.5	100.0	777.0	0.0	12.4	.6	21.5	.7	no	fit	no	fit
F_{C6}	2.5	96.4	202.2	.4	53.8	.3	35.3	.7	26.4	3.5	26.4	.2
F_{75}	1.9	98.1	192.2	4.3	71.5	1.9	53.1	.4	no	fit	no	fit
F_{B1}	8.5	97.3	4799	.1	61.0	3.8	301.8	.1	no	fit	no	fit
F_{84}	5.4	98.9	87.6	1.9	25.5	1.2	58.9	.7	no	fit	no	fit
F_{A2}	5.2	94.8	75.9	.9	5.0	2.6	152.0	.3	no	fit	no	fit

participation in the test force range, F_m , in percent.

When comparing the linear stiffness term, K_1 , off-diagonal block models F_{71} through F_{A2} are shown to be nominally the same, within 5% for F_{71} through F_{C6} and within 10% for F_{75} through F_{A2} . The linear stiffness parameters, K_1 , contribute more than 94% to the measured transmitted force, $\%F_m$. Participation percentages are presented so that the importance of the identified parameter can be weighted. For example, small discrepancies are seen in the quadratic and cubic stiffness parameters, K_2 and K_3 , when their participation is approximately 10%. In contrast, large discrepancies in identified parameters occur with small participation. The linear damping term, D_1 , varies within 60% for participation of greater than two percent.

Note that the linear damping has less than 5% participation in the transmitted force range tested for the F_{71} through F_{C6} models. Dynamic hysteresis slip forces, F_s , and stiffnesses, K_b , show variation of less than 20% for the low pretension. As the pretension increases the nonlinear terms, in general, participate less resulting in an increase in the parameter discrepancies.

In summary identified parameters for the off-diagonal block of the full twelve d.o.f. component model have been presented and compared to the diagonal block models of section 6.2. They show the same fundamental behavior and only differ within 10% of the overall transmitted loads. Alternatives to computing these model parameters were explored by using the measured applied loads data to estimate the measured reactions. Here, the models F_{71} through F_{A2} are shown to be equivalent, within parameter discrepancy and participation bounds, when using either estimated or measured reaction forces for the identification.

Repeatability tests

A full identification of the MODE adjustable pretension component has been presented with premise on a fixed component structure. With the removal and replacement of the bracing wires a significant component reassembly was performed. Repeatability data after this reassembly was taken and the same models were fit to the data as in the applied load to unconstrained d.o.f. identification case.

After the cables were removed to test the pure longeron bay configuration (see Figure 6.7) the component was reassembled and further identification performed of the diagonal block models F_{11} through F_{42} . Table 6.5 shows the comparison of the original parameters to the reassembled parameters as a percent of the original parameters. In each column the parameter participation in the test transmitted force range is given.

Repeatability of the component after disassembling and reassembling the diagonal tensioning cables and longeron pin mechanisms is poor for low pretension. Small errors in replacing the cables result in a significant adjustment in the pretension at the low pretension level. High and medium pretension data showed variation generally within 10% for the linear stiffness terms. Quadratic and cubic stiffness terms varied significantly at all pretensions with increasing participation as the pretension decreased. This indicates that the quadratic and cubic stiffness terms, while not strong in participation, depend strongly on pretension cable arrangement and attachment. The dissipation mechanism represented by the linear damping term and the two parameter dynamic hysteresis model also varied significantly for all pretensions. Preloaded pin-sleeve friction and cable rubbing at the joint-cleat interface appear to have been strongly effected by the reassembly process.

Table 6.5: Six d.o.f. stiffness comparison of the MODE adjustable bay for original and replaced wires at 7.6 Hz test frequency(given in percent of original model parameters). For each parameter column the percentage difference in identified parameter is followed by that parameters participation percentage in the test force range.

Models F_{ij}	Parameters											
	$\%K_1$	$\%F_m$	$\%K_2$	$\%F_m$	$\%K_3$	$\%F_m$	$\%D_1$	$\%F_m$	$\%F_s$	$\%F_m$	$\%K_b$	$\%F_m$
Low Pretension												
F_{11}	22.5	94.6	260.1	6.5	3.0	7.8	49.0	3.7	18.9	6.7	8.5	2.5
F_{22}	23.9	97.6	600.8	1.0	72.6	7.7	64.6	3.4	39.9	7.2	21.9	2.7
F_{33}	6.4	103.0	130.0	1.8	244.6	2.6	100.3	2.2	no	fit	no	fit
F_{44}	11.6	95.4	111.1	.3	45.2	3.2	32.5	2.4	3.9	6.5	28.5	.9
F_{55}	12.7	98.3	299.5	2.1	3.8	3.3	43.3	2.6	12.9	5.3	70.8	.5
F_{66}	2.1	100.2	972.9	.9	18.1	9.0	10.8	3.3	13.8	7.1	17.1	3.1
F_{1b}	21.9	90.3	49.2	2.5	127.6	3.5	334.4	1.2	no	fit	no	fit
F_{b1}	24.0	102.6	266.9	8.1	108.5	17.3	16.8	10.9	no	fit	no	fit
F_{24}	4.2	103.3	170.7	.8	42.6	2.7	56.1	3.0	no	fit	no	fit
F_{42}	30.3	111.3	277.1	2.5	81.5	19.5	39.3	11.2	no	fit	no	fit
Med. Pretension												
F_{11}	1.9	95.1	1286.0	.7	13309	.0	19.5	1.8	9.7	6.8	10.0	1.1
F_{22}	5.1	96.9	88.8	2.0	194.0	.8	11.2	1.8	62.8	4.4	34.2	.5
F_{33}	.2	101.8	2530.9	.3	42.2	2.6	6.0	1.9	no	fit	no	fit
F_{44}	6.4	93.2	188.8	1.0	4.4	1.0	10.7	1.6	21.5	10.0	28.8	1.4
F_{55}	.7	94.4	2341.4	.1	98.2	.1	19.5	1.7	17.6	4.1	16.7	.3
F_{66}	.7	98.6	120.9	1.3	19.0	4.0	7.6	2.5	1.8	8.14	.1	2.3
F_{1b}	7.9	97.2	139.4	1.7	469.2	.0	4.0	1.2	no	fit	no	fit
F_{b1}	1.4	106.1	550.1	1.5	55.9	6.9	9.8	5.0	no	fit	no	fit
F_{24}	16.3	97.1	55.0	1.3	5399.4	.0	57.1	1.2	no	fit	no	fit
F_{42}	5.5	102.7	101.5	2.6	168.0	4.0	10.1	4.0	no	fit	no	fit
High Pretension												
F_{11}	6.0	99.5	1372.2	.1	273.8	.7	16.9	.7	31.8	1.0	5.6	.0
F_{22}	1.4	99.4	30.1	.3	1221.2	.1	59.6	.4	102.1	1.0	66.1	.0
F_{33}	1.1	103.9	194.1	2.1	128.2	1.9	21.4	1.0	no	fit	no	fit
F_{44}	.1	102.5	158.2	2.4	98.8	2.6	19.3	1.3	no	fit	no	fit
F_{55}	.9	100.1	441.1	.1	142.8	1.1	33.0	1.2	no	fit	no	fit
F_{66}	4.0	98.2	163.4	.8	119.3	.7	42.6	.7	86.9	2.5	48.9	.2
F_{1b}	2.5	97.5	280.6	1.0	205.5	.5	13.5	.5	no	fit	no	fit
F_{b1}	.8	100.0	1688.1	.2	53.0	2.2	27.8	1.5	no	fit	no	fit
F_{24}	5.2	101.2	108.5	2.8	35.4	2.3	34.3	.2	no	fit	no	fit
F_{42}	1.2	100.3	3692.6	.0	22.1	.9	33.2	.9	no	fit	no	fit

Applied load, reaction force and repeatability data and model fits all serve purpose to confirm the fundamental dynamic hysteresis present in the adjustable pretension component. A full identification of the adjustable component was presented as a complete application of the multiple d.o.f. component identification methodology. This component is the major subcomponent (in number) in all global structure configurations of the MODE hardware.

6.3 Erectable Bay

A component used to connect the deployable hardware in various MODE configurations is the erectable bay. Data on the erectable bay is presented as evidence of its linearity with tight joints and its vibration induced nonlinear behavior. All tests for the erectable bay were performed at 7.5 Hz test frequency with data sampled at 200 Hz over a 10.235 seconds test time.

Two sets of tests were performed on the erectable component of the MODE hardware. The first set of tests mapped the essentially linear behavior of the bay with tightly fastened joints. Vibration induced loosening of the erectable joints led to the second set of tests on the component, those with deliberately loosened joints. Space *v.s.* ground data transfer functions (see Figure 2.2) for the torsion mode suggests increased dissipation in the space data. Loosening erectable joints provides a mechanism that may have increased dissipation.

Erectable bay data was taken with the set of inputs that decoupled the unconstrained d.o.f. as was the case with the adjustable pretension bay. In order to fit the tight and loose joint data the decoupled d.o.f. identification algorithm procedure was used with linear least squares.

Erectable bay with tight joints

Applied load to unconstrained d.o.f. tight joint erectable bay data was fit with the model of Equations 3.20 and 3.21. The model captures the dominant linear behavior, K_1 and D_1 , while allowing (de)stiffening by including up to cubic order analytic terms, K_2 and K_3 . Reaction force identification using the same models may be found in tabulated form in appendix A.

Figure 6.8 shows the u_x , θ_x and θ_z test data maps and mapped model fit error. Data maps are again shown with 90% of the linear stiffness contribution removed. In contrast to the medium and low pretension adjustable bay data the erectable data show predominantly linear response. The model fit error is shown to be within 1% of the test force range in Figure 6.8. Representative coupling term data, corresponding to models F_{41} , F_{14} , F_{51} , F_{15} , F_{36} and F_{63} , are shown in Figure 6.9. Although some local curvature is shown on the maps the data is predominantly linear. These coupling data are weak when compared to appropriate diagonal data.

Model fit parameters are listed in Table 6.6. Each parameter is accompanied by its participation in the test load range as defined in section 6.2. Models of Equations 3.20 and 3.21 were identified with no constraints of symmetry and similarity. First note that the participation factors listed in Table 6.6 show that the models are

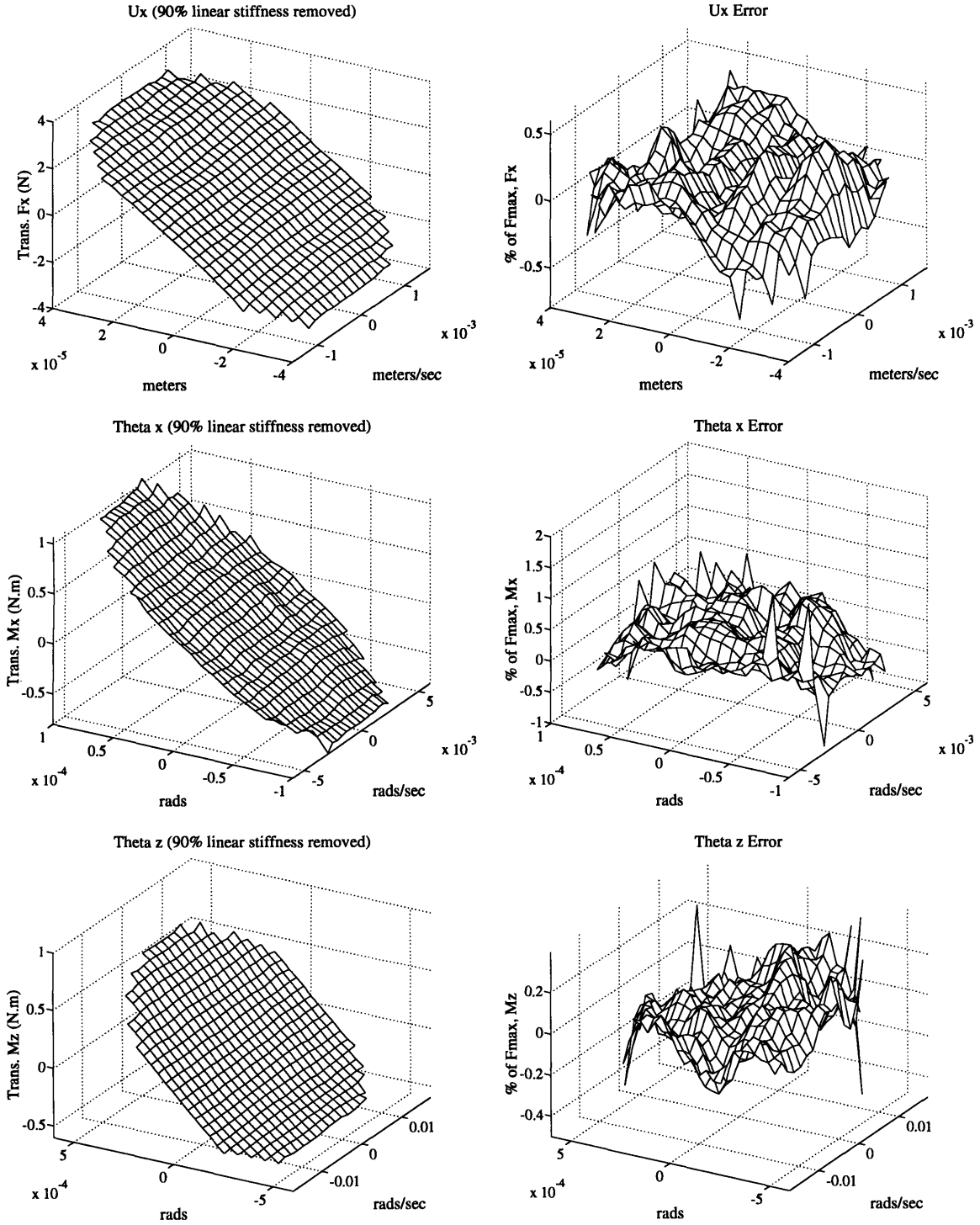


Figure 6.8: Tight joint erectable MODE bay data force-state maps for diagonal u_x , θ_x and θ_z (left column), 90% linear stiffness removed, with corresponding model fit error maps (right column).

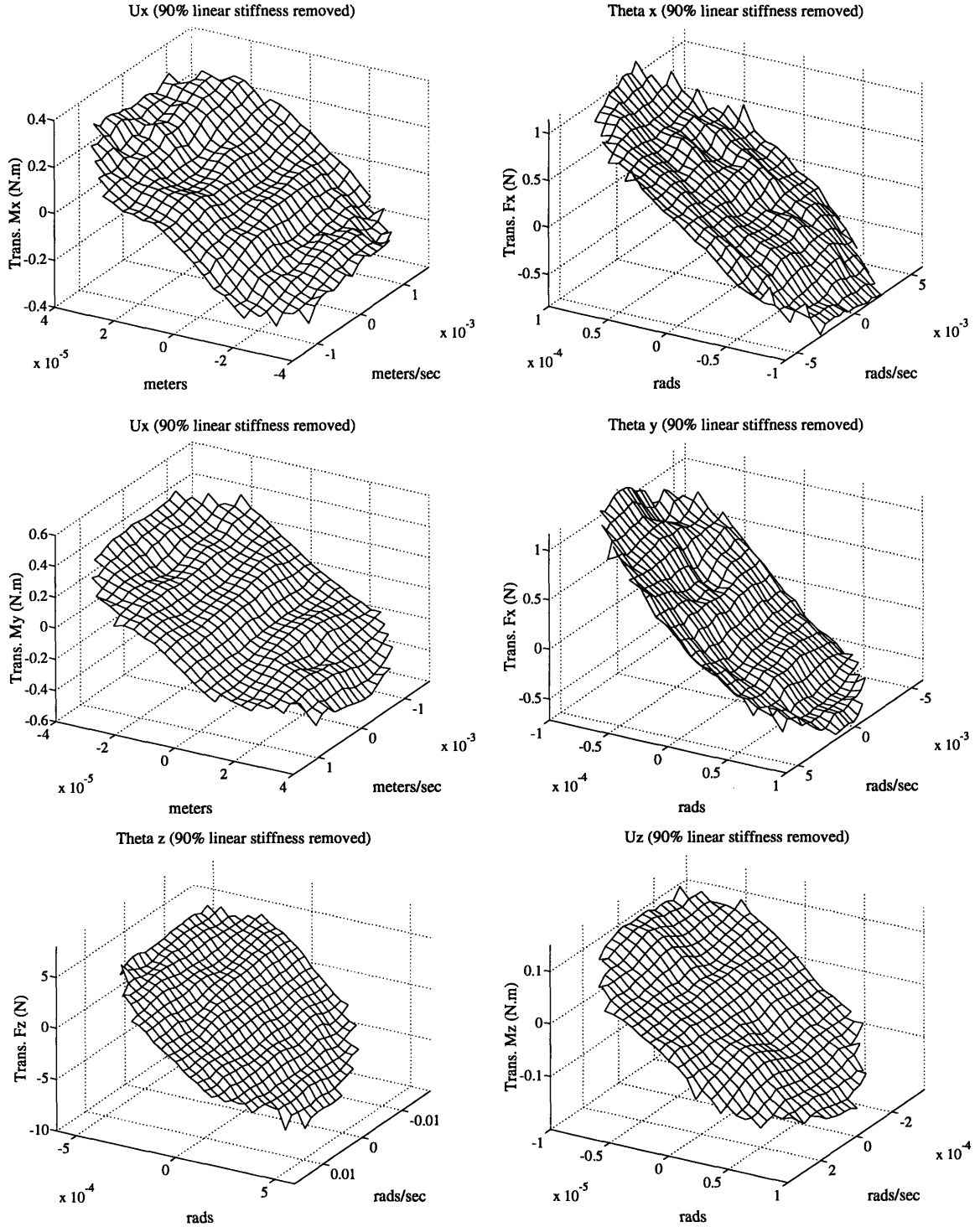


Figure 6.9: Tight joint erectable MODE bay data force-state maps for coupling in u_y , u_x , θ_y and θ_x tests, 90% linear stiffness removed. Left and right columns contrast the symmetric data; *e.g.* top row data corresponds to models F_{41} (left) and F_{14} (right).

Table 6.6: Six d.o.f. applied load to unconstrained d.o.f. model of the MODE erectable bay in SI units (*e.g.* N/m , N/m^2 , N/m^3 and $N/m/s$ respectively for the first three diagonal elements) for 7.5 Hz test frequency. Each identified parameter is followed by its participation in the test applied load range.

Models F_{ij}	Parameters							
	K_1	% Fm	K_2	% Fm	K_3	% Fm	D_1	% Fm
F_{11}	8.293×10^5	100.4	-4.833×10^7	.3	-6.834×10^{11}	.2	8.254×10^1	.4
F_{22}	8.062×10^5	102.4	-3.547×10^8	1.8	-1.806×10^{12}	.4	2.216×10^1	.1
F_{33}	7.454×10^5	99.4	1.806×10^{10}	2.4	2.283×10^{14}	.3	4.086×10^2	.3
F_{44}	8.093×10^4	99.7	1.159×10^7	1.6	3.660×10^{10}	.6	7.782×10^0	.5
F_{55}	8.121×10^4	99.8	-1.447×10^7	2.0	3.820×10^{10}	.6	7.750×10^0	.5
F_{66}	1.676×10^4	101.5	5.282×10^5	1.5	-2.042×10^5	.3	8.176×10^{-1}	.2
F_{14}	8.312×10^4	98.7	1.226×10^7	1.7	4.724×10^{10}	.7	5.814×10^0	.4
F_{41}	7.878×10^4	100.7	-7.824×10^5	.0	-9.056×10^{11}	2.2	2.102×10^1	1.2
F_{15}	-1.009×10^5	100.7	3.265×10^7	3.6	-1.259×10^{11}	1.5	-4.534×10^0	.2
F_{51}	-9.937×10^4	98.3	-1.306×10^7	.6	4.482×10^{10}	.1	-1.843×10^1	.8
F_{24}	9.789×10^4	99.3	1.267×10^7	1.5	6.443×10^{10}	.9	3.375×10^0	.2
F_{42}	9.201×10^4	98.7	-3.944×10^7	1.7	1.638×10^{12}	2.8	-1.175×10^1	.6
F_{25}	7.406×10^4	97.2	-1.327×10^5	1.9	1.461×10^{11}	2.3	7.876×10^0	.5
F_{52}	7.842×10^4	102.5	-6.297×10^7	3.3	-3.285×10^{12}	.7	7.463×10^0	.5
F_{36}	-1.580×10^5	101.4	-7.200×10^5	2.2	-6.178×10^5	.1	-1.004×10^1	.3
F_{63}	-1.591×10^5	99.5	-3.730×10^5	2.3	-8.334×10^{12}	.5	-6.919×10^{-1}	.0

predominantly linear and lightly dampened. Models that should nominally be similar, F_{11} *v.s.* F_{22} and F_{44} *v.s.* F_{55} , are the same within 5% for K_1 and 8% for D_1 . Off-diagonal linear stiffness terms that should be similar, preserving linear stiffness symmetry, are so within 7%.

Loosened joints

After multiple tests, with the connecting erectable joints initially tight, increased nonlinear dissipation and softening was observed in the erectable component test data. This led to testing the component with purposefully loosened joints.

Longeron and diagonal sleeve joints were loosened so that loads across the component, greater than half the maximum dynamic loads, resulted in joint slip. Force-state maps of the loosened joint diagonal data are presented in Figure 6.10 with 90% of the identified linear stiffness dependence removed. Significant nonlinearity can be seen in the maps when compared to Figure 6.8.

Parameter fits were performed using bicubic splines (see Equations 3.3 through 3.5). A sum 366 parameters were used in the applied load to unconstrained d.o.f. identification. Loose joint force-state map data motivated the suggested model of Equation 3.22 illustrated in Figure 3.4. This model is not fit here but rather it is used to compare the underlying mechanism. Displacement dependent dissipation was evident in the U_x and θ_z data as planar twist about the initial position. Velocity

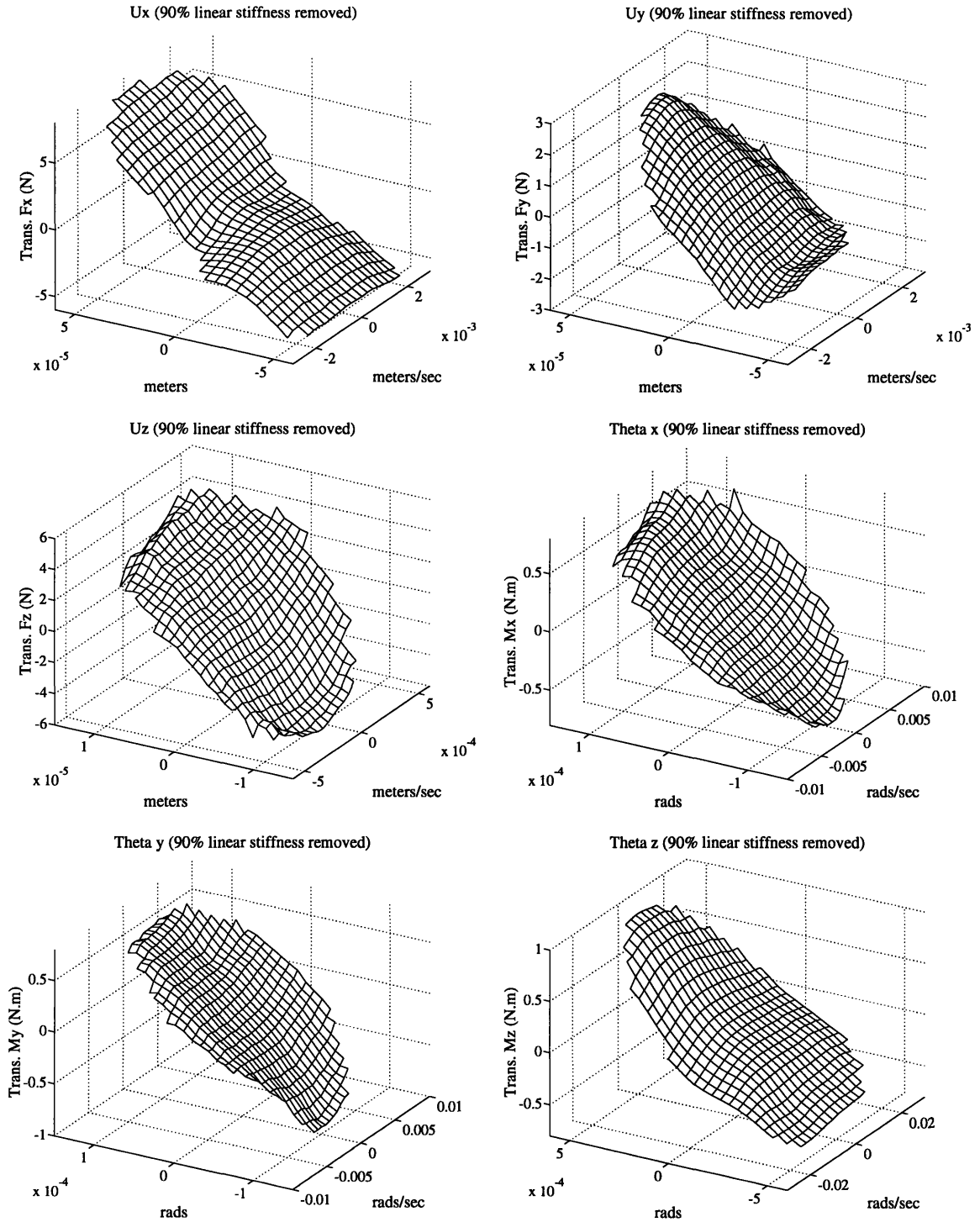


Figure 6.10: 7.5 Hz erectable MODE bay data force-state maps for diagonal u_x , u_y , u_z , θ_x , θ_y and θ_z tests. Connecting joints loosened.

Table 6.7: Six d.o.f. bicubic model of the loosened joint MODE erectable bay, in SI units, for 7.5 Hz test frequency. Each identified parameter is followed by its participation in the test applied load range.

Parameters C_{ij}	Sample Models					
	F_{11}	$\%F_{max}$	F_{44}	$\%F_{max}$	F_{66}	$\%F_{max}$
C_{01}	2.816×10^2	2.0	1.016×10^1	.9	2.477×10^0	1.0
C_{02}	-1.380×10^5	3.2	1.068×10^3	.8	-4.166×10^2	5.2
C_{03}	-1.461×10^7	1.1	4.134×10^5	2.5	8.497×10^3	3.4
C_{10}	6.436×10^5	97.2	6.655×10^4	106.3	1.410×10^4	101.5
C_{20}	3.933×10^8	4.0	-4.320×10^6	1.0	7.463×10^5	3.1
C_{30}	1.152×10^{13}	8.0	-9.507×10^{10}	3.3	9.508×10^8	2.2
C_{11}	6.366×10^5	3.1	-6.261×10^4	.8	1.907×10^3	.4
C_{12}	1.731×10^9	2.7	-6.321×10^7	7.0	-1.397×10^6	10.1
C_{13}	1.289×10^{12}	6.5	4.722×10^8	.4	2.588×10^7	5.9
C_{21}	-1.063×10^{11}	3.5	9.747×10^8	1.9	-2.474×10^6	.3
C_{22}	6.893×10^{13}	7.3	3.238×10^{11}	5.3	1.362×10^9	5.6
C_{23}	4.561×10^{15}	1.6	4.765×10^{12}	.7	-4.437×10^{10}	5.8
C_{31}	-1.444×10^{15}	3.2	7.958×10^{12}	2.3	-3.836×10^{10}	2.9
C_{32}	7.324×10^{17}	5.3	3.656×10^{15}	8.9	6.782×10^{12}	16.0
C_{33}	-6.142×10^{20}	14.2	4.020×10^{17}	8.2	-9.407×10^{13}	7.0

dependent dissipation was evident in the θ_y and θ_z test data as planar slope and curvature changes in the constant displacement planes. These maps compare to the postulated models shown in Figure 3.5. This suggests conglomerate effects of the one-way nature of the loosened lug-sleeve joints. The conglomerate effects are one-way velocity and displacement dependent dissipation. Note that the increased dissipation does not occur without stiffness loss. This is shown by comparing linear stiffness parameters, C_{10} in Table 6.7 to K_1 in Table 6.6.

Table 6.7 lists sample analytic bicubic models fit to the data. Model fit error maps for the diagonal data of Figure 6.10 are shown in Figure 6.11. The reference models used in the error map generation were bicubic splines. Model fit error was within 1% of the maximum transmitted for the u_y , u_z , θ_x , and θ_y diagonal fits. Quartic and higher order analytic terms can be seen in the error constant velocity planes of the u_x and θ_z maps. This error was locally within 1% and could have been recovered by expanding the parameterization (870 parameters are required for a biquartic fit).

In whole, the data shows softening and increased dissipation when compared to the tight joint data. Softening occurred with joint slip due to saturation transmitted load paths. Dampening was a result of the accumulated friction of multiple rubbing surfaces. Various erectable joints may have loosened to various degrees in any one MODE dynamics test providing the increased dissipation witnessed in the space dynamics data. However, it is not clear that corresponding softening is also witnessed in the space data. While these quasistatic erectable tests may not recreate the conditions under which the MODE dynamics tests were performed they do provide necessary

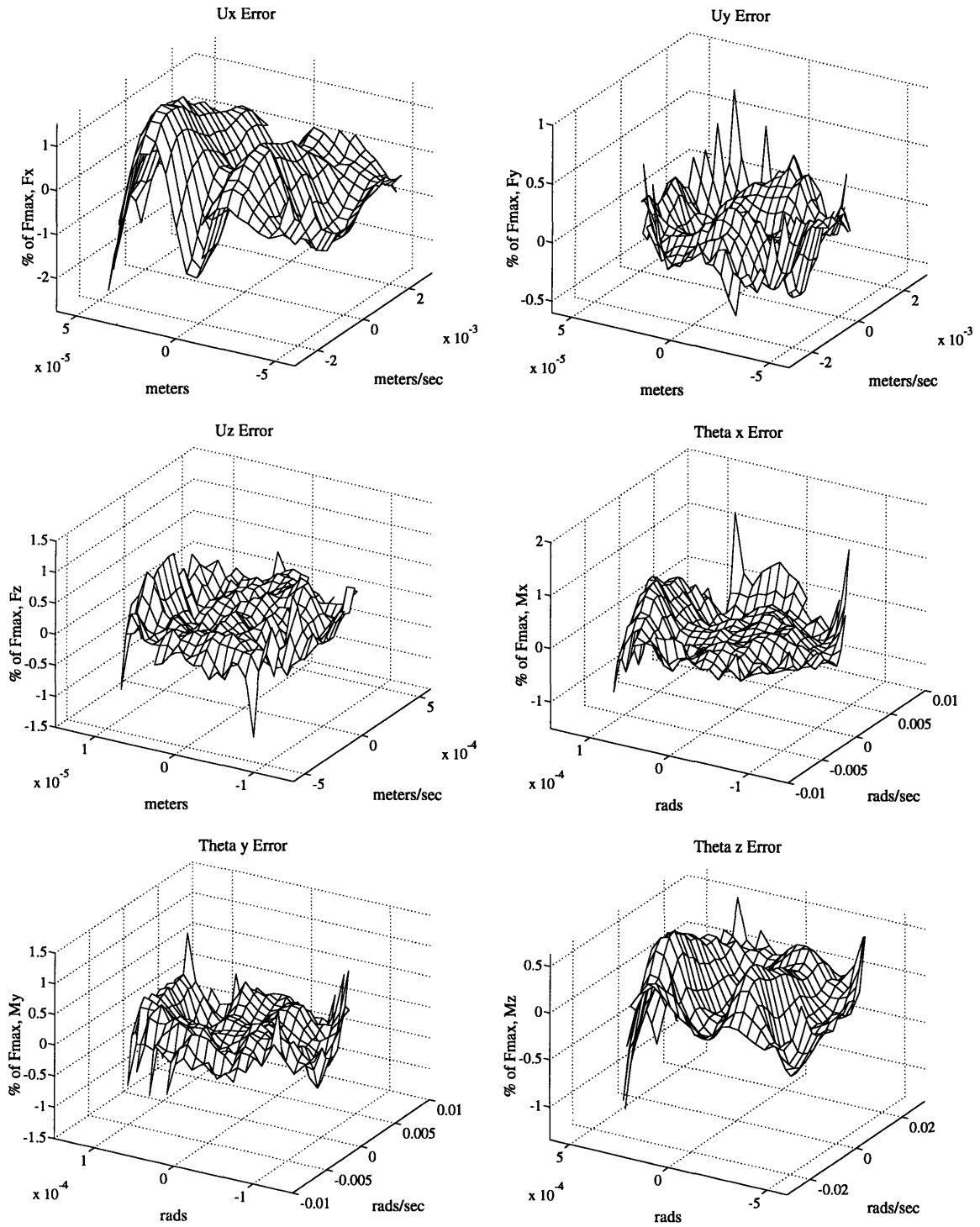


Figure 6.11: 7.5 Hz erectable MODE bay model error force-state maps for diagonal u_x , u_y , u_z , θ_x , θ_y and θ_z tests. Connecting joints loosened.

insight into the joint loosening effects on the component properties.

6.4 Alpha joint bay

Another joint used to interconnect deployable hardware was the MODE alpha joint bay. The alpha joint is that which allows axial rotation of one section of structure relative to another using a preloaded friction mechanism. This section presents the data and fit models of the MODE alpha joint bay.

Alpha joint bay tests were performed at the two possible mechanical preloads on the joint rotation axis. All alpha joint bay tests were performed at 5 Hz test frequency with data sampled at 200 Hz over 10.235 seconds. For each preload data taken spanned the six d.o.f. generalized applied loads space through a set of six decoupled applied loads tests. Residual applied loads in each individual test required that the weakly coupled loads identification algorithm be used (see section 4.4). Note that this is in contrast to the independent d.o.f. tests of the adjustable and erectable components. Decoupled applied loads were desired for the alpha joint bay tests in order to minimize extraneous dynamic preloads on the rotation mechanism that would be correlated with the rotation d.o.f. response.

Both high and low preload sets of data were first fit with analytic bicubic models (see Equations 3.3 through 3.4). These are first presented for both high and low preload as models of the diagonal data. Only the axial rotation model was further modeled in terms of the micro and macro slip models presented in section 3.3. For each of the preloads the micro and macro slip data and models follow the analytic models.

Simultaneous reaction force measurement was also made for the alpha joint. The models reported in this section are for applied load to unconstrained d.o.f. Reaction force identification of the alpha joint bay can be found in appendix A.

In both mechanical preload states presented in this section the possibility of joint walk existed when the bay was excited at high axial moment amplitudes. That is, after testing at high amplitudes, causing relative motion at the joint friction pad, the joint came to rest at a different finite rotation state, θ_z , than that at which the test was initiated. This is called joint walk and is associated with zero joint stiffness or rigid body relative motion. The high amplitude M_z data presented in this section was carefully corrected for this very low frequency behavior by AC coupling the data with 1 Hz corner frequency. This correction was made realizing that even order analytic dependencies are skewed in the process.

High preload

High preload diagonal data is presented in Figure 6.12 for F_x through M_y tests, *i.e.* not the M_z test. Each map employs the result of weakly coupled loads identification fitting analytic bicubic models. The transmitted force, or vertical axes, of the force-state maps of Figure 6.12 are corrected for structural force contributions from the d.o.f. not plotted (see the example in section 3.3).

Diagonal map data shown in Figure 6.12 is shown with 90% of the identified linear stiffness removed. These data show significant nonlinearity when compared to the erectable data in Figure 6.10. The bearing and friction pad axial mechanism effects the load transmission properties of the alpha joint up to 10% all directions shown.

Significant dissipation, slopes and curvatures in the constant displacement planes, is introduced by the bearing interfaces. F_y , F_z , M_x , and M_y test data all show complicated stiffness behavior with varying degrees of velocity dependent and displacement dependent dissipation.

Error in the bicubic model fits is shown in Figure 6.13. Model error corresponding to the data in Figure 6.12 is within a few percent (at most) of the maximum transmitted structural forces. Some higher order analytic behavior can be seen within the F_x and M_x error maps. This error was deemed to be within experiment variation and was not further pursued in terms of higher order analytic models.

Fit parameters are listed in Table 6.8. With the parameters is a measure of parameter effectiveness as a percentage of the maximum transmitted force within the test range, $\%F_m$ (as was presented for the deployable and erectable components). The SI units of each parameter value is consistent with the order of the subscripts in the parameter listing. For example, C_{23} of model F_{11} has units $N \cdot s^3/m^5$.

Parameters listed in Table 6.8 show the strength of the nonlinearity in the data shown in Figure 6.12. Nonlinear parameters (all those except C_{01} and C_{10}) contribute less than 10% to the transmitted force for diagonal models F_{11} , F_{33} and F_{55} . The model fits show strong nonlinear transmission in the F_{22} and F_{44} models.

Consistency of the data can be checked by comparing similar axes linear stiffness parameters weighted by their parameter participation percentage. Parameter participation need be considered for true comparison of strongly nonlinear components. Nonlinear analytic model fits do not distinguish the physical nonlinearities from the physical linear terms. Consistency arguments for this section are based on the physical linear stiffness, not the least squares fit C_{10} , or secant, $(F_{ii}(x_0) - F_{ii}(x_1))/\Delta x$, linear stiffnesses. For example, F_{11} and F_{22} fit linear stiffness terms, C_{10} , are similar to about 6% while their relative weights differ by 7% in the same sense as the stiff-

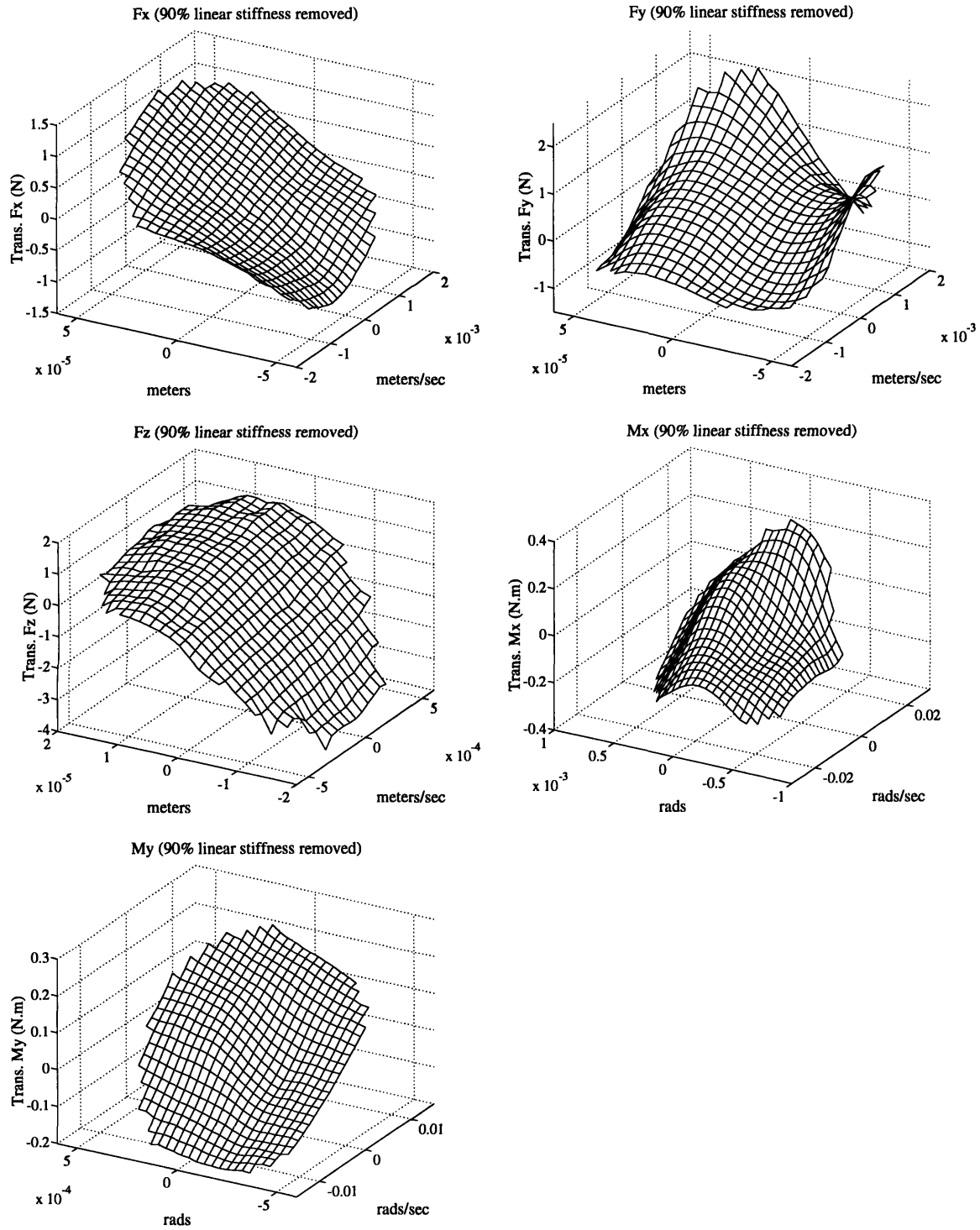


Figure 6.12: 5 Hz MODE alpha joint data force-state maps for diagonal F_x , F_y , F_z , M_x , and M_y tests. Alpha joint in high preload.

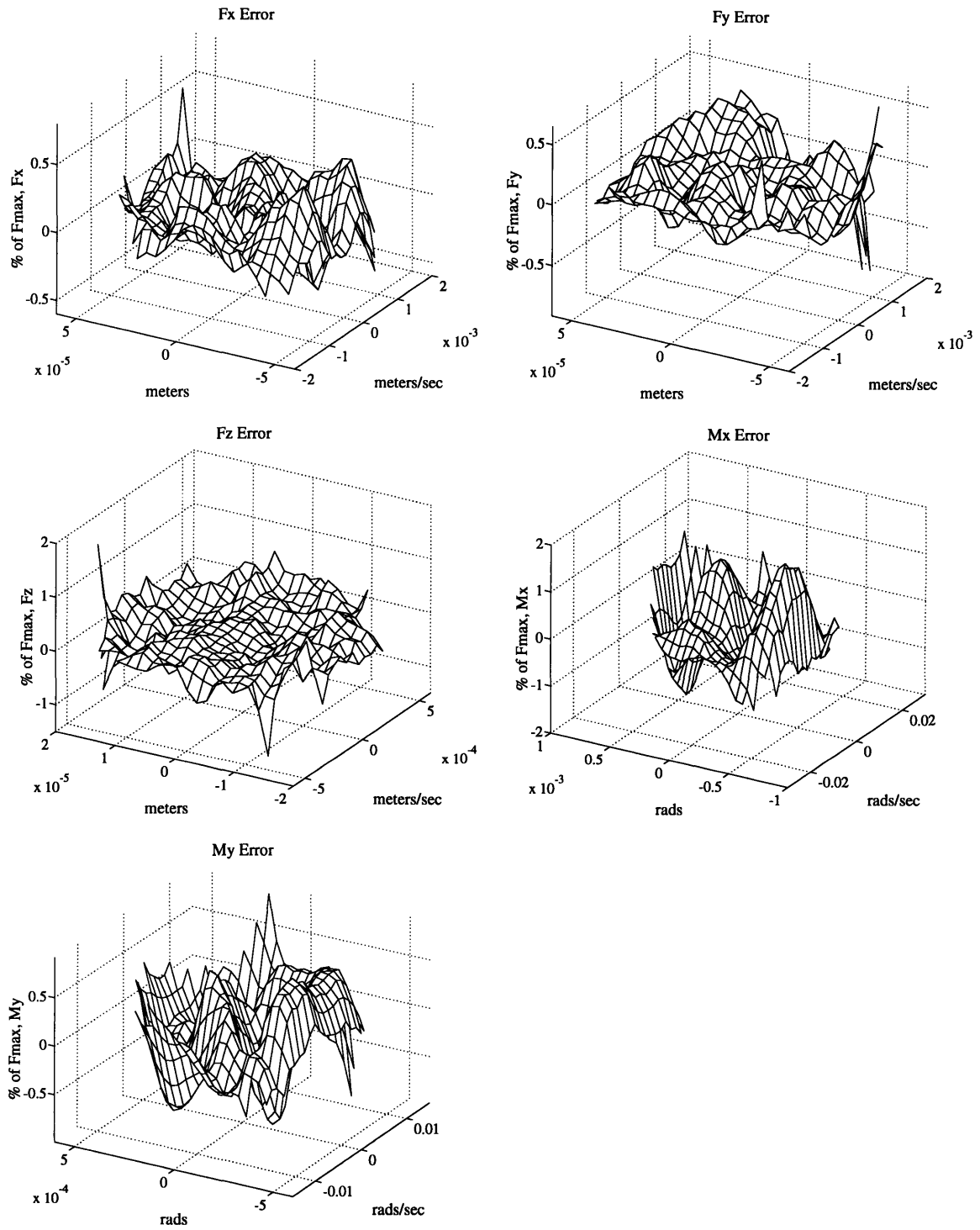


Figure 6.13: 5 Hz MODE alpha joint data force-state bicubic model error maps for diagonal F_x , F_y , F_z , M_x , and M_y tests. Alpha joint in high preload.

Table 6.8: Six d.o.f. applied load to unconstrained d.o.f. bicubic model of the high preload MODE alpha joint, in SI units, for 5 Hz test frequency. Each identified parameter is followed by its participation in the test applied load range.

Parameters C_{ij}	Sample Models									
	F_{11}	$\%Fm$	F_{22}	$\%Fm$	F_{33}	$\%Fm$	F_{44}	$\%Fm$	F_{55}	$\%Fm$
C_{01}	2.817×10^2	4.7	4.538×10^2	9.1	9.204×10^2	2.4	1.166×10^1	13.0	1.356×10^1	12.5
C_{02}	5.349×10^4	1.7	-1.694×10^4	.8	-2.597×10^5	.5	1.914×10^2	5.7	-9.987×10^1	1.4
C_{03}	-3.632×10^7	2.2	-2.832×10^7	3.4	-9.668×10^7	.1	2.257×10^3	1.8	-1.501×10^2	.0
C_{10}	1.890×10^5	99.3	1.964×10^5	107.0	1.372×10^6	109.4	2.767×10^3	84.9	3.327×10^3	102.1
C_{20}	-1.151×10^7	.4	7.578×10^7	2.8	-4.446×10^9	7.7	-6.433×10^5	14.5	1.656×10^4	.3
C_{30}	4.315×10^{11}	.8	-9.707×10^{12}	23.5	-6.740×10^{13}	2.5	-8.203×10^8	13.6	-8.321×10^8	6.4
C_{11}	1.256×10^6	1.3	-3.903×10^6	5.2	5.429×10^6	.3	9.132×10^2	.7	4.425×10^3	2.0
C_{12}	-2.323×10^9	4.4	-3.711×10^8	1.2	-6.272×10^{10}	2.6	-1.533×10^6	33.5	-1.248×10^6	8.6
C_{13}	1.275×10^{12}	4.6	3.503×10^{12}	28.2	-5.565×10^{13}	1.7	-4.605×10^7	26.8	1.206×10^7	1.2
C_{21}	9.097×10^9	.5	1.342×10^{11}	12.0	4.617×10^{11}	.6	-1.259×10^7	7.6	5.061×10^5	.1
C_{22}	1.823×10^{13}	2.1	-6.877×10^{12}	1.5	1.934×10^{15}	1.8	-1.072×10^9	17.2	2.565×10^8	.9
C_{23}	1.742×10^{16}	3.8	-2.143×10^{16}	11.5	-8.242×10^{17}	.5	-5.893×10^7	.0	2.056×10^{10}	1.1
C_{31}	-1.033×10^{14}	.4	-2.486×10^{14}	1.5	3.187×10^{15}	.1	2.510×10^{10}	11.1	5.711×10^9	.7
C_{32}	-5.242×10^{17}	3.6	1.405×10^{18}	20.5	-1.004×10^{20}	2.0	3.982×10^{12}	47.1	2.873×10^{12}	4.9
C_{33}	-3.339×10^{20}	4.4	9.609×10^{19}	3.4	1.043×10^{23}	1.5	1.255×10^{14}	39.6	8.346×10^{13}	2.1

Table 6.9: Low amplitude micro slip model parameters fit to the MODE alpha joint high preload M_z data.

Model F_{ij}	Parameters		
	K_1 (N.m/rad)	K_F (N.m/rad)	δ (rads)
F_{66}	8030	1135	3.066×10^{-4}

ness discrepancy. This indicates good consistency. Inspecting the F_{44} and F_{55} linear stiffness terms show that they are similar to about 20% while the relative weights differ by about 20%, in the same sense as the stiffness discrepancy. The conclusion is that the diagonal models, F_{11} , F_{22} , F_{44} and F_{55} are internally consistent.

Axial moment data (M_z test) was fit with the alpha joint physical models of section 3.3 using nonlinear least squares. The two alpha joint models were fit to the data corresponding to micro and macro slip modes of alpha joint operation. The two models describe the rotation mechanism as an accumulated micro friction device at low amplitudes and a displacement dependent friction device at high amplitudes. The micro slip model, consistent Prandtl's laws, yields dynamic hysteresis phenomena similar to that witnessed in the adjustable pretension deployable component.

Low amplitude data show remarkable similarities between the adjustable pretension bay of Figure 6.3 and alpha joint low amplitude hysteretic behavior shown in Figure 6.14. This softening hysteresis is modeled using two stiffness terms, K_1 and K_F , and a slip distribution function parameterized in terms of one parameter, δ (Equation 3.26), where K_F is the added stiffness at very low amplitudes and K_1 is the asymptotic stiffness after all the allowable microfriction interfaces have slipped. Micro slip accumulation follows from the slip distribution and the integral relations in section 3.3.

Figure 6.15 shows the data in force-state map form with 90% of the linear stiffness removed. Model fit error maps show a good fit to the data by the three parameter model. At first model fits were performed using trial distributions that showed significant error. It was found that the micro slip model with the given two point slip distribution in Equation 3.26 captures the softening as well as the hysteretic behavior within 1% of the transmitted thru put. Table 6.9 shows the fit parameters.

At high amplitudes the alpha joint broke into a macro friction mode of operation. High amplitude data and model fit are over-plotted in Figure 6.16. The macro slip model for this mode of operation was fit to the data using nonlinear least squares. The fit macro slip model parameters are listed in Table 6.10. Identified micro slip model parameters of Table 6.9 were used in the macro friction model (Equation 3.27) for branches 2 and 5 shown in Figure 6.16, directly after a change in the sense of

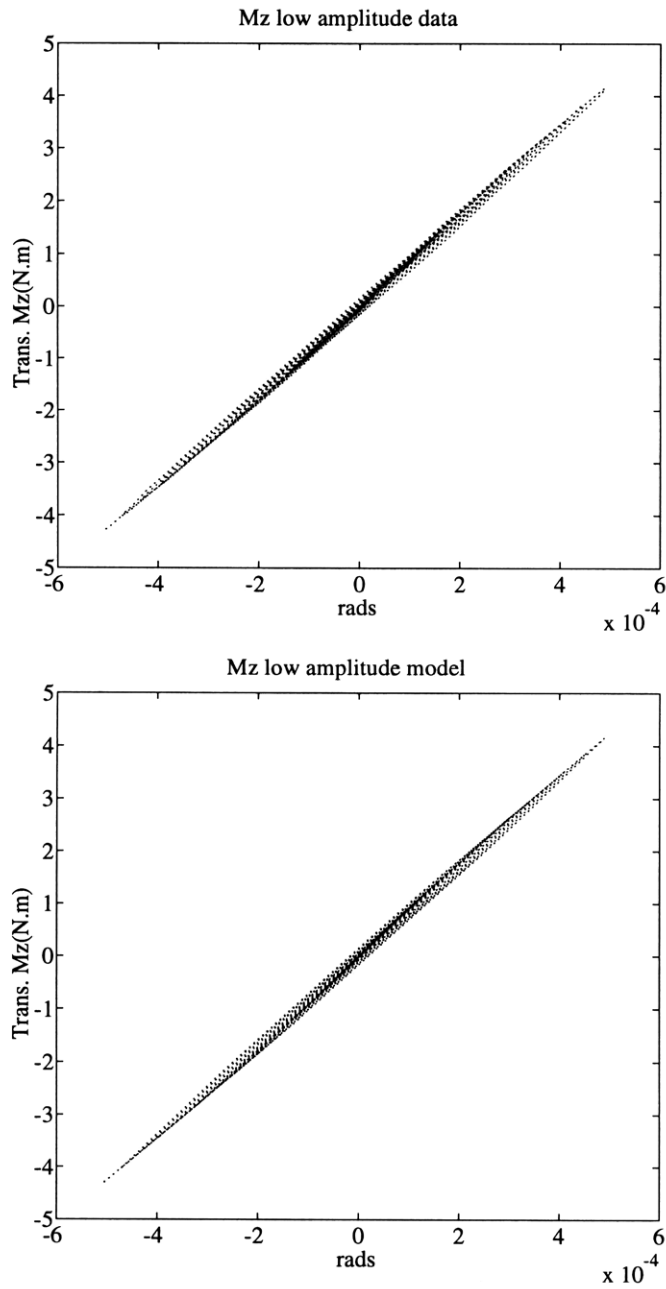


Figure 6.14: MODE alpha joint high preload low amplitude M_z data and dynamic hysteresis model.

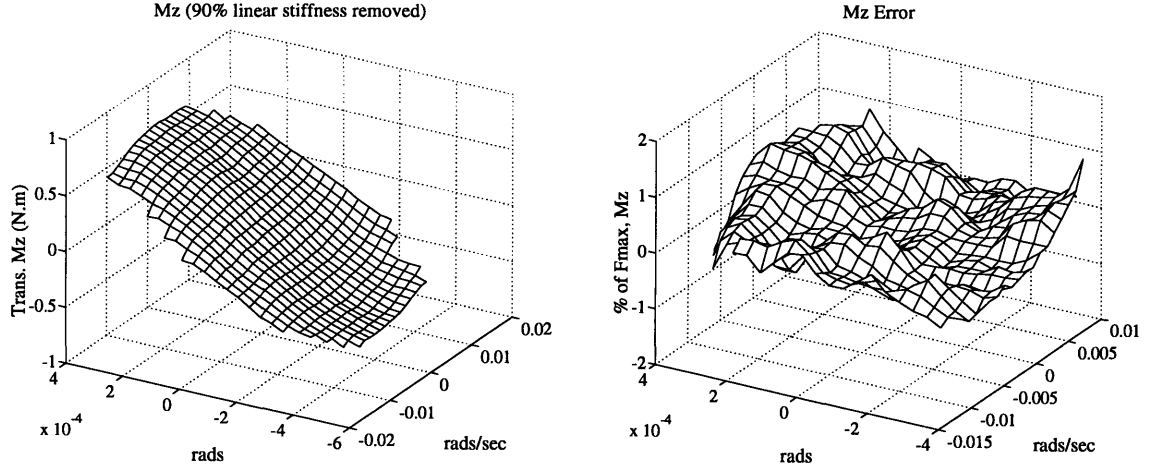


Figure 6.15: MODE alpha joint high preload low amplitude M_z force-state map data and model fit error map.

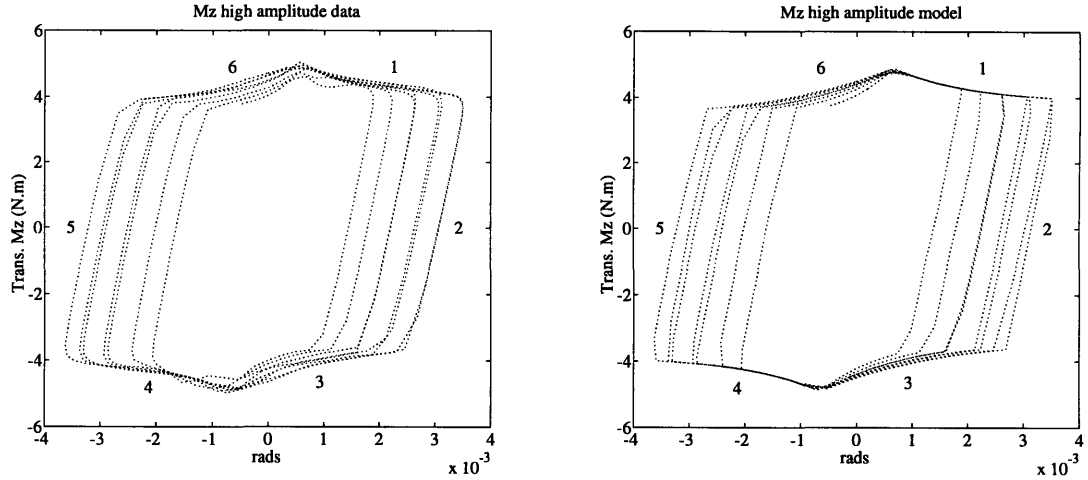


Figure 6.16: MODE alpha joint high preload high amplitude M_z load-stroke data and fit model.

direction.

Both the data and the model clearly show increased dissipation of the alpha joint as box like hysteresis loops. Simple models would predict a load saturation level (break load), with stiffness decreasing and dissipation increasing linearly with the amplitude. The refined modeling of section 3.3 is required to capture the displacement dependent friction in branches 1,3,4 and 6, and no slip stiffness in branches 2 and 5 of the alpha joint data.

Displacement dependent friction is seen at the extrema of the transmitted load (branches 1,3,4 and 6) and are modeled as exponentials with weights depending on the branch of the load-stroke curve. In the branches 3 and 6 of the model the relaxation

Table 6.10: High amplitude macro slip model parameters fit to the MODE alpha joint high preload M_x data.

Model F_{ij}	Parameters				
	δ_{ma} (rads)	μ_1	μ_2	δ_r (rads)	F_{ms} (N)
Branches 1 and 4 $F_{\theta\theta}$	6.44×10^{-4}	1.00	.27	1.35×10^{-3}	3.88
Branches 3 and 6 $F_{\theta\theta}$	6.44×10^{-4}	.85	.42	$0.60 \times \delta_n$	3.88

constant, δ_r , is set equal to $0.6\delta_n$. Where δ_n is the value of the rotation amplitude at the last change in sense of direction. Relative weights μ_1 and μ_2 are also altered in these branches, as listed in Table 6.10, with their sum constant at 1.27.

The model does a good job of capturing the macro friction displacement dependent phenomena with only five parameters. Since the displacement dependent function is purely *ad hoc* (not physically motivated) it is of limited value for extrapolating the fine details of the response to higher amplitudes than those tested.

Low preload

Examination of the high preload data and models results in the conclusion that the adjusting the preload should strongly effect the nonlinear load transmission of the joint. The effect of lowering the preload on the alpha joint bay load transmission is next investigated.

Alpha joint low preload data is presented in similar fashion to the high preload data. Figure 6.17 shows the corresponding diagonal data maps, F_x , F_y , F_z , M_x , and M_y , with 90% of the linear stiffness removed.

As seen in the high preload data the low preload data exhibits strong nonlinear behavior. Data in the F_y , F_z and M_y maps show some similar trends to the high preload tests while the F_x and M_x data appear significantly different. In general the effect of lowering the axial rotation preload on the diagonal models shown in Figure 6.17 has been to alter the nonlinear behavior.

Bicubic model error maps for the low preload are shown in Figure 6.18. The data is captured within percent accuracy, for the most part, in all of the five diagonal models shown. Some higher order analyticity can be seen in the F_x , M_x and M_y error maps. Again this error was deemed to be within experiment variation.

Table 6.11 show bicubic model parameters and participation factors for the low preload data of Figure 6.17. The fit parameters highlight the altered nonlinear behavior when compared to the high preload model. For example, F_{11} appears to have

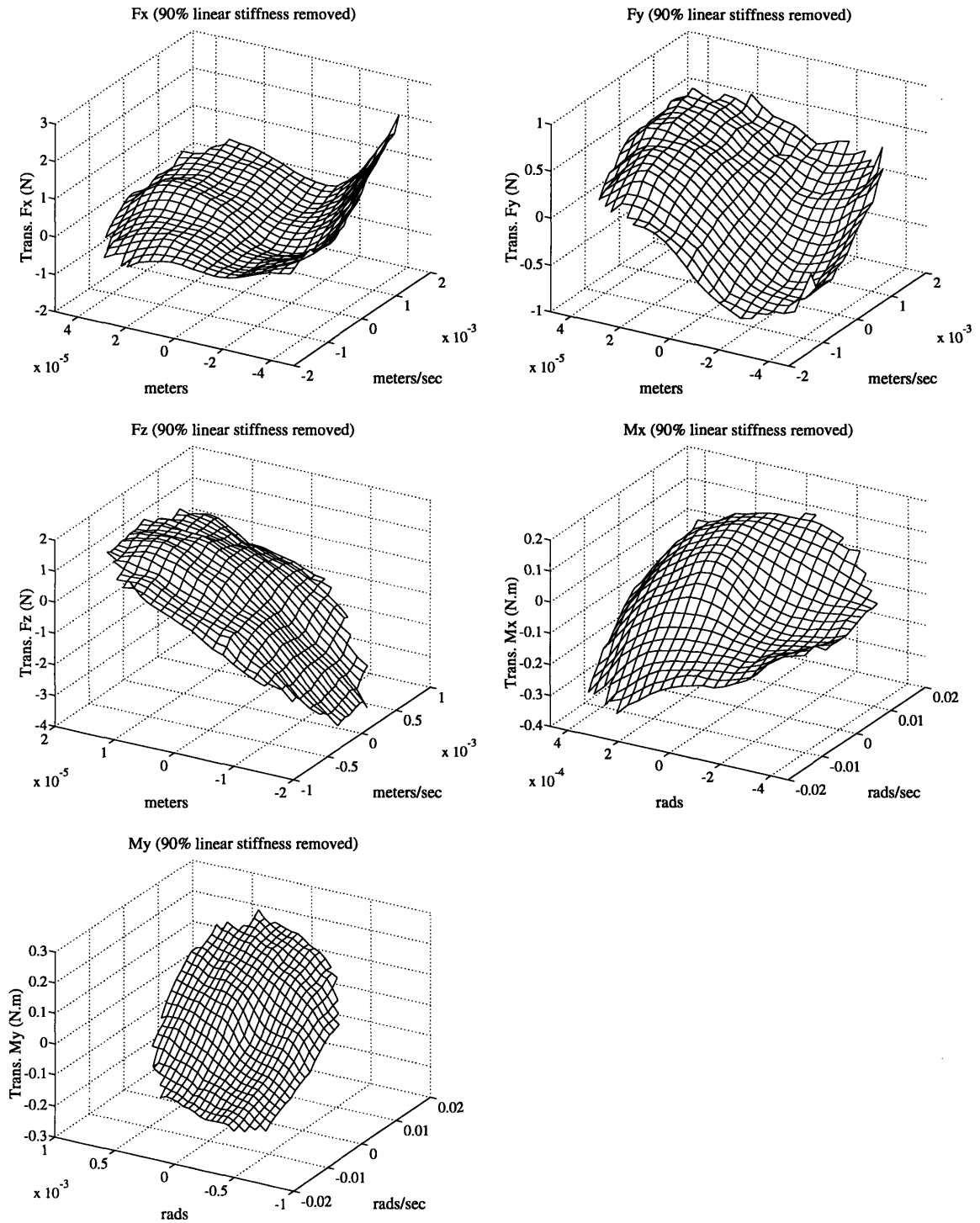


Figure 6.17: 5 Hz MODE alpha joint data force-state maps for diagonal F_x , F_y , F_z , M_x , and M_y tests. Alpha joint in low preload.

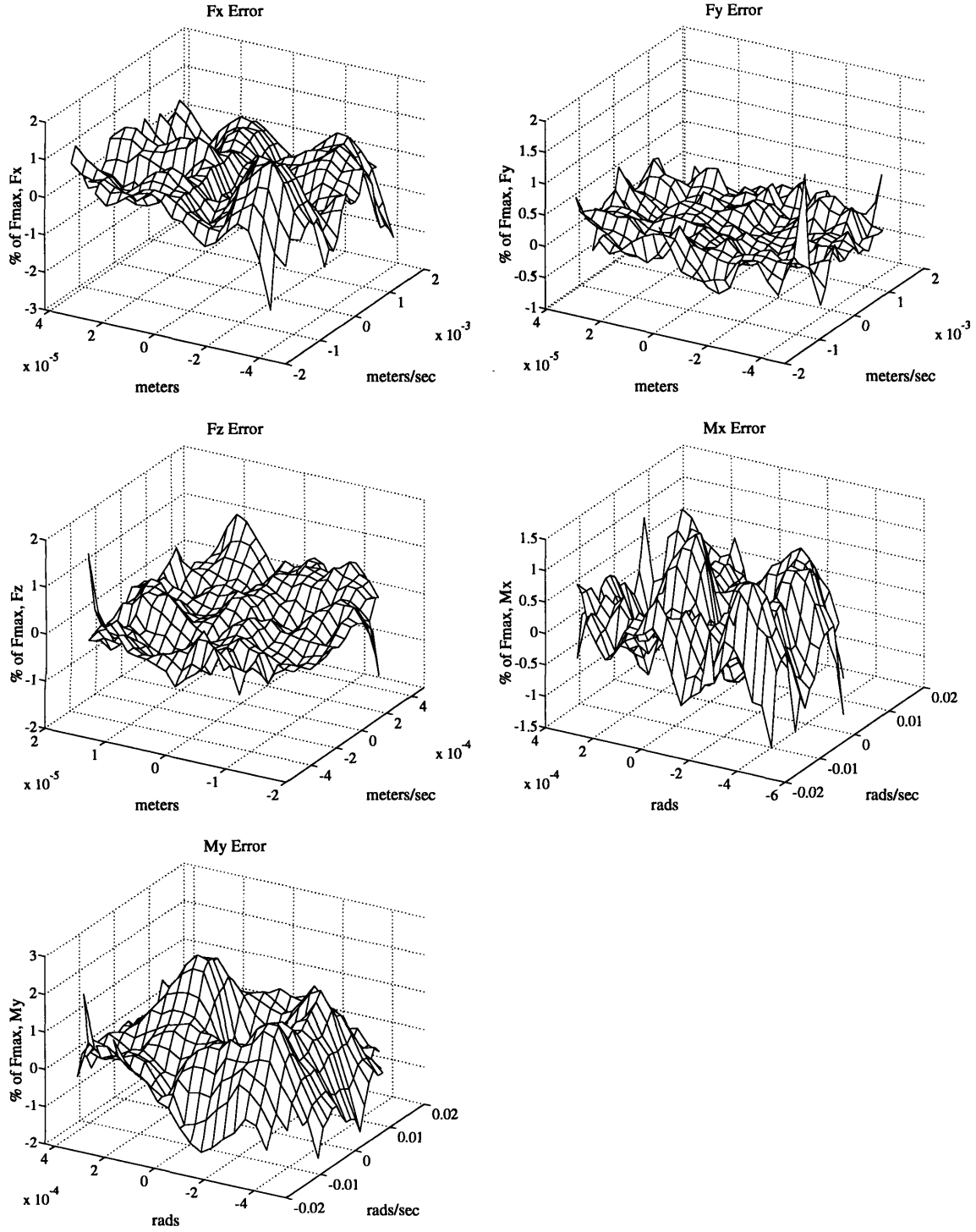


Figure 6.18: 5 Hz MODE alpha joint data force-state bicubic model error maps for diagonal F_x , F_y , F_z , M_x , and M_y tests. Alpha joint in low preload.

Table 6.11: Six d.o.f. applied load to unconstrained d.o.f. bicubic model of the low preload MODE alpha joint, in SI units, for 5 Hz test frequency. Each identified parameter is followed by its participation in the test applied load range.

Parameters C_{ij}	Sample Models									
	F_{11}	% Fm	F_{22}	% Fm	F_{33}	% Fm	F_{44}	% Fm	F_{55}	% Fm
C_{01}	1.645×10^2	2.6	1.861×10^2	3.3	9.694×10^2	2.6	1.330×10^1	18.1	1.411×10^1	14.8
C_{02}	5.859×10^4	1.7	-3.418×10^4	1.2	-9.965×10^5	2.0	-4.736×10^1	1.3	9.106×10^1	1.9
C_{03}	1.877×10^7	1.0	1.625×10^7	1.2	-5.619×10^8	.8	-7.432×10^3	4.2	-1.584×10^4	6.4
C_{10}	2.479×10^5	122.9	2.316×10^5	115.1	1.304×10^6	108.5	3.318×10^3	122.3	3.036×10^3	99.8
C_{20}	3.263×10^8	9.5	4.431×10^7	1.3	-3.228×10^9	6.0	-4.306×10^5	8.8	5.630×10^4	1.1
C_{30}	-1.670×10^{13}	28.3	-8.386×10^{12}	13.5	-5.883×10^{13}	2.5	-2.142×10^9	24.2	-2.602×10^8	3.2
C_{11}	1.927×10^6	1.7	-5.467×10^6	5.5	5.741×10^7	3.5	1.205×10^4	9.1	8.030×10^2	.5
C_{12}	-6.211×10^9	10.3	-3.272×10^9	6.8	-1.609×10^{11}	7.3	-2.552×10^6	39.1	-7.398×10^5	9.4
C_{13}	1.628×10^{12}	5.0	7.951×10^{11}	3.4	-2.553×10^{14}	8.5	-7.599×10^7	23.7	1.013×10^7	2.6
C_{21}	2.687×10^{11}	14.3	9.721×10^{10}	5.6	-1.740×10^{12}	2.4	-2.154×10^7	9.0	-1.514×10^7	6.0
C_{22}	-1.008×10^{13}	1.0	3.553×10^{13}	4.2	3.897×10^{15}	4.0	-2.359×10^8	2.0	-9.232×10^8	7.2
C_{23}	-3.521×10^{16}	6.3	-1.760×10^{16}	4.2	7.884×10^{18}	5.9	-3.345×10^9	.6	3.395×10^{10}	5.2
C_{31}	-2.932×10^{15}	9.1	1.602×10^{15}	5.3	-1.868×10^{17}	5.8	3.520×10^9	.8	7.831×10^9	1.9
C_{32}	-1.040×10^{18}	5.9	1.494×10^{17}	1.0	3.483×10^{20}	7.8	7.131×10^{12}	33.5	1.448×10^{12}	7.0
C_{33}	-2.852×10^{20}	2.8	3.147×10^{20}	4.3	7.817×10^{23}	13.1	4.246×10^{14}	40.6	1.491×10^{13}	1.4

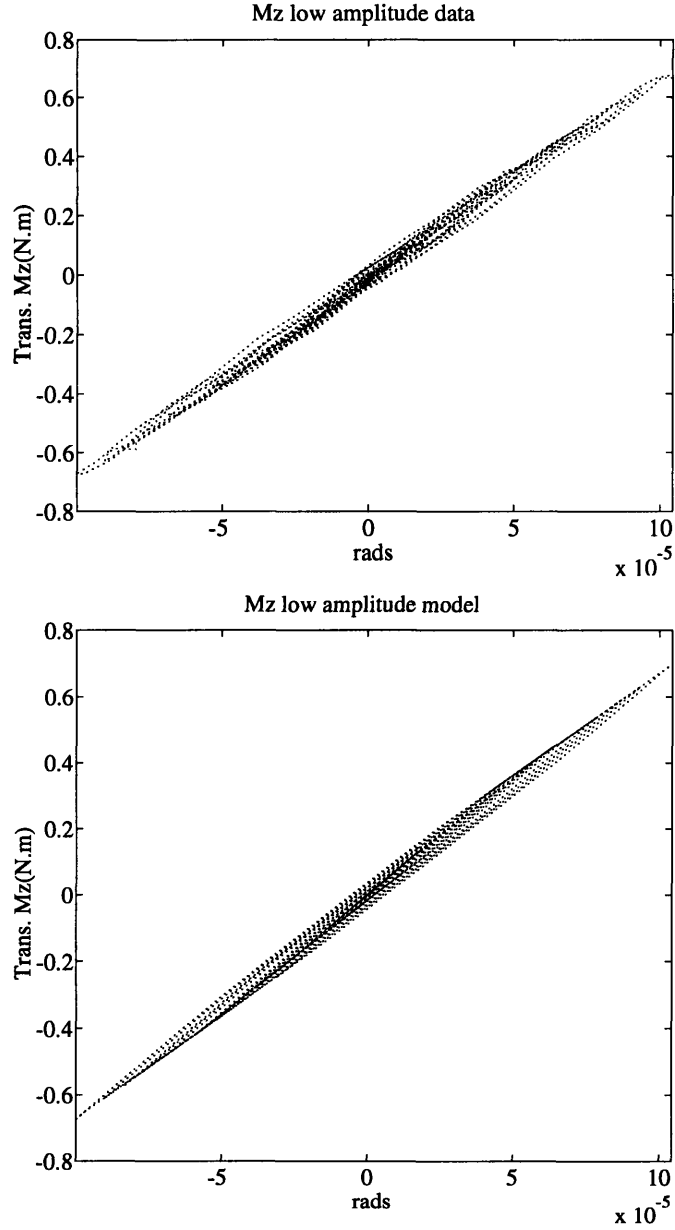


Figure 6.19: MODE alpha joint low preload low amplitude M_z data and dynamic hysteresis model.

increased in nonlinear participation while F_{22} appears to have decreased in nonlinear participation.

Consistency of the linear stiffness terms is good for the F_{11} and F_{22} models and only fair for the F_{44} and F_{55} models. In whole, the linear stiffness terms of these models compare to the high preload data within approximately 20%. Both the F_{11} and F_{22} linear stiffness terms, C_{10} , have stiffened significantly at low preload with corresponding increase in participation factor.

Low preload, low amplitude, M_z test data and fit model are shown in load stroke

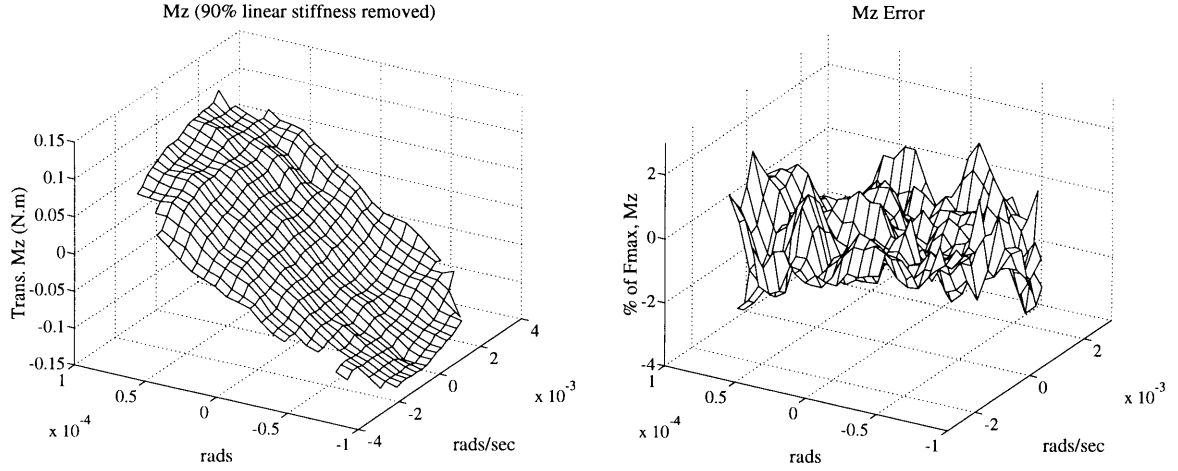


Figure 6.20: MODE alpha joint low preload low amplitude M_z force-state map data and model fit error map.

Table 6.12: Low amplitude micro slip model parameters fit to the MODE alpha joint low preload M_z data.

Model	Parameters		
	K_1 (N.m/rad)	K_F (N.m/rad)	δ (rads)
F_{66}	6187	1340	6.021×10^{-5}

form in Figure 6.19. The data, although substantially more noisy, shows the expected similarity to the high preload low amplitude data (see Figure 6.14). Again the micro slip accumulation appears as softening dynamic hysteresis. Comparison of the force-state maps of Figures 6.20 and 6.15 shows the regular dynamic hysteresis curvature for both preloads with the low preload corrupted by amplitude quantization. Subsequently the low preload data was fit with the same micro slip model as in the high preload case. Fit parameter values are tabulated in Table 6.12 and a model error map (Figure 6.20) shows the fidelity of the fit.

The linear stiffness term, K_1 , is significantly less than the high preload equivalent which suggests the stiffening effect of the joint friction pad mechanism under axial preload. Low amplitude added stiffness, K_F , the sum stiffness of the slip interface springs, is 20% larger than the corresponding high preload parameter. This K_F stiffening does not compensate for the drop in K_1 stiffness. The slip distribution parameter, δ , is reduced from the high preload fit by a factor of five. Comparing the parameters in Tables 6.9 and 6.12 shows that the micro slip model describes more than just accumulated friction of the alpha joint bearing race. If the micro slip model were solely descriptive of bearing race friction then the dynamic hysteresis parameters

Table 6.13: High amplitude macro slip model parameters fit to the MODE alpha joint low preload M_z data.

Model F_{ij}	Parameters				
	δ_{ma} (rads)	μ_1	μ_2	δ_r (rads)	F_{ms} (N)
Branches 1 and 4 F_{66}	2.6×10^{-4}	.96	.34	$0.7 \times \delta_n$.71
Branches 3 and 6 F_{66}	2.6×10^{-4}	1.00	.31	5.3×10^{-4}	.71

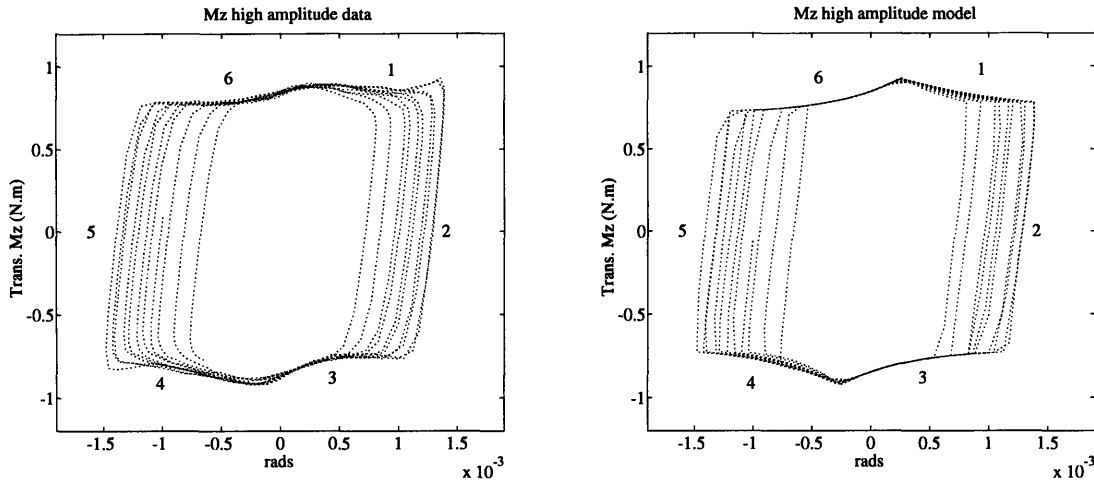


Figure 6.21: MODE alpha joint low preload high amplitude M_z load-stroke data and fit model.

K_F and δ would be similar irrespective of preload. The conclusion is that the micro slip model incorporates friction pad low amplitude slip behavior as well as bearing race motion.

High amplitude low preload data shows similar displacement dependent friction behavior as in the high preload data. Figure 6.21 shows the low preload high amplitude data and model fit. The overall break load has been reduced from approximately 3.9 to .7 N-m by releasing the cleat on the friction pad. Again the dissipation increases linearly with the amplitude while the stiffness decreases linearly with the amplitude.

In order to be consistent the low preload macro slip model retained the same form as the high preload model. Different branch behavior in the low preload data, 1 and 4 *vs.* 3 and 6, resulted in alternate sets of relative weights used in the fitting process. Table 6.13 lists the fit parameters for the macro slip model. The macro slip model is shown in Figure 6.21. The model appears to be a less accurate representation of the physics for the low preload. However, the macro slip model still captures the general behavior. Fine detail behavior, in branches 1,3,4 and 6 of Figure 6.16 and 6.21 is therefore a non uniform function of the friction pad preload.

The alpha joint data and model fits have shown two regimes of operation. Low amplitude operation is shown to behave essentially linearly with approximately 10% accumulated micro slip witnessed in the axial rotation transmission range. High amplitude operation shows coulomb-like friction with the friction pad interface fully engaged. Component load transmission directions other than axial rotation axis are shown to be strongly nonlinear (up to 20% of the range) and are effected by the friction pad preload in a complicated fashion.

6.5 Summary

Four components were tested and presented in this chapter; a nominally *linear* calibration bay; the MODE adjustable pretension deployable bay; the MODE erectable bay; and the MODE alpha joint. Calibration bay data served as a benchmark against which the experiment concept and identification techniques were be investigated and compared. Adjustable pretension bay data showed fundamental dynamic hysteresis at all preloads with the nonlinearity increasing as the preload decreased. Reaction force identification and repeatability data were also reported as proof of the underlying mechanism. Analytic and non analytic models were fit to the data where necessary. Erectable bay data was linear, as expected, until multiple tests caused vibration induced loosening of the joints. Bicubic analytic models were used to investigate the effects of joint loosening in the erectable data. Alpha joint data showed the strongest nonlinear behavior of all the joints tested. The axial rotation d.o.f. was investigated with a physical model while all others were fit with analytic bicubic parameterizations. In the axial rotation data dynamic hysteresis was identifiable at the low amplitudes and showed strong similarity to the deployable bay data. Models motivated by micro slip distributions were used to fit this data. The accumulated micro slip model was shown to be fundamental to the description of accumulated solid friction. High amplitude alpha joint data showed displacement dependent coulomb-like friction when exceeding the joint break load.

The remaining task of the report is to use these identified component nonlinear models to formulate simple model predictions of the global structure dynamics and compare the predictions to modal dynamics data.

Chapter 7

Assembled component modeling and modal prediction

This chapter assembles some of the component models identified in chapter 6 into dynamic models of the entire MODE structures. The resulting nonlinear models of the MODE structures are solved iteratively to find the linearized response of the structures to inputs equivalent to the ground and space modal tests. The predicted natural frequencies and damping ratios of the models of the MODE structures are compared to the modal parameters identified from ground and space dynamics tests [Barlow, 1992].

MODE configurations modeled in this chapter are the baseline and alpha configurations shown in Figure 2.1 [2]. The baseline configuration consists of two four bay deployable sections joined in the center by an erectable bay. The baseline is a straight nine bay truss configuration. In one of the four bay deployable sections the adjustable pretension bay resides. The rest of the deployable bays are fixed at the nominally high pretension of the adjustable bay. The alpha structure is similar to the baseline in arrangement with the erectable bay replaced by the alpha joint bay. Rigid body axial rotation of one deployable section with respect to the other was enabled by the alpha joint inclusion.

Specifically, the MODE baseline and alpha structures models will be of the torsion mode only. This involves motion of the torsional (θ_z) d.o.f., and allows simple prediction of the first fundamental structural mode of the nonlinear MODE structures.

7.1 Assembled component structures

Torsion d.o.f component models of the adjustable pretension bay, erectable bay and alpha joint bay are assembled to model the baseline and alpha MODE configurations.

This section describes which component models are used and how they are assembled for analysis.

Three assembled models are required to analyze the MODE baseline configuration. The three models are of the entire baseline structure with adjustable pretension bay in high, medium and low pretensions respectively. Each assembled model of the baseline structure uses torsion d.o.f. adjustable pretension bay and erectable bay component models from chapter 6.

Full identification of the adjustable pretension bay resulted in component models F_{66} and F_{C6} , from which it is assumed $F_{6C} = F_{C6}$ and $F_{66} = F_{CC}$. These models represented the relationship between the component torsion d.o.f. and the transmitted axial moment, each for a given pretension on the bracing wires. The influence of component d.o.f. other than the torsion d.o.f on the transmitted axial moment is considered negligible. For the dynamics analysis it is further assumed that

$$F_{6C} = F_{66} \quad (7.1)$$

$$F_{C6} = F_{66} \quad (7.2)$$

Equations 7.1 and 7.2 are enforced for each pretension. Tables 6.2 and 6.3 of chapter 6 show this to be a fair assumption.

For the baseline model the physical adjustable pretension bay model, F_{66} , is (least squares) approximated by an analytic model, F_{D6} . The analytic model, F_{D6} , is therefore a smoothed version of the component model and approximates the nonlinear memory of the component. The appropriate physical model F_{66} from Table 6.2 is first simulated using a dense state space, θ and $\dot{\theta}$. A bicubic parameterization is next fit to the simulated model data to give F_{D6} . The resulting model, F_{D6} , is a smoothed component model. This is not the same as fitting the component data of chapter 6 directly with a bicubic parameterization. The physically derived component model, F_{66} , can be interpolated by evaluating transmitted force using a dense state space.

The model F_{D6} represents the adjustable pretension component in the final assembled nonlinear model shown in Figure 7.1. In Figure 7.1 the baseline structure consists of the analytic adjustable pretension bay models, F_{D6i} , $i = 1, 2, 3, 4, 6, 7, 8, 9$, and an erectable model, F_{E6} . The erectable model is the identified linear spring and dashpot of F_{66} of Table 6.6 in chapter 6. The axial d.o.f. to axial transmitted force coupling of the erectable component, F_{63} is ignored in the baseline models.

The model for F_{D6_3} shown in Figure 7.1 was appropriately selected to represent high, medium and low pretension baseline models. The remaining F_{D6i} , $i \neq 3$, were

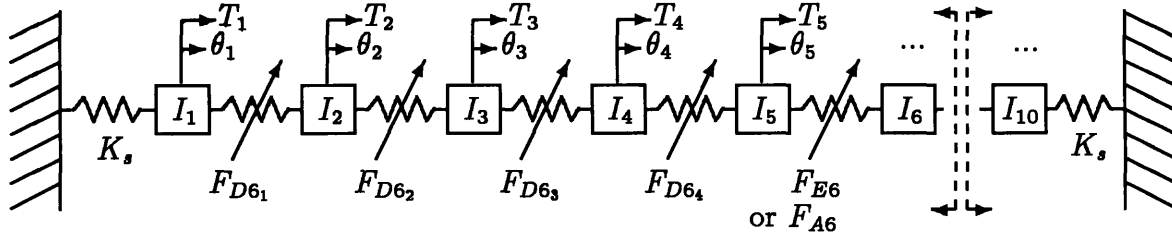


Figure 7.1: Ten d.o.f. model of MODE torsion axis. Adjustable pretension bay models are F_{D6i} . The center spring is the erectable F_{E6} or alpha F_{A6} respectively for the baseline and alpha analysis.

all high pretension component models. The baseline models were grounded with linear suspension springs at each end of the structure that mimic the (1 Hz plunge mode) ground dynamics test suspension springs, $K_s = 54$ N-m/rad. For the space test analyses these springs were reduced to $K_s = 4$ N-m/rad to simulate free end conditions.

The inertias shown in Figure 7.1 lump that of the components and the MODE structure end masses. The inertias used for the baseline model are

$$\begin{aligned}
 I_1 &= I_{em} + I_{act} + .5I_{ad} \\
 I_2 &= I_{ad} \\
 &= I_3 = I_4 = I_7 = I_8 = I_9 \\
 I_5 &= .5I_{ad} + .5I_{er} \\
 &= I_6 \\
 I_{10} &= I_{em} + I_{ad}
 \end{aligned} \tag{7.3}$$

$$\begin{aligned}
 I_{em} &= .713 \text{ kg} - \text{m}^2 \\
 I_{act} &= .01 \text{ kg} - \text{m}^2 \\
 I_{ad} &= .02 \text{ kg} - \text{m}^2 \\
 &= I_{er}
 \end{aligned} \tag{7.4}$$

The end mass inertia, I_{em} , dominates the inertia matrix. The adjustable pretension bay inertia is I_{ad} . The erectable bay inertia I_{er} is assumed equal to the inertia of the adjustable pretension bay. Actuator inertia, I_{act} is added to I_1 to model the proof mass actuator that forces the structure.

Two assembled component models are required to analyze the MODE alpha configuration. The two models represent the assembled structure with the alpha joint

in high and low preload respectively. In the alpha configuration the alpha joint component models replace the erectable component model. Figure 7.1 shows the alpha joint model as F_{A6} .

For each alpha joint preload, the model F_{A6} is an analytic model approximating a combined micro and macro slip alpha joint model. The micro and macro slip alpha joint models were presented in section 6.4. As was the case with the adjustable pretension models, the analytic model is a smooth version of the physical component model and approximates the memory in the physical component model.

Forming the models, F_{A6} , for each preload is performed in three steps. First, micro slip and macro slip models, F_{66} , are combined at the macro slip break amplitudes, δ_{ma} (listed in Tables 6.10 and 6.13) to yield a continuous physical model of the alpha joint for each of the two operational preloads. Second, the combined micro and macro slip physical models of the alpha joint are simulated with a dense state space, θ and $\dot{\theta}$. Third, for each of the simulated models two biquartic parameterizations are fit to the simulated data. The first biquartic parameterization was fit to the amplitude range $[0, 1.2\delta_{ma}]$. The second biquartic parameterization was fit to the amplitude range $[\delta_{ma}, 4\delta_{ma}]$. Therefore, each of the two models F_{A6} , that model high and low preload respectively, consists of two analytic biquartic models that overlap in range. Overlapping the state range allows a transition within each alpha joint model, F_{A6} , at δ_{ma} . This transition is now mildly discontinuous in transmitted force since both biquartic parameterizations are fit to an intersecting set of data points.

In the MODE alpha configuration models the adjustable pretension component model, F_{D6i} , represents the high pretension component model for all $i = 1 - 4, 5 - 9$. The ground and space suspension springs are equivalent to that used in the baseline analysis. The inertia matrix remains unchanged except for I_5 and I_6 which incorporated the inertia of the alpha joint, $I_{al} = .05 \text{ kg} - \text{m}^2$, instead of the erectable bay, I_{er} .

7.2 Model refinement

Before the dynamic analysis is conducted, the component models F_{D6i} , F_{E6} and F_{A6} are adjusted to be consistent with the low amplitude input force ground tests. Two types of adjustment were performed. The first type of adjustment is a second generation model update that represents gravity loading of the structure suspended in the laboratory. The second type of adjustment is a third generation model update where the linear stiffness terms of the adjustable pretension and alpha component models are refined to reflect the low amplitude force ground test resonant frequencies.

Gravity loads were present in the MODE baseline and alpha ground dynamics tests. The gravity loads were generated, in part, by the off-set of the end mass center of gravity from the suspension connect points. This end moment was partially countered by the distributed weight of the structure. The static gravity loads in the structure further preloaded the pin joints of the deployables and the friction pad of the alpha joint.

For the ground analyses the nonlinear terms in the smoothed component models (those other than the linear stiffness and damping terms) are multiplied by a participation factor of 0.6. Reducing the participation of the nonlinear parameters is approximately equivalent to preloading the sliding interfaces of the components. This simulates a gravity preload on the structure. In the alpha joint models the transition amplitudes, δ_{ma} , were increased by a factor of 1.5 before fitting the analytic approximations. Increasing the physical break amplitude simulates the dynamic rotation required to break the mechanism into macro slip under a gravity induced preload. The gravity induced preload serves to further load the rotational interface over and above the existing device preload.

Adjustment of the linear stiffness terms in the adjustable pretension bay and alpha joint bay component models is performed and maintained for both ground and space analyses. The adjustments result from comparing eigenanalysis of the 10 d.o.f. MODE assembled component models and the low force ground dynamics data. The linear stiffness terms of the adjustable pretension bay models, F_{D6} , are multiplied by a factor of .9 for the high and medium pretensions and by a factor of 1.3 for the low pretension. These adjustments are within the repeatability data presented in Table 6.5 and also reflect a measured trend in the static bracing wire pretensions. Measured pretensions in the deployable test article of the MODE structure were approximately 7, 13 and 27 lbs for low, medium and high pretensions respectively while the adjustable component measured pretensions were approximately 4, 15 and 32 lbs respectively. The linear stiffness terms in the alpha joint models, F_{A6} , were also (updated) multiplied by .9, for both preloads, based on low force ground dynamics data. This is possibly due to slightly different break loads in the MODE alpha device and the alpha joint test component.

The linear stiffness adjustments only incorporate ground dynamics test information for low force and represent a third generation update of the component models. This allows confirmation of the nonlinear component models for higher forcing levels in the ground predictions. Space predictions are next made using the updated models for all forcing levels (after removing gravity loads and linear suspension springs).

7.3 Iterated Response

Computing the response of nonlinear dynamics models of the MODE baseline and alpha configurations was a difficult task. The difficulty arose from the low damping present in the 10 d.o.f. MODE models. In this section an algorithm for computing the response of the MODE models is presented. First, other methods (some attempted unsuccessfully) are briefly discussed.

The objective of computing the response of the MODE models was to compare the natural frequencies and damping ratios presented in Barlow [2] with the assembled component model predictions. Selected dynamics test data, presented in Barlow [2], was shown in chapter 2 of this report and is repeated later in this chapter for comparative purposes. This data shown in Figures 7.4, 7.5, 7.6 and 7.7 are presented as point wise frequency domain ratios of the output harmonic amplitude (in g's) to the input harmonic amplitude (in lbf). These discrete frequency domain curves were circle fit by Barlow [17] to give natural frequencies and damping ratios. The natural frequencies and damping ratios, fit to the data, are presented for comparative purposes in Tables 7.2 and 7.3.

A computational method was required to compute the response of the MODE models. In order to make a fair comparison between the MODE models and the data the computational method need be able to compute the output harmonic amplitude resulting from input at a specific set of frequencies.

Existing methods

Many methods exist to realize the objective of computing the response of the MODE models. This section lists them in order of decreasing computation time (time integration being the most computationally intensive), a summary of which were attempted and their success or failure is given.

Some methods for computing the response of nonlinear sets of equations are

- Forward marching Time Integration (TI).
- Alternating Frequency-Time domain analysis (AFT).
- Residual Force, plus the method of embedded parameters (RF).
- Incremental Harmonic Balance and Harmonic Balance (HB).
- Describing Function analysis (DF).

Good references for direct time integration of nonlinear structural dynamics equations are by K.C. Park [18, 31]. In these formulations the nonlinear stiffness and damping matrices of a second order structural dynamics system (M, C, K) are linearized and projected forward at each time step. Some prediction and some correction updates the response and the next time step before moving forward in time. A specialized explicit central difference method was applied to the MODE baseline high pretension model. A spurious low frequency mode was generated in the discretization of the model. The spurious mode beat with the lightly dampened fundamental structural mode. Artificially increasing the damping of the fundamental mode (to $> 1\%$) removed the spurious beating effects but corrupted the results by over dampening the memory mechanism. Shortening of the time step did not remove the spurious mode.

The alternating frequency-time domain direct method is described in section 4.4 [7]. The direct method presented relies on a linearized dynamics model. This model is driven by the input forces to which the nonlinear joint forces are added. Convolution of the linearized model and the summed input forces is performed in the frequency domain *via* DFT multiplication. The discrete time domain response is converged upon through successive iteration. If the nonlinearity contributes less than 10% of the response then the direct algorithm was found to converge [7]. If the nonlinearity was stronger, but generally less than 30%, then a gradient method such as Broydens method could be used [6]. When the AFT method was applied to the MODE models the predicted response diverged. Again the problem was that the fundamental structural mode was lightly dampened. Small amounts of softening of the fundamental mode results in large differences between the linearized model response and the actual response. The differences were too large for the AFT direct algorithm or the AFT-Broydens algorithm to converge.

Residual force techniques such as that described in Chapman [8] fail for the same reason that the AFT fails. Residual force techniques reformulate the second order structural dynamics equations with the linearized (or linear parts) model on the left hand side (LHS) while the driving forces are summed with the residual nonlinear nodal forces as the right hand sides (RHS). Light damping again causes the nonlinear forces to be extremely large with respect to the driving forces. The extremely large nonlinear forces can be viewed as high gain state feedback in the equations. The high gain subsequently destabilizes the linear LHS model.

The incremental harmonic balance technique presented by Lau *et al.* [26] was not tried due to the large amount of analytical work required to formulate the incremental second order system matrices $(\Delta C, \Delta K)$.

Further techniques listed, but not tried, are the multiple frequency harmonic bal-

ance technique and the single frequency harmonic balance technique or describing functions. HB methods depend on finding fourier phase and quadrature coefficient matrices in response to a harmonic input (the multiple frequency HB method extends this to include sub and super harmonics of the input). Good references for these methods are Arfken [1] and Vander Velde [20].

Direct Linearization Analysis

Direct linearization analysis is derived from a combination of the above methods and was found to succeed for the nonlinear MODE models. In this section Direct Linearization Analysis (DLA) is presented as a combination of the AFT and the single frequency HB (or DF) methods. Another way of looking at the HB methods is direct iteration on the dynamic system matrices (M, C, K) and the time domain response. The objective of the DLA is to step through a discrete frequency window computing the linearized (M, C, K) and complex response at each frequency point.

DLA iterates on the linear stiffness and damping matrices that fit the response of the model in a least squares sense at each frequency point (the inertia matrix is assumed constant and is so for the MODE models). The underlying concept is that convergence of the fit stiffness and damping matrices means convergence of the linearized response at a discrete frequency. The method relies on the existence of an average linear model.

Figure 7.2 shows the flow of the DLA algorithm that was applied to the MODE baseline and alpha models. The logic shown in Figure 7.2 is as follows;

Step 1. The linear stiffness and damping matrices K_L and C_L are formulated from component models at very low amplitudes. M_L is constant for the MODE models.

Step 2. The system matrices, M_L , C_L and K_L are used to compute the frequency domain structural operator $\Delta(\omega)$ at the input force frequency, ω_o , according to Equation 7.5.

$$\Delta = -\omega^2 M_L + j\omega C_L + K_L \quad (7.5)$$

Step 3. The frequency domain vector of applied (co)sinusoidal torques $T(\omega)$ is generated. For the MODE models the applied forces are on I_1 of Figure 7.1.

Step 4. The complex linear response, Θ , at the input frequency ω_o , is computed by inverting the complex structural operator and premultiplying it to the vector of applied torques T .

Step 5. The complex response Θ is used to generate the time domain response $\theta(t)$ and $\dot{\theta}(t)$. If necessary, a ramped sinusoids are appended to the beginning of the constant amplitude sinusoids for memory model computations. For the MODE

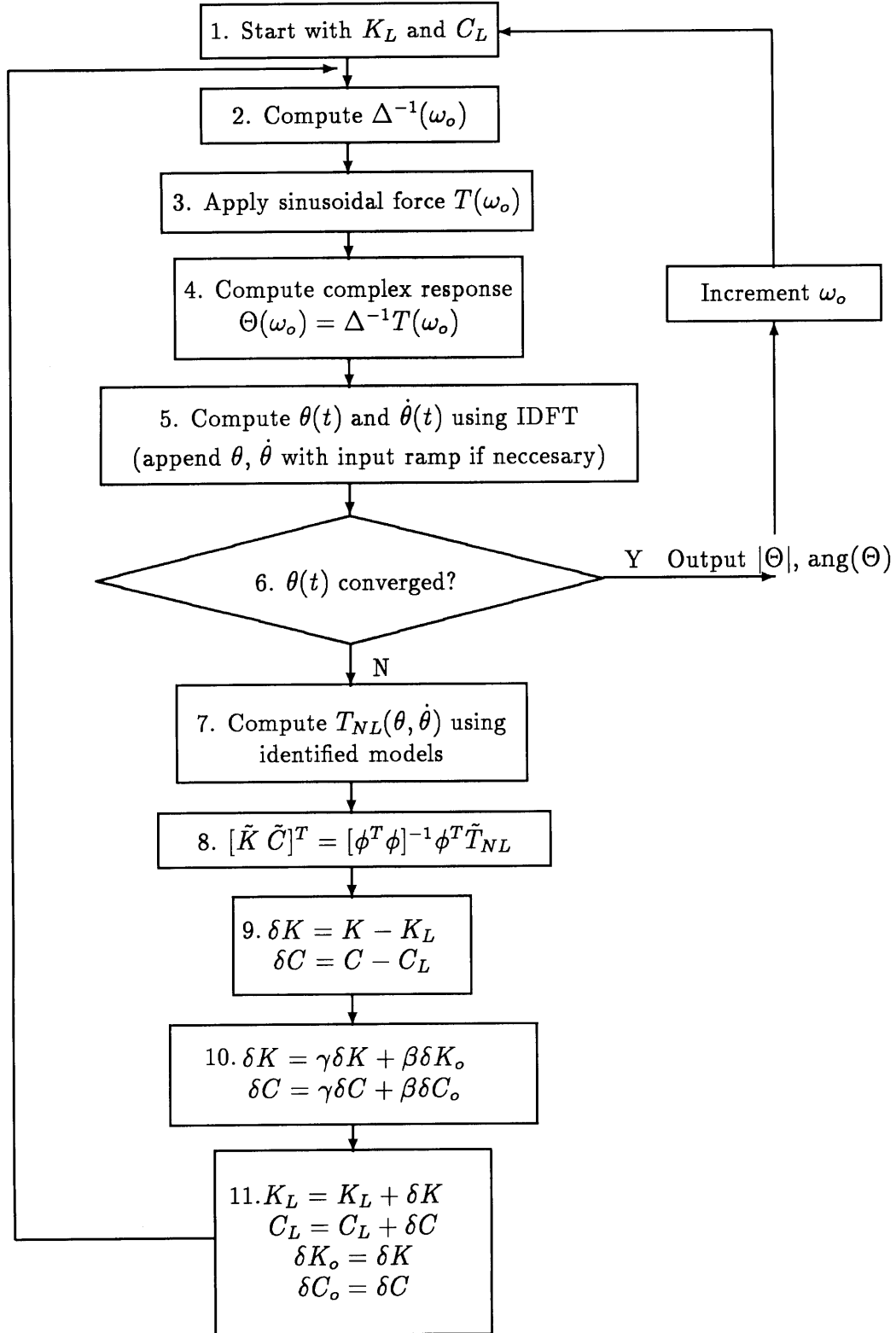


Figure 7.2: Flow for Direct Linearization Analysis.

models this is not necessary due to the analytic smoothing of the component models.

Step 6. Convergence of the time domain response is next tested. For the MODE models a relative error check was used. The relative error is described in Equation 7.6.

$$\theta_{err} = \frac{\int |\theta_i(t) - \theta_{i-1}(t)| dt}{\int \theta_{i-1}^2(t) dt} \quad (7.6)$$

The tolerance used for the MODE models was 1%.

Step 7. If convergence is not achieved; the matrix of quasistatic component torques, $T_{NL}(\theta, \dot{\theta})$, is computed using the current nonlinear MODE model. The i th column of T_{NL} is the quasistatic force generated in the i th bay of the MODE model.

Step 8. Linear parameters are least squares fit, arranged as the appropriate vector $[\tilde{K} \ \tilde{C}]^T$, to the matrix of torques, arranged as the appropriate vector \tilde{T}_{NL} . Equation 7.7 shows how the simulated data matrix ϕ is formulated.

$$\phi = [(\theta_2 - \theta_1) \dots (\theta_{10} - \theta_9) (\dot{\theta}_2 - \dot{\theta}_1) \dots (\dot{\theta}_{10} - \dot{\theta}_9)] \quad (7.7)$$

Block 8 in Figure 7.2 shows the least squares fit equation.

Step 9. The perturbation stiffness and damping matrices, δK and δC , are obtained by subtracting off the previous linear part.

Step 10. This step relaxes δK and δC with the last iteration solution providing some smoothing to the procedure. For the MODE model computations $\gamma = 2/5$ and $\beta = 3/5$ were used. Terms previous to the last solution can be used at the expense of memory storage.

Step 11. In this step the next linear stiffness and damping matrix pair, K_L and C_L , are found. The results of the iteration are stored before restarting at step 2.

When converged on the time domain response the output is the complex amplitude and angle of the response. At this point the complex response is stored and the driving frequency is incremented. The solutions from the last frequency step, K_L and C_L , are now used as an initial guess for the new driving frequency.

The two discretizations used in the DLA are in the time domain and frequency domain. The frequency domain discretization governs the spacing between successive drive frequencies. The method essentially bootstraps itself, in frequency, from a low amplitude linear response to a high amplitude nonlinear response (this depends on the nonlinearity). The time domain discretization is independent of the frequency domain discretization. The time domain discretization is used for the linear sinusoidal response and is important for convergence in the least squares torque fit.

Results of DLA are similar to the MODE data in that a ratio of output harmonic response to harmonic input is computed. Even though the MODE physical structure

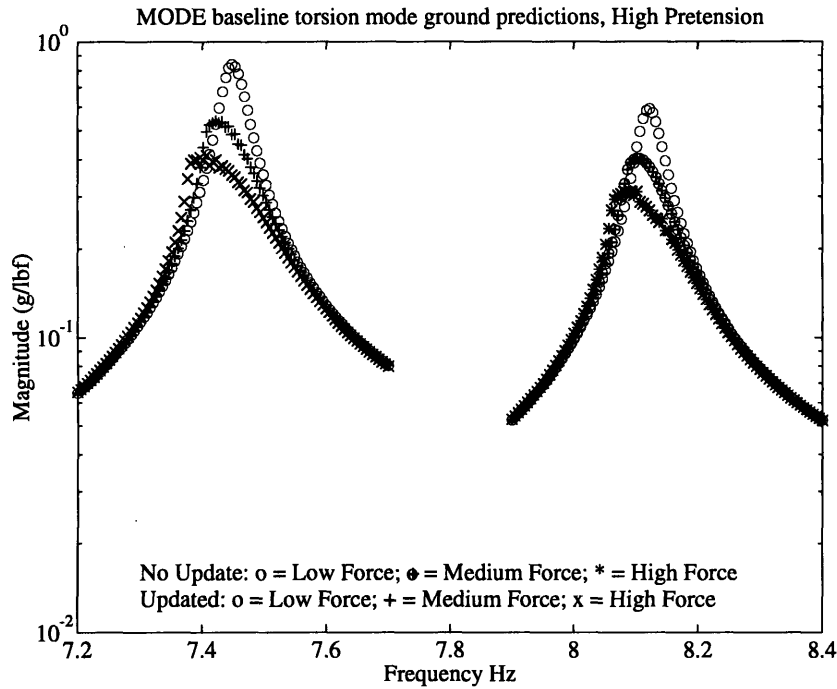


Figure 7.3: Third generation updated and non updated ground baseline predictions.

(infinite d.o.f.) and the MODE models (10 d.o.f.) are fundamentally different the results should be fairly accurate in terms of frequencies and damping ratios. This assumption is based on the fact that near the fundamental mode of the structure the torsion d.o.f. dominate the structural response.

7.4 Predictions and MODE modal data

This section presents the results of applying the DLA to the MODE models and compares the results to test data. First a comparison of the updated and non updated ground baseline (high pretension) models is presented. The inputs and outputs of the DLA of the MODE models are next specified. The results of the DLA of the MODE baseline and alpha models follows respectively. The results are compared to ground and space modal test data in terms of discrete frequency domain response, fit natural frequencies and fit damping ratios.

Figure 7.3 shows the third generation model update applied to the ground high pretension baseline model. The update was based on the low force ground data natural frequency only. The updated model resonant frequencies have decreased from the non updated model frequencies by 5% reflecting the multiplication of the linear stiffness term of the high pretension adjustable model by .9. Similar updates decreased the

Table 7.1: Input Torques for the MODE models.

Config.	Simul. Environ.	Approx. Freq. (Hz)	Amp. 1 (N-m)	Amp. 2 (N-m)	Amp. 3 (N-m)
Baseline	Ground	7.7	.021	.101	.179
	Space	7.6	.024	.134	.240
Alpha	Ground	7.3	.021	.103	.170
	Space	7.2	.023	.137	.247

linear stiffness of the medium preload adjustable model to 90% of the original value while increasing the low pretension adjustable model linear stiffness by 30%. Similar updates of the linear stiffnesses of the alpha joint models was described in section 7.2. These third generation updated models are those used in the DLA of the MODE baseline and alpha configurations.

The inputs that drive the MODE models are torques generated by the MODE Proof-Mass Actuator (PMA). Input torques drive the model at I_1 (see Figure 7.1) which is consistent with the PMA location at one end of the MODE truss [2]. The torques that were used to drive the baseline and alpha MODE models are listed in Table 7.1. These were computed from measured PMA forces reported in Barlow [2].

Predictions from the DLA are shown in this section as the harmonic ratio of the acceleration $\ddot{\theta}_1$ (see Figure 7.1), in units of gravity, to input PMA force, in units of lbf. The predictions are plotted in the discrete frequency domain to be consistent with the previously presented MODE data. The predictions were circle fit with the same routine as the MODE data and tabulated values of natural frequency and damping ratio are compared.

Baseline configuration

Figures 7.4, 7.5 and 7.6 show the MODE baseline data for both space and ground (top plots) *vs* DLA predictions (bottom plots). The three Figures 7.4, 7.5 and 7.6 are for high, medium and low pretensions, respectively, in the adjustable pretension bay. The Figures show the predicted response on the same frequency scale as the data.

In general, the ground data magnitudes compare well to that predicted. Both in the predictions and in the data the space magnitudes are less than the ground magnitudes. This is, to a lesser degree, due to the increased damping in both the space data and predictions. The majority of the decrease in magnitudes between space and ground is caused by the removal of the suspension system. The space predictions

clearly do not decrease in magnitude as severely as the space data. However, the space data includes residues from bending and breathing modes of the actual structure as well as residues from actuator dynamics.

The predictions, shown in Figures 7.4, 7.5 and 7.6, clearly capture nonlinear dynamic hysteresis in the discrete frequency domain. The predictions show a softening and dampening fundamental mode as the input amplitude is increased. This is seen in both the ground and space predictions for all pretensions. These results are consistent with the data. Agreement of the data and predicted nonlinear behavior is best in the ground data.

Space predictions also show softening and dampening which is, in part, consistent with the space data. Clearly, some other phenomena is present the space data, not predicted by the DLA. The increased dissipation in the space data maybe due to erectable joint loosening. Although, as shown in chapter 6, joint loosening does not occur without softening of the erectable component, which is not clearly evident in the data. Another guise of apparent increased harmonic dissipation is randomly transitional behavior, or chaos [36,44].

Low input forces result in the most linear and lightly dampened fundamental mode predictions. This is consistent with the MODE dynamics data shown and also with the low amplitude component data. The low amplitude adjustable pretension component model is linear and lightly dampened.

Slight noise in the predicted response plots was due to convergence problems in the DLA. The solution tended to two distinct but slightly varying solutions. This solution bifurcation may be the result of multiple solutions or the fact that the direct method incorporated numerical limit cycles.

Table 7.2 shows the comparison of the circle fit natural frequencies and damping ratios of the ground baseline data and model predictions. The fit modal parameters show agreement in frequency of 0.5% and in damping of 25% (good by any measure of damping at this level). When comparing the ground predictions to the data it must be reiterated that a third generation update was performed based on the ground low force measured natural frequencies. Given that the update was performed on the linear stiffness the nonlinear MODE model compares favorably with the data in predicting shifts in frequency and damping with increased excitation amplitude.

Table 7.3 shows the comparison of the circle fit natural frequencies and damping ratios of the space baseline data and model predictions. These modal parameters show good agreement in frequency of approximately 0.5% and disagreement in damping. The good agreement in frequency occurs after removal of suspension and gravity effects in the model. This shows that the model predicts stiffness effects of the

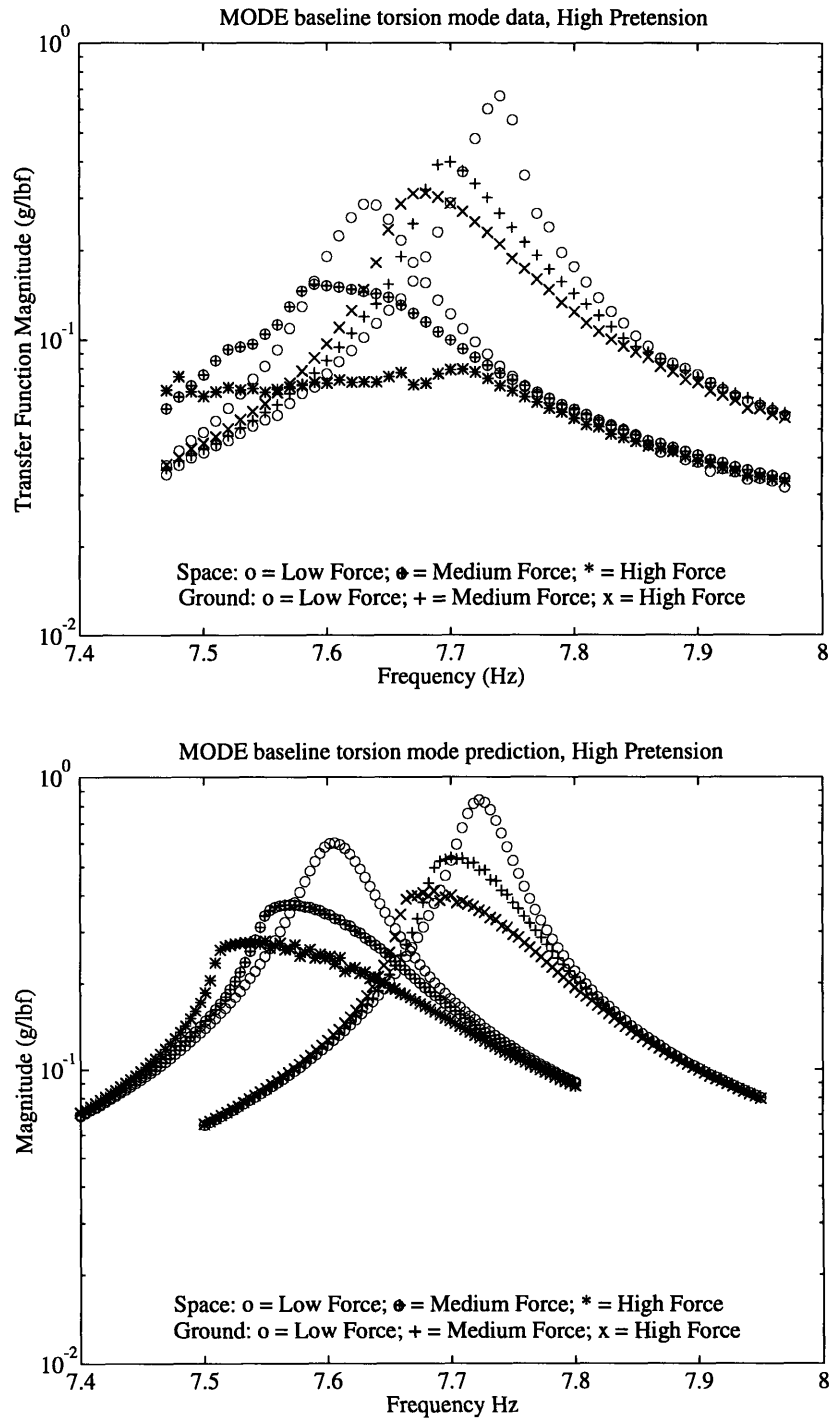


Figure 7.4: Ground *vs* space comparison of modal data and 10 d.o.f. predicted response for MODE baseline with high pretension in the adjustable pretension bay.

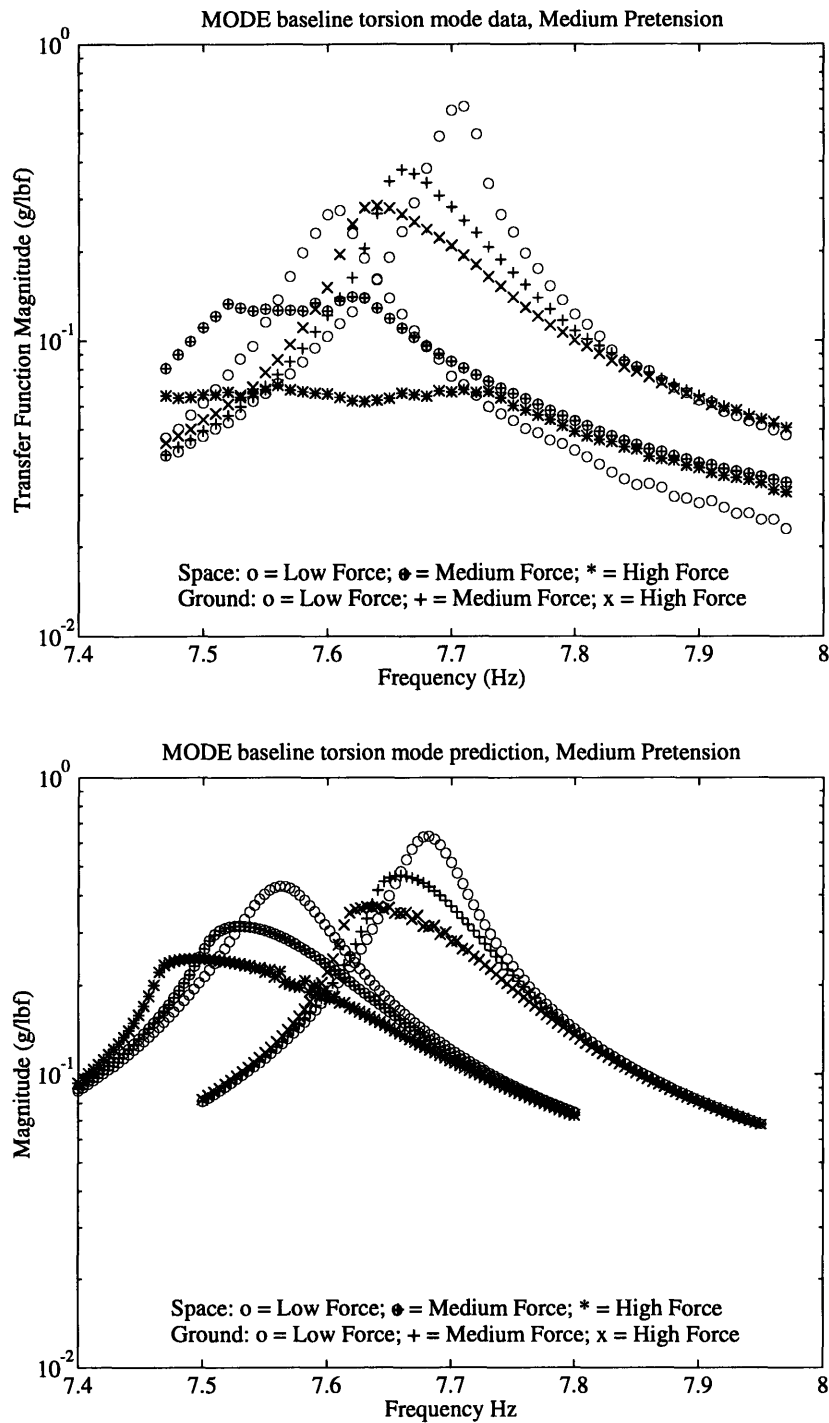


Figure 7.5: Ground *vs* space comparison of modal data and 10 d.o.f. predicted response for MODE baseline with medium pretension in the adjustable pretension bay.

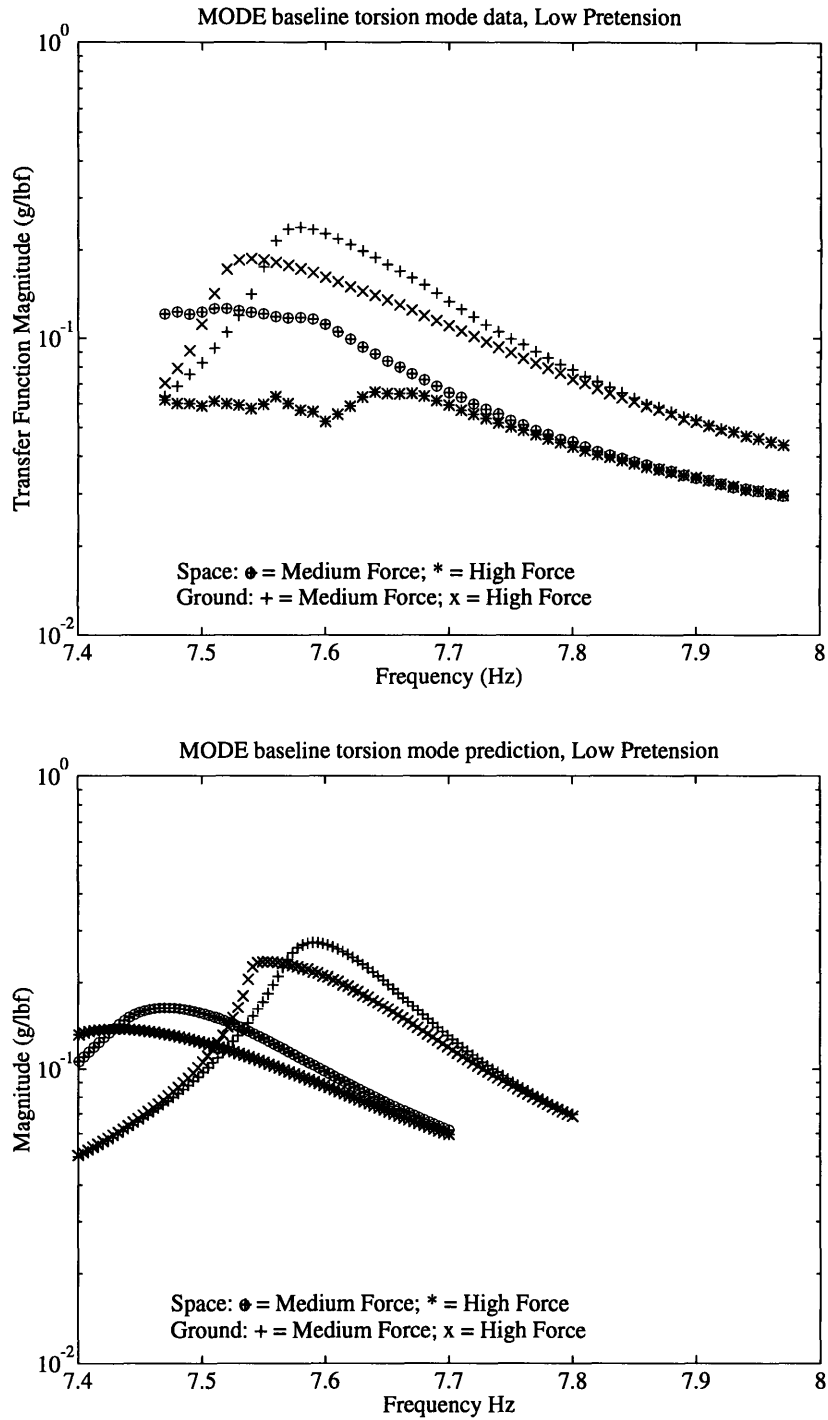


Figure 7.6: Ground *vs* space comparison of modal data and 10 d.o.f. predicted response for MODE baseline with low pretension in the adjustable pretension bay.

Table 7.2: Comparison of ground modal test and predicted natural frequencies and damping ratios for the MODE baseline configuration.

Amplitude	Modal Parameters			
	Modal Data Fit		Prediction	
	ω Hz	ζ %	ω Hz	ζ %
High Pretension				
low	7.74	0.24	7.72	0.26
med.	7.70	0.40	7.70	0.44
high	7.67	0.54	7.68	0.57
Medium Pretension				
low	7.71	0.27	7.68	0.34
med.	7.66	0.42	7.66	0.49
high	7.64	0.57	7.63	0.62
Low Pretension				
med.	7.58	0.67	7.59	0.60
high	7.54	0.86	7.55	0.74

Table 7.3: Comparison of space modal test and predicted natural frequencies and damping ratios for the MODE baseline configuration.

Amplitude	Modal Parameters			
	Modal Data Fit		Prediction	
	ω Hz	ζ %	ω Hz	ζ %
High Pretension				
low	7.63	0.40	7.60	0.36
med.	7.59	0.92	7.57	0.62
high	7.57	no fit	7.54	0.81
Medium Pretension				
low	7.61	0.34	7.56	0.50
med.	7.57	no fit	7.52	0.71
high	7.53	no fit	7.48	0.89
Low Pretension				
med.	7.52	no fit	7.47	1.01
high	7.49	no fit	7.42	1.19

change in gravity environment. The disagreement in damping is obvious in Figures 7.4, 7.5 and 7.6 where it can be seen that the space data exhibits flattened magnitude behavior. The tabulated space predictions show increased damping with amplitude but not of the same order as the data.

In general the predictions have captured the frequency shifts with change in excitation amplitude as well as change in gravity environment. The predictions show the space data to include behavior that is inconsistent with the ground dynamics tests.

Alpha configuration

Results of the MODE alpha predictions are shown in Figures 7.7, 7.8 and 7.9. The predictions are shown for high and low preloads in the alpha joint (bottom plots) and are plotted on the same frequency scale as the data (top plots). In the MODE alpha model the nonlinear behavior of the adjustable pretension bays in high pretension are compounded with that of the alpha joint bay.

Figure 7.7 shows the ground and space data and predictions for the high preload MODE alpha configuration. First, note the change in fundamental frequency after the inclusion of the alpha joint. This can be seen by comparing Figures 7.4 and 7.7, keeping in mind that a third generation update has been performed on the alpha joint model. Further comparison of these two figures shows that the softening and dampening of the fundamental mode with increased input amplitude is of greater severity in the alpha data and predictions. The ground data and predictions show that micro slip dynamic hysteresis, which is present in the alpha joint bay, serves to further soften and dampen the response over that of the baseline depicted in Figure 7.4.

Again the space magnitude data presented tends to severely dampen and flatten out with increased input amplitude. The space results predicted show similar softening and dampening with increased amplitude but again with damping not of the order of the data. The high force response space predictions did not converge to a solution in the frequency range 7.3 to 7.5 Hz. This region is where the alpha joint breaks into full macro slip. The solutions of the DLA in this region were seen to vary without ever converging. Full macro slip motion in the alpha joint results in a drastic change in the structure. The high preload space data shows a substantial region, below 7.37 Hz, where the magnitude of the response has been severely reduced. This indicates that the alpha joint is macro slipping.

Figure 7.8 and 7.9 show the low preload MODE alpha data and prediction for ground and space respectively. The ground and space results have been separated for clarity.

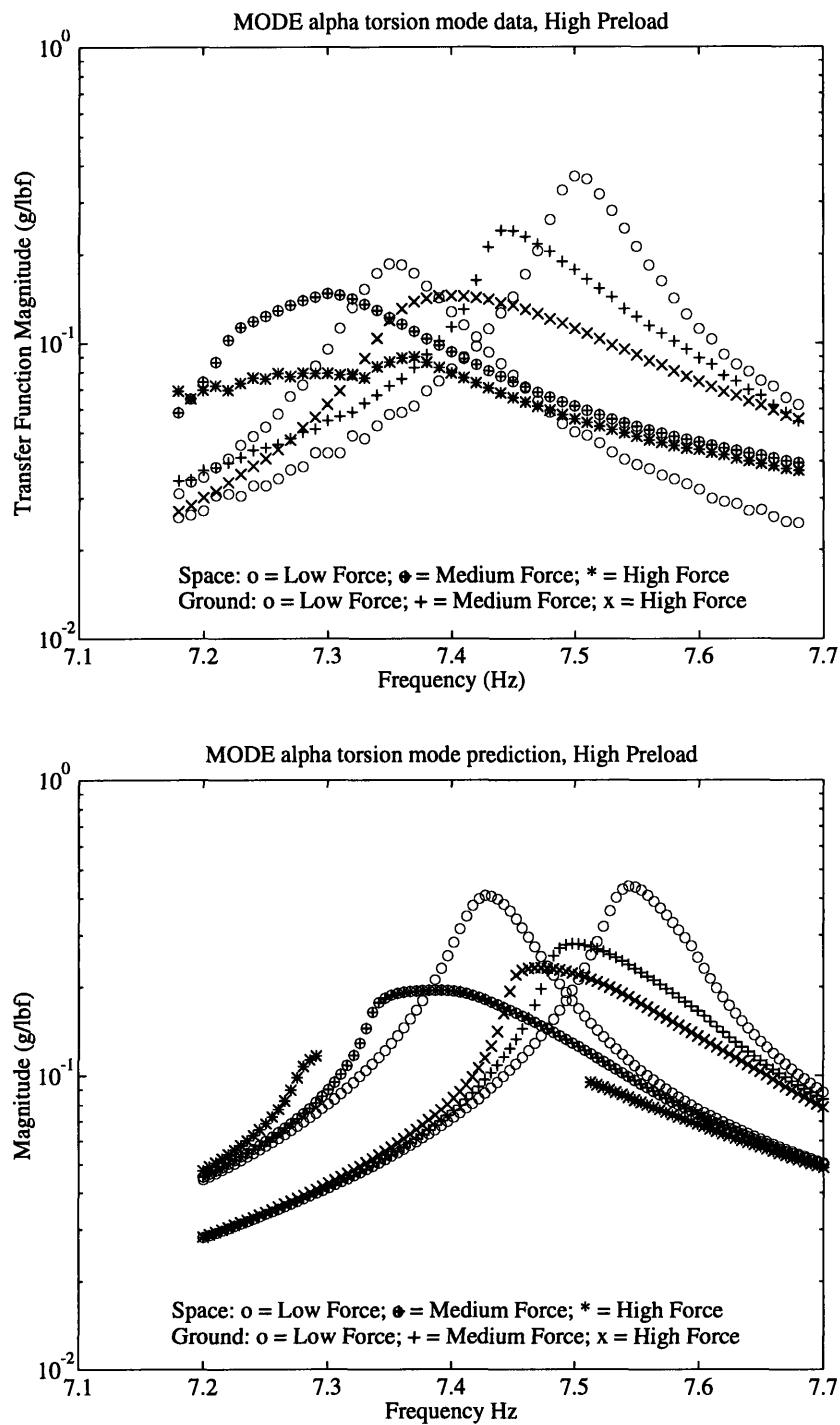


Figure 7.7: Ground *vs* space comparison of modal data and 10 d.o.f. predicted response for MODE alpha with high preload in the alpha joint bay.

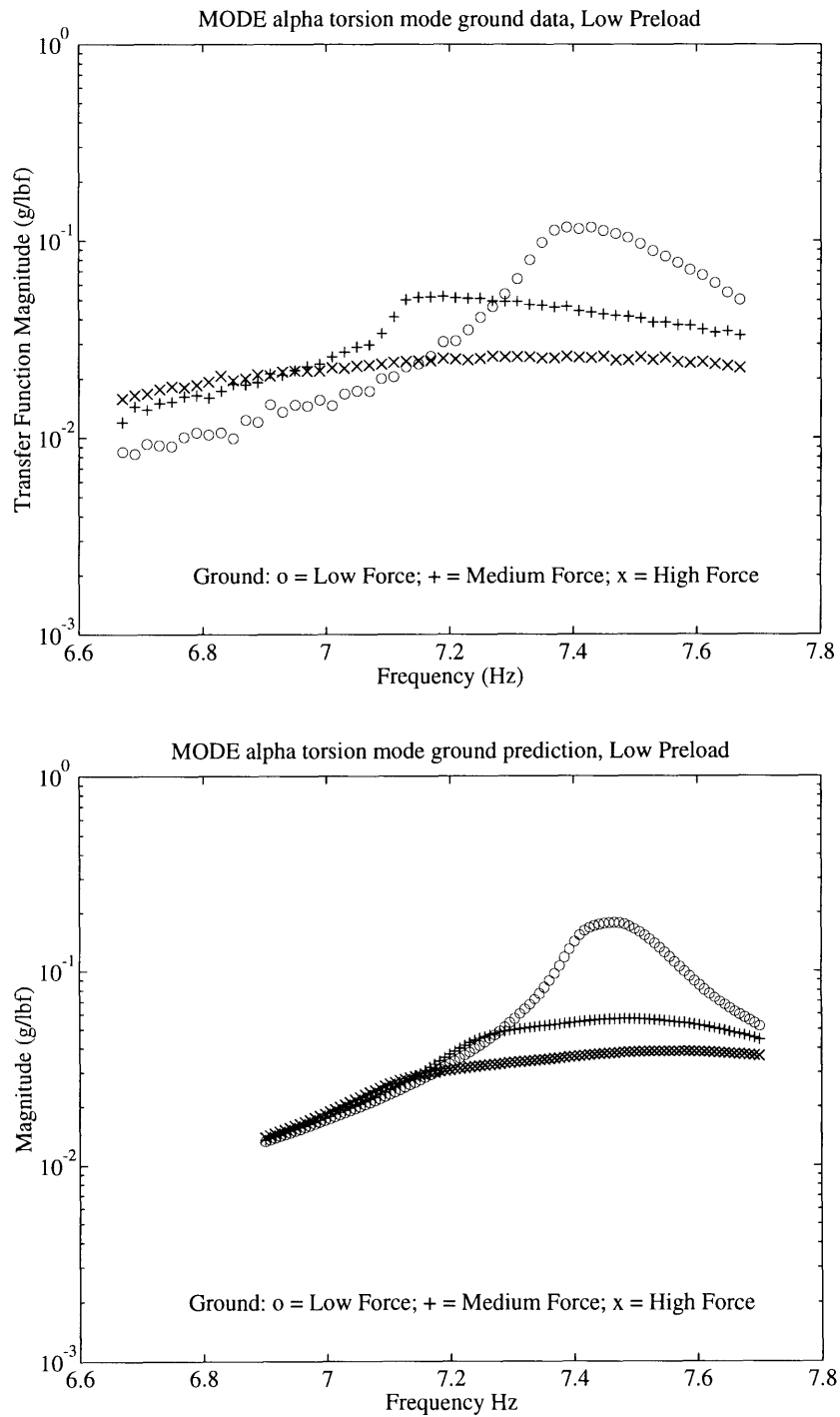


Figure 7.8: Comparison of ground modal data and 10 d.o.f. predicted response for MODE alpha with low preload in the alpha joint bay.

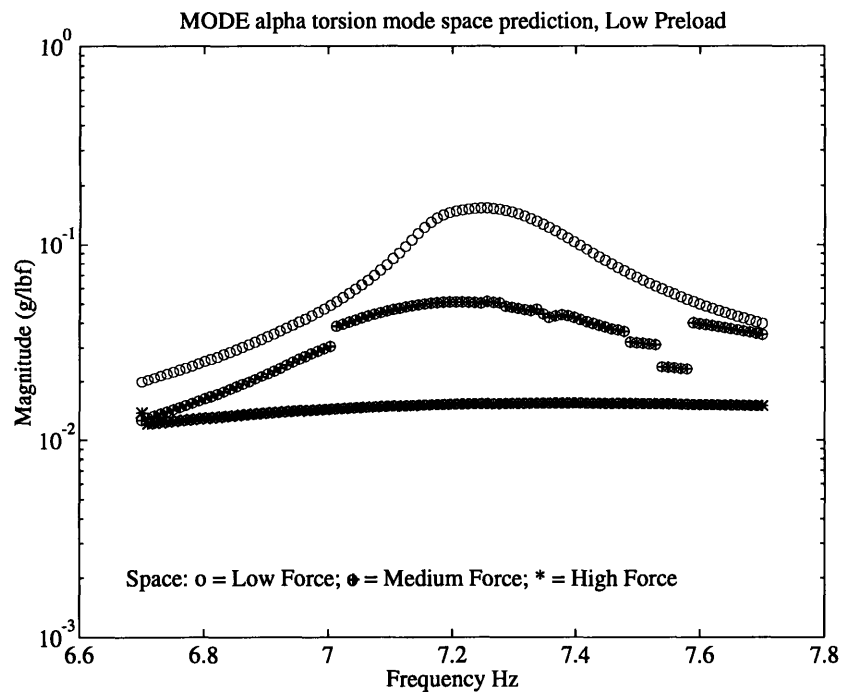
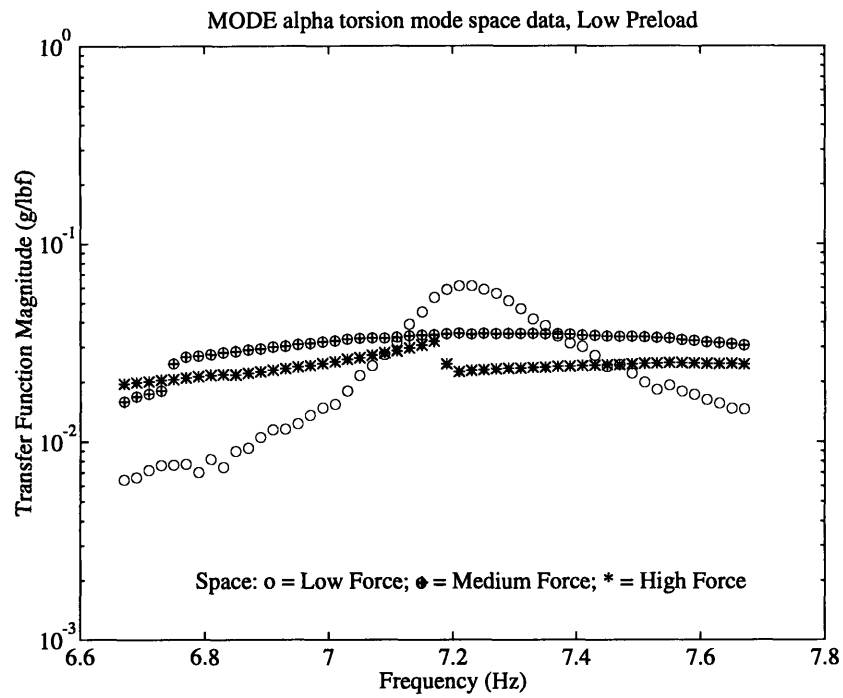


Figure 7.9: Comparison of space modal data and 10 d.o.f. predicted response for MODE alpha with low preload in the alpha joint bay.

Table 7.4: Comparison of ground modal test and predicted natural frequencies and damping ratios for the MODE alpha configuration.

Amplitude	Modal Parameters			
	Modal Data Fit		Prediction	
	ω Hz	ζ %	ω Hz	ζ %
High Preload				
low	7.50	0.37	7.54	0.39
med.	7.44	0.53	7.49	0.60
high	7.39	1.13	7.46	0.72
Low Preload				
low	7.41	1.37	7.45	1.01
med.	7.16	2.50	7.35	> 10
high	no fit	no fit	no fit	no fit

Low preload ground predictions, shown in Figure 7.8, show the mode magnitude flattening with increased amplitude. The flattening of the magnitude with increased excitation amplitude is consistent with that shown in the ground data. In the ground predictions the alpha joint is forced to remain in micro slip by the gravity preloads. The micro slip alpha component model included gravity preload as described in section 7.2.

The data of Figure 7.9 show the MODE alpha configuration in space. Gravity loading no longer forces the alpha joint to remain in micro slip. Macro slip behavior is witnessed in both the data and in the predictions as strongly nonlinear jump behavior. The predictions show jumps similar to that occurring in the space data. Jumps are predicted at medium and high forcing levels. The medium force predicted response shows multiple jumps in the region that the alpha joint is in macro slip, 7.03 Hz to 7.56 Hz. For the high input force the MODE alpha predictions show the alpha to break into macro slip at around 6.7 Hz and not recover micro slip behavior within the frequency window. This shows remarkable similarity to the high input force data.

The effect of the alpha joint macro slip is to separate the deployable structural sections with a spring and dashpot. The spring and dashpot both soften and dampen linearly with increased response amplitude. The alpha joint transmits loads to the rest of the structure while in macro slip, however, the drastic drop in stiffness and increase in damping with response amplitude serve to flatten out the fundamental mode.

Predicted modal parameters are compared to the modal parameters fit to the data in Tables 7.4 and 7.5. For the comparison of the ground modal parameters it is again

Table 7.5: Comparison of space modal test and predicted natural frequencies and damping ratios for the MODE alpha configuration.

Amplitude	Modal Parameters			
	Modal Data Fit		Prediction	
	ω Hz	ζ %	ω Hz	ζ %
High Preload				
low	7.35	0.51	7.43	0.41
med.	7.30	1.07	7.37	0.95
high	7.24	no fit	no fit	no fit
Low Preload				
low	7.21	1.21	7.32	0.98
med.	no fit	no fit	no fit	no fit
high	no fit	no fit	no fit	no fit

reiterated that an update of the alpha joint models was made based on the low force ground data natural frequencies. The parameters show that the predicted ground natural frequencies are good to within 1% where appropriate. Increased damping with increased input amplitude is predicted within 30% for the ground results. This shows that the compounded dynamic hysteresis mechanisms of the deployables and the alpha joint provide increased softening and dampening, with increased excitation amplitude, over that witnessed in the baseline data and predictions.

Space results reported in Table 7.5 show the frequencies are predicted within 1.5% while the increase in damping is predicted within 25% for the shown modal parameter fits. As with the baseline results, the change in environment has been adequately predicted by the model.

Severely nonlinear jump behavior is predicted and shows the structural response to be extremely sensitive to dynamic loading of the alpha joint. The predictions and data that exhibited strongly nonlinear behavior in the response were not fit with modal parameters.

In whole, the alpha joint model provides good predictions of both space and ground data while the joint is in its micro slip regime of operation. The analysis also predicts strongly nonlinear behavior such as jump phenomenon which is consistent with the data and is seen to occur when the alpha joint breaks into macro slip. The predictions, in general, show increased softening and dampening of the fundamental mode with increased input amplitude. This, again, is consistent with the data.

7.5 Summary

Torsion d.o.f. component models were refined and assembled into 10 d.o.f. models of the MODE baseline and alpha structures. To these MODE models gravity loads and suspension systems were added to simulate ground testing conditions. The MODE baseline and alpha models were updated based on the low input force ground data fundamental natural frequencies. Nonlinear predictions were made of the first fundamental structural mode of the MODE structures using updated component models and the DLA, point wise in frequency.

The predictions showed good agreement with the data when comparing frequency shifts due to amplitude of input and changes in environment. Ground predictions provided a good measure of damping while space predictions of damping indicate more complex behavior in the space data. Strongly nonlinear behavior was also predicted for the MODE alpha configuration.

Chapter 8

Conclusions and recommendations

Methodology

The force-state mapping approach was successfully extended to the characterization of multi degree of freedom systems with memory effects. A general constitutive model between quasi static transmitted force and mechanical state was developed, which distinguishes analytic effects from non analytic effects, and rate dependent effects from true memory effects.

The model was then specialized for deployable truss structures, erectable truss structures and a typical rotary joint. A purely analytic model was found to be a sufficient model for the erectable hardware. Models that included analytic, non analytic and memory terms were needed for the adjustable pretension and alpha joint hardware. Modeling the adjustable pretension and alpha joint hardware led to the discovery of fundamental dynamic hysteresis. The dynamic hysteresis models are representative of micro slipping of the dozens of frictional interfaces; at the pins of a deployable truss; and in the mechanism of the rotary joint. The DHM's have fundamental basis in bifurcating statistics and are consistent with Prandtl's postulated laws (1928).

Identification algorithms were developed which fit the component models to data. A linear parameter extended least squares algorithm was developed to evaluate potential inputs to a test component. Two sets of inputs, those that decoupled the applied loads and those that decoupled the response d.o.f., both ramped sinusoids, were found to be good choices for the MODE components. Iterative identification algorithms that fit the component models to the data were derived that relied on the nature of the inputs and on the nature of the component models.

A unique component testing device was constructed which allows controllable independent inputs of six axes of generalized load, measurements of six generalized

loads at each end of a cantilevered test bay, and measurements of six generalized d.o.f. at the unconstrained end. Computer control of the inputs allowed arbitrary time history and spatial direction of the unsteady force, in the presence of a potentially non-zero arbitrary steady preload.

The identified parameters for an nominally linear elastic calibration bay provide a good check of internal consistency, accuracy and precision. The iterative (decoupled d.o.f.) algorithm fit to the calibration bay data returned linear parameters quite close to the linear procedure supporting its use for the MODE components.

MODE Components

Overall nonlinear behavior in the MODE adjustable pretension bay data increases with decreased pretension. Bracing wire pretension is seen to effect the overall component stiffness and dissipation properties in all load transmission directions. Dynamic hysteresis, specifically softening and increased dissipation with increased amplitude, is more evident in the data as the pretension decreases. The majority of the nonlinear transmitted loads through the component are due to the frictional response of the preloaded deployable joints.

The identified parameters for the adjustable pretension MODE deployable bay are internally consistent and fit the data well. In particular, the dynamic hysteresis model is shown to be the dominant nonlinearity of the component. Models fit to the repeatability data, with the bracing cables disassembled and reassembled, reveal that the identified model is extremely sensitive to the bracing wire pretensions. In whole, the MODE adjustable pretension bay was found to be more nonlinear at low pretensions with the identified nonlinear parameters (at low pretensions) participating more in the test force range.

Erectable bay data shows the component to be essentially linear and close to symmetric in all load transmission directions. Identified models and participation factors confirmed that the component is essentially linear with the connecting joints tight. Vibration was found to induce erectable joint loosening. Purposefully loosened joints tests on the erectable component resulted in mild to strong nonlinear transmission properties in all directions across the component.

Data on the alpha joint bay, at both levels of preload, show significant nonlinearity when compared to the erectable bay data. Analytic model fits to the alpha joint data showed that the rotation mechanism strongly affects the load transmission properties, in all directions across the joint, in an unpredictable fashion with change in preload.

Data on the axial rotation d.o.f. operation of the alpha joint bay, at both levels

of preload, showed two regimes of hysteretic behavior. At low rotation amplitudes the alpha joint was found to behave in a mildly nonlinear fashion with dynamic hysteresis present, similar to that of the adjustable bay (softening and dampening with increased amplitude). At rotation amplitudes above the break amplitude (the break amplitude increased with preload) the alpha joint rotation mechanism was seen to be fully engaged, exhibiting coulomb-like softening and increased dissipation with increasing rotation amplitude.

Physical models of the MODE alpha joint bay were of the two regimes of rotation d.o.f. operation for both preloads. The micro slip dynamic hysteresis model fit the data well for both preloads reiterating the accumulated friction nature of the device at low amplitudes. The macro slip model fit the data reasonably well at high amplitudes for both preloads. The displacement dependent friction terms of the macro slip model model approximated the behavior seen in the data quite well for high preload and to a lesser degree at low preload.

Dynamics analysis

Assembled component models were formed to investigate the torsion mode of the MODE baseline and alpha structures in both ground and space dynamics tests. These models needed to be updated based on information from the low force ground dynamics tests. A Dynamic Linearization Analysis algorithm (DLA) was developed that stepped discretely in excitation frequency and computed the (successively linearized) nonlinear response of the models for multiple levels of excitation.

Predictions from the DLA algorithm compared well with the data confirming that the component nonlinear mechanisms, acting quasistatically, are major contributors to the overall nonlinear structural response. Further nonlinear effects present in the space data appeared to have severely dampened the fundamental mode at high amplitudes of excitation and are apparently not due to the quasistatic nonlinear nature of the components. Fit modal parameters predicted changes in frequency and damping, of the fundamental mode, with increased amplitude of excitation and change in gravity environment.

The MODE alpha model DLA also predicted strongly nonlinear jump phenomena in the discrete frequency response consistent with that witnessed in data. Jump phenomena are observed when the alpha joint changes operational regimes and the structure subsequently goes under a major structural change.

Further work need be done to understand the nature of the mode dampening in the space dynamics data. MODE model investigations using a full harmonic balance

technique, that includes sub and super harmonics, need be performed to investigate the possibility of randomly transitional behavior in the space dynamic response, which was not observed in the ground data. Further space tests will also show whether the dampening phenomena is repeatable under similar test conditions.

References

- [1] Arfken, G., "Mathematical Methods for Physicists", Academic Press, New York, 1970.
- [2] Barlow, M.S., "Modeling and Ground Modal Identification of Space Structures," S.M. thesis, MIT Cambridge, Ma., Jan. 1992.
- [3] Balmes, E., "Experimental/Analytical Predictive Models of Damped Structural Dynamics," PhD Thesis, Massachusetts Institute of Technology, May 1993.
- [4] Belvin, W.K. "Modeling of Joints for the Dynamic Analysis of Truss Structures." RPT: NASA-TP-2661.
- [5] Bowden, M.L., Dugundji, J., "Effects of Joint Damping and Joint Nonlinearity on the Dynamics of Space Structures," AIAA paper no. 88-2480.
- [6] Broyden, C.G., "A new Method of Solving Nonlinear Simultaneous Equations", Computer Journal, Vol. 12, pp. 94-99.
- [7] Cameron, T.M., Griffin, J.H., "An Alternating Frequency/Time Domain Method for Calculating the Steady-State Response of Nonlinear Dynamic Systems", Journal of Applied Dynamics, March 1989, Vol. 56, pp. 149-154.
- [8] Chapman, J.M., Shaw, F.H., Russell, W.C., "Nonlinear Transient Analysis of Joint Dominated Structures", AIAA paper no. 87-0892.
- [9] Craig, R.R., "A Review of Time-Domain and Frequency Domain Component Mode Synthesis", International Journal of Analytical and Experimental Modal Analysis, 1987, Vol. 2, No. 2, pp. 39-72.
- [10] Craig, R.R. *Structural Dynamics: An Introduction to Computer Methods*. John Wiley & Sons, 1981.
- [11] Crawley, E.F., O'Donnell, K.J., "Force-State Mapping Identification of Nonlinear Joints," AIAA Journal, Vol 25, NO. 7, pp. 1003-1010, July 1987.
- [12] Crawley, E.F., Aubert, A.C., "Identification of Nonlinear Structural Elements by Force-State Mapping," AIAA Journal, Vol. 24, Jan. 1986, pp. 155-162.

- [13] Crawley, E.F., Sigler, J.L., van Schoor, M.C., "Prediction and Measurement of Damping in Hybrid Scaled Space Structure Models." Dept. Aeronautics and Astronautics, MIT, SSL Report NO. 7-88, 1988.
- [14] Crawley, E.F., Barlow, M.S., van Schoor, M.C., "Variation in the Modal Parameters of Space Structures." 33rd SDM 1992. AIAA
- [15] Crawley, E.F., Barlow, M.S., van Schoor, M.C., Masters, B.P., Bicos, A.S., "Mid-deck Zero-Gravity Dynamics Experiment: Comparison of Ground and Flight Test Data," 43rd Congress of Int. Astr. Fed., Washington DC., Aug 28-Sep 5, 1992, to appear in AIAA Journal of Guidance, Control and Dynamics.
- [16] Dahl, R.P., Wilder, R. "Math Model of Hysteresis in Piezo-Electric Actuators for Precision Pointing Systems." Advances in the Astronautical Sciences, vol. 57, paper AAS-011.
- [17] Ewins, D.J., Modal Testing: Theory and Practice, John Wiley and Sons, Inc., New York, NY, 1984.
- [18] Felippa, C.A, Park, K.C., "Computational Aspects of Time Integration Procedures in Structural Dynamics." Journal of Applied Mechanics, September 1978, Vol. 45, pp. 595-602.
- [19] Fletcher, R., "Practical Methods of Optimization." 2nd ed., Wiley, New York, 1987.
- [20] Gelb, A. and Vander Velde, W.E., "Multiple-Input Describing Functions and Nonlinear System Design", McGraw-Hill, 1968.
- [21] Grocott, S.C.O., McMartin, D.G., Miller, D.W., "Experimental Implementation of a Multiple Model Technique for Robust Control of the MACE Test Article," Third Int. Conf. on Adaptive Structures, San Diego, CA, 1992.
- [22] Gronet, M.J., Crawley, E.F., Kienholz, D. "Design, Analysis, and Testing of a Hybrid-Scale Structural Dynamic Model of the Space Station." AIAA Paper No. 89-1340, 1989.
- [23] Gill, P. E., Murray, W., Wright, M. H., "Practical Optimization." Academic Press, London, UK, 1981.
- [24] Hertz, T.J., Crawley, E.F., "Displacement Dependent Friction in Space Structure Joints," AIAA Journal, Vol. 24, Dec. 1985, pp. 1998-2000.
- [25] Kienholz, D. A., Crawley, E. F., and Harvey, T. J. "Very Low Frequency Suspension Systems for Dynamic Testing." AIAA paper 89-1194.
- [26] Lau, S.L., Cheung, Y.K., Wu, S.Y., "Incremental Harmonic Balance Method With Multiple Time Scales for Aperiodic Vibration of Nonlinear Systems", Journal of Applied Mechanics, December 1983, Vol. 50, pp 871-876.

- [27] Ling, F.H., Wu, X.X. "Fast Galerkin Method and its Application to Determine Periodic Solutions of Nonlinear Oscillators", Int. Journal of Nonlinear Mechanics, 1987, Vol. 22, No. 2, pp 89-98.
- [28] Ludwigsen, J.S., "An Assessment of the Effects of Nonlinear Behavior on the Dynamic Performance of Large Orbiting Space Structures," Ph.D. thesis, Dept. of Civil Engineering, MIT, Sept. 1987.
- [29] Masters, B.P., Crawley, E.F., "Multiple Degree of Freedom Force-State Component Identification," 34th SDM, AIAA paper no. 93-1654, April 1992.
- [30] NATO Advanced Study Institute on Polynomial and Spline Approximation, "Polynomial and Spline Approximation: theory and Applications: Proceedings of the NATO Advanced Study Institute." Calgary Canada, August 26- September 2, 1978.
- [31] Park, K.C., "An Improved Stiffly Stable Method for Direct Integration of Nonlinear Structural Dynamic Equations." Journal of Applied Mechanics, 1975, Vol. 42, pp. 464-470.
- [32] Pinson, L.D. and Hanks, B.R. "Large Space Structures Raise Testing Challenges." *Astronautics and Aeronautics*, Vol. 21, No. 10, p. 34, 1983.
- [33] Prandtl, L., "Ein Gedankenmodell zur kinetischen Theorie der festen Korper." *Zeitschrift fur angewandte Mathematik und Mechanik*, Bd. 8 (1928), S-85-106.
- [34] Press, W.H., Flannery, B.P., Teukolsky, S.A. and Vetterling, W.T., *Numerical Recipes - The Art of Scientific Computing*. Cambridge University Press, 1986.
- [35] Rey, D. A., Alexander, H.F., "Gravity and Laboratory Suspension Effects on the Dynamics of Controlled Flexible Spacecraft." MIT SERC report 17-92, Dec. 1992.
- [36] Rudowski, J., Szemplinska-Stupnicka, W., "On an Approximate Criterion for Chaotic Motion in a Model of a Buckled Beam", *Ingenieur-Archiv* 57, pp. 243-255, 1987.
- [37] Saito, H., Sato, K., Yutani, T., "Nonlinear Forced Vibrations of a Beam Carrying Concentrated Mass Under Gravity", *Journal of Sound and Vibration*, 22 June 1976, 46(4), pp. 515-525.
- [38] Sarver, G.L., "Energy Transfer and Dissipation in Structures with Discrete Nonlinearities," Ph.D. thesis, Dept. Aeronautics and Astronautics, MIT, November 1987.
- [39] Spanos, J.T., Mingori, D.L., "Newton Algorithm for Fitting Transfer Functions to Frequency Response Measurements." *AIAA Journal of Guidance, Control, and Dynamics*, Vol. 16, No. 1, pp 34-39, February 1993.

- [40] Storer, D.M., Tomlinson, G.R., "Recent Developements in the Measurements and Interpretation of Higher Order Transfer Functions from Nonlinear Structures", Journal of Mechanical Systems and Signal Processing, 1993, Vol. 7, No. 2, pp. 173-189.
- [41] Szemplinska-Stupnicka, W., Bajkowski, J., "The 1/2 Subharmonic Resonance and Its Transistion To Chaotic Motion in a Nonlinear Oscillator", Int. Journal Non-Linear Mechanics, Vol. 21, No. 5, pp401-419, 1986.
- [42] Tseng, W.Y., Dugundji, J., "Nonlinear Vibrations of a Buckled Beam Under Harmonic Excitation", Journal of Applied Mechanics, Vol. 38, series E, No. 2, pp. 467-476.
- [43] Ueda, Y., "Explosions of Strange Attractors Exhibited by Duffings Equation", Ann. N.Y. Acad. Sci., Vol. 357, pp. 422-433, 1980.
- [44] Ueda, Y., "Randomly Transitional Phenomena in the Sytems Governed by Duffings Equation", Journal of Statistical Physics, Vol. 20, pp. 181-196, 1979.
- [45] Urabe, M., Reiter, A., "Numerical Computation of Nonlinear Forced Oscillations by Galerkin's Procedure", Journal of Mathematical Analysis and Applications, 1966, Vol. 14, pp. 107-140.
- [46] Wada, B.K., "Extension of Ground-Based Testing for Large Space Structures," AIAA SDM Conference, Apr. 1985, pp. 477-483. AIAA 85-0757.
- [47] Wada, B.K., "Ground Test of Large Flexible Structures," Tech. Rep. N87-24510, NASA, 1987.
- [48] Webster, M., Vander Velde, W., "Modeling Beam-Like Trusses with Nonlinear Joints with Application to Control." Dept. Aeronuatics and Astronautics, MIT, SERC Report NO. 5-91, 1991.

Appendix A

Off-diagonal block models

Reaction force to unconstrained d.o.f. models for the erectable bay and alpha joint bay are presented in this appendix.

A.1 Erectable bay

The erectable reaction force data was fit with the same basic model as the applied load to unconstrained d.o.f. data. The model is a cubic stiffness polynomial and a linear damping term. Table A.1 shows the fit models and participation factors.

The participation factors in Table A.1 show that the component is dominantly

Table A.1: Six d.o.f. reaction force to unconstrained d.o.f. model of the MODE erectable bay in SI units (*e.g.* N/m , N/m^2 , N/m^3 and $N/m/s$ respectively for the first three diagonal elements) for 7.5 Hz test frequency. Each identified parameter is followed by its participation in the test applied load range.

Models F_{ij}	Parameters							
	K_1	% Fm	K_2	% Fm	K_3	% Fm	D_1	% Fm
$-F_{71}$	8.414×10^5	100.2	-2.024×10^7	1.1	1.190×10^{10}	.0	8.254×10^1	.6
$-F_{82}$	8.019×10^5	102.9	-3.318×10^8	1.7	-9.344×10^{12}	1.9	2.216×10^1	.8
$-F_{93}$	7.464×10^5	101.2	1.098×10^{10}	1.4	4.452×10^{14}	.6	4.086×10^2	.0
$-F_{A4}$	6.222×10^4	101.5	1.322×10^7	2.5	-8.957×10^{10}	.2	7.782×10^0	.4
$-F_{B5}$	6.005×10^4	100.6	-5.042×10^5	.9	9.794×10^9	.2	7.750×10^0	.4
$-F_{C6}$	1.601×10^4	101.0	4.171×10^5	1.2	-3.048×10^8	.4	0.818×10^0	4.0
$-F_{74}$	8.358×10^4	104.4	1.216×10^7	1.8	-3.942×10^{11}	6.6	5.814×10^0	1.0
$-F_{A1}$	6.881×10^4	93.4	3.886×10^7	2.3	2.267×10^{12}	5.9	2.102×10^1	.6
$-F_{75}$	-9.019×10^4	94.3	1.213×10^7	1.4	-4.061×10^{11}	5.1	-4.534×10^0	2.7
$-F_{B1}$	8.982×10^4	97.3	-6.891×10^5	.0	1.818×10^{12}	3.8	-1.843×10^1	2.2
$-F_{84}$	8.215×10^4	96.8	2.514×10^7	3.4	1.260×10^{11}	2.0	3.375×10^0	1.4
$-F_{A2}$	-9.067×10^4	93.6	1.817×10^7	.7	-2.533×10^{12}	4.2	-1.175×10^1	1.4
$-F_{85}$	6.886×10^4	94.5	-7.418×10^5	.1	-1.815×10^{10}	.3	7.876×10^0	3.5
$-F_{B2}$	7.463×10^4	100.5	-2.840×10^7	1.5	-7.763×10^{11}	1.7	7.463×10^0	1.2
$-F_{96}$	-9.225×10^4	95.5	-1.201×10^7	5.8	-1.151×10^{10}	2.6	-1.004×10^1	2.6
$-F_{C3}$	-1.673×10^5	101.0	-8.835×10^8	5.3	5.201×10^{13}	3.1	-0.692×10^0	1.3

Table A.2: Six d.o.f. reaction force to unconstrained d.o.f. bicubic model of the high preload MODE alpha joint, in SI units, for 5 Hz test frequency. Each identified parameter is followed by its participation in the test applied load range.

Parameters C_{ij}	Models					
	F_{11}	% F_m	F_{22}	% F_m	F_{33}	% F_m
C_{01}	6.710×10^2	11.3	7.710×10^2	15.3	1.696×10^3	4.1
C_{02}	-6.494×10^3	.2	-1.356×10^4	.5	-6.086×10^5	1.0
C_{03}	-1.517×10^7	.9	1.699×10^7	1.4	-9.912×10^8	1.0
C_{10}	1.893×10^5	101.3	1.828×10^5	104.4	1.371×10^6	109.7
C_{20}	2.892×10^7	1.0	1.104×10^8	3.7	-3.606×10^9	6.2
C_{30}	-4.347×10^{11}	.9	-5.478×10^{12}	10.6	-1.503×10^{14}	5.6
C_{11}	-3.063×10^6	.3	-5.846×10^6	6.7	-1.358×10^7	.7
C_{12}	3.570×10^8	.7	-4.990×10^9	11.6	-1.176×10^{11}	4.0
C_{13}	-2.131×10^{11}	.7	2.194×10^{12}	10.3	-3.957×10^{12}	.1
C_{21}	1.045×10^9	.1	3.732×10^9	.3	-1.218×10^{12}	1.4
C_{22}	-2.063×10^{13}	2.4	1.017×10^{14}	13.8	3.298×10^{15}	2.4
C_{23}	-3.529×10^{16}	7.5	-5.631×10^{16}	15.4	5.483×10^{18}	2.6
C_{31}	-1.261×10^{14}	.4	9.645×10^{14}	3.8	3.416×10^{16}	.8
C_{32}	-1.406×10^{18}	9.7	6.898×10^{17}	5.4	-1.139×10^{20}	1.8
C_{33}	1.585×10^{20}	2.0	-5.117×10^{20}	8.1	-2.038×10^{23}	2.1

linear as was the case for the diagonal block models.

A.2 Alpha joint bay

The alpha joint reaction force data was fit with analytic bicubic models only. For both preloads the axial rotation model is for low amplitude motion and is not further investigated in terms of the micro slip model of section 3.3. The axial rotation reaction force data, however, do show similar trends to the micro slip model. Tables A.2, A.3, A.4 and A.5 show the fit diagonal models, F_{ii} , to the reaction force data.

Participation factors listed confirm the strongly nonlinear behavior in the alpha joint bay at both preload levels. Nonlinear term participation as high as 30% is again seen in the models. This is consistent with the diagonal block models of section 6.4.

Table A.3: Six d.o.f. (reaction force to unconstrained d.o.f.) bicubic model of the high preload MODE alpha joint continued.

Parameters C_{ij}	Models					
	F_{44}	% F_m	F_{55}	% F_m	F_{66}	% F_m
C_{01}	4.757×10^0	5.3	2.110×10^0	2.4	6.197×10^0	2.4
C_{02}	-2.682×10^1	.7	8.940×10^1	1.2	3.238×10^0	.1
C_{03}	-8.374×10^2	.5	-2.342×10^4	3.5	6.704×10^4	3.3
C_{10}	3.046×10^3	92.0	2.676×10^3	98.1	8.635×10^3	103.4
C_{20}	-5.181×10^5	9.8	-1.119×10^5	1.5	1.624×10^5	.7
C_{30}	-4.709×10^5	5.6	-5.356×10^5	2.6	-1.612×10^5	2.5
C_{11}	-2.641×10^4	18.5	1.613×10^4	6.7	-4.202×10^3	.6
C_{12}	-1.587×10^5	25.9	-3.028×10^5	14.5	-1.874×10^5	2.9
C_{13}	-3.484×10^7	13.2	-1.694×10^7	.9	6.185×10^7	1.1
C_{21}	-3.479×10^7	15.3	-3.067×10^7	4.6	2.750×10^7	1.3
C_{22}	-1.194×10^9	12.2	-4.802×10^9	8.3	-1.700×10^9	.9
C_{23}	4.157×10^{10}	9.8	7.511×10^{11}	14.8	1.731×10^{10}	.1
C_{31}	5.090×10^{10}	14.0	-1.119×10^{11}	6.1	6.058×10^{10}	1.1
C_{32}	4.024×10^{12}	25.7	3.283×10^{11}	.2	-6.420×10^{12}	1.3
C_{33}	1.157×10^{14}	17.2	1.658×10^{15}	11.8	-1.046×10^{15}	2.4

Table A.4: Six d.o.f. reaction force to unconstrained d.o.f. bicubic model of the low preload MODE alpha joint, in SI units, for 5 Hz test frequency. Each identified parameter is followed by its participation in the test applied load range.

Parameters C_{ij}	Models					
	F_{11}	% F_m	F_{22}	% F_m	F_{33}	% F_m
C_{01}	1.054×10^3	14.9	6.793×10^2	12.8	2.201×10^3	5.2
C_{02}	8.633×10^4	2.2	4.706×10^4	1.7	-1.173×10^5	1.8
C_{03}	1.995×10^7	.9	1.859×10^6	.1	-1.761×10^9	1.8
C_{10}	2.220×10^5	101.2	1.993×10^5	108.7	1.409×10^5	108.2
C_{20}	1.055×10^5	2.8	1.064×10^5	3.1	-3.611×10^9	5.8
C_{30}	-1.254×10^{12}	1.9	-5.821×10^{12}	9.3	-1.604×10^{14}	5.5
C_{11}	-2.915×10^5	2.4	-5.979×10^5	6.1	-2.369×10^7	1.2
C_{12}	-1.459×10^9	2.1	-5.592×10^9	10.7	-1.879×10^{11}	6.2
C_{13}	-2.004×10^{12}	5.2	6.751×10^{11}	2.4	1.177×10^{12}	.0
C_{21}	9.983×10^{10}	4.6	1.134×10^{10}	.6	-2.971×10^{12}	3.2
C_{22}	-1.177×10^{14}	9.7	-6.306×10^{10}	.0	7.442×10^{15}	5.2
C_{23}	-1.775×10^{17}	2.6	4.795×10^{13}	.0	1.026×10^{19}	4.7
C_{31}	2.723×10^{15}	7.2	1.088×10^{14}	.3	6.235×10^{15}	1.4
C_{32}	-2.988×10^{18}	14.2	1.186×10^{18}	6.6	-8.531×10^{19}	1.3
C_{33}	-2.155×10^{21}	18.2	-2.193×10^{20}	2.3	-3.380×10^{23}	3.3

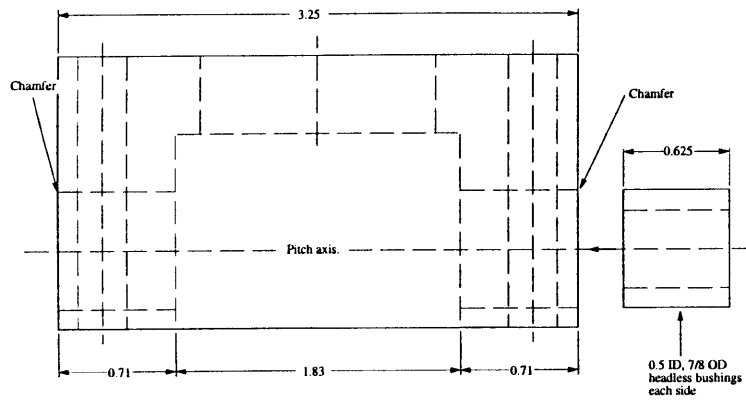
Table A.5: Six d.o.f. (reaction force to unconstrained d.o.f.) bicubic model of the low preload MODE alpha joint continued.

Parameters C_{ij}	Models					
	F_{44}	$\%F_m$	F_{55}	$\%F_m$	F_{66}	$\%F_m$
C_{01}	7.034×10^0	8.1	2.991×10^0	2.6	2.993×10^0	1.3
C_{02}	-1.152×10^2	2.5	-3.467×10^1	.6	8.178×10^2	1.0
C_{03}	4.185×10^3	1.8	-3.666×10^3	1.1	1.910×10^6	6.9
C_{10}	3.171×10^3	101.7	3.224×10^3	92.1	7.725×10^3	106.8
C_{20}	-3.936×10^5	6.8	-3.288×10^5	5.5	-3.201×10^5	.4
C_{30}	-1.218×10^9	11.2	1.838×10^8	1.8	-5.444×10^{10}	6.4
C_{11}	-1.685×10^4	10.4	1.039×10^4	5.4	1.727×10^5	6.9
C_{12}	-1.159×10^6	13.7	-6.484×10^5	6.2	-5.574×10^7	6.4
C_{13}	7.535×10^6	1.7	-3.038×10^7	5.3	-2.727×10^{10}	9.1
C_{21}	-2.456×10^7	8.1	-1.865×10^6	.6	3.051×10^9	11.2
C_{22}	-1.399×10^9	8.9	7.695×10^7	.4	-1.326×10^{11}	1.4
C_{23}	1.202×10^{10}	1.5	3.209×10^{10}	3.3	-6.555×10^{14}	20.1
C_{31}	5.923×10^{10}	10.5	-3.053×10^{10}	5.5	-3.615×10^{13}	12.3
C_{32}	8.302×10^{12}	28.2	-3.505×10^{11}	1.2	2.960×10^{15}	2.9
C_{33}	1.444×10^{14}	9.4	1.637×10^{14}	9.9	7.631×10^{18}	21.6

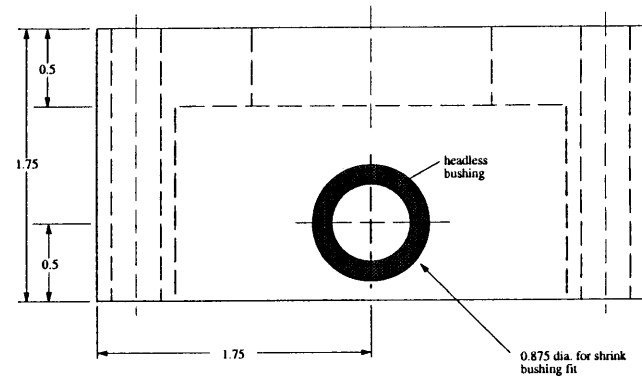
Appendix B

Component tester drawings

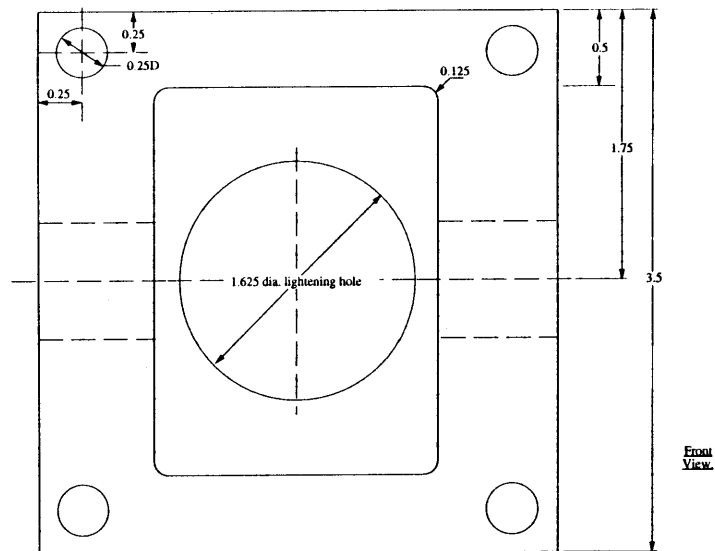
This appendix presents selected MODE component tester mechanical drawings.



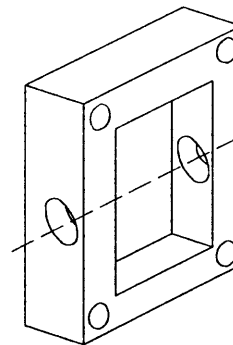
Plan View.



Side View.



Front View.




Pitch Axis.

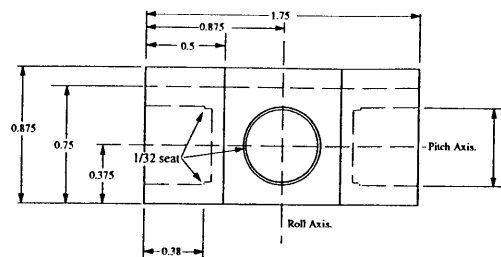
Perspective.

N.B Perspective not to scale.

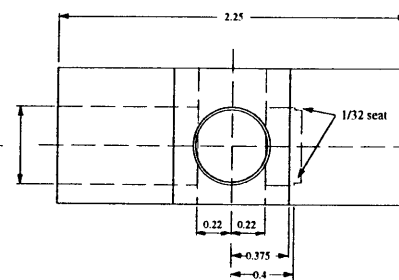
Notes

1. Material; Aluminum 6061
2. Tolerances ± 0.0005
3. Headless bushings required for shrink fit
4. Two teflon spacers/washers required
ID 0.50, OD 0.875 x 0.040 thick.
5. Li

Tolerances Unless Noted Otherwise .0 \pm .10 .00 \pm .02 .000 \pm .005 Angular $\pm 0^{\circ}30'$		 M.I.T. Space Engineering Research Center	
Surface Finish (Unless Noted)	Date: June 21	Scale: 2:1	
Drawn Brett Masters	Title: Component tester bearing housing part one.		
Engineer			
	Drawing No. mode-02-1	Rev. March 14	

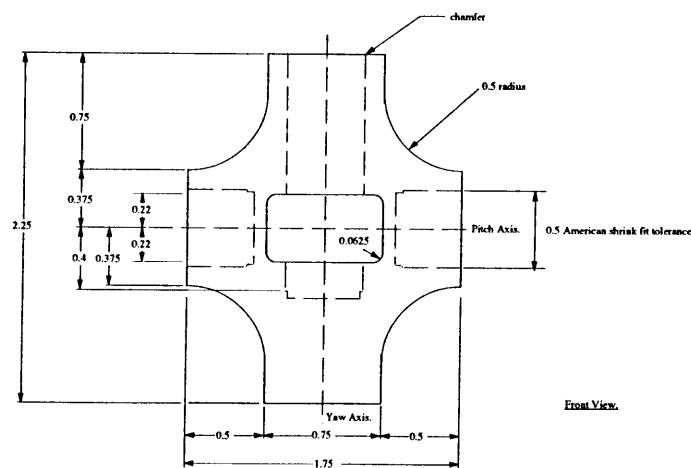


Plan View.

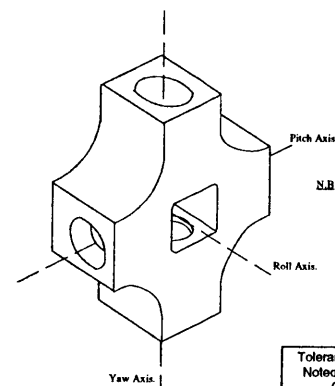


Side View.

0.5 American shrink fit tolerance
class 6




Front View.

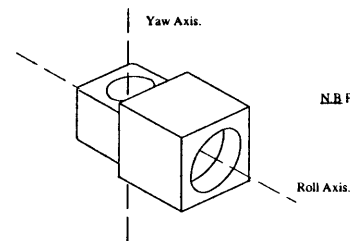
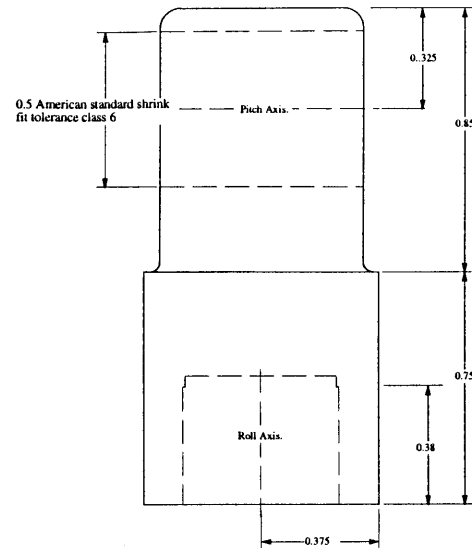
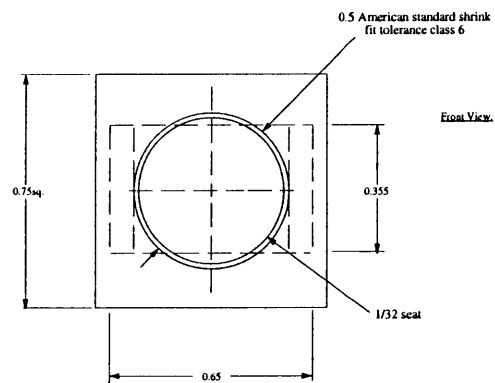
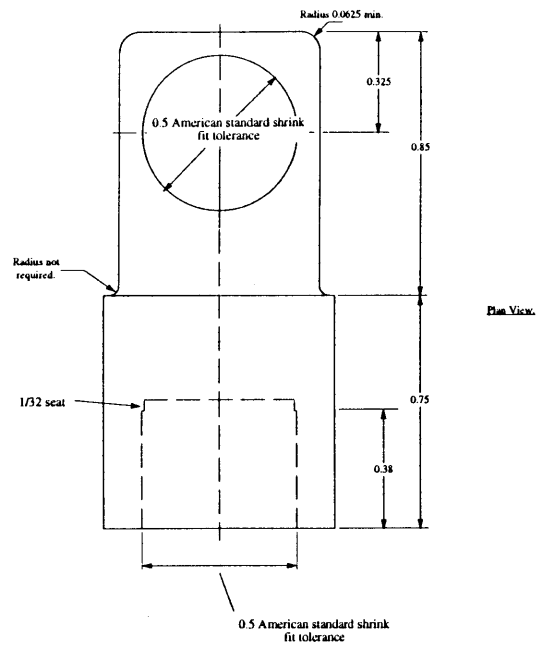


N.B perspective not to scale.

Notes

1. Material; steel suitable for shrink fitting
2. Tolerances for bearing seats and channels optimum for American standard shrink fits
3. Other tolerances ± 0.001
4. Two teflon spacers required ID 0.5 OD 0.625 x 0.0425 thick


Tolerances Unless Noted Otherwise 0 ± .10 .00 ± .02 .000 ± .005 Angular ±0°30'	 <div>M.I.T. Space Engineering Research Center</div>		
Surface Finish (Unless Noted)	Date: June 25.	Scale: 1:2	
Drawn Brett Masters	Title: Mode Bearing Housing Part 2		
Engineer	Drawing No. MODE-02-2		Rev. March 1

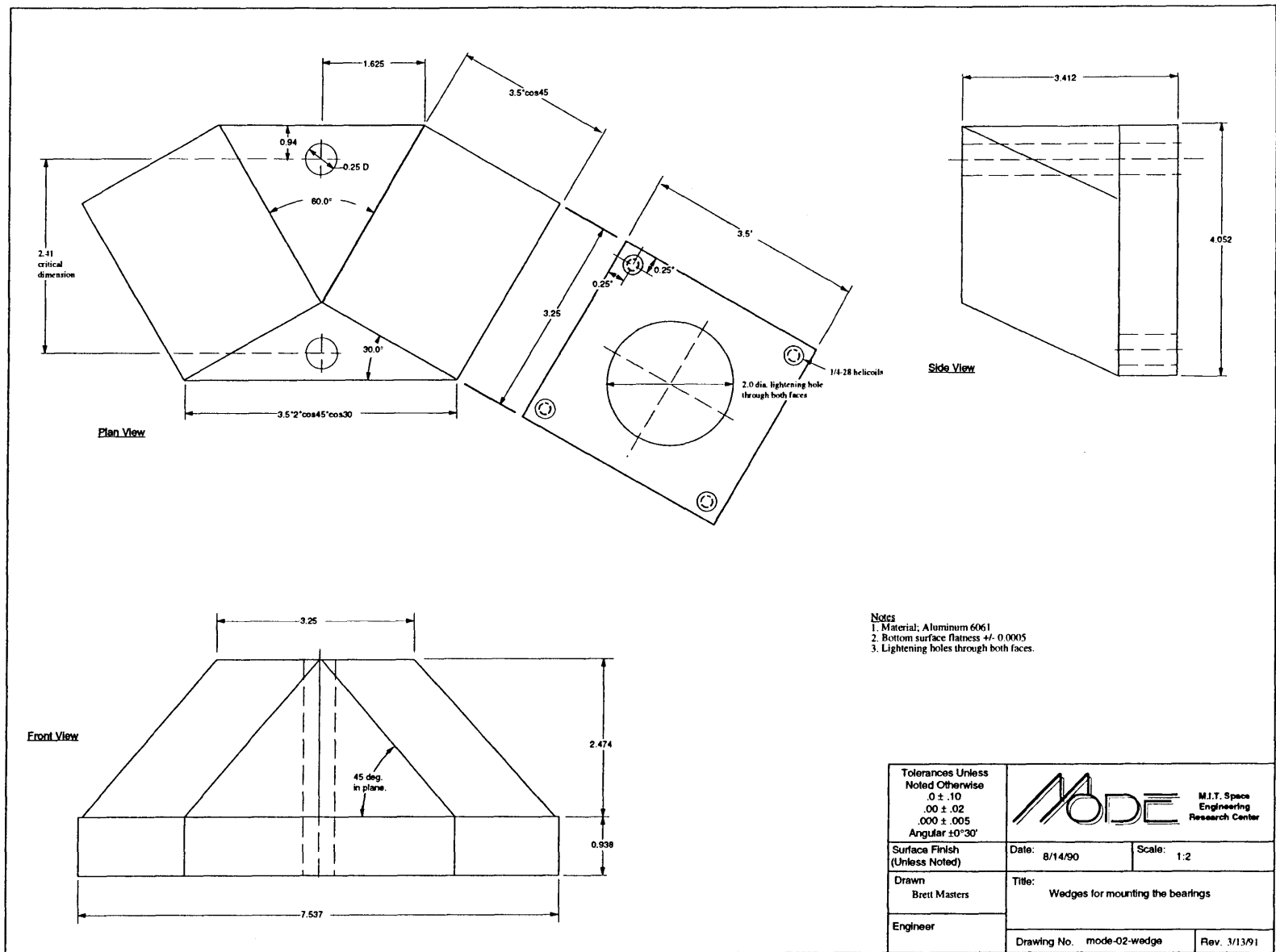


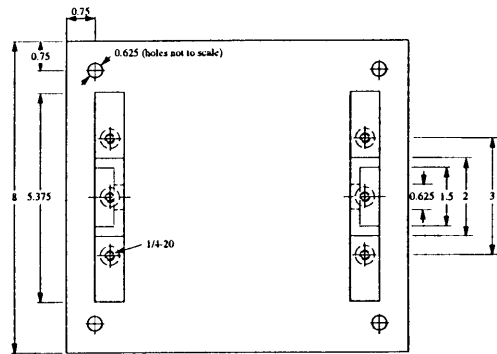
N.B. Perspective not to scale.

Notes

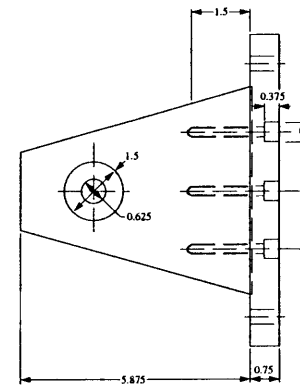
1. Material; Steel suitable for shrink fit
2. Tolerances for bearing fits - American standard class 6.
3. All other tolerances ± 0.001
4. Female bearing mate to this part can be found in drawing mode-sting-1

Tolerances Unless Noted Otherwise .0 \pm .10 .00 \pm .02 .000 \pm .005 Angular $\pm 0^{\circ}30'$	 M.I.T. Space Engineering Research Center	
Surface Finish (Unless Noted)	Date: summer 90	Scale: 4:1
Drawn Brett Masters	Title: Mode Bearing Housing Part 3	
Engineer	Drawing No. mode-02-3	Rev. March 15

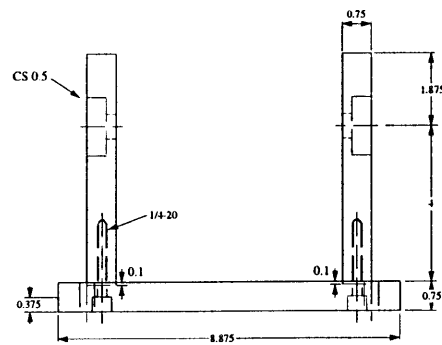




Plan View




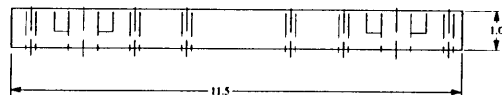
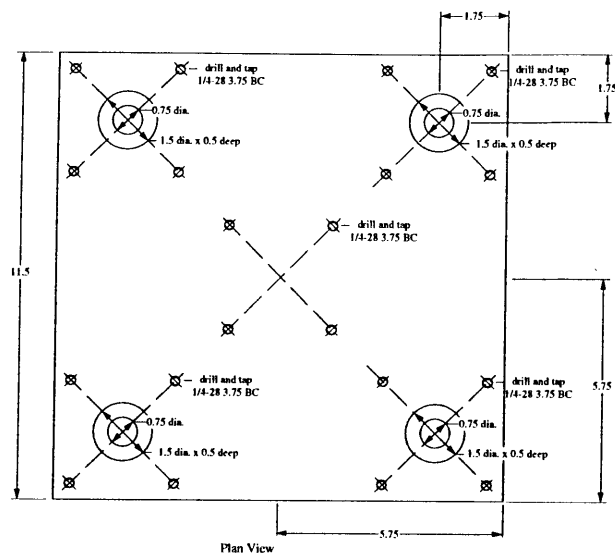
Side Elevation




Front Elevation

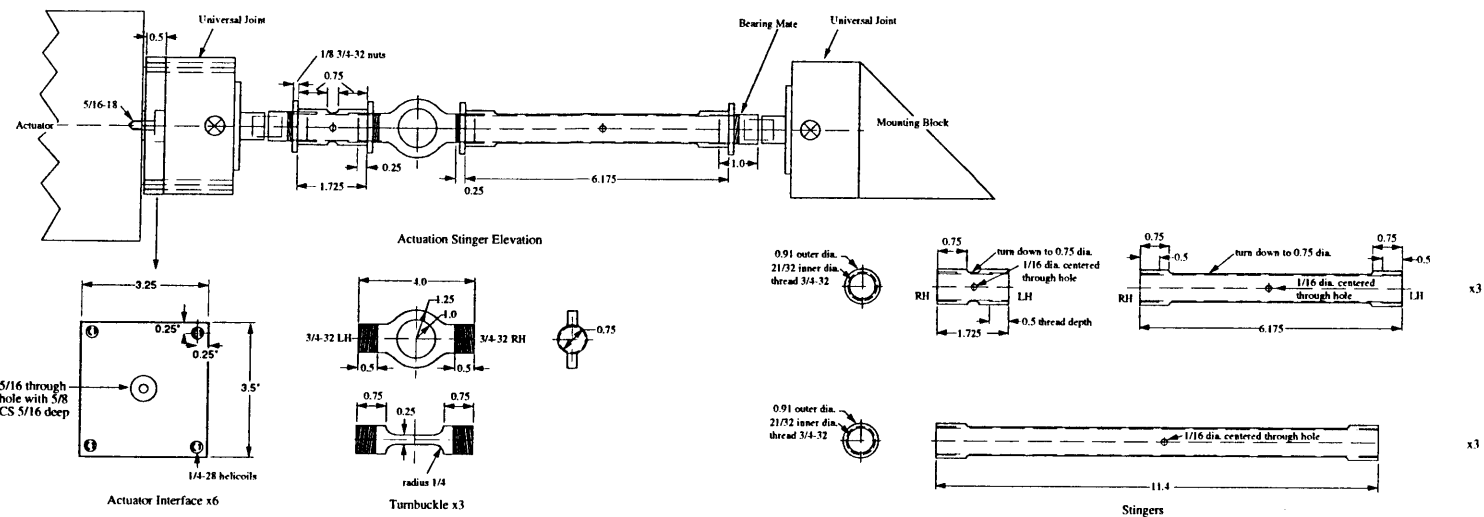
- Notes
1. Material: Aluminum 6061
 2. Bottom surface flatness equivalent to the bottom plate
 3. Attach holes enlarged for maneuverability

Tolerances Unless Noted Otherwise 0 ± .10 .00 ± .02 .000 ± .005 Angular ±0°30'				M.I.T. Space Engineering Research Center
Surface Finish (Unless Noted)		Date: Feb 28	Scale: 1:2	
Drawn Brett Masters		Title: Actuator Stands		
Engineer		Drawing No. mode-act-1		Rev. March 11




- Notes
1. Material: 1018
 2. Top surface flatness ± 0.0005

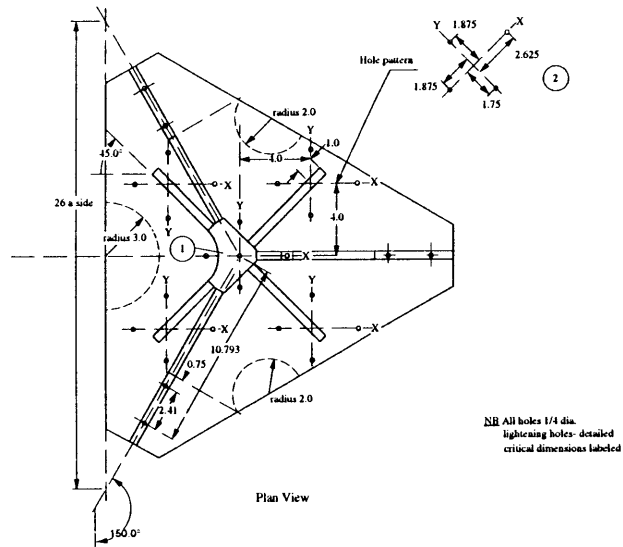
Tolerances Unless Noted Otherwise .0 \pm .10 .00 \pm .02 .000 \pm .005 Angular $\pm 0^{\circ}30'$	 M.I.T. Space Engineering Research Center	
Surface Finish (Unless Noted)	Date: March 7	Scale: 1:2
Drawn Brett Masters	Title: Base For Mode STA Bay	
Engineer	Drawing No. mode-box-2	Rev. March 12



Notes

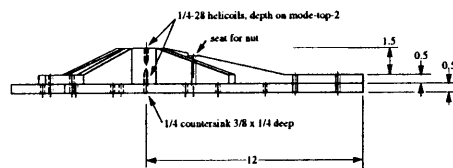
1. Turnbuckle
 - Quantity 3 required
 - Material: Aluminum 6061 hard coated, 2 mil
 - LH, RH thread as detailed
2. Stingers
 - Quantity three of each required
 - Inner threads teflon coated
 - Material: Aluminum 6061 hard coated, 2 mil
3. Bearing Mate
 - Material 1018 Steel
 - Use american standard shrink fit tolerances for 0.5 dia.
 - Quantity 6 LH thread required.
 - Quantity 6 RH thread required.
4. Actuator Interface
 - Quantity 6 required
 - Material: Aluminum 6061


Tolerances Unless Noted Otherwise .0 ± .10 .00 ± .02 .000 ± .005 Angular ±0°30'	 M.I.T. Space Engineering Research Center	
Surface Finish (Unless Noted)	Date: Feb 25 1991	Scale: 1:2 unless otherwise stated
Drawn Brett Masters	Title: Mode Stinger Arrangement for Component/Bay Tester	
Engineer	Drawing No. mode-sting-1	Rev. March 13

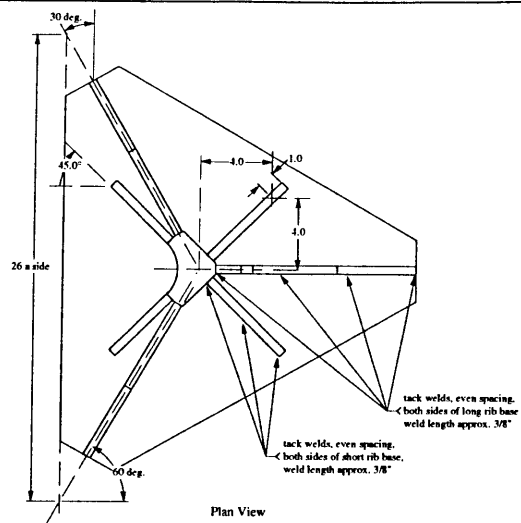


- 1 Center piece, drawing follows.
- 2 The specific hole pattern matches a mounting plate for the JR3 force balances. It was chosen so as not to coincide with the ribs. Note the left-handed arrangement for the top left hand corner of the STA

Notes
1. Material; cast aluminum
2. Bottom surface flatness ± 0.0005



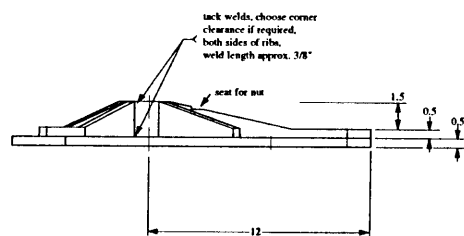
Tolerances Unless Noted Otherwise .0 ± .10 .00 ± .02 .000 ± .005 Angular ±0°30'			M.I.T. Space Engineering Research Center
Surface Finish (Unless Noted)	Date:	Scale:	6:26
Drawn	Title: Top Plate of Mode Component Tester		
Engineer	Drawing No.	mode-top-1	Rev.



Plan View




Side Elevation

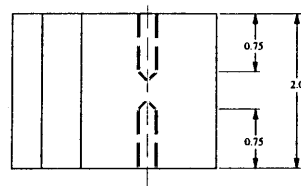
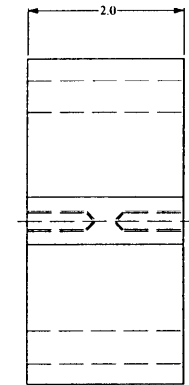
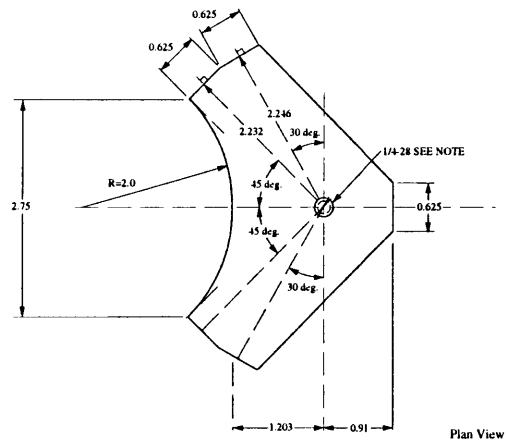


Front Elevation

Notes

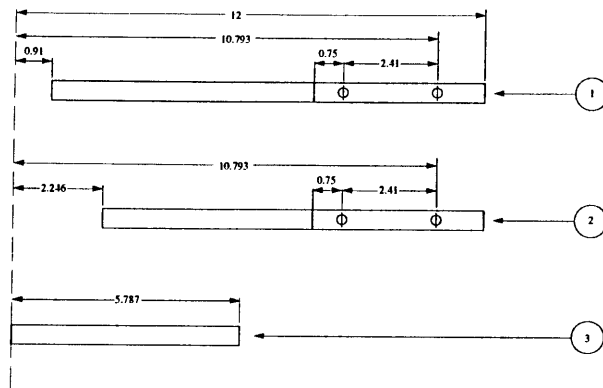
1. Material: Aluminum jig plate.
2. Long ribs require 3 evenly spaced 1/4-20 CS pins.
3. Short ribs require 2 evenly spaced 1/4-20 CS pins.
4. Center piece requires 3 arranged 1/4-20 CS pins to plate.
5. Only welds, ribs to center piece.
6. Hole pattern on next drawing.
7. Bottom surface flatness after hole pattern ± 0.0005

Tolerances Unless Noted Otherwise .0 \pm .10 .00 \pm .02 .000 \pm .005 Angular $\pm 0^{\circ}30'$	 M.I.T. Space Engineering Research Center	
Surface Finish (Unless Noted)	Date:	Scale: 6:26
Drawn	Title: Top Plate of Mode Component Tester	
Engineer	Drawing No. mode-top-1_assembly	Rev. March 12

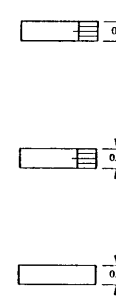


- Notes
1. Material; Cast Aluminum
 2. Tap and drill after attachment to plate.

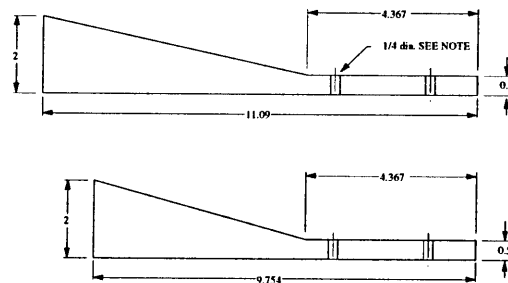
<p>Tolerances Unless Noted Otherwise</p> <p>.0 ± .10 .00 ± .02 .000 ± .005 Angular ±0°30'</p>	<p>MODE M.I.T. Space Engineering Research Center</p>	
<p>Surface Finish (Unless Noted)</p>	<p>Date: Feb 27</p>	<p>Scale: 1:1</p>
<p>Drawn Ben Masters</p>	<p>Title: Top Plate Center Piece</p>	
<p>Engineer</p>	<p>Drawing No. mode-top-2</p>	<p>Rev. March 11</p>



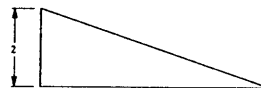
Plan View



Side Elevation




Front Elevation



Parts

1. Quantity one required
2. Quantity two required
3. Quantity four required

NB Ribs to be welded to top plate
as in drawing mode-top-1 assembly
before hole pattern drilled.

Tolerances Unless Noted Otherwise .0 ± .10 .00 ± .02 .000 ± .005 Angular ±0°30'	 M.I.T. Space Engineering Research Center	
Surface Finish (Unless Noted)	Date: Feb 28	Scale: 1:2
Drawn Brett Masters	Title: Ribs for Actuation Plate.	
Engineer	Drawing No. mode-top-3	Rev. March 11

3504-11